

# Optimal Control of a DC Microgrid with Renewable Energy Sources

---

Gulin, Marko

Doctoral thesis / Disertacija

2019

*Degree Grantor / Ustanova koja je dodijelila akademski / stručni stupanj:* **University of Zagreb, Faculty of Electrical Engineering and Computing / Sveučilište u Zagrebu, Fakultet elektrotehnike i računarstva**

*Permanent link / Trajna poveznica:* <https://urn.nsk.hr/urn:nbn:hr:168:029039>

*Rights / Prava:* [In copyright](#)/[Zaštićeno autorskim pravom.](#)

*Download date / Datum preuzimanja:* **2024-07-28**



*Repository / Repozitorij:*

[FER Repository - University of Zagreb Faculty of Electrical Engineering and Computing repository](#)





University of Zagreb

FACULTY OF ELECTRICAL ENGINEERING AND COMPUTING

Marko Gulin

**OPTIMAL CONTROL OF A DC  
MICROGRID WITH RENEWABLE  
ENERGY SOURCES**

DOCTORAL DISSERTATION

Zagreb, 2019



University of Zagreb

FACULTY OF ELECTRICAL ENGINEERING AND COMPUTING

Marko Gulin

**OPTIMAL CONTROL OF A DC  
MICROGRID WITH RENEWABLE  
ENERGY SOURCES**

DOCTORAL DISSERTATION

Supervisor: Professor Mario Vašak, PhD

Zagreb, 2019



Sveučilište u Zagrebu

FAKULTET ELEKTROTEHNIKE I RAČUNARSTVA

Marko Gulin

**OPTIMALNO UPRAVLJANJE  
ISTOSMJERNOM MIKROMREŽOM S  
OBNOVLJIVIM IZVORIMA ENERGIJE**

DOKTORSKI RAD

Mentor: Prof. dr. sc. Mario Vašak

Zagreb, 2019.

Doctoral dissertation was written at the University of Zagreb Faculty of Electrical Engineering and Computing, Department of Control and Computer Engineering

Supervisor: Professor Mario Vašak, PhD

Thesis contains 107 pages

Thesis no.:

DOCTORAL DISSERTATION EVALUATION COMMITTEE

Professor Mato Baotić, PhD

University of Zagreb Faculty of Electrical Engineering and Computing, Croatia

Associate Professor Hrvoje Pandžić, PhD

University of Zagreb Faculty of Electrical Engineering and Computing, Croatia

Associate Professor Danijel Pavković, PhD

University of Zagreb Faculty of Mechanical Engineering and Naval Architecture, Croatia

DOCTORAL DISSERTATION DEFENSE COMMITTEE

Professor Mato Baotić, PhD

University of Zagreb Faculty of Electrical Engineering and Computing, Croatia

Associate Professor Hrvoje Pandžić, PhD

University of Zagreb Faculty of Electrical Engineering and Computing, Croatia

Associate Professor Danijel Pavković, PhD

University of Zagreb Faculty of Mechanical Engineering and Naval Architecture, Croatia

Date of doctoral dissertation defense: September 27, 2019

*To my wife Iva.*

---

## ABOUT THE SUPERVISOR

Mario Vašak was born in Bjelovar, Croatia, in 1980. He earned his bachelor's and doctoral degrees in electrical engineering from the University of Zagreb Faculty of Electrical Engineering and Computing (UNIZG-FER), Croatia, in 2003 and 2007, respectively. His research interests are in the domain of dynamic system predictive control with application to systems in the low-carbon energy sector, including wind turbines and photovoltaic systems, energy-efficient buildings, microgrids, water distribution systems, and electrified railway transport.

After earning his bachelor's degree, he was employed at the Department of Control and Computer Engineering (ZARI) within UNIZG-FER, where he currently holds positions of Full Professor and Head of the Laboratory for Renewable Energy Systems (LARES). He is the main inventor of US patent WO2012140455A2 for fault-tolerant control of wind turbine generators. He designs hierarchical and modular energy management for buildings with integrated microgrids, economically optimizing interoperation. He had a leading or collaborator role on several research projects funded by the European Union or Croatian national funds related to implementation and verification of this concept, from consumption control in individual buildings to coordination of infrastructure and buildings in a smart city environment (Interreg Danube 3Smart, ERDF PC-ATE Buildings, ENHEMS-Buildings and FER-KIET, HRZZ 3CON, FP7 UrbanWater and DYMASOS). He is author or co-author of more than 100 internationally reviewed papers.

He is a member of the professional associations IEEE and the Croatian Society for Communications, Computing, Electronics, Measurements and Control (KoREMA). He has received more than 10 acknowledgments and awards for his scientific and professional achievements, in particular "Top Scholarship for Top Students" from "Nacional" weekly magazine in 2002, the silver plaque of the award "Josip Lončar" from FER for outstanding doctoral dissertation and the "Končar Award" for doctoral dissertation with industrial applications in 2007, and the "National Science Award of the Republic of Croatia" for young scientists in the field of technical sciences and "Vera Johanides Award" from the Croatian Academy of Engineering (HATZ) in 2008.



---

## O MENTORU

Mario Vašak rođen je 1980. godine u Bjelovaru, Hrvatska. Diplomirao je i doktorirao u polju elektrotehnike na Sveučilištu u Zagrebu Fakultetu elektrotehnike i računarstva (FER), Hrvatska, 2003. i 2007. godine, tim redom. Njegovi istraživački interesi su u području prediktivnog upravljanja dinamičkim sustavima s primjenama na sustave iz niskougličnog energetskog sektora, uključujući energetske učinkovite zgrade, vjetroagregate, fotonaponske sustave, mikromreže, elektrificirani željeznički promet i vodoopskrbne sustave.

Po završetku studija zapošljava se u Zavodu za automatiku i računalno inženjerstvo (ZARI) na FER-u, gdje je trenutno redoviti profesor i voditelj Laboratorija za sustave obnovljivih izvora energije (LARES). Glavni je izumitelj US patenta WO2012140455A2 za upravljanje vjetroagregatima otporno na kvarove generatora. Radi na razvoju hijerarhijskog i modularnog gospodarenja energijom u zgradama s integriranim mikromrežama za omogućavanje ekonomski optimalnog međudjelovanja. Bio je voditelj ili suradnik na nekoliko istraživačkih projekata financiranih iz fondova Europske unije i nacionalnih fondova vezanih uz implementaciju i provjeru navedenog koncepta, od upravljanja potrošnjom u pojedinim zgradama do koordinacije sustava distribucije električne energije i vode u okruženju naprednog (pametnog) grada (Interreg Danube 3Smart, EFRR PC-ATE Buildings, ENHEMS-Buildings, i FER-KIET, HRZZ 3CON, FP7 UrbanWater i DYMASOS). Autor je ili koautor više od 100 međunarodno recenziranih radova.

Član je stručnih udruga IEEE i Hrvatskog društva za komunikacije, računarstvo, elektroniku, mjerenja i automatiku (KoREMA). Primio je više od 10 različitih priznanja i nagrada za svoj znanstveni i stručni rad, među kojima se ističu "Top stipendija za top studente" tjednika "Nacional" 2002. godine, srebrna plaketa "Josip Lončar" FER-a za posebno istaknuti doktorski rad i nagrada koncerna Končar za doktorski rad s primjenom u industriji 2007. godine, te "Državna nagrada za znanost" za znanstvene novake u području tehničkih znanosti i "Vera Johanides" nagrada Akademije tehničkih znanosti Hrvatske (HATZ) 2008. godine.

---

## ACKNOWLEDGMENTS

*There is nothing better in the world  
than to be in the grace of God.*

— Josemaría Escrivá, *The Way* (1939)

Throughout my doctoral dissertation work I have received support and assistance making my job as researcher more interesting and joyful. Foremost, I thank my supervisor, Prof. Mario Vašak, for enormous patience and commitment, which goes beyond words. Thank you professor for always representing my best interests and for all advice that improved the dissertation and helped me grow as researcher and engineer! I am also greatly indebted to my mentor, Prof. Nedjeljko Perić, for giving me the opportunity to become a member of his research group and to learn from his vast experience. I can only hope that someday I also reach the level of enthusiasm and experience of both.

To all professors, colleagues, and friends with whom I had the honor to work with, thank you. To Prof. Jadranko Matuško for explaining complex topics simply and intuitively, Prof. Mato Baotić for his valuable contributions and for making it possible to visit and learn from other research groups, Prof. Ivan Petrović for ensuring funds for our research laboratory, Tomislav Pavlović for always being ready to help in the laboratory, from cabling to discussing research results, Boško Milešević for countless discussions on how to *save* the world, Vinko Lešić for being there when I needed to share satisfying and frustrating research moments, Doug Maly for proofreading critical parts of the dissertation, Damir Josić for his valuable advice, *teta* Blanka for helping me fight the administration beast, and to all Faculty services for being there when needed. A special thanks also goes to the doctoral dissertation evaluation and defense committee for their valuable suggestions.

To all developers that contribute to the open-source community and selflessly make their work available, thank you. Just to mention a few of the tools used here, L<sup>A</sup>T<sub>E</sub>X with MiKTeX and Texmaker to typeset the dissertation, PGF/TikZ languages to draw schematics and diagrams, *circuitikz* package to create electrical drawings, *pgfplots* package to generate plots, and YALMIP with ILOG CPLEX to implement and solve optimization problems.

None of this would have been possible without love and support from my family. I will always be grateful to my mom Mirjana for directing me towards education from my earliest years, dad Ivica for planting the seed of my affection for everything technical, and brother Ivan for having faith in me. To my wife Iva for her immense love and patience, standing by my side throughout the entire period of work on the dissertation and helping me in every way possible, thank you. This work is dedicated to you and our son Lovro!

Marko Gulin  
Zagreb, March 2020



---

## ABSTRACT

A microgrid is a cluster of distributed generation sources, storage devices and loads that operate together. Ideally, they improve reliability and quality of the power supply and the power system. Microgrids are expected to significantly reduce power transmission losses and enable integration of a large share of renewable energy sources. This doctoral dissertation primarily develops control algorithms for residential grid-connected DC microgrids with renewable energy sources to improve stability and optimize techno-economic microgrid operation. To that aim, the dissertation addresses several important aspects: (i) modeling of all systems included in the microgrid; (ii) prediction of day-ahead production and consumption in a microgrid by means of machine learning and artificial intelligence, which is especially challenging due to strong correlation of predicted variables with atmospheric conditions; (iii) power flow management based on convex optimization and the model predictive control scheme with receding horizon principle, which is developed in a stochastic framework to account for production and consumption prediction uncertainty; and (iv) DC link (bus) voltage control with power flow reference tracking, whereas optimal power references are generated by the power flow management control loop. Control (decision) variables in the system under consideration are charge and discharge profiles for local energy storage devices, that serve as an energy buffer which improves system stability and enables joining a decentralized electricity market. In the simplest scenario, a microgrid would buy electricity during low electricity price intervals and sell during high price intervals, which reduces microgrid operating costs. However, the decision of when to buy and sell energy to the utility grid and in which amount, i.e., when to charge and discharge storage devices, is a complex function of the predicted microgrid load, power production, current storage device state of charge, and of the predicted electricity price provided by the electricity market. Together, this is the central subject of the conducted research. Note that all concepts developed in this dissertation can also be applied to AC microgrids.

The residential DC microgrid under consideration was constructed at the Laboratory for Renewable Energy Systems (LARES) at the University of Zagreb Faculty of Electrical Engineering and Computing (UNIZG-FER), Croatia. The developed concepts are verified by experiments in LARES based on real meteorological and electricity price data, i.e., they are tested in a real operating environment. Predictions of relevant meteorological variables, which are used as inputs to predict day-ahead production and consumption in the microgrid, are provided by the Croatian Meteorological and Hydrological Service (DHMZ).

**KEY WORDS:** dc microgrid, smart grid, renewable energy systems, distributed storage, photovoltaic system, machine learning, artificial intelligence, load prediction, battery state of charge estimation, Kalman filter, ultracapacitor, fuel cell, power flow management, convex optimization, linear program, model predictive control, stochastic control framework, voltage stability

---

## SAŽETAK

Mikromreža je skup distribuiranih sustava za proizvodnju i pohranu energije i lokalnih potrošača koji djeluju zajedno s ciljem povećanja pouzdanosti energetske sustava i kvalitete opskrbe energijom. Očekuje se da će mikromreže znatno smanjiti gubitke u prijenosu električne energije, te kroz distribuiranu pohranu omogućiti integraciju veće količine obnovljivih izvora energije. S obzirom na to da je većina sustava za proizvodnju i pohranu električne energije u mikromrežama, kao i većina današnjih potrošača u kućanstvima i zgradama, izvedena u istosmjernoj tehnologiji, prirodan odabir tehnologije izvedbe energetske sabirnice koja povezuje komponente mikromreže bio bi istosmjerna tehnologija. Tako bi se iz upotrebe mogli izbaciti ispravljači u gotovo svim kućanskim uređajima. Istraživanja su pokazala da bi izbacivanje AC-DC pretvorbe u kućanstvima na globalnoj razini dovelo do povećanja energetske učinkovitosti od čak 5–15%.

Brzim razvojem tehnologije sustava obnovljivih izvora energije oni postaju sve konkurentniji tradicionalnim sustavima za proizvodnju električne energije temeljenim na fosilnim i nuklearnim gorivima. Slijedom toga, državna poticajna sredstva za energiju proizvedenu iz obnovljivih izvora uskoro će se u potpunosti ukinuti, što je već slučaj u zemljama s visokim udjelom proizvodnje iz obnovljivih izvora. Tada će do posebnog izražaja doći mikromreže koje će, zbog mogućnosti lokalne pohrane energije, moći odlučiti kada i koliko energije razmijeniti s elektroenergetskom mrežom na temelju brojnih tehničkih i ekonomskih kriterija i ograničenja. Također je bitno istaknuti i potrebu za regulacijom energetske sustava na strani potražnje, budući da se u proizvodnoj strukturi energetske sustava s velikom količinom obnovljivih izvora energije sve više smanjuje udio i regulacijski kapacitet elektrana na fosilna goriva. Upravljive mikromreže postaju važnim elementom za funkcionalnost upravljanja potražnjom putem dinamičkih cijena energije, te isto tako za funkcionalnost odgovora potražnje. Tome u prilog ide i činjenica da će prema Direktivi (EU) 2018/844 sve nove zgrade od 2020. godine u zemljama članicama Europske unije trebati biti tzv. *zero-net-energy* zgrade. Zamisao je da svaka nova zgrada proizvodi električnu energiju za lokalnu upotrebu, uglavnom temeljeno na fotonaponskim sustavima, a eventualni manjak ili višak razmjenjuje s elektroenergetskom mrežom. Prije nego mikromreže uđu u široku upotrebu, potrebno je riješiti brojne tehničke, ekonomske i regulatorne izazove. U ovom doktorskom radu predložena su rješenja za neke od tehničkih izazova s ciljem šire primjene istosmjernih mikromreža.

Mikromreže se uglavnom temelje na obnovljivim izvorima energije, sustavima za pohranu energije koji omogućavaju vremenski pomak između proizvodnje i potrošnje energije, te na učinskim pretvaračima koji predstavljaju upravljačke točke u mikromreži i koji pravilnim radom osiguravaju stabilnost sustava i kvalitetu isporučene električne energije. Za optimalan rad mikromreže, modeli svih sustava obuhvaćenih mikromrežom moraju biti poznati. Ovdje se prvenstveno misli na modele za estimaciju stanja napunjenosti i upravljanje spremnicima energije, te za predikciju dostupnosti izvora energije i potrošnje u mikromreži. S obzirom na to da su izvori energije najčešće temeljeni na obnovljivim izvorima energije čija je proizvodnja nestalna zbog snažne ovisnosti o atmosferskim prilikama, u ovom doktorskom radu poseban je naglasak stavljen na predikciju proizvodnje energije iz fotonaponskog sustava s opisom nesigurnosti, za što su korištene tehnike strojnog učenja.

Upravljanje razinom napona na energetskej sabirnici mikromreže veoma je važno sa stajališta pouzdanosti i kvalitete opskrbe električnom energijom. Većina istraživačkih radova u literaturi koji se bave temom upravljanja razinom napona u mikromreži odnose se na izmjenične mikromreže. Upravljanje u istosmjernoj mikromreži jednostavnije je utoliko što nema potrebe za sinkronizacijom i upravljanjem tokovima jalove snage. Upravljački algoritmi razinom napona mogu se podijeliti na (i) decentralizirane, u kojima svi sustavi mikromreže (podjednako) sudjeluju u regulaciji napona na sabirnici, te (ii) centralizirane, u kojima jedan sustav preuzima zadatak regulacije napona, dok ostali sustavi imaju slobodu u smislu tokova snage u okviru svojih ograničenja. U ovom doktorskom radu razmatra se centralizirani pristup regulacije napona, kako bi se na sustave koji ne sudjeluju u regulaciji napona mogli primijeniti unaprijed izračunati profili tokova snage dobiveni iz nadređenog kruga upravljanja, koji osiguravaju optimalan tehno-ekonomski rad mikromreže.

Procedura proračuna optimalnih tokova snage u mikromreži u uvjetima nesigurnosti veoma je važna u scenariju s decentraliziranim tržištem električne energije, odnosno pri dinamičkim promjenama cijene razmjene električne energije s elektroenergetskom mrežom. Za optimalan rad mikromreže, procedura u obzir treba uzimati brojne tehničke i ekonomske kriterije i ograničenja, npr. učinkovitost punjenja i pražnjenja spremnika energije kao i utjecaj na životni vijek spremnika, profil kretanja cijene električne energije itd. Također je važno uzeti u obzir i uvjete u kojima mikromreža radi, npr. stanje napunjenosti spremnika, predikcija dostupnosti izvora energije i potrošnje u mikromreži itd. Pitanje kako ugraditi postavne veličine tokova snage na razini upravljivih komponenata mikromreže te u isto vrijeme osigurati stabilnost napona sabirnice i kvalitetnu opskrbu energijom, predstavlja poseban izazov u upravljanju mikromrežom.

Doktorski rad podijeljen je u 6 poglavlja organiziranih u 3 dijela: (i) dio "General considerations" (Uvodna razmatranja) sadrži 2 poglavlja: "Introduction" (Uvod) i "Laboratory setup" (Laboratorijski postav); (ii) dio "System identification" (Identifikacija sustava) sadrži 2 poglavlja: "Photovoltaic system" (Fotonaponski sustav) i "Load prediction" (Predikcija potrošnje); (iii) dio "Optimal control" (Optimalno upravljanje) sadrži 2 poglavlja: "Power flow management" (Upravljanje tokovima snage) i "Power flow reference tracking" (Slijeđenje postavnih vrijednosti snaga).

U Dijelu I. "General considerations" predstavljene su opće informacije o mikromrežama te je postavljena hipoteza istraživačkog problema. U Poglavlju 1. "Introduction" dani su motivacija za provedeno istraživanje i kratki pregled trenutnog stanja područja istraživanja u literaturi, postavljen je istraživački problem, te su predstavljeni glavni istraživački doprinosi dokorskog rada. U Poglavlju 2. "Laboratory setup" opisan je laboratorijski postav istosmjerne mikromreže u Laboratoriju za sustave obnovljivih izvora energije (LARES) na Sveučilištu u Zagrebu Fakultetu elektrotehnike i računarstva (FER). Uz opis mikromreže, predstavljeni su i fotonaponska elektrana te meteorološka stanica u LARES-u, koji su također korišteni za razvoj i provjeru metoda razvijenih u dokorskome radu.

U Dijelu II. "System identification" razvijeni su modeli svih sustava obuhvaćenih mikromrežom, koji su korišteni za razvoj i parametrisiranje sustava optimalnog upravljanja. U Poglavlju 3. "Photovoltaic system" razvijen je nadomjesni električni model fotonaponskog sustava s novim numeričkim algoritmima za bržu identifikaciju parametara modela, te je razvijen inovativni koncept predikcije proizvodnje električne energije za jedan dan unaprijed s vremenskom rezolucijom od jednog sata, zajedno s opisom nesigurnosti predikcije proizvodnje. Glavni ulazi u predikcijski model proizvodnje su predikcije relevantnih meteoroloških varijabli, tj. komponenata Sunčevog ozračenja i temperature zraka, koje su dobivene od strane Državnog hidrometeorološkog zavoda (DHMZ), Hrvatska. U Poglavlju 4. "Load prediction" razvijen je predikcijski model potrošnje zgrade, te je provedena statistička analiza značaja odabranih ulaznih varijabli za predikciju potrošnje. Za opis nesigurnosti predikcije potrošnje primijenjena je tzv. *Unscented* transformacija, koja je proširena tako da osim nesigurnosti ulaznih varijabli uzme u obzir i nesigurnost koju unosi sami predikcijski model.

U Dijelu III. "Optimal control" razvijene su dvije razine upravljanja istosmjernom mikromrežom u uvjetima nesigurnosti temeljene na konveksnoj optimizaciji i modelskom prediktivnom upravljanju s pomičnim horizontom. U Poglavlju 5. "Power flow management" razvijen je sustav optimalnog upravljanja tokovima snage u mikromreži s vremenskom rezolucijom od jednog sata. Izlazi sustava upravljanja su profili punjenja i pražnjenja lokalnih spremnika energije i razmjene energije s elektroenergetskom mrežom koji omogućavaju optimalan rad mikromreže u tehničkom i ekonomskom smislu poštujući zadana ograničenja sustava, dobiveni na temelju (i) trenutnog stanja napunjenosti spremnika energije, (ii) predikcije proizvodnje i potrošnje u mikromreži, te (iii) predikcije cijene električne energije dobivene od strane (decentraliziranog) tržišta električne energije. Kako bi se uzela u obzir i nesigurnost predikcije proizvodnje i potrošnje električne energije, sustav upravljanja je razvijen u uvjetima nesigurnosti. U Poglavlju 6. "Power flow reference tracking" razvijen je sustav upravljanja razinom napona istosmjerne sabirnice mikromreže temeljen na centraliziranoj strukturi upravljanja, koji uzima u obzir optimalne profile punjenja i pražnjenja spremnika energije dobivenih od nadređene razine upravljanja. Cilj ove razine upravljanja je da napon istosmjerne sabirnice bude čim stabilniji uz slijeđenje optimalnih profila punjenja i pražnjenja na satnoj razini, te uz čim blaži profil razmjene električne energije s elektroenergetskom mrežom.

KLJUČNE RIJEČI: istosmjerna mikromreža, napredna energetska mreža, distribuirana pohrana, fotonaponski sustav, obnovljivi izvori energije, strojno učenje, umjetna inteligencija, predviđanje proizvodnje i potrošnje, estimacija stanja napunjenosti baterije, Kalmanov filter, superkondenzator, gorivni članak, upravljanje tokovima snage, konveksna optimizacija, linearni program, modelsko prediktivno upravljanje, upravljanje u uvjetima nesigurnosti, stabilnost napona

---

# CONTENTS

<b>I</b>	<b>General considerations</b>	<b>1</b>
<b>1</b>	<b>Introduction</b>	<b>2</b>
1.1	Smart grid . . . . .	2
1.2	Microgrid concept . . . . .	4
1.3	Original scientific contributions . . . . .	6
1.4	Outline of the dissertation . . . . .	8
<b>2</b>	<b>Laboratory setup</b>	<b>9</b>
2.1	DC microgrid . . . . .	9
2.2	Photovoltaic power plant . . . . .	12
2.3	Meteorological station . . . . .	12
<b>II</b>	<b>System identification</b>	<b>14</b>
<b>3</b>	<b>Photovoltaic system</b>	<b>15</b>
3.1	Introduction . . . . .	15
3.2	Experimental setup . . . . .	18
3.2.1	Experimental setup with the single PV panel . . . . .	19
3.2.2	Experimental setup with the PV array . . . . .	20
3.2.3	Numerical weather prediction model ALADIN . . . . .	20
3.2.4	Data preparation procedure . . . . .	21
3.3	Performance indicators . . . . .	22
3.4	Power production models . . . . .	23
3.4.1	Power production model of a single PV panel . . . . .	23
3.4.2	Solar irradiance on a tilted surface . . . . .	29
3.4.3	Power production model of a PV array . . . . .	32
3.5	Predictor-corrector method . . . . .	35
3.5.1	Neural-network structure used for correction models . . . . .	35
3.5.2	Static PV array power production model . . . . .	36
3.5.3	Static and dynamic correction of a prediction sequence . . . . .	39
<b>4</b>	<b>Load prediction</b>	<b>46</b>
4.1	Introduction . . . . .	46
4.2	One-hour-ahead prediction . . . . .	47
4.2.1	Input variables selection . . . . .	47
4.2.2	Neural network structure . . . . .	51

4.2.3	Performance verification .....	53
4.2.4	On-line model tuning .....	53
4.3	One-day-ahead prediction .....	56
4.3.1	Input data uncertainty .....	56
4.3.2	Model uncertainty .....	57
4.3.3	Unscented transformation extension .....	59
4.3.4	Performance verification .....	61
<b>III</b>	<b>Optimal control</b> .....	<b>62</b>
<b>5</b>	<b>Power flow management</b> .....	<b>63</b>
5.1	Introduction .....	63
5.2	DC microgrid model .....	65
5.2.1	Power balance .....	65
5.2.2	Dynamic system model .....	66
5.2.3	Augmented dynamic system model .....	67
5.2.4	Electricity price .....	67
5.3	Power flow management in deterministic framework .....	67
5.3.1	Objective function .....	67
5.3.2	System constraints .....	68
5.3.3	LP formulation .....	69
5.3.4	Closed-loop control .....	69
5.3.5	Simulation results .....	69
5.4	Power flow management in stochastic framework .....	73
5.4.1	Objective function .....	73
5.4.2	System constraints .....	73
5.4.3	LP formulation .....	74
5.4.4	Closed-loop control .....	74
5.4.5	Simulation results .....	75
5.5	Multilevel optimal control in a building .....	78
5.5.1	Microgrid optimization problem .....	78
5.5.2	Closed-loop control .....	79
5.5.3	Simulation results .....	79
<b>6</b>	<b>Power flow reference tracking</b> .....	<b>83</b>
6.1	Introduction .....	83
6.2	DC microgrid model .....	84
6.2.1	Power balance .....	84
6.2.2	Dynamic system model .....	85
6.3	Tracking problem formulation .....	85
6.3.1	Objective function .....	86
6.3.2	System constraints .....	87
6.3.3	LP formulation .....	87
6.3.4	Closed-loop control .....	87
6.4	Simulation results .....	88
	<b>Bibliography</b> .....	<b>96</b>



---

## LIST OF FIGURES

1.1	Transition from traditional electric grid to smart grid . . . . .	4
1.2	Example of a residential microgrid with renewable energy sources, distributed energy storage, and smart metering . . . . .	5
1.3	Data flow diagram of the proposed hierarchical microgrid control structure . . . . .	6
2.1	Single-pole schematic diagram of the 48-V DC microgrid formed in LARES . . . . .	10
2.2	Equipment in LARES. . . . .	13
3.1	Data-flow diagram of dynamic model for PV array power production prediction . . . . .	16
3.2	Data-flow diagram of the proposed predictor-corrector method . . . . .	18
3.3	Schematic diagram of the experimental setup with the single PV panel and with the PV array formed in LARES . . . . .	19
3.4	Timeline illustration of the numerical weather prediction model ALADIN operation . .	21
3.5	Scatter plots of incident solar irradiance versus PV panel and PV array temperature for verification of power production models . . . . .	22
3.6	Probability density function of a stochastic variable that follows the Gaussian distribution	23
3.7	Single-diode equivalent electrical circuit of a PV panel . . . . .	24
3.8	Contour plot of the PV panel single-diode model absolute power error at the MPP for STC	25
3.9	Criterion functions used to solve the single-diode model implicit equation . . . . .	27
3.10	Comparison between the PV panel power production model output and the maximum power obtained by experiments with artificial sun . . . . .	28
3.11	Equivalent electrical circuit of the system used in experiments with the single PV panel	29
3.12	Performance indicators of the PV panel power production model . . . . .	30
3.13	Angles of a tilted surface . . . . .	31
3.14	Equivalent electrical circuit of the system used in experiments with the PV array . . . . .	32
3.15	ABB PVS300-TL-3300W-2 solar inverter conversion efficiency versus operating power	33
3.16	Performance indicators of array and joined models . . . . .	34
3.17	Scatter plots of the PV array power production model . . . . .	37
3.18	Surface plot of the PV panel power production at the MPP . . . . .	38
3.19	Data-flow diagram of the PV array power production model with static correction . . . .	38
3.20	Standard deviation of the prediction sequence error with respect to the prediction step	42
3.21	Measurements and predictions of relevant meteorological variables for the considered exemplary period . . . . .	43
3.22	Example of series of corrections performed over a single prediction sequence . . . . .	44
4.1	Time instances of lagged load data used as prediction model inputs . . . . .	48
4.2	RMSE considering different number of input variables and neurons in hidden layer . . .	52
4.3	Performance of the best performing neural network with optimal structure for one-hour-ahead prediction considering only the validation data set . . . . .	54

4.4	Performance of the best performing neural network with optimal structure for one-hour-ahead prediction considering only the next-week data set . . . . .	55
4.5	Model error mean and standard deviation for each hour instant in the exemplary day .	57
4.6	Estimated pdf of the prediction model error and its approximation by normal distribution for each hour instant in the exemplary day . . . . .	58
4.7	One-day-ahead load prediction assessment for best- and worst-performing week periods in the next-week data set . . . . .	61
5.1	Power balance diagram of the DC microgrid formed in LARES . . . . .	65
5.2	Revenue at the end of the one-year period for different prediction horizon lengths and final price values . . . . .	70
5.3	Revenue at the end of the one-year period when the final price value is determined as the mean electricity price over the prediction horizon . . . . .	71
5.4	Profiles for closed-loop control simulation over 48-h exemplary period beginning on 1 Jul 2013 at 00:00, using MPC scheme with $N = 24$ and $p_{\text{pct}} = 90\%$ . . . . .	72
5.5	Profiles for closed-loop control simulation over 48-h exemplary period beginning on 6 Aug 2014 at 00:00, using SMPC scheme with $N = 24$ and $\alpha = 0.50$ . . . . .	76
5.6	Profiles for closed-loop control simulation over 48-h exemplary period beginning on 6 Aug 2014 at 00:00, using SMPC scheme with $N = 24$ and $\alpha = 0.05$ . . . . .	77
5.7	Microgrid operating costs and total electricity exchanged with the utility grid at the end of the four-month period . . . . .	80
5.8	Profiles for closed-loop control simulation over 48-h exemplary period beginning on 6 Jul 2014 at 00:00, using MPC scheme with $N = 24$ . . . . .	81
5.9	Meteorological profiles over 48-h exemplary period beginning on 6 Aug 2014 at 00:00 .	82
6.1	Power balance diagram in the considered DC microgrid . . . . .	84
6.2	Power output of the PV array in LARES on 9 Aug 2016 in 1-h and 1-s time bases . . . . .	88
6.3	Profiles for closed-loop control simulation in 1-s time base over 1-h exemplary period beginning on 9 Aug 2016 at 07:00 for case when utility grid state of charge deviation is penalized the least . . . . .	90
6.4	Profiles for closed-loop control simulation in 1-s time base over 1-h exemplary period beginning on 9 Aug 2016 at 07:00 for case when battery state of charge deviation is penalized the least . . . . .	91
6.5	Profiles for closed-loop control simulation in 1-s time base over 1-h exemplary period beginning on 9 Aug 2016 at 07:00 for case when battery state of charge deviation is penalized the least and it operates near its physical limits . . . . .	92
6.6	Profiles for closed-loop control simulation in 1-s time base over 1-h exemplary period beginning on 9 Aug 2016 at 14:00 for case when utility grid state of charge deviation is penalized the least . . . . .	93
6.7	Profiles for closed-loop control simulation in 1-s time base over 1-h exemplary period beginning on 9 Aug 2016 at 14:00 for case when battery state of charge deviation is penalized the least . . . . .	94
6.8	Profiles for closed-loop control simulation in 1-s time base over 1-h exemplary period beginning on 9 Aug 2016 at 14:00 for case when battery state of charge deviation is penalized the least and it operates near its physical limits . . . . .	95

---

## LIST OF TABLES

3.1	Performance indicators for experiments with the single PV panel during the 4-month time period . . . . .	28
3.2	Performance indicators of array and joined models on the 2-year data set . . . . .	35
3.3	Performance indicators of the PV array power production model on the considered four data sets . . . . .	37
5.1	Microgrid parameters used in simulation . . . . .	70
5.2	Revenue in EUR at the end of the one-year period . . . . .	71
5.3	Performance indicators for different closed-loop control schemes . . . . .	75
6.1	Microgrid parameters used in simulation . . . . .	89
6.2	Numeric values of control-related parameters for the considered simulation scenarios .	89

---

## ACRONYMS

BAT	Battery
cdf	Cumulative distribution function
DHMZ	Croatian Meteorological and Hydrological Service
FC	Fuel cell
FCE	Fuel cell with electrolyzer
FER	Faculty of Electrical Engineering and Computing
ICT	Information and communication technology
IVS	Input variables selection
LARES	Laboratory for Renewable Energy Systems
LP	Linear program
MBE	Mean bias error
MILP	Mixed integer linear program
MLP	Multilayer perceptron
MPC	Model predictive control
MPP	Maximum power point
MPPT	Maximum power point tracking
MSE	Mean squared error
NI	National Instruments
pdf	Probability density function
PMI	Partial mutual information
PV	Photovoltaic
RMSE	Root mean square error
SMPC	Stochastic model predictive control
SoC	State of charge
STC	Standard test conditions
UC	Ultracapacitor
UG	Utility grid
UNIZG	University of Zagreb
UT	Unscented transformation
UTC	Coordinated Universal Time
VRLA	Valve-regulated lead-acid
WT	Wind turbine

## **Part I**

# **General considerations**

# Chapter 1

## Introduction

This chapter presents the motivation and hypothesis of the research presented in the doctoral dissertation. The next evolutionary step of the electric grid, called a *smart grid*, is introduced first, followed by the microgrid concept. The latter is a basic building block of the smart grid and the central subject of the conducted research. This chapter concludes with a brief discussion of original scientific contributions, followed by an outline of the dissertation.

### 1.1 Smart grid

The electric grid is a vast physical and human network connecting thousands of electrical generators to billions of consumers. Today's electric grid was conceived more than 130 years ago<sup>1</sup> when electricity needs were simple. Power generation was centralized and built near communities mainly to reduce electricity transmission losses, while most households had only modest energy demands such as powering few lamps. From nearly the start of the industrial revolution, the engine of Western civilization has run on fossil fuels [1], and the fuel supply has not changed much since. Power generation today is mainly based on large (centralized) power plants which use fossil and nuclear fuels. These are limited in total supply and produce a lot of waste, e.g., nuclear waste remains radioactive and is hazardous to health for thousands of years. In order to cope with these problems, the world today is turning to alternative (distributed) power sources [2, 3] such as renewable energy sources [4] like wind turbines and photovoltaic systems. Integrating renewable energy sources into the existing electric grid poses a challenge however, due to intermittent power production from strong dependence on atmospheric conditions [5]. This requires significant operating reserves to help with the power system regulation, which is expensive.

A fundamental postulate in the electric grid is that power production and consumption must be matched at all times [6]. Otherwise, voltage and frequency deviate which results in poor power quality, including blackouts, power cuts, and brownouts. Electricity demand patterns are mostly influenced by domestic heating and air-conditioning which lead to peaks in the daily electricity demand. Peak demands are met by specialized power plants which have relatively low utilization and are most commonly based on gas turbines due to their low capital cost and fast start-up times. However, overall operation costs of peak power plants are high relative to traditional coal and nuclear based power plants. Ultimately, these costs are passed on to consumers in the form of increased tariffs, i.e., electricity prices. With the advent of renewable energy sources, the problem of matching power production and consumption in the electric grid becomes even more prominent. Power production from renewable energy sources is intermittent due to strong dependence on atmospheric

---

<sup>1</sup> The first AC power system in Croatia and one of the first in the world was the hydroelectric power plant Jaruga on the Skradinski Buk falls of Krka river, produced and installed by the Hungarian company Ganz Works. The Jaruga plant supplied around 340 streetlights and some electrified houses 12 km away in the city Šibenik, making it the first city in the world with streetlights powered by a polyphase AC system. This system began in operation on August 28, 1895, only a few days after the first hydroelectric power plant in the world, the Adams Plant on the Niagara Falls which was designed by Nikola Tesla and built by George Westinghouse.

conditions, and must be compensated [7–9] in order not to affect stability of the electric grid. This can be achieved either by adding more peak generators or by integrating distributed energy storage systems [10] which buffer power production and consumption. To that respect, most countries have significantly reduced incentives for renewable energy sources [11], which have already reached a mature level. Some countries created incentives for integrating distributed energy storage with the electric grid. This enables consumers to passively participate in the electricity market by providing peak-shaving services, i.e., by charging energy storage devices at night when electricity demand is low and consuming stored electricity locally during peak demands. In that respect, batteries in fast-emerging plug-in electric and hybrid vehicles are expected to play a significant role. However, due to the centralized and highly regulated nature of electricity markets [12,13], consumers still do not directly influence electricity prices.

Most countries in the world today employ a fixed tariff system with higher electricity prices during the daytime, i.e., during electricity peak demands that need to be covered by peak generators. In order to enable active participation of consumers<sup>2</sup>, the electricity market should be decentralized, thus allowing everyone to buy and sell electricity via energy transactions and blockchain technology. This is now possible thanks to rapid development of information and communication technology (ICT), which is one of the main enablers to transition from a centralized, unidirectional, and stiff electric grid in which only (privileged) few participate, to a decentralized, bidirectional, flexible, and robust electric grid open to all. The latter is often termed the *smart grid*, owing to the addition of ICT and other technologies that make the electric grid behave *smarter*. This is the next evolutionary step of the traditional electric grid that will change the way we use and think of energy. An illustration of the described transition from the electric grid to the smart grid is shown in Fig. 1.1.

One of the first definitions of the smart grid was provided by the USA's Energy Independence and Security Act of 2007 (Pub.L. 110-140 [14]), Title XIII – Smart Grid, Sec. 1301. Statement of Policy on Modernization of Electricity Grid, as follows: "It is the policy of the United States to support the modernization of the Nation's electricity transmission and distribution system to maintain a reliable and secure electricity infrastructure that can meet future demand growth and to achieve each of the following, which together characterize a Smart Grid: (1) Increased use of digital information and controls technology to improve reliability, security, and efficiency of the electric grid; (2) Dynamic optimization of grid operations and resources, with full cyber-security; (3) Deployment and integration of distributed resources and generation, including renewable resources; (4) Development and incorporation of demand response, demand-side resources, and energy-efficiency resources; (5) Deployment of "smart" technologies (real-time, automated, interactive technologies that optimize the physical operation of appliances and consumer devices) for metering, communications concerning grid operations and status, and distribution automation; (6) Integration of "smart" appliances and consumer devices; (7) Deployment and integration of advanced electricity storage and peak-shaving technologies, including plug-in electric and hybrid electric vehicles, and thermal-storage air conditioning; (8) Provision to consumers of timely information and control options; (9) Development of standards for communication and interoperability of appliances and equipment connected to the electric grid, including the infrastructure serving the grid; (10) Identification and lowering of unreasonable or unnecessary barriers to adoption of smart grid technologies, practices, and services." This definition proves that governments are aware of problems and challenges that face the electric grid, and it is now up to governments, scientists and engineers to make the smart grid possible [15–27]. The current implementation of the electric grid simply cannot cope with requirements imposed by the modern world.

<sup>2</sup> In this context some authors use the term *prosumer*, which denotes electricity users that not only consume but also produce energy and participate in the electricity market.

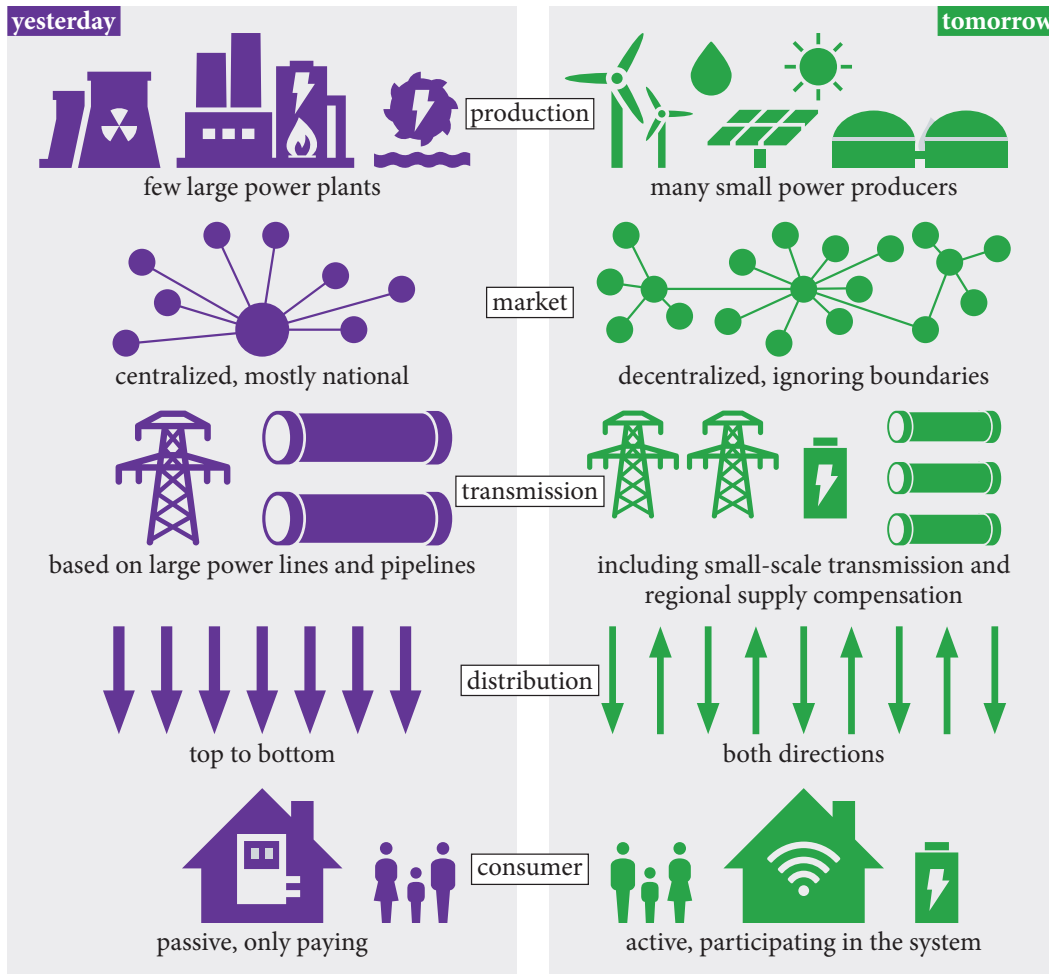


Figure 1.1: Transition from traditional electric grid (on the left) to smart grid (on the right). [4]

## 1.2 Microgrid concept

A microgrid is a cluster of distributed generation sources, storage devices and loads that operate together. Ideally, they improve reliability and quality of the power supply and the power system [28–32]. An example of a residential microgrid with renewable energy sources and distributed storage is shown in Fig. 1.2. Power converters represent controllable points in the microgrid that ensure quality and stability of the local power supply and enable connecting different systems to a common power link. With respect to the power link design technology there are DC and AC microgrids. The most important difference between them is that the frequency must be controlled in addition to the bus voltage level in AC microgrids. A number of recent research studies [33–36] indicate that DC microgrids might be a better choice than AC microgrids, as most loads and distributed generation sources and storage devices naturally operate with DC technology. By avoiding unnecessary DC to AC conversions, the power system efficiency on a global scale could be improved by 5–15% [33]. Studies have also shown that 380-Vdc is 28% more efficient than 208-Vac and 7% more than 415-Vac equivalents. It requires less space and is more reliable, which is why many data centers already use DC power architectures [34]. In this dissertation, a 48-Vdc residential microgrid is considered. It consists of a wind turbine emulator and photovoltaic array, batteries, fuel cells with electrolyzer, ultracapacitor, and controllable load. The microgrid is connected to the utility grid via a bidirectional DC/AC converter. The 48-Vdc power link standard is selected over 380-Vdc for safety and compatibility with microgrids installed in off-grid telecommunication stations.



Disparate microgrid time constants call for hierarchical microgrid control approach [38–40], where lower-level controllers receive commands from higher-level controllers. (i) In the lowest level in the hierarchy of microgrid controllers exist controllers for power converters. These are implemented in the converters themselves and can track voltage or current set points imposed by a higher-level controller. Power converter control loop time constants are in the millisecond range, unless additional technical constraints preserve the corresponding system. For example, fuel-cell systems have strict requirements for current ripple and rate of change, which significantly retards transient responses. Such control is not considered in the dissertation, i.e., it is assumed that power converters have built-in controllers implemented by the manufacturer. (ii) In the highest level the power flow management algorithm decides how to drive controllable systems in the microgrid, i.e., how to charge and discharge distributed storage devices and exchange electricity with the utility grid. However, a decision of when to buy and sell energy to the utility grid and in which amount, i.e., when to charge and discharge storage devices, is a complex function of the predicted microgrid load, power production (mainly by renewable energy sources), current storage device state of charge, and of the predicted electricity price provided by the (decentralized) electricity market. Sample time at this control level is determined by the time resolution of power production and consumption predictions, usually in the range of minutes or hours. (iii) In the middle level an algorithm manages microgrid bus stability by issuing voltage and current set points to power converters, while accommodating power references received from the power flow management algorithm. The main task of this control level is to locally mitigate fast stochastic changes in power production and consumption predictions. Such would otherwise propagate to the electric grid, thus polluting the grid with high-frequency harmonics. Sample time at this control level is determined by the microgrid capacity and power rating of microgrid systems, usually in the range of seconds.

In this dissertation, the middle and high microgrid control levels are considered [41–44] together with models of all components needed for their proper design [45–49]. Research includes power production and consumption prediction [50–52]. For the sake of brevity, the battery state of charge estimation algorithm is not discussed but is presented in [53]. Special emphasis is applied to employing information about prediction uncertainty, i.e., the control algorithm is developed in a stochastic framework for optimal microgrid techno-economic operation in real-world environments.

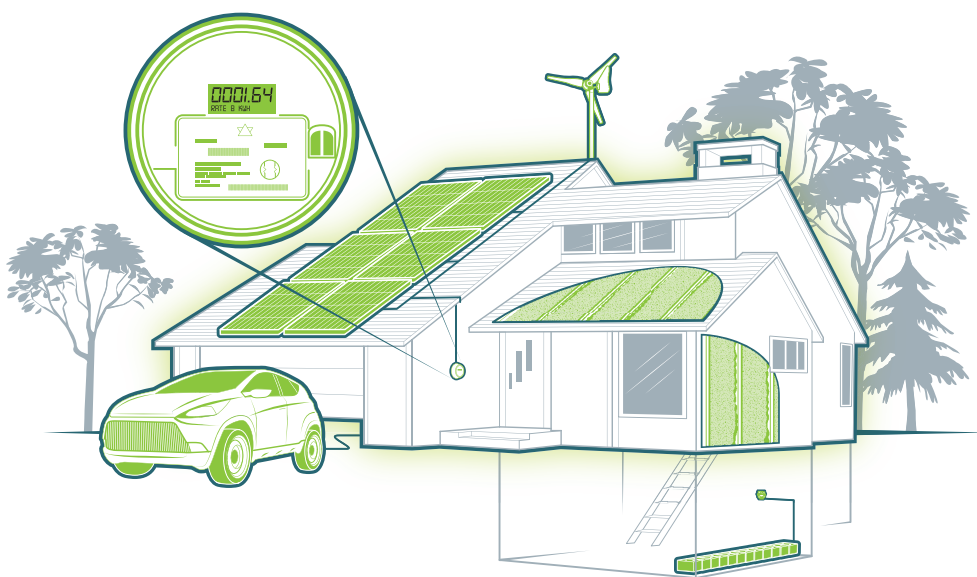


Figure 1.2: Example of a residential microgrid with renewable energy sources, distributed energy storage, and smart metering. (Image courtesy of MCKIBILLO [37])

### 1.3 Original scientific contributions

Data flow diagram of the proposed hierarchical microgrid control structure is shown in Fig. 1.3. Predictions of relevant meteorological variables are provided by DHMZ every 6 h with 4-h delay for the next 72-h period with 1-h resolution. Power production and consumption in the microgrid are predicted every hour for the next 24-h period with 1-h resolution, based on predicted meteorological variables and local power measurements. Power flow management is done every hour based on (i) current storage device state of charge, (ii) predictions of power production and consumption in the microgrid, and (iii) predicted electricity price provided by the (decentralized) electricity market. Outputs of the power flow management are charge and discharge profiles for the battery and energy exchange plan with the utility grid to achieve optimal techno-economic microgrid operation. Power flow references are adapted on a much faster time scale, i.e., every 10 s, to account for fast stochastic disturbances in power production and consumption predictions. Microgrid voltage is controlled by the ultracapacitor in the centralized voltage control configuration. Power flow reference tracking algorithm makes sure that the ultracapacitor state of charge is always at half of its usable capacity to be ready to compensate voltage sag and swell. A real-time industrial controller is an interface to the microgrid, i.e., to power converters which represent controllable points in the microgrid. The controller performs low-level tasks such as data acquisition and filtering, power metering, state of charge (SoC) estimation, maximum power point tracking (MPPT) of the photovoltaic array etc.

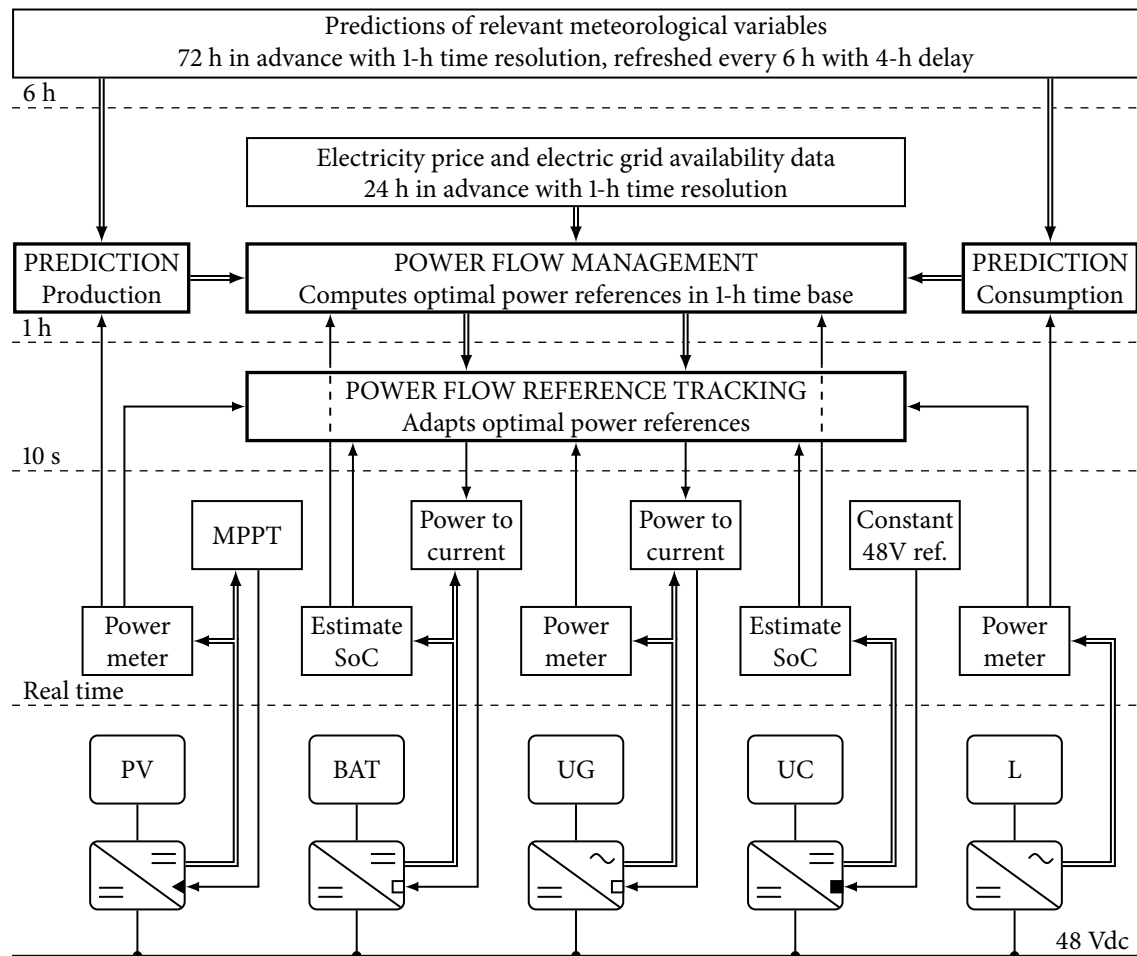


Figure 1.3: Data flow diagram of the proposed hierarchical microgrid control structure (PV is photovoltaic array, BAT is battery, UG is utility grid, UC is ultracapacitor, L is microgrid load, □ and ■ symbols in power converters represent microgrid-side current and voltage controllers, and ◀ is PV-side voltage controller).

Original scientific contributions presented here are summarized as "modeling and optimal control of a residential grid-connected DC microgrid with renewable energy sources." A brief elaboration of the contribution follows in the sequel.

- × Modeling and identification of DC microgrid components, aiming to coordinate control and optimize techno-economic microgrid operation.

This contribution models predictions of (i) power produced by the photovoltaic system based on predictions of relevant meteorological variables, and (ii) power consumption in the microgrid. Power production and consumption predictions are performed hourly for one day in advance with one-hour time resolution. An important aspect of power profile prediction is uncertainty characterization, as predicted variables strongly depend on atmospheric conditions and other stochastic phenomena. Power predictions are used by the microgrid control algorithm to improve stability and optimize techno-economic microgrid operation.

- × Stochastic predictive control of the voltage level on the DC microgrid power link to adhere to technical constraints of microgrid components.

This contribution is a control algorithm for the DC link voltage level based on the centralized voltage control configuration, i.e., one microgrid system (ultracapacitor in particular) controls the DC link voltage, while other systems can generate any power within their operation constraints. It should be noted that the system in charge of the DC link voltage control must both sink and source current in order to compensate sudden voltage swell or sag, respectively. The algorithm is tuned to keep the ultracapacitor at half of its usable state of charge, whereas any deviation from that state is penalized in the algorithm, but not strictly forbidden. Consequently, the ultracapacitor will compensate all short-term stochastic disturbances that act on the microgrid, which smooths out the energy exchange profile with the battery and the electric grid.

- × Method for calculating optimal power flow in a microgrid which also adheres to uncertainty in state and parameter estimation of microgrid energy storage devices.

This contribution is an algorithm for power flow management in the microgrid with one-hour time resolution. The algorithm outputs charge and discharge profiles for microgrid storage devices. It optimizes techno-economic microgrid operation within defined system constraints based on current and future (predicted) microgrid operating conditions. The model predictive control scheme with receding horizon principle is employed for closed-loop microgrid control. The control algorithm is developed in a stochastic framework to account for power prediction uncertainty.

- × Method for tracking computed power flow references on the microgrid component level with suitable adjustment of lower microgrid control levels.

This contribution is an algorithm for power flow reference tracking which adjusts the hour-based power references that achieve optimal microgrid techno-economic operation obtained by the power flow management algorithm. Operating conditions in the microgrid in terms of (volatile) power production and consumption can significantly deviate from hour-based averages used by the power flow management algorithm. Accordingly, adjustments are needed on a much faster time scale, i.e., every 10 seconds in the proposed solution. The power flow reference tracking algorithm is developed for support of the DC link voltage control algorithm by ensuring that the ultracapacitor state of charge does not deviate significantly from half of its usable state of charge, making it ready to compensate both voltage sag and swell. The model predictive control scheme with receding horizon principle is employed for closed-loop power flow reference tracking.

## 1.4 Outline of the dissertation

The doctoral dissertation consists of 6 chapters organized in 3 parts: (i) part "General considerations" consists of 2 chapters: Chapter 1. "Introduction" and Chapter 2. "Laboratory setup"; (ii) part "System identification" consists of 2 chapters: Chapter 3. "Photovoltaic system" and Chapter 4. "Load prediction"; (iii) part "Optimal control" consists of 2 chapters: Chapter 5. "Power flow management" and Chapter 6. "Power flow reference tracking".

- × CHAPTER 2. In this chapter a grid-connected DC microgrid constructed at the Laboratory for Renewable Energy Systems (LARES) at the University of Zagreb Faculty of Electrical Engineering and Computing (UNIZG-FER) is described, with technical details of all systems included in the microgrid. Besides the DC microgrid, a photovoltaic plant and meteorological station in LARES are described, which were also used to develop and verify methods presented in the dissertation.
- × CHAPTER 3. In this chapter an equivalent electrical model of a photovoltaic system is developed, together with novel numerical algorithms for faster model identification from the datasheet parameters only. A model to calculate solar irradiance incident with a tilted surface oriented at an arbitrary position is described. An innovative concept to predict power production from the photovoltaic system for one day in advance with one-hour time resolution is developed and verified. A special emphasis is put on the power prediction uncertainty characterization, needed for the microgrid optimal control in a stochastic framework. The main inputs to the prediction model are predictions of relevant meteorological variables, i.e., solar irradiance components and air temperature, which are provided by the Croatian Meteorological and Hydrological Service (DHMZ).
- × CHAPTER 4. In this chapter a load prediction model for one day in advance with one-hour time resolution is developed. The prediction model was trained and verified on historical consumption data for UNIZG-FER building and historical meteorological data provided by DHMZ. Statistical analysis based on partial mutual information was performed to select only the most relevant inputs for the prediction. The Unscented transformation was used for prediction uncertainty characterization, and its extension from the original form is proposed to also include the prediction model uncertainty.
- × CHAPTER 5. In this chapter a power flow management in the microgrid with one-hour time resolution is developed. The outputs of the power flow management algorithm are charge and discharge profiles for microgrid storage devices that achieve optimal techno-economic microgrid operation within defined system constraints. The optimal profiles are obtained by solving an optimization problem based on a linear program that includes (i) different storage device charge and discharge efficiency and their current state of charge, (ii) predictions of power production and consumption in the microgrid, and (iii) predicted electricity price profile which is defined by the (decentralized) electricity market. The model predictive control scheme with receding horizon principle is employed for closed-loop control. The control algorithm is developed in a stochastic framework in order to address the production and consumption prediction uncertainty.
- × CHAPTER 6. In this chapter a DC link voltage control algorithm based on the centralized structure is developed, i.e., one microgrid system controls the DC link voltage (ultracapacitor in particular), while other systems can generate any power within their operation constraints. A special emphasis is put on tracking the storage device charge and discharge profiles received from the power flow management algorithm, which optimize microgrid techno-economic operation. The power flow reference tracking algorithm is developed for support of the DC link voltage control algorithm and is based on a linear program with 10-s sample time. It ensures that the ultracapacitor state of charge does not deviate significantly from half of its usable state of charge.

## Chapter 2

### Laboratory setup

The Laboratory for Renewable Energy Systems (LARES) is formed within University of Zagreb Faculty of Electrical Engineering and Computing (UNIZG-FER). This chapter gives description of the 48-V residential DC microgrid, photovoltaic plant and meteorological station in LARES, which were used for experimental verification of the proposed control concept.

#### 2.1 DC microgrid

The DC microgrid formed in LARES operates at 48 V, and consists of: (i) distributed generation sources: photovoltaic array and wind turbine emulator; and (ii) distributed energy storage systems: valve-regulated lead-acid (VRLA) batteries stack, fuel-cells stack with electrolyzer, and ultracapacitor. The microgrid is connected to the utility grid via bidirectional power converter and is equipped with external capacitor bank for improved voltage stability and performance. Single-pole schematic diagram of the DC microgrid formed in LARES is shown in Fig. 2.1.

##### § PHOTOVOLTAIC ARRAY

The photovoltaic array consists of eight poly-Si PV panels (Solvis SV-48-190) arranged in two parallel branches, facing south and placed at fixed tilt angle to horizontal surface. Performance of the PV array under standard test conditions is as follows: (i) open-circuit voltage is 119.2 V, (ii) short-circuit current is 16.7 A, and (iii) maximum output power is 1520 W. The PV array is connected to the DC link via custom-made 1.5-kW unidirectional DC/DC buck converter, which is controlled to track voltage reference either on PV side or on microgrid side. The communication with external industrial controller is via 0–10 V analog signals for measurements, 0–20 mA analog signal for reference, and 0–24 V digital signal for control mode selection. The maximum power point tracking (MPPT) algorithm is not implemented in the converter itself, but in the external industrial controller that issues appropriate PV-side voltage reference based on PV array voltage and current measurements.

##### § WIND TURBINE EMULATOR

The wind turbine emulator is based on a mechanically coupled motor-generator system, in which motor emulates wind and generator operates as a wind turbine generator. The generator is connected to the DC link via two power converters: (i) 5-kW unidirectional AC/DC converter by Danfoss, and (ii) custom-made 2-kW unidirectional DC/DC buck converter. Unlike the power converter for PV array, the DC/DC power converter for wind turbine is not controllable, i.e., it transfers all available energy from the generator to the microgrid by keeping the high-voltage side at constant 600 V. The wind turbine emulator system was originally designed for experimental verification of the fault-tolerant control of a wind turbine subject to generator electromechanical faults. It should be noted that components of the wind turbine emulator are not shown in the single-pole schematic diagram of the microgrid, for more details see [21].

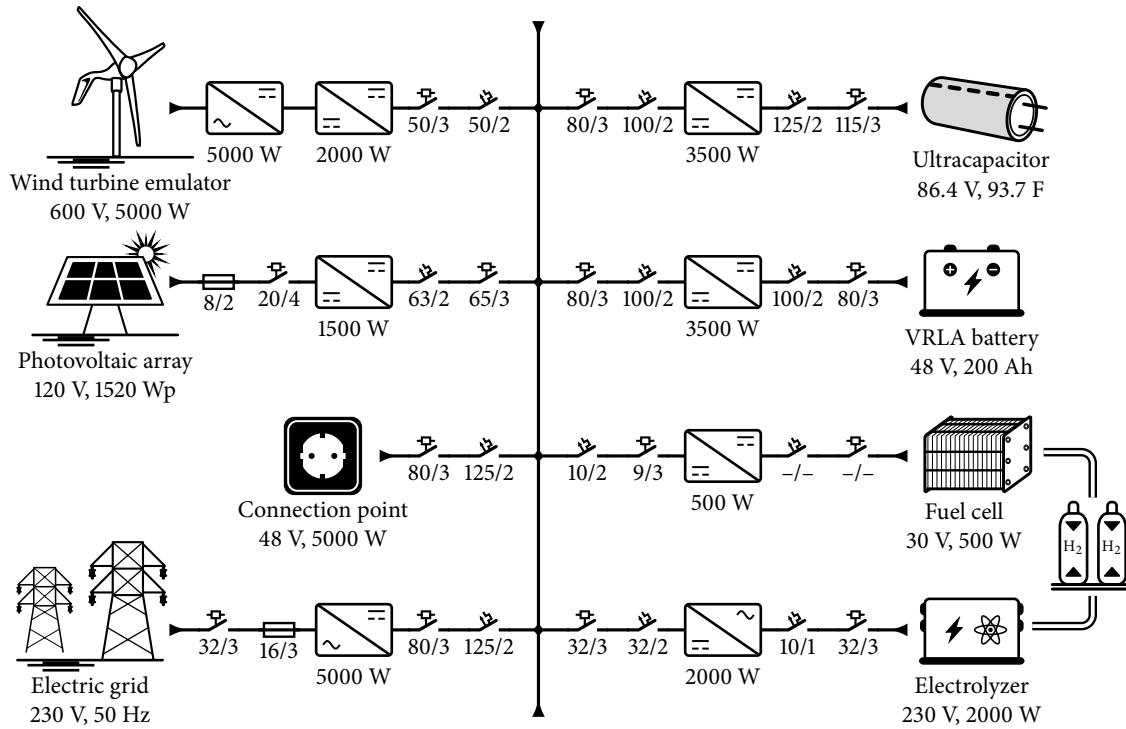


Figure 2.1: Single-pole schematic diagram of the 48-V DC microgrid formed in LARES.

#### § BATTERIES STACK

The batteries stack consists of four VRLA gel batteries (FirstPower LFP12200G) connected in series with the following stack parameters: (i) open-circuit voltage is 48 V, and (ii) C10 capacity is 200 Ah. The batteries stack is connected to the DC link via custom-made 3.5-kW bidirectional DC/DC buck-boost converter, which is controlled in one of two modes: (i) battery-side current reference tracking mode, or (ii) microgrid-side voltage reference tracking mode. The communication with external industrial controller is via 0–10 V analog signals for measurements, 0–20 mA analog signal for reference, and 0–24 V digital signal for control mode selection. The power converter provides both microgrid- and battery-side voltage and current measurements and is equipped with a custom-made soft-start mechanism. Battery current is also measured via two unidirectional Hall probes with 0–10 V output, while voltage of each battery in the stack is normalized to 0–10 V range via external custom-made device, both connected directly to the industrial controller.

#### § ULTRACAPACITOR

The ultracapacitor consists of one block (Alfatec LSUM 086R4C 0093F EA) with the following parameters: (i) capacity of 93.7 F, and (ii) maximum voltage of 86.4 V. The ultracapacitor is connected to the microgrid via custom-made 3.5-kW bidirectional DC/DC buck-boost converter, which is controlled in one of two modes: (i) ultracapacitor-side current reference tracking mode, or (ii) microgrid-side voltage reference tracking mode. Maximum energy stored in the ultracapacitor is 97.15 Wh, which means that the ultracapacitor can provide full power for no longer than 100 s. Considering maximum energy stored in the battery, ultracapacitor is not used for power flow management, but to smooth-out battery and utility grid power profiles. The communication with external industrial controller is via 0–10 V analog signals for measurements, 0–20 mA analog signal for reference, and 0–24 V digital signal for control mode selection. The power converter is equipped with a custom-made soft start mechanism.

### § FUEL-CELLS STACK WITH ELECTROLYZER

The fuel-cells stack consists of 32 proton exchange membrane (PEM) fuel cells connected in series, with 1.2-kW electrolyzer for on-site hydrogen production and with two metal-hydride tanks with overall storage capacity of 1800 L for hydrogen storage. The basic parameters of the fuel-cells stack are as follows: (i) maximum voltage is 30 V, (ii) maximum current is 30 A, and (iii) maximum power is 500 W. The fuel-cells stack is connected to the microgrid via custom-made 500-W unidirectional DC/DC boost converter which operates in fuel-cell-side current reference tracking mode. The power converter is specifically designed to have low current ripple in order to prolong fuel-cell lifetime. The communication with external industrial controller is via 0–10 V analog signals for measurements and 0–20 mA analog signal for reference. The electrolyzer is connected to the microgrid via custom-made 2.0-kW single-phase unidirectional DC/AC converter which is not controllable by an external controller, i.e., it generates 230 V, 50 Hz at the output from the 48-V input. The electrolyzer current is measured at the microgrid side via unidirectional Hall probe with 0–10 V output connected directly to the industrial controller. For more details on the fuel-cell system in LARES see [26].

### § UTILITY GRID

The microgrid is connected to the electrical grid via custom-made 5-kW bidirectional three-phase AC/DC power converter, which is controlled in one of two modes: (i) microgrid-side current reference tracking mode, or (ii) microgrid-side voltage reference tracking mode. The communication with external industrial controller is via Modbus protocol over half-duplex RS-485, which is used to set control mode, voltage and current references, and to get all measurements from the converter.

### § LOAD AND SOURCE

The microgrid has two connection points for external loads and sources up to 5 kW per connection point. Each connection point has a dedicated unidirectional Hall probe to measure current, with 0–10 V output directly connected to the industrial controller.

### § POWER CONVERTERS

Power converters are critical components in a microgrid that enable different systems to connect to a common power link. Most of the power converters in the considered microgrid are custom-made by EL-UR d.o.o. and Mareton d.o.o. with respect to an extensive list of requirements. All power converters are also equipped with contactors and automatic circuit breakers on both input and output sides. Since most contactors are made for AC systems, they are selected with significant current margin. For example, if three-pole contactors are used on the DC side, all three poles are shorted and connected to positive wire only. On the contrary, automatic circuit breakers are always connected to both positive and negative wires.

### § INDUSTRIAL CONTROLLER

Microgrid control is implemented on a real-time industrial controller (NI cRIO-9022) with an on-board FPGA chip and a number of modules for digital and analog communication with microgrid systems such as power converters, contactors, temperature probes etc. All analog input signals are sampled at 10 kHz sample rate and filtered on the FPGA. Real time controller downloads measurements from the FPGA and saves them in a database at regular time intervals, and also performs high-level decisions like control mode and references for individual power converters.

## 2.2 Photovoltaic power plant

Photovoltaic power plant consists of six PV arrays with fifteen poly-Si PV panels (Solvis SV-60-235) connected in series within each array, facing south and placed at fixed tilt angle to horizontal surface. It should be noted that the six PV arrays are not connected to the microgrid in any way. Performance of a single PV array under standard test conditions is as follows: (i) open-circuit voltage is 558.0 V, (ii) short-circuit current is 8.4 A, and (iii) maximum output power is 3525 W. Three PV arrays named A–C are connected to the grid via dedicated 3.3-kW single-phase solar inverter (ABB PVS300), whereas each inverter is connected to a different phase for better power balance. These inverters operate autonomously in the maximum power point tracking (MPPT) mode. Other three PV arrays named D–F are connected to the grid via dedicated 3.5-kW custom-made three-phase solar inverter. These inverters are controlled to track voltage reference on PV side, i.e., MPPT algorithm is implemented on the external industrial controller. All six solar inverters communicate to the industrial controller via Modbus protocol over half-duplex RS-485.

Three-phase multimeters (ABB DMTME-I-485) are placed at the output of each solar inverter, whereas PV arrays A–C share one multimeter as they are connected to the grid as single-phase systems, while PV arrays D–F have their own three-phase multimeters. The multimeters communicate to the industrial controller via Modbus protocol over half-duplex RS-485. Each PV array is also equipped with two PT100 temperature probes, which are mounted on the back of PV panels that are on opposite ends of the PV array by using a special thermal-conductive glue. Temperature probes are connected directly to the industrial controller. The industrial controller samples power production and temperature data for all PV arrays at 1 Hz sample rate.

## 2.3 Meteorological station

Meteorological station within LARES consists of air temperature, humidity and pressure sensors, wind speed and direction sensors, and a number of solar irradiance sensors (pyranometers and pyrhemometers) by Kipp&Zonnen. All sensors communicate to the industrial controller via 4–20 mA analog signals and are sampled at 1 Hz sample rate. The meteorological station is installed on the rooftop of the UNIZG-FER skyscraper ( $45^{\circ}48' N$ ,  $15^{\circ}58' E$ ), approximately 60 m above the ground surface, and the top-floor ground surface type is pebble.

Each PV array, including the PV array connected to the microgrid, has its dedicated solar irradiance sensor (first class CMP6 pyranometer) which is placed in the middle of the PV array, and its sensing surface is placed in the same plane as the PV array active surface. Three main solar irradiance components (direct normal, diffuse horizontal and global horizontal) are measured by solar irradiance sensors (first class CHP1 pyrhemometer and two secondary standard CMP11 pyranometers) mounted on a dual-axis sun tracker (Solys2) with closed-loop sun tracking and shading balls for diffuse solar irradiance. For these solar irradiance components it is essential to track the Sun position with high accuracy. An additional solar irradiance sensor (secondary standard CMP11 pyranometer) is placed 0.5 m above the ground surface, facing ground surface to measure ground-reflected solar irradiance component. This data, together with PV array power production and temperature data, enable research on how different atmospheric conditions affect PV array output. According to the manufacturer's recommendations, all mentioned solar irradiance sensors are calibrated every two years in a certified laboratory for highest possible measurements accuracy. Figure 2.2 shows exemplary systems within the microgrid, photovoltaic power plant, and meteorological station in LARES.





Figure 2.2: Equipment in LARES. From left to right, top to bottom: (i) PV arrays placed at fixed tilt angle to horizontal surface, (ii) Solys2 sun tracker with CHP1 pyrheliometer, two CMP11 pyranometers, and shading balls for diffuse solar irradiance, (iii) three-phase multimeters placed at solar inverter output, (iv) electrical cabinet with microgrid industrial controller and its peripheral, (v) pyranometer to measure solar irradiance incident with the PV array active surface, and (vi) electrical cabinet with microgrid power converters, contactors, automatic circuit breakers etc.

## **Part II**

# **System identification**

### 3.1 Introduction

Supply and demand in the electric power system must always be matched, otherwise voltage and frequency deviations occur [54]. From the power system control point of view, renewable energy systems, such as wind and solar (photovoltaic) systems, behave as disturbances since their power production is intermittent due to strong dependence on atmospheric conditions [55, 56]. The intermittent power production effect is addressed today by employing a large amount of generation reserve to balance between power production and consumption, operation of which is very expensive [57]. In order to be allowed to participate in electricity markets, owners of all (renewable) power plants will have to deliver a short-term power production plan [58, 59], which will reduce the need for engagement of a costly power generation reserve, and thus reduce the overall operating costs of the system. For a local microgrid [60] accurate prediction of power production, together with prediction of power consumption [52], enables optimal operation of storage units [41, 61, 62] and maximization of gain from investments in both local renewables and energy efficiency measures [43]. Information on power production and consumption prediction uncertainty can also be exploited for optimal microgrid operation in real-world conditions [42, 63]. Monitoring [64, 65] and diagnostics [66] of a PV system can also benefit from the operational power production prediction as a continuous mismatch of predicted and actual power production beyond the prediction 99% confidence interval should in principle be characterized as a malfunction of the PV system, e.g., due to permanent shading, dirt on the active surface or contacts corrosion. For the reasons mentioned many researchers recently focus on PV system power production prediction [67–75].

Research presented in this chapter is published in the following papers:

- ▣ M. Gulin, T. Pavlović, and M. Vašak, "A one-day-ahead photovoltaic array power production prediction with combined static and dynamic on-line correction," *Solar Energy*, vol. 142, pp. 49–60, 2017.
- ▣ M. Gulin, T. Pavlović, and M. Vašak, "Photovoltaic panel and array static models for power production prediction: Integration of manufacturers' and on-line data," *Renewable Energy*, vol. 97, pp. 399–413, 2016.
- ▣ M. Gulin, M. Vašak, and N. Perić, "Dynamical optimal positioning of a photovoltaic panel in all weather conditions," *Applied Energy*, vol. 108, pp. 429–438, 2013.
- ▣ M. Gulin, M. Vašak, and J. Matuško, "Predictor-Corrector Method for Weather Forecast Improvement using Local Measurements," in *Proceedings of the 18th International Conference on Electrical Drives and Power Electronics, EDPE 2015*, pp. 167–172, Tatranská Lomnica, The High Tatras, Slovakia, 2015.
- ▣ M. Gulin, M. Vašak, and T. Pavlović, "Model Identification of a Photovoltaic System for a DC Microgrid Simulation," in *Proceedings of the 16th International Power Electronics and Motion Control Conference and Exposition, PEMC 2014*, pp. 501–506, Antalya, Turkey, 2014.
- ▣ M. Gulin, M. Vašak, and M. Baotić, "Estimation of the global solar irradiance on tilted surfaces," in *Proceedings of the 17th International Conference on Electrical Drives and Power Electronics, EDPE 2013*, pp. 334–339, Dubrovnik, Croatia, 2013.
- ▣ M. Vašak, M. Gulin, J. Čeović, D. Nikolić, T. Pavlović, and N. Perić, "Meteorological and weather forecast data-based prediction of electrical power delivery of a photovoltaic panel in a stochastic framework," in *2011 Proceedings of the 34th International Convention on Information and Communication Technology, Electronics and Microelectronics, MIPRO 2011*, pp. 93–98, Opatija, Croatia, 2011.

## § METHODOLOGY

A data-flow diagram of a dynamic model for PV array power production prediction along a prediction horizon is shown in Fig. 3.1. The dynamic power production model of the PV array consists of [46,76] (i) the static power production model, and (ii) the dynamic thermal model. Since solar irradiance predictions are only available for direct, diffuse, and global solar irradiance components [77], a model to calculate global solar irradiance incident on a tilted surface [48,78–81] is also considered as a part of the prediction model. Except for the three solar irradiance components and the tilted surface orientation, solar zenith and azimuth angles are also used as inputs to the tilted surface model, which are calculated by the solar position algorithm [82]. Inputs to the static power production model of the PV array are incident solar irradiance (i.e., the output of the tilted surface model) and the PV array temperature (i.e., the output of the dynamic thermal model).

Since PV power production is strongly dependent on atmospheric conditions, the most critical inputs to the prediction model are predictions of meteorological variables, such as solar irradiance components and the air temperature [45]. Through a straightforward application of the meteorological variables prediction sequence, the PV array power production prediction is refreshed with the frequency of new predictions generation by the meteorological service, which is usually less frequent than the discrete time step of the prediction sequence [51]. In the considered case study, a refreshed prediction sequence of meteorological variables is available every 6 h for the 72-h time period with a time step of 1 h, whereas the prediction sequence becomes available with a nearly 4-h lag. It should be noted that predictions of the PV array power production are usually very uncertain [83], mainly due to the uncertainty of input meteorological variables predictions [84], but also due to the prediction model itself [45].

In this chapter the following model and method are developed and verified: (i) static model of a PV array power production, which is a fundamental part of dynamic model for its power production prediction, and (ii) predictor-corrector method to improve quality of the PV array power production prediction along a prediction horizon, i.e., to eliminate prediction bias and reduce uncertainty. Performance verification and uncertainty assessment of the static power production model are performed on data obtained by experiments with a single PV panel and with a PV array, during 4-month and 2-year time periods, respectively, conducted in LARES. In the sequel, the *static power production model* will be for the sake of brevity termed as the *power production model*. The power production model of the PV panel is also verified on data obtained by experiments with artificial sun, conducted at the PV panel manufacturer’s research facility. Correctors in the proposed predictor-corrector method are realized as neural networks which are trained, validated and tested on a real PV plant through experiments performed in LARES during the 2-year time period, whereas historical predictions of relevant meteorological variables are provided by DHMZ.

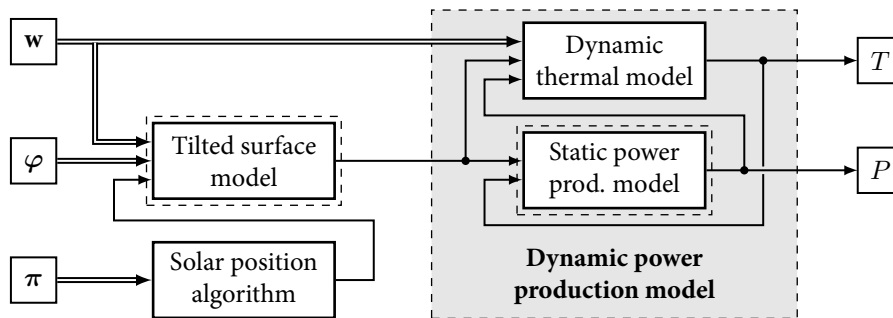


Figure 3.1: Data-flow diagram of dynamic model for PV array power production prediction ( $w$  is predicted weather data series,  $\varphi$  are tilted surface tilt and azimuth angles, and  $\pi$  are geographical and time data).

## § POWER PRODUCTION MODELS

To develop a power production model of a PV array, first the power production model of a single PV panel is developed based on manufacturers' data only. The two most popular models of a PV panel reported in literature are single- and double-diode equivalent electrical models [85, 86]. Although the double-diode model tends to be more accurate than the single-diode model, for most practical applications the single-diode model is accurate enough and is therefore used here. Many authors discuss ways to identify unknown parameters of the single-diode model based on manufacturers' data only [87–92]. In this chapter a brute-force search method combined with fast numerical algorithms is proposed to solve an implicit equation that stems from the single-diode model. The power production model of a single PV panel is generated as a lookup table by a numerical procedure, using the identified single-diode model and the developed fast numerical algorithms. It is verified on the static current-voltage characteristics of the PV panel, with the incident solar irradiance and the PV panel temperature measurements, obtained by experiments in LARES during the 4-month time period. The power production model is also verified on data obtained by experiments with artificial sun, although it must be noted that these experiments were limited to a constant PV panel temperature corresponding to the standard temperature test condition.

Prior to the PV array power production model, a short review of the tilted surface model [80] is given, whereas the Hay's anisotropic model [81] is used to calculate the diffuse solar irradiance on a tilted surface. The PV array power production model is developed as an extension to the PV panel power production model, and it is verified on the 2-year data set, alone and when operating together with the tilted surface model. These two cases are for brevity termed as *the array model* and *the joined model*, respectively. The array model is verified on measurements of the incident solar irradiance, while the joined model is verified on measurements and predictions of solar irradiance components (direct, diffuse and global) which are used as inputs to the tilted surface model to calculate the global solar irradiance incident on the PV array's active surface. Historical predictions of solar irradiance components are provided by DHMZ, and the PV array temperature measurements are used for verification of both models. The final goal of this performance verification is to assess limit performance of the PV array power production model in real-world conditions by using high-quality solar irradiance measurements and predictions, and to check how the tilted surface model uncertainty affects its performance.

## § PREDICTOR-CORRECTOR METHOD

The predictor-corrector method proposed in this chapter proceeds in two steps: (i) prediction step calculates a rough prediction sequence of the PV array power production based on identified power production model and predictions of meteorological variables, which is performed as soon as new (refreshed) predictions of meteorological variables become available, i.e., in the considered case study every 6 h for the 72-h time period with a 4-h lag; (ii) correction step refines the initial prediction sequence obtained by the prediction step as soon as new averaged power production measurement becomes available, i.e., every 1 h for the next 24-h time period. In this way it is possible to refresh the prediction sequence as soon as new local measurements become available. It should be noted that only 24-h-ahead corrections of the original 72-h-ahead prediction sequence are considered here, as near-history realizations are only relevant to correct near-future predictions, i.e., up to 8 h ahead as it will be shown by the performance verification. A data-flow diagram of the proposed predictor-corrector method for a correction step performed at the time instant  $t + 6$ , where  $t + 1$  is the starting time instant of meteorological prediction sequence, is shown in Fig. 3.2.

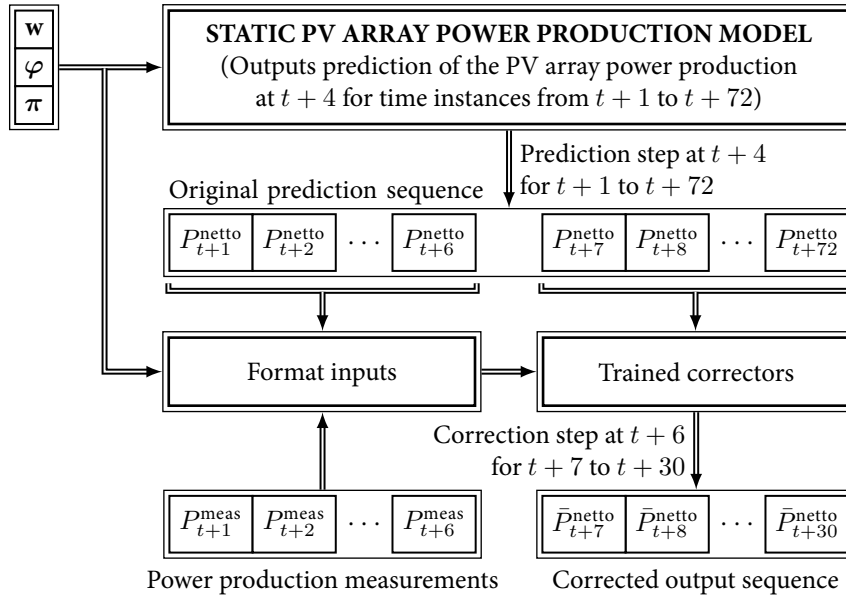


Figure 3.2: Data-flow diagram of the proposed predictor-corrector method for a correction step performed at time instant  $t + 6$  ( $w$  is predicted weather data series,  $\varphi$  are tilted surface tilt and azimuth angles,  $\pi$  are geographical and time data, whereas  $P_{t+i}^{netto}$ ,  $\bar{P}_{t+i}^{netto}$ , and  $P_{t+i}^{meas}$  are the PV array power production prediction, corrected prediction, and realization, respectively, at the time instant  $t + i$  on the 72-h prediction horizon).

The identified power production model, used to calculate the PV array power production based on concurrent predicted weather conditions, is implemented as a lookup table with incident predicted solar irradiance and the PV array temperature as inputs [45]. Evolution of the PV array temperature along the prediction horizon is usually modeled by a first-order nonlinear differential equation [46, 49, 76, 93, 94]. However, these dynamic thermal models are highly complex and very difficult to tune, even in laboratory test conditions. Since the goal is to develop a concept that can be used practically for any operating conditions and environments, a simple approximation of the PV array temperature with the air temperature is rather used, whereas the correctors are expected to fix (learn) the model approximation error. Prior to the predictor-corrector method analysis a limit performance of such temperature approximation is given.

## § CHAPTER STRUCTURE

This chapter is organized as follows. In Section 3.2 are described (i-ii) experimental setup with a single PV panel and a PV array formed in LARES, (iii) timing of the numerical weather prediction model ALADIN used by DHMZ, and (iv) data preparation procedure. Statistical methods used to analyze power production models and predictor-corrector method are given in Section 3.3. In Section 3.4 the PV panel and PV array power production models are developed and verified, and in Section 3.5 the predictor-corrector method is developed and verified.

## 3.2 Experimental setup

In this section the following subjects are discussed: (i-ii) experimental setup with a single PV panel and a PV array formed in LARES shown in Fig. 3.3, (iii) timing of the numerical weather prediction model ALADIN used by DHMZ, and (iv) data preparation procedure. Experiments with the single PV panel were conducted from 1 Aug 2015 to 30 Nov 2015 (4-month time period), while experiments with the PV array were conducted from 1 Nov 2014 to 31 Oct 2016 (2-year time period).

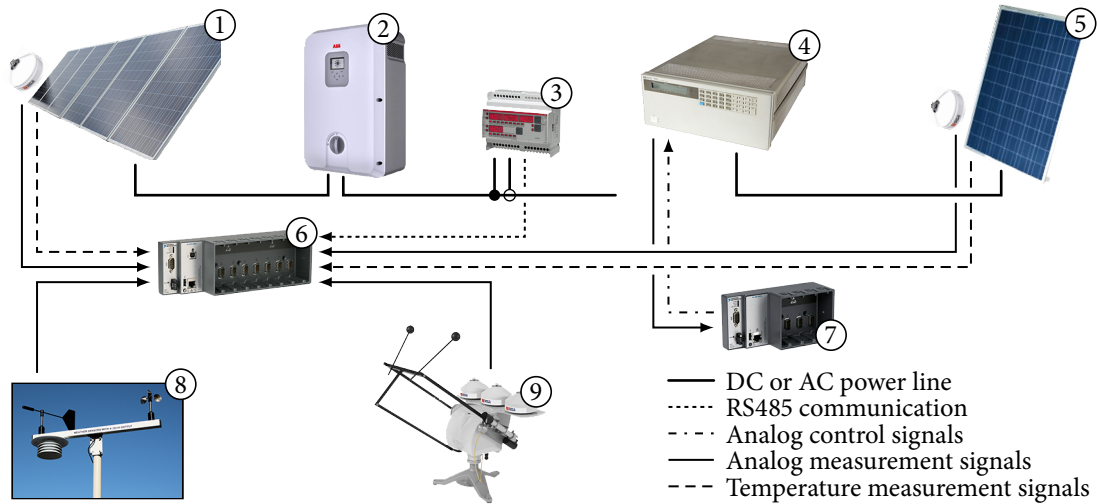


Figure 3.3: Schematic diagram of the experimental setup with the single PV panel (on the right) and with the PV array (on the left) formed in LARES: (1) photovoltaic array with 15 PV panels (Solvis SV60-235) connected in series with solar irradiance sensor (Kipp&Zonnen CMP6) placed in the same plane as the PV array active surface; (2) single-phase solar inverter (ABB PVS300) that operates in MPPT mode; (3) three-phase multimeter (ABB DMTME-I-485) to measure active and reactive power output of the PV array; (4) DC electronic load (Agilent HP6050A mainframe with HP60504B load module) to load the PV panel; (5) single PV panel (Solvis SV60-235) with solar irradiance sensor (Kipp&Zonnen CMP6) placed in the same plane as the PV panel active surface; (6) real-time industrial controller (National Instruments cRIO-9066); (7) real-time industrial controller (National Instruments cRIO-9076); (8) weather station (Intech Instruments) to measure air temperature, humidity and pressure, and wind speed and direction; (9) three solar irradiance sensors (two Kipp&Zonnen CMP11 and one CHP1) to measure diffuse and global horizontal and direct normal solar irradiance components, with sun tracker (Kipp&Zonnen Solys2) and sun sensor for active tracking.

### 3.2.1 Experimental setup with the single PV panel

In experiments with the single PV panel, a poly-Si PV panel (Solvis SV60-235) is considered with a nominal output power of 235 W at the standard test conditions, which is connected to a DC electronic load (Agilent HP6050A mainframe with a HP60504B load module) with a nominal power rating of 600 W. The PV panel is tilted  $30^\circ$  from the horizontal and is facing to the south. A First Class<sup>1</sup> pyranometer (Kipp&Zonnen CMP6) is placed in the same plane as the PV panel active surface, and a single PT100 temperature probe is mounted on the back of the PV panel by using a special thermal-conductive glue.

The incident solar irradiance and the PV panel temperature are recorded with a 1-s time step using a real-time embedded industrial controller (NI cRIO-9066). The DC electronic load is controlled by another industrial controller (NI cRIO-9076), such that the load voltage is linearly increased from 0 V to 50 V with a 220-ms time step during a 55-s period (this corresponds to a 200-mV voltage step), after which it is dropped to 0 V for the next 5 s. This procedure is repeated every minute during daylight hours. Voltage and current measured at the DC electronic load side are acquired with a 2-ms sample time, and a low-pass first-order digital filter with a cut-off frequency at 25 Hz is applied to remove unwanted high-frequency noise. Measurements of the voltage and the current at the DC load side are recorded every 220 ms, just before new voltage reference is issued to the DC electronic load, in order to ensure that measurements are recorded in a steady-state condition. The two real-time industrial controllers are time-synchronized in order to be able to pair the measurements of meteorological and electrical variables.

<sup>1</sup> According to the ISO 9060:1990 classification, Secondary Standard pyranometers are of higher quality than First Class.

### 3.2.2 *Experimental setup with the PV array*

In experiments with the PV array, an array that consists of 15 poly-Si PV panels (Solvis SV60-235) connected in series is considered, with the PV array nominal power rating of 3525 W at the standard test conditions. The PV array is connected to the utility grid via single-phase solar inverter (ABB PVS300-TL-3300W-2), which is constantly working in a maximum power point tracking (MPPT) mode. A three-phase multimeter (ABB DMTME-I-485) is placed at the solar inverter output to measure the netto output power of the PV array. The PV array is tilted  $55^\circ$  from the horizontal and is facing to the south. A First Class pyranometer (Kipp&Zonnen CMP6) is mounted in the middle of the PV array, and its sensing surface is placed in the same plane as the PV array active surface. Two PT100 temperature probes are mounted on the back of PV panels that are on opposite ends of the PV array, by using a special thermal-conductive glue, whereas the average temperature between the two probes is used as the PV array temperature. The PV array is placed at the top of the UNIZG-FER skyscraper ( $45^\circ 48' \text{ N}$ ,  $15^\circ 58' \text{ E}$ ), whereas the top floor is 60 m above the ground, and the top-floor ground surface type is pebble. The PV array lowest point is placed approximately 0.5 m and the two temperature probes are placed approximately 2 m above the top-floor ground surface. The wind speed is measured 5 m above the PV array, i.e., 65 m relative to the ground, with all meteorological equipment being within few meters of the PV array.

The incident solar irradiance, the PV array temperature, and the netto output power are recorded with a 1-s time step using a real-time embedded industrial controller (NI cRIO-9066). Except for these, measurements of several other relevant meteorological variables are also recorded with a 1-s time step: (i-ii) diffuse and global horizontal solar irradiance components, (iii-iv) wind speed and direction, and (v-vii) air temperature, pressure, and humidity. The diffuse and global horizontal solar irradiance components are measured by Secondary Standard pyranometers (Kipp&Zonnen CMP11), while direct (normal) solar irradiance component is measured by a First Class pyrliometer (Kipp&Zonnen CHP1), all three mounted on a Solys2 sun tracker with a sun sensor for active tracking.

### 3.2.3 *Numerical weather prediction model ALADIN*

Numerical weather prediction model ALADIN<sup>2</sup> is run in DHMZ every 6 h for a 72-h time period, i.e., calculation of new prediction sequence is commenced every day at 00:00, 06:00, 12:00, and 18:00 for the next 72-h time period with a 1-h time resolution, for a spatial grid of  $2 \times 2$  km. Note that ALADIN is state-of-the-art weather prediction model for the region of Croatia and is also simultaneously used in over 20 countries in Europe and northern Africa. ALADIN uses the initial lateral boundary conditions from the ARPEGE<sup>3</sup> and the IFS<sup>4</sup> global numerical weather prediction models [95]. All times of day in this chapter will be in the Coordinated Universal Time (UTC) standard. Timestamps correspond to the end of an integration period, e.g., a sample with a timestamp 01:00 represents mean value of a variable in period from 00:00 to 01:00. This notation will be used as a timestamp standard throughout the chapter.

Due to the complexity of the numerical weather prediction model in terms of computational effort, a prediction sequence of meteorological variables is available with a nearly 4-h lag, e.g., a prediction sequence commenced at 00:00 will become available at 03:55 (that day), for the period from 01:00 (that day) to 00:00 (3 days ahead). Timeline illustration of the numerical weather prediction model ALADIN operation is shown in Fig. 3.4. Predictions adapted for the exact location of the experimental setup in LARES [96] are available for the following meteorological variables:

<sup>2</sup> Aire Limitée Adaptation Dynamique développement InterNational

<sup>3</sup> Action de Recherche Petite Echelle Grande Echelle, used by Météo-France

<sup>4</sup> Integrated Forecast System, used by the European Centre for Medium-Range Weather Forecast (ECMWF)



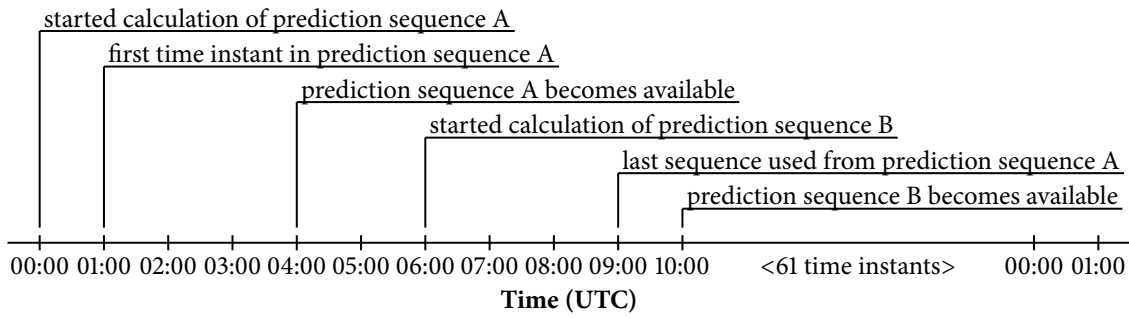


Figure 3.4: Timeline illustration of the numerical weather prediction model ALADIN operation.

(i-ii) diffuse and global horizontal solar irradiance components, (iii) direct (normal) solar irradiance component, (iv-v) wind speed and direction at 10 m and 40 m altitudes, (vi-vii) air temperature and relative humidity at 2 m above the ground, (viii) air pressure at sea level, and (ix-xii) total, high, mean, and low cloud covers.

### 3.2.4 Data preparation procedure

Prior to the verification of the PV panel and PV array power production models and the predictor-corrector method, data obtained by experiments are filtered in order to retain only relevant and high-quality measurement samples.

#### § PV PANEL DATA

Data obtained by experiments with the single PV panel are analyzed for each minute, since the PV panel voltage is increased from 0 V to 50 V during the 55-s period followed by the 5-s resting period when the voltage is set to 0 V. During this 60-s period, the PV panel static current-voltage characteristics is recorded with an incremental voltage step of 200 mV. A one-minute sequence, i.e., the static current-voltage characteristics with the incident solar irradiance and the PV panel temperature measurements, is filtered out if one of the following conditions is satisfied: (i) the mean of the solar zenith angle is greater than  $90^\circ$ , which implies the nighttime, (ii) the difference between the maximum and the minimum incident solar irradiance in a sequence is greater than 2% of the sequence mean value, or (iii) the difference between the maximum and the minimum PV panel temperature in a sequence is greater than  $1^\circ\text{C}$ . The latter two conditions are used to remove all one-minute sequences for which the recorded current-voltage characteristics have a distorted shape due to the rapid change of the incident solar irradiance or the PV panel temperature during the 60-s period. From one-minute sequences that passed the filtering procedure, the mean of the incident solar irradiance and of the PV panel temperature are calculated, as well as the maximum output power within the one-minute sequence. Figure 3.5 (on the left) shows combinations of the incident solar irradiance and the PV panel temperature data samples for verification of the PV panel power production model, with 22906 samples in total.

#### § PV ARRAY DATA

Since ALADIN outputs predictions with 1-h time step, the measured PV array power production data have to be numerically integrated within one-hour time frame, for every whole hour within a day. Following the same numerical integration procedure used by meteorological services, the data are integrated only if there are more than 80% valid samples of a variable of interest within the integration period. Otherwise, the integrated sample is omitted from the data analysis. Furthermore,

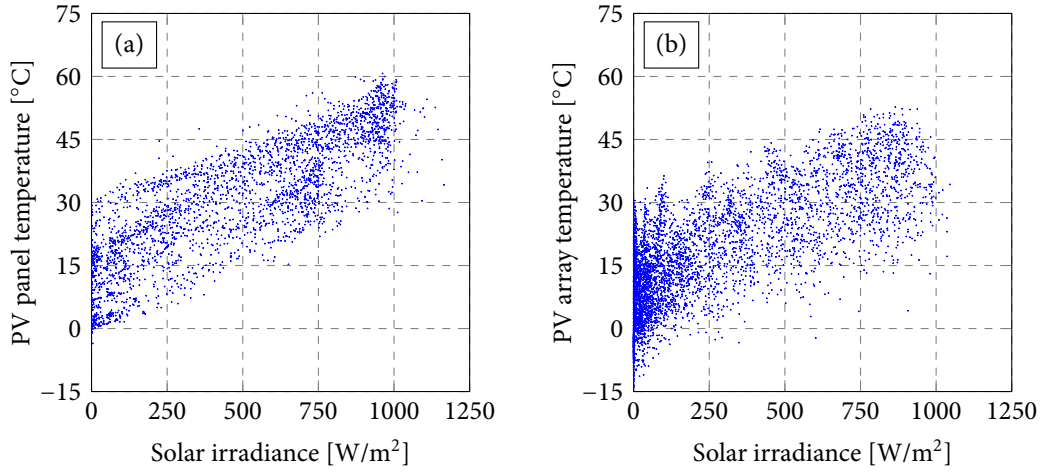


Figure 3.5: Scatter plots of incident solar irradiance versus PV panel temperature (on the left) and PV array temperature (on the right) for verification of power production models.

all one-hour samples for which the solar zenith angle is greater than  $90^\circ$  are also omitted from the data analysis, since there is no power production by the PV array during the nighttime. Figure 3.5 (on the right) shows combinations of the incident solar irradiance and the PV array temperature data samples for verification of the PV array power production model, with 9351 samples in total.

### 3.3 Performance indicators

In this section all performance indicators used for power production models and predictor-corrector method performance verification are defined. A model error is defined as the difference between measured and predicted values, as follows:

$$e_s = x_s^{\text{meas}} - x_s^{\text{mdl}}, \quad (3.1)$$

where  $x$  is a variable of interest, e.g., the PV panel or array output power, and  $s$  is an integer denoting the sample index within the verification data set. The mean bias error (MBE) and the root mean square error (RMSE) performance indicators are defined as follows:

$$\text{MBE} = \frac{1}{N} \sum_{s=1}^N e_s, \quad \text{RMSE} = \sqrt{\frac{1}{N} \sum_{s=1}^N e_s^2}, \quad (3.2)$$

where  $N$  is the total number of samples in the verification data set. Additionally, a normalized RMSE performance indicator is also used, defined with respect to a nominal or a mean value in the verification data set, as follows:

$$\text{RMSE}_n = \frac{\text{RMSE}}{x_n} \cdot 100, \quad \text{RMSE}_m = \frac{\text{RMSE}}{x_m} \cdot 100, \quad (3.3)$$

where  $x_n$  is the nominal value of the variable  $x$ , and  $x_m$  is the mean value within the verification data set  $\{x_1^{\text{meas}}, \dots, x_N^{\text{meas}}\}$ . Normalized RMSE usually gives better information on the prediction model quality than MBE or RMSE alone.

The mean squared error (MSE) performance indicator is often used for neural network training, which is basically squared RMSE, as follows:

$$\text{MSE} = \text{RMSE}^2 = \frac{1}{N} \sum_{s=1}^N e_s^2. \quad (3.4)$$

The model error probability density function (pdf) gives an insight into the error distribution. Ideally, the model error pdf can be approximated by a white noise that follows the Gaussian distribution. Figure 3.6 shows the pdf of a stochastic variable  $\tilde{x}$  that follows the Gaussian distribution,  $\tilde{x} \sim \mathcal{N}(\bar{x}, \sigma)$ , where  $\bar{x}$  is the mean (or expected) value, and  $\sigma$  is the (unbiased) standard deviation of the stochastic variable  $\tilde{x}$ , defined as:

$$\bar{x} = \frac{1}{N} \sum_{s=1}^N x_s, \quad \sigma = \sqrt{\frac{1}{N-1} \sum_{s=1}^N (x_s - \bar{x})^2}, \quad (3.5)$$

where  $x_s$  are observations of the stochastic variable  $\tilde{x}$ , and  $N$  is the number of observations. Probability that the stochastic variable  $\tilde{x}$  will take value in interval  $\bar{x} \pm \sigma$  is equal to 68.27%, and for interval  $\bar{x} \pm 3\sigma$  is equal to 99.73%. Note that it is a desirable property of the model error to be well approximated by the white noise, since that implies that all deterministic phenomena that occur in the system are captured by the model. It should be noted that the standard deviation is a better performance indicator than RMSE, since RMSE also accounts for the bias which can be easily eliminated, especially considering the fact that correctors are implemented as neural networks. Smaller standard deviation indicates better prediction since that implies less dispersion of the prediction error around its mean.

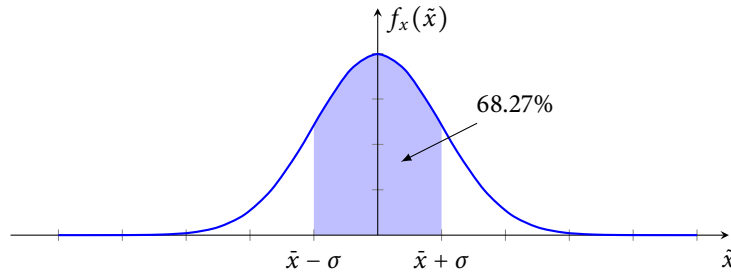


Figure 3.6: Probability density function of a stochastic variable  $\tilde{x}$  that follows the Gaussian distribution.

## 3.4 Power production models

In this section power production models of the single PV panel and the PV array are developed and verified, as follows: (i) PV panel power production model is based on a single-diode equivalent electrical model and fast numerical algorithms to solve its implicit current-voltage equation, and is verified on the 4-month experimental data obtained in LARES, as well as on experimental data obtained with artificial sun; (ii) tilted surface model to transform solar irradiance components to global solar irradiance incident with a tilted surface is briefly discussed; and (iii) PV array power production model is obtained as an extension of the PV panel power production model in series with the tilted surface model, and is verified on the 2-year experimental data obtained in LARES.

### 3.4.1 Power production model of a single PV panel

In this subsection power production model of a single PV panel is developed and verified. Performance verification of the developed model is performed on experimental data obtained by experiments (i) conducted in LARES during the 4-month time period, and (ii) with artificial sun at the PV panel constant temperature corresponding to the standard temperature test condition (25 °C), conducted at the PV panel manufacturer's research facility.

## § SINGLE-DIODE MODEL OF A PV PANEL

Figure 3.7 shows a single-diode equivalent electrical circuit of a PV panel. An implicit equation of the current-voltage static characteristics  $f_{PV}(I, V)$  can be derived from the equivalent electrical circuit as follows:

$$I = f_{PV}(I, V) = I_{ph} - \underbrace{I_0 \left[ \exp\left(\frac{V + I \cdot R_{ser}}{a \cdot V_t}\right) - 1 \right]}_{I_d} - \underbrace{\frac{V + I \cdot R_{ser}}{R_{sh}}}_{I_{sh}}, \quad (3.6)$$

where  $I$  and  $V$  are the PV panel terminal current and voltage,  $I_{ph}$  and  $I_0$  are the PV panel photo-current and the diode saturation current,  $R_{ser}$  and  $R_{sh}$  are the equivalent series and shunt resistances,  $V_t = N_s \frac{kT}{q}$  is the thermal voltage of the PV panel with  $N_s$  cells connected in series ( $N_s$  is usually listed in the PV panel datasheet),  $q$  and  $k$  are the electron charge<sup>5</sup> and the Boltzmann<sup>6</sup> constants,  $T$  is the PV panel thermodynamic temperature, and  $a$  is the diode ideality factor. In Eq. (3.6) there are five unknowns which are usually not provided in the datasheet:  $I_{ph}$ ,  $I_0$ ,  $R_{ser}$ ,  $R_{sh}$ , and  $a$ . These parameters can be determined from three characteristic points<sup>7</sup> that are usually provided in the datasheet for standard test conditions<sup>8</sup> (STC).

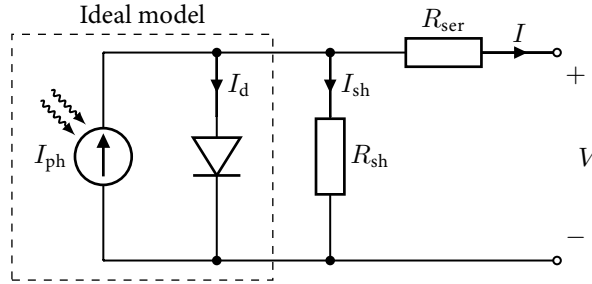


Figure 3.7: Single-diode equivalent electrical circuit of a PV panel.

The photo-current depends linearly on the incident solar irradiance  $G$ , and is also influenced by the PV panel temperature, as follows [87]:

$$\frac{I_{ph}}{I_{ph,STC}} = \frac{G}{G_{STC}} \left[ 1 + K_I (T - T_{STC}) \right], \quad (3.7)$$

where  $I_{ph,STC}$  is the photo-current at STC, and  $K_I$  is the current coefficient provided in the datasheet. The diode saturation current can be modeled as [87]:

$$\frac{I_0}{I_{0,STC}} = \left[ \frac{T}{T_{STC}} \right]^3 \exp \left[ \frac{q}{ak} \left( \frac{E_{g,STC}}{T_{STC}} - \frac{E_g}{T} \right) \right], \quad (3.8)$$

where  $I_{0,STC}$  is the diode saturation current at STC, and  $E_g$  is the semiconductor bandgap energy. Bandgap energy depends on material, and for silicon it can be modeled as [97]:

$$\frac{E_g}{E_{g,STC}} = 1 - 0.0002677(T - T_{STC}), \quad (3.9)$$

where  $E_{g,STC}$  is the bandgap energy at STC (1.12 eV for the polycrystalline silicon at 25 °C [97]).

<sup>5</sup> Electron charge constant is  $q = 1.60217662 \cdot 10^{-19}$  C

<sup>6</sup> Boltzmann constant is  $k = 1.38064852 \cdot 10^{-23}$  J/K

<sup>7</sup> Characteristic points usually provided in the PV panel datasheet for standard test conditions are: (i) short-circuit current ( $I_{sc}, 0$ ), (ii) open-circuit voltage ( $0, V_{oc}$ ), and (iii) maximum power point ( $I_{mpp}, V_{mpp}$ ).

<sup>8</sup> Standard test conditions (STC) usually assume an incident solar irradiance of  $G_{STC} = 1000$  W/m<sup>2</sup>, a PV panel temperature of  $T_{STC} = 25$  °C, and an air mass index of 1.5.

## § IDENTIFICATION OF THE SINGLE-DIODE MODEL PARAMETERS

The photo-current at STC can be determined from the short-circuit condition at STC as follows:

$$I_{\text{ph,STC}} \approx I_{\text{sc,STC}}, \quad I_{\text{ph}} > I_{\text{sc}}, \quad (3.10)$$

i.e., the photo-current is just slightly greater than the short-circuit current, considering that  $R_{\text{ser}}$  is small which results in a mV-range voltages on the diode, and that  $R_{\text{sh}}$  is large.

The diode saturation current at STC can be determined from the open-circuit condition at STC, assuming that the photo-current is approximately equal to the short-circuit current, as follows:

$$I_{0,\text{STC}} = \frac{I_{\text{ph,STC}}}{\exp\left(\frac{V_{\text{oc,STC}}}{aV_{t,\text{STC}}}\right) - 1}, \quad (3.11)$$

where  $I_{\text{ph,STC}}$  is determined in Eq. (3.10). Note that the equivalent series and shunt resistances are neglected for determination of  $I_{\text{ph,STC}}$  and  $I_{0,\text{STC}}$  since their values are unknown in this step, i.e., it is assumed that  $R_{\text{ser}}$  is small and that  $R_{\text{sh}}$  is large.

The three remaining unknown parameters ( $a$ ,  $R_{\text{ser}}$ , and  $R_{\text{sh}}$ ), can be determined in a number of ways [86, 87]. Here the three parameters are fitted in such a way that the model maximum power point (MPP) coincides with the one in the datasheet. Since the PV panel is expected to operate at the MPP most of the time [98], it seems reasonable to fit the model so that it has a good approximation ability in the vicinity of the MPP for STC. Therefore, unknown parameters are determined so that

$$\underbrace{f_{\text{PV}}(I_{\text{mpp,STC}}, V_{\text{mpp,STC}}) \cdot V_{\text{mpp,STC}}}_{P_{\text{mdl,mpp,STC}}} \approx P_{\text{ds,mpp,STC}}, \quad (3.12)$$

where  $P_{\text{mdl,mpp,STC}}$  and  $P_{\text{ds,mpp,STC}}$  are maximum powers predicted by the model and the value from the datasheet for STC, respectively. Although some authors use genetic and evolutionary algorithms to find the best-performing values of the three remaining parameters, here a brute-force search method combined with fast numerical algorithms to solve the PV panel's implicit equation is proposed. Note that there are only two independent variables in the parameters space, since  $R_{\text{sh}}$  can be determined from Eq. (3.12) for any pair  $(R_{\text{ser}}, a)$  under the condition that  $R_{\text{sh}} > 0$ , whereas the parameters space is uniformly discretized between  $(0 \text{ m}\Omega, 1)$  and  $(1000 \text{ m}\Omega, 2)$ . A contour plot of the single-diode model absolute power error at the MPP is shown in Fig. 3.8.

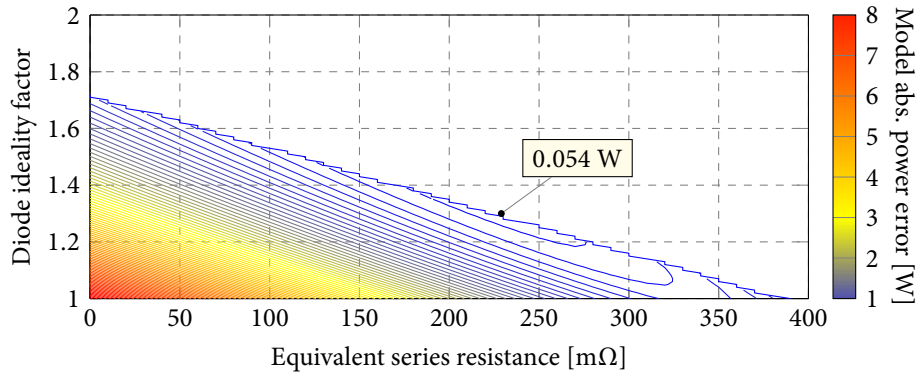


Figure 3.8: Contour plot of the PV panel single-diode model absolute power error at the MPP for STC. The model error minimum of 0.054 W is achieved for  $R_{\text{ser}}^* = 229 \text{ m}\Omega$  and  $a^* = 1.3$ , whereas  $R_{\text{sh}}^* = 642.85 \text{ k}\Omega$ .

## § FAST NUMERICAL ALGORITHMS TO SOLVE THE IMPLICIT EQUATION

The single-diode model of a PV panel has a serious limitation in terms of computational efficiency, since its equation is given in an implicit form that has no analytic solution<sup>9</sup>. This could significantly slow down the calculation of the MPP [47]. In order to overcome that, a PV panel power production model can be implemented as a lookup table with the incident solar irradiance and the PV panel temperature as inputs, as follows:

$$P_{\text{mpp}} = \mathcal{P}(G, T), \quad I_{\text{mpp}} = \mathcal{I}(G, T), \quad (3.13)$$

where  $\mathcal{P}(\cdot, \cdot)$  and  $\mathcal{I}(\cdot, \cdot)$  are lookup tables for the PV panel power and the current at the MPP.

Lookup tables are calculated by a numerical procedure for all combinations of (i) the incident solar irradiance from  $0 \text{ W/m}^2$  to  $1400 \text{ W/m}^2$  with a step of  $10 \text{ W/m}^2$ , and of (ii) the PV panel temperature from  $-20 \text{ }^\circ\text{C}$  to  $+80 \text{ }^\circ\text{C}$  with a step of  $5 \text{ }^\circ\text{C}$ . The MPP is determined for each irradiance-temperature pair  $(G, T)$  using the identified single-diode model, such that the Eq. (3.6) is solved for the current at a finite number of voltage values ranging from  $0 \text{ V}$  to  $50 \text{ V}$  with a step of  $0.1 \text{ V}$ . The lookup tables  $\mathcal{P}(\cdot, \cdot)$  and  $\mathcal{I}(\cdot, \cdot)$  fully define the static power production model of a single PV panel.

Since the single-diode electrical model equation is given in an implicit form, the equation can be numerically solved either with the voltage or the current as the equation input: (i) if the equation input is the PV panel voltage  $V^*$  then the Newton's gradient-based method is used, and (ii) if the model input is the PV panel current  $I^*$  then the bisection method is used. It should be noted that the bisection method is in general much slower than the Newton's gradient-based method for cases where the gradient-based method can be applied. The equation in (3.6) can be rewritten as:

$$f_{\text{PV}}^*(I, V) = I - f_{\text{PV}}(I, V) = 0, \quad (3.14)$$

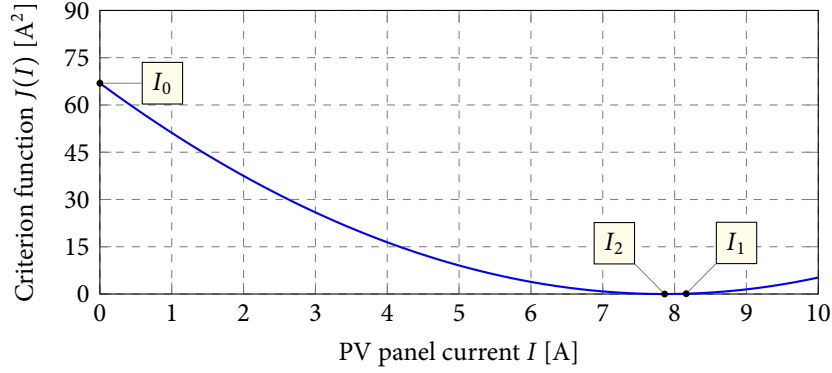
where either the voltage  $V$  or the current  $I$  is used as the implicit equation input. Note that the exact solution of the implicit equation (3.6) is the root of the function  $f_{\text{PV}}^*(\cdot, \cdot)$ .

If the voltage is used as the equation input, then the criterion function used for numerical optimization to find unknown  $I^*$  is defined as  $J(I) = f_{\text{PV}}^*(I, V^*)^2$ , which is in fact the square of the solution error in terms of the PV panel current. The criterion function is equal to zero at the exact solution ( $I = I^*$ ), and it is greater than zero elsewhere ( $I \neq I^*$ ). Newton's gradient-based method finds the solution in an iterative manner as follows:

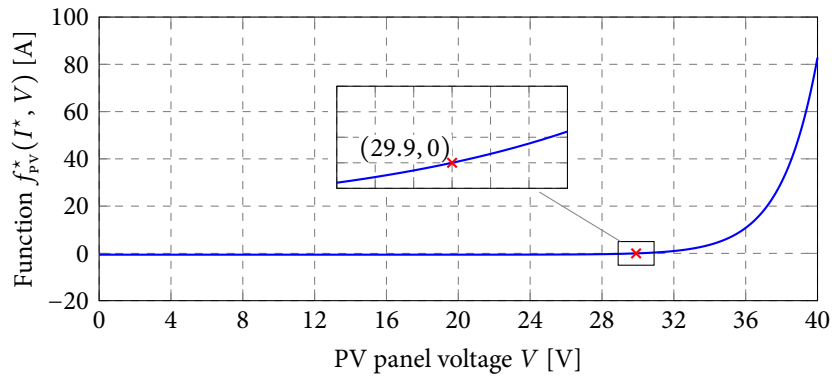
$$I_{n+1} = I_n - \frac{J'(I_n)}{J''(I_n)}, \quad n \geq 0, \quad (3.15)$$

where  $n$  is the iteration index,  $I_0$  is the initial guess of the PV current, while  $J'(I_n)$  and  $J''(I_n)$  are the first and the second derivative of the criterion function  $J(\cdot)$  with respect to  $I$ , evaluated at  $I_n$ . Note that if  $J(\cdot)$  is a quadratic function, then the exact extremum (minimum) is found in a single step. Also, closer the initial guess  $I_0$  is to the exact solution  $I^*$ , fewer steps are required to find the exact solution, whereas in this example it can be safely set to  $I_0 = 0 \text{ A}$ . Figure 3.9a shows a typical shape of the criterion function  $J(I)$  with respect to the PV panel current and for the constant PV panel voltage  $V^* = 29.9 \text{ V}$ , which corresponds to the PV panel voltage at the MPP. It can be seen that the criterion function has a similar shape to that of a quadratic function, which is why Newton's gradient-based method fits well for solving the implicit equation in (3.6) when the equation input is the PV panel voltage. This method is tested on a large number of different scenarios, and the error of the found solution in terms of the PV panel current is in  $\mu\text{A}$ -range after no more than 2 iterations.

<sup>9</sup> Note that analytic solution exists if the equivalent series and shunt resistances,  $R_{\text{ser}}$  and  $R_{\text{sh}}$ , are neglected.



(a) The criterion function  $J(I) = f_{PV}^*(I, V^*)^2$  with respect to the PV panel current  $I$ , and for the constant PV panel voltage  $V^* = 29.9$  V.



(b) The criterion function  $f_{PV}^*(I^*, V)$  with respect to the PV panel voltage  $V$ , and for the constant PV panel current  $I^* = 7.86$  A.

Figure 3.9: Criterion functions used to solve the single-diode model implicit equation.

Figure 3.9b shows a typical shape of the function  $f_{PV}^*(\cdot, \cdot)$  with respect to the PV panel voltage and for the constant PV panel current  $I^* = 7.86$  A, which corresponds to the PV panel current at the MPP. In this case the bisection method (sometimes referred to as the *interval halving method*) is proposed to find the exact solution  $V^*$ . The bisection method is applicable for numerically solving an equation  $g(x) = 0$  for the real variable  $x$ , where  $g(\cdot)$  is a continuous function defined on the interval  $[a, b]$ , whereas  $g(a)$  and  $g(b)$  are of opposite signs. This holds true for the considered criterion function  $f_{PV}^*(I^*, V)$  under condition that the interval  $[a, b]$  is chosen so that the exact solution  $V^*$  lies inside that interval. In general, the bisection method requires more iterations to find the exact solution compared to the Newton's gradient-based method, but due to the shape of the function  $f_{PV}^*(\cdot, \cdot)$  it is better to use the bisection method in this case.

#### § VERIFICATION ON EXPERIMENTS WITH THE ARTIFICIAL SUN

Power production model of the single PV panel in (3.13) is verified on experimental data obtained by experiments with artificial sun, conducted at the PV panel manufacturer's research facility. Experiments were carried out for incident solar irradiances from  $200 \text{ W/m}^2$  to  $1200 \text{ W/m}^2$  with a step of  $100 \text{ W/m}^2$ , and at the constant PV panel temperature of  $25 \text{ }^\circ\text{C}$ . Figure 3.10 shows comparison between the PV panel power production model output and the maximum power obtained by experiments on the PV panel of the same type, for different incident solar irradiances. Performance indicators for the eleven test points are shown in Table 3.1a. They indicate that the PV panel power production model shows a very good performance at the nominal PV panel temperature.

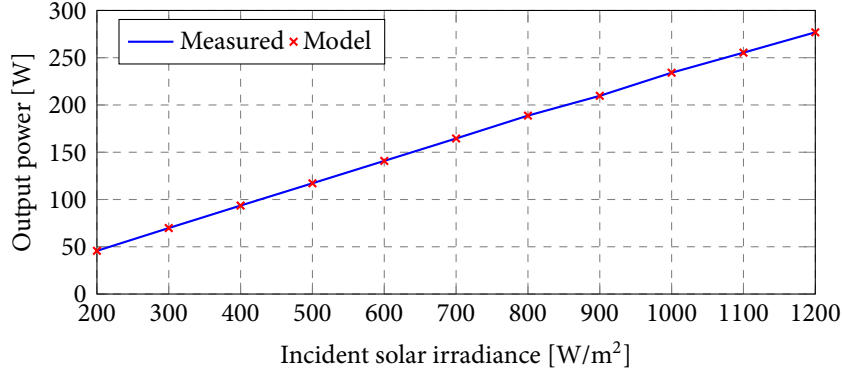


Figure 3.10: Comparison between the PV panel power production model output and the maximum power obtained by experiments with artificial sun.

#### § VERIFICATION ON EXPERIMENTS CONDUCTED IN LARES

Performance verification presented here gives a full insight into the PV panel power production model overall performance, unlike verification performed on experiments with artificial sun which gave insight into the performance only for the nominal PV panel temperature of 25 °C.

In the system used for experiments with the single PV panel there are additional resistances that are not taken into account by the single-diode model, such as resistances of power lines, connections etc. An equivalent electrical circuit of the system used for experiments with the single PV panel is shown in Fig. 3.11. The total additional resistance that accounts for the aforementioned parasitic resistances can be estimated as:

$$R_{ser}^+ = \frac{V_{PV} - V_{meas}}{I_{PV}}, \quad (3.16)$$

where  $V_{meas}$  and  $I_{PV}$  are voltage and current measured at the DC electronic load side, and  $V_{PV}$  is voltage measured at the PV panel side. The total additional resistance was estimated to be 440 mΩ by performing a sequence of current-voltage measurements for the considered system.

The PV panel netto output power delivered to the load, taking into account  $R_{ser}^+$ , is defined as:

$$P_{netto} = P_{mpp} - I_{mpp}^2 R_{ser}^+, \quad (3.17)$$

where  $I_{mpp}^2 R_{ser}^+$  are the ohmic losses on the additional resistance. Note that the netto output power prediction of a single PV panel is very sensitive to the estimated value of the additional resistance, especially for large currents  $I_{mpp}$ .

Table 3.1: Performance indicators for experiments with the single PV panel during the 4-month time period

(a) Experiments with artificial sun at 25 °C					
PV panel	MBE [W]	RMSE [W]	$\sigma$ [W]	RMSE <sub>n</sub>	RMSE <sub>m</sub>
SV60-235	-0.06	2.32	2.43	0.99%	1.42%
(b) Experiments with single PV panel conducted in LARES					
$R_{ser}^+$ [mΩ]	MBE [W]	RMSE [W]	$\sigma$ [W]	RMSE <sub>n</sub>	RMSE <sub>m</sub>
440	-7.41	11.83	9.23	5.04%	13.07%
810	0.42	4.70	4.68	2.00%	5.19%



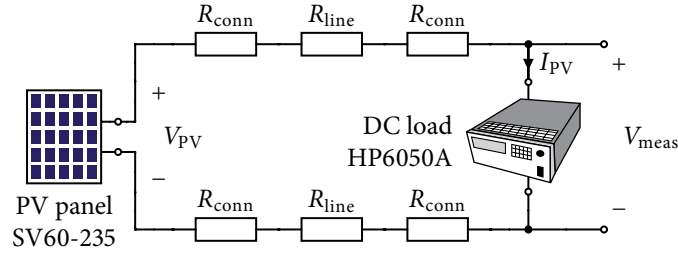


Figure 3.11: Equivalent electrical circuit of the system used in experiments with the single PV panel, conducted in LARES ( $R_{\text{conn}}$  and  $R_{\text{line}}$  are connection and line resistances, respectively).

Figure 3.12a shows performance indicators of the PV panel power production model on experiments conducted in LARES during the 4-month time period, for all values of  $R_{\text{ser}}^+$  from 0 m $\Omega$  to 1400 m $\Omega$  with a step of 10 m $\Omega$ . It can be seen that the best-performing additional resistance considering the model RMSE is 810 m $\Omega$ , which is almost double of the estimated value. Reasons for this include resistance fluctuations due to the temperature, measurement noise etc. The shape of the estimated model error pdfs, shown in Fig. 3.12b and Fig. 3.12c, indicate that there might be additional phenomena in the system that are not captured by the PV panel power production model.

Performance indicators of the PV panel power production model for experiments conducted in LARES, given in Table 3.1b, are comparable to performance indicators obtained by verification on experiments with artificial sun. This confirms validity of the PV panel power production model for a wide range of irradiance-temperature pairs. A small discrepancy between performance indicators for the two experiments are mainly due to the measurement noise which is present in experiments conducted in LARES, as well as due to the fact that the single-diode model does not collect all temperature effects on the PV panel power production.

### 3.4.2 Solar irradiance on a tilted surface

Predictions of solar irradiance components are only available for the direct (normal), and for diffuse and global horizontal solar irradiance components. The global solar irradiance incident on a tilted surface comprises of three basic components: (i) the direct  $B_\varphi$  (ii) the sky diffuse  $D_\varphi$ , and (iii) the reflected solar irradiance component  $R_\varphi$ , as follows:

$$G_\varphi = B_\varphi + D_\varphi + R_\varphi, \quad (3.18)$$

where  $\varphi = (\beta, \gamma)$  is the tilted surface orientation, while  $\beta$  and  $\gamma$  are the tilt and azimuth angles. There are many tilted surface models reported in literature [48, 78–81], with main difference between them being in the concept of whether or not the diffuse irradiance is isotropically distributed over the sky dome. In this subsection a short review of the used tilted surface model is given, since the tilted surface model is considered as a part of the PV array power production model.

#### § DIRECT (TILTED) SOLAR IRRADIANCE COMPONENT

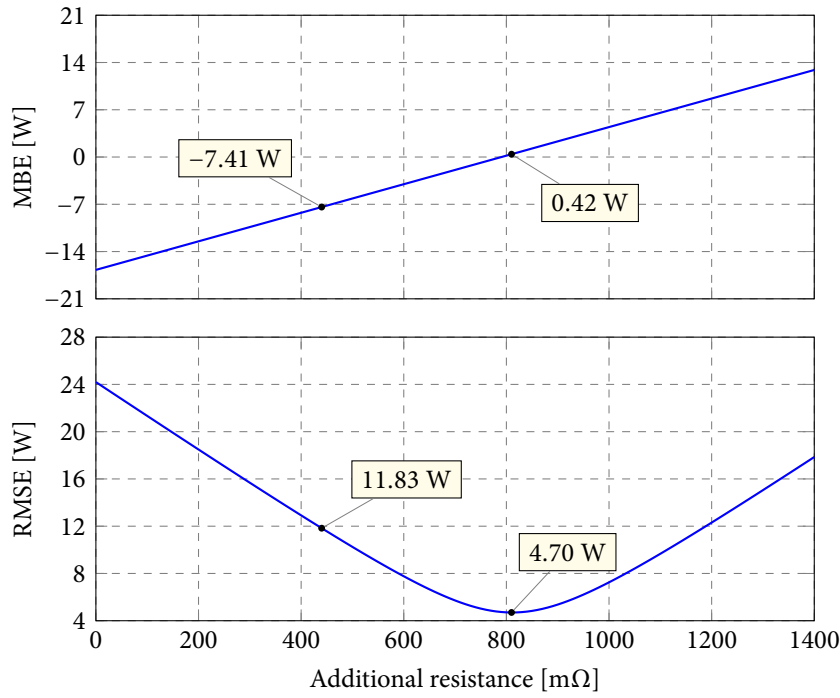
Calculation of the direct solar irradiance incident on a tilted surface is purely geometrical [80]:

$$B_\varphi = B_n \cdot \cos \theta, \quad (3.19)$$

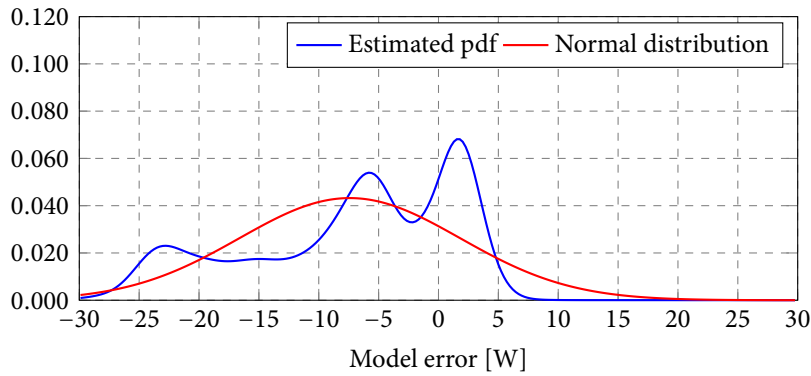
where  $B_n$  is the direct (normal) solar irradiance component, and  $\theta$  is the angle of incidence [80], i.e., the angle between the sun direction and the normal of a tilted surface (see Fig. 3.13):

$$\cos \theta = \cos \theta_z \cos \beta + \sin \theta_z \sin \beta \cos(\gamma_s - \gamma). \quad (3.20)$$

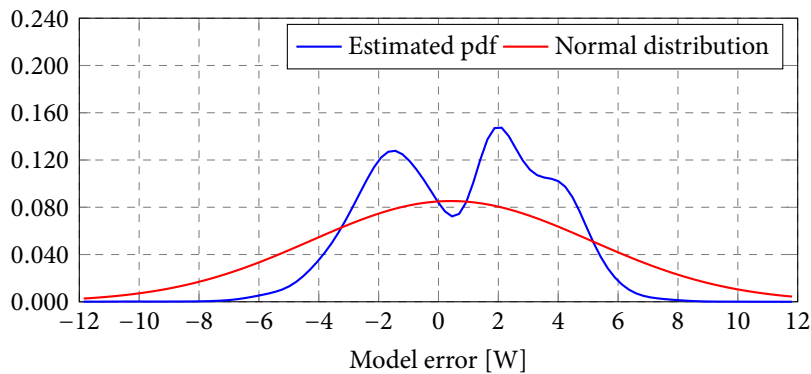
where  $\theta_z$  and  $\gamma_s$  are the solar zenith and azimuth angles, respectively.



(a) MBE and RMSE of the PV panel power production model tested for different  $R_{ser}^+$ .



(b) Probability density function of the PV panel power production model error for the estimated additional resistance  $\hat{R}_{ser}^+ = 440$  m $\Omega$ .



(c) Probability density function of the PV panel power production model error for the best-performing additional resistance  $R_{ser}^{++} = 810$  m $\Omega$ .

Figure 3.12: Performance indicators of the PV panel power production model on experiments conducted in LARES during the 4-month time period.

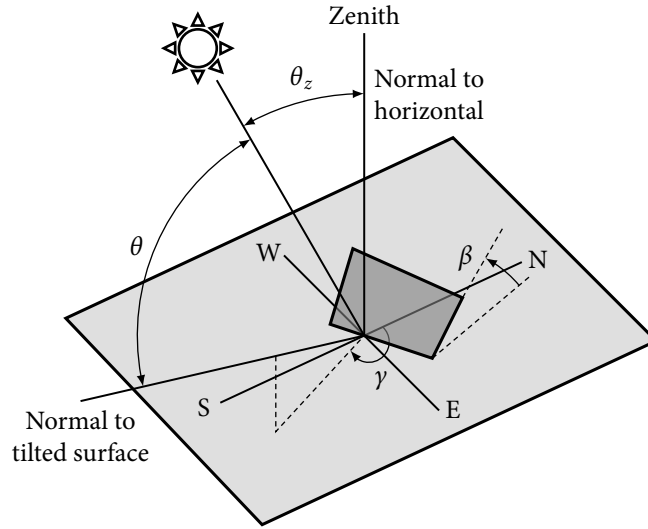


Figure 3.13: Angles of a tilted surface ( $\theta$  is angle of incidence of a tilted surface,  $\beta$  and  $\gamma$  are tilted surface tilt and azimuth angles, while  $\theta_z$  and  $\gamma_s$  are solar zenith and azimuth angles) [80].

#### § DIFFUSE (TILTED) SOLAR IRRADIANCE COMPONENT

Diffuse (tilted) solar irradiance component can be calculated as:

$$D_\varphi = D_h \cdot r_d, \quad r_d \geq 0, \quad (3.21)$$

where  $D_h$  is the diffuse (horizontal) solar irradiance component, and  $r_d$  is the diffuse irradiance transposition factor that is defined differently for each model in literature. Here the Hay's anisotropic model [81] is used, which defines the diffuse irradiance transposition factor as follows:

$$r_{d,Ha} = \frac{B_n}{G_{ext}} \frac{\cos \theta}{\cos \theta_z} + \left(1 - \frac{B_n}{G_{ext}}\right) \frac{1 + \cos \beta}{2}, \quad (3.22)$$

where  $G_{ext}$  is the extra-atmospheric solar radiation which varies depending on the Earth's position relative to the Sun. To simplify the model, one can use an approximation  $G_{ext} = 1367 \text{ W/m}^2$ .

#### § REFLECTED (TILTED) SOLAR IRRADIANCE COMPONENT

The classical approach to modeling reflected solar irradiance assumes that reflected rays are diffuse and coefficients of reflection of direct and diffuse rays are identical. The evaluation of ground reflected diffuse irradiance is thus dependent on the transposition factor for ground reflection [78]:

$$R_\varphi = \rho \cdot G_h \cdot r_r, \quad r_r = \frac{1}{2}(1 - \cos \beta), \quad (3.23)$$

where  $\rho \cdot G_h$  is ground reflected solar irradiance component,  $\rho \in [0, 1]$  is the foreground's albedo which is usually unknown,  $G_h$  is global (horizontal) solar irradiance, and  $r_r$  is the transposition factor for ground reflection. Here  $\rho = 0.2$  is used, which is a typical value for urban environments [99].

#### § THE TILTED SURFACE MODEL

Instead of using the measured direct (normal) solar irradiance component, prediction of which is not that common, its estimated value is used instead:

$$\hat{B}_n = \frac{G_h - D_h}{\cos \theta_z}. \quad (3.24)$$

The tilted surface model inputs are: (i-ii) diffuse and global horizontal solar irradiance components, (iii) estimated direct solar irradiance component, and (iv-vii) solar and tilted surface angles.

### 3.4.3 Power production model of a PV array

In this subsection the netto power production model of a single PV panel is extended to a PV array. A joined tilted surface and PV array power production model is also discussed. As already explained in Section 3.1, these two models are denoted as *the array model* and *the joined model*. Performance verification of both models is performed on experimental data obtained by experiments with the PV array during the 2-year time period, using measurements of solar irradiance components.

#### § EXTENSION OF THE POWER PRODUCTION MODEL OF SINGLE PV PANEL TO PV ARRAY

Photovoltaic array consists of a certain number of PV panels placed in the same plane, electrically organized in  $n_p$  parallel branches, whereas each branch consists of  $n_s$  PV panels connected in series. Equivalent electrical circuit of the system used in experiments with the PV array is shown in Fig. 3.14. The netto power production model of a single PV panel given in Eq. (3.17) can be extended to a PV array, denoted as the array model, as follows:

$$P_{\text{netto}} = \left[ (n_s n_p) P_{\text{mpp}} - (n_p I_{\text{mpp}})^2 R_{\text{ser}}^+ \right] \frac{\eta_{\text{INV}}}{100\%}, \quad (3.25)$$

where  $P_{\text{netto}}$  is the PV array netto output power, i.e., power at the solar inverter output,  $R_{\text{ser}}^+$  is the equivalent series resistance that accounts for resistances of power lines and connections,  $\eta_{\text{INV}}$  is the solar inverter conversion efficiency, while  $P_{\text{mpp}}$  and  $I_{\text{mpp}}$  are the power and the current of a single PV panel in the PV array at the MPP for the given incident solar irradiance and the PV panel temperature, as defined in Eq. (3.13).

The solar inverter conversion efficiency can be estimated as a product of the inverter electrical efficiency (usually around 95% for commercially available inverters), and the maximum power point tracking (MPPT) algorithm efficiency (usually around 98% in real-world conditions). The solar inverter used in the experiments has a conversion efficiency of 96% at the nominal output power [100]. It must be noted that the solar inverter conversion efficiency is not constant as assumed here, but it depends on the output power and the operating voltage at the DC side. Figure 3.15 shows a conversion efficiency curve of the solar inverter used in experiments, obtained with respect to the standard *Overall efficiency of grid connected photovoltaic inverter* (EN 50530). It can be seen that the solar inverter conversion efficiency drops significantly for power output below 30% of the inverter maximum output power, whereas the considered solar inverter nominally operates at 450 V.

Photovoltaic panels in a PV array are usually connected in series to increase the PV array voltage, in order to keep the PV array current as small as possible due to ohmic losses, i.e.,  $n_p$  is usually small compared to  $n_s$ . Therefore, the additional resistance  $R_{\text{ser}}^+$  does not affect the netto output power as much as the solar inverter conversion efficiency. Additional resistance is set to an approximate value of  $R_{\text{ser}}^+ = 800 \text{ m}\Omega$ , which is inside the typical range.

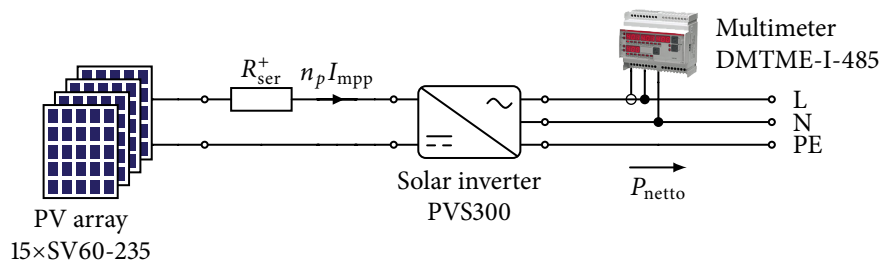


Figure 3.14: Equivalent electrical circuit of the system used in experiments with the PV array during the 2-year time period. The PV array consists of 15 PV panels (Solvis SV60-235) connected in series.

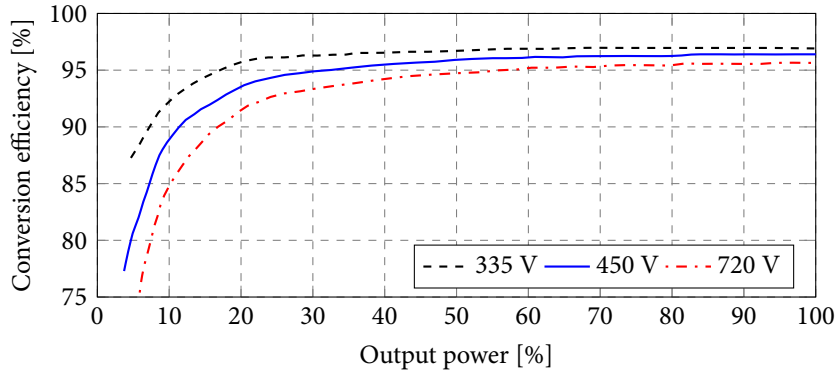


Figure 3.15: ABB PVS300-TL-3300W-2 solar inverter conversion efficiency versus operating power, for different operating voltages at the DC side [100], with respect to EN 50530. The considered PV array operates at 450 V.

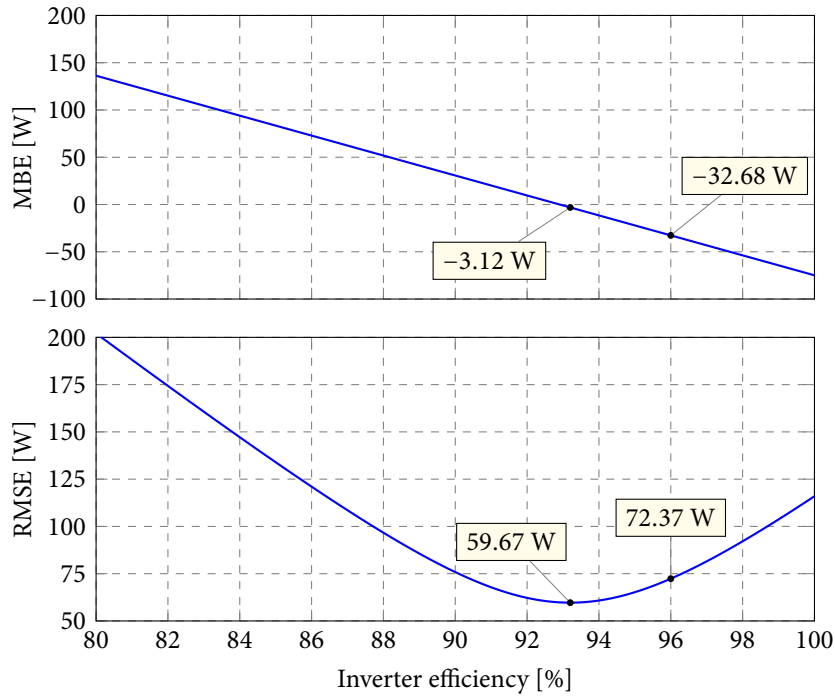
#### § VERIFICATION OF THE ARRAY MODEL

To show how the inverter conversion efficiency affects performance of the array model, all efficiencies from 80% to 100% with a step of 0.1% were tested on the 2-year experimental data set, and the results are shown in Fig. 3.16a. It can be seen that the best-performing inverter conversion efficiency considering the model RMSE is  $\eta_{INV}^* = 93.2\%$ , which should not be considered as the actual efficiency as its value is fitted for experimental data which are subject to disturbances. The shape of the estimated model error pdf, shown in Fig. 3.16b, indicates that there might be additional deterministic phenomena in the system which are not captured by the array model.

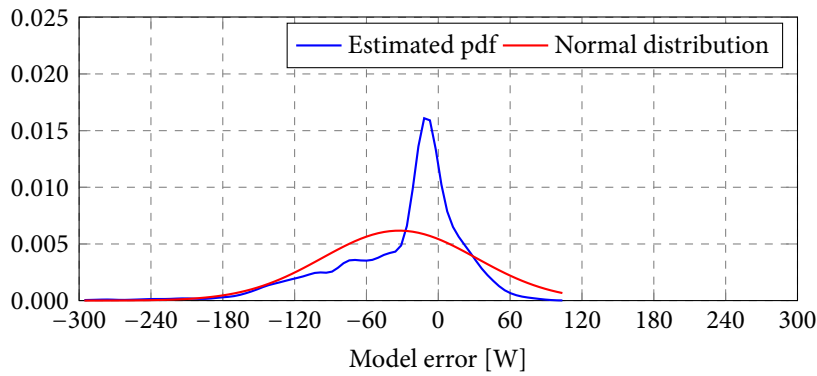
Performance indicators of the array model on the 2-year experimental data set are shown in Table 3.2a. Except for the datasheet and the best-performing conversion efficiency, performance of the array model was also tested by using the detailed conversion efficiency model  $\eta(P)$  shown in Fig. 3.15, implemented as a lookup table. It can be seen that the performance indicators are somewhat improved by using the detailed conversion efficiency model instead of the constant efficiency from the datasheet, in terms of the model MBE. The main reason why performance indicators are not improved significantly by using the detailed conversion efficiency model is because the detailed model differs from the constant value found in the datasheet only at low output powers, i.e., at output powers that are below 30% of the inverter maximum power, which have lower impact on performance indicators. However, it is unlikely that end-users will have the detailed conversion efficiency model at the disposal, and the presented verification shows that it is sufficient to use the constant conversion efficiency from the datasheet.

#### § VERIFICATION OF THE JOINED MODEL

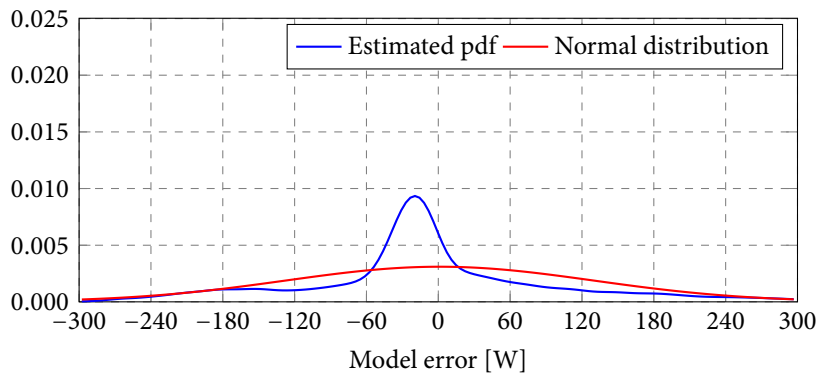
Performance verification of the joined tilted surface and PV array power production models, denoted as the joined model, is presented here. The reason to join these two models is that solar irradiance predictions are, if at all, only available for the direct (normal), diffuse and global horizontal solar irradiance components, and to get the prediction of the global solar irradiance incident on a tilted surface oriented at some arbitrary  $\varphi = (\beta, \gamma)$ , the tilted surface model has to be employed. For this analysis the Hay's anisotropic model defined in Eq. (3.22) was used. As for the two submodels' user-defined parameters, the following were used: (i) solar inverter conversion efficiency of  $\eta_{INV} = 96\%$ , (ii) total additional resistance of  $R_{ser}^+ = 800 \text{ m}\Omega$ , and (iii) albedo of  $\rho = 0.2$ . Note that the datasheet efficiency of the solar inverter was used instead of the best-performing efficiency  $\eta_{INV}^*$ , since the value of  $\eta_{INV}^*$  cannot be determined without expensive solar irradiance sensors.



(a) MBE and RMSE of the array model versus the inverter conversion efficiency.



(b) Probability density function of the array model error, with the constant inverter conversion efficiency from the datasheet  $\eta_{INV} = 96\%$ .



(c) Probability density function of the joined model error with the following parameters:  $\eta_{INV} = 96\%$ ,  $R_{ser}^+ = 800 \text{ m}\Omega$ , and  $\rho = 0.2$ .

Figure 3.16: Performance indicators of array and joined models on the 2-year data set.

Table 3.2: Performance indicators of array and joined models on the 2-year data set

(a) The array model performance indicators					
$\eta_{\text{INV}}$	MBE [W]	RMSE [W]	$\sigma$ [W]	RMSE <sub>n</sub>	RMSE <sub>m</sub>
96%	-32.68	72.37	64.57	2.05%	7.38%
$\eta_{\text{INV}}^*$	-3.12	59.67	59.60	1.69%	6.08%
$\eta(P)$	-17.92	73.14	70.92	2.08%	7.46%

(b) The joined model performance indicators					
$\eta_{\text{INV}}$	MBE [W]	RMSE [W]	$\sigma$ [W]	RMSE <sub>n</sub>	RMSE <sub>m</sub>
96%	1.10	128.64	128.64	3.65%	13.13%
$\eta(P)$	16.79	132.14	131.08	3.75%	13.48%

Performance indicators of the joined model are given in Table 3.2b, and the estimated model error pdf is shown in Fig. 3.16c. As expected, the two submodels' errors both affect the joined model performance, since the two submodels operate in series, as shown in Fig. 3.1. The RMSE of the joined model is around 3.5% of the PV array nominal output power, and around 13% of the mean output power on the 2-year experimental data set, which indicates that the joined model is still good enough to be used as a reliable prediction model. The detailed inverter conversion efficiency model  $\eta(P)$  does not improve performance indicators significantly for the same reasons as in the case of the PV array power production model, i.e., of the array model, alone.

### 3.5 Predictor-corrector method

In this section the predictor-corrector method is developed and verified to improve prediction sequence statistics, i.e., to reduce prediction error mean and standard deviation along the prediction horizon by using near-history realizations of the predicted variable. Correctors are realized as neural networks which are trained, validated and tested on the 2-year data set which consists of (i) PV array power production data obtained by experiments in LARES, and (ii) historical meteorological variables predictions provided by DHMZ. It should be noted that the proposed method can be applied for any prediction variable, and not only for the PV array power production prediction [51].

#### 3.5.1 Neural-network structure used for correction models

All correction models are realized as a multilayer perceptron (MLP) neural network with a single hidden layer in Neural Network Toolbox [101] for MATLAB. The cost function used for neural network training is MSE, which is defined as the average squared error between the neural network's output  $f_{\text{MLP}}(\cdot, \cdot)$  and the target value  $y$  over all input-output pairs  $(\mathbf{x}_k, y_k)$ ,  $\mathbf{x}_k \in \mathbf{X}$ ,  $y_k \in \mathbf{Y}$ , as follows:

$$\mathfrak{J}(\mathbf{X}, \mathbf{Y}, \boldsymbol{\theta}) = \frac{1}{N} \sum_{k=1}^N (y_k - f_{\text{MLP}}(\mathbf{x}_k, \boldsymbol{\theta}))^2, \quad (3.26)$$

where  $N$  is the total number of input-output pairs in the training data set, and  $\boldsymbol{\theta}$  is a vector of neural network's parameters. For neural network training well-known gradient-based Levenberg-Marquardt algorithm [102] is used, whereas the training is repeated 25 times for 10 different numbers of neurons uniformly distributed from 5 to 50, organized in a single hidden layer.

The 2-year data set is divided into three subsets: (i) training, (ii) validation, and (iii) testing data subsets. Training and validation data subsets are composed of randomly selected valid samples in the period from 1 Nov 2014 to 31 Oct 2015 (a 1-year time period) with a ratio of 75:25, whereas the testing data subset is composed of all valid samples in the period from 1 Nov 2015 to 31 Oct 2016 (a 12-month time period). Note that the neural network parameters are tuned based on the training data subset only, whereas training stopping criteria are implemented as follows: (i) the maximum number of iterations is reached (1000 iterations is used), or (ii) the neural network performance on the validation data subset shows no improvement after some predefined number of iterations (20 iterations is used), which is also known as the implicit regularization, i.e., the validation data subset does not participate in neural network's parameters fitting but is used to stop the training procedure in order not to overtrain the neural network. A corrector for each correction type is chosen as the best performing neural network out of  $25 \times 10$  trained neural networks on the validation data subset. The testing data subset does not participate in neural network training in any way, and is thus the most relevant to check performance of trained neural networks, i.e., correctors.

### 3.5.2 Static PV array power production model

In this subsection a performance verification of the developed PV array power production model is given, on the real measurements obtained by experiments in LARES during the 2-year time period, whereas only the daylight hours are taken into account. Limit performance of the PV array power production model is also assessed by introducing neural-network-based static correction which sets a target for the predictor-corrector method developed later in this section.

#### § THERMAL MODEL APPROXIMATION

A dynamic thermal model of a PV panel [49, 76, 93, 94] is highly complex and very difficult to tune, even under laboratory test conditions. The main reason for this is the thermal interaction between the PV panel and the environment which is very difficult to model. Since the final goal is to develop a concept that can be used practically for any operating conditions and environments, instead of using the dynamic thermal model a simple approximation of the PV array thermal model by the air temperature along the prediction horizon is used. In this way, the PV array power production model is no longer dynamic but rather static, which proves to be more efficient and numerically stable.

#### § PERFORMANCE VERIFICATION

The most important inputs to calculate PV array netto power production are incident solar irradiance and the PV array temperature. The following four data sets are considered for performance verification: (a) measurements of incident solar irradiance and the PV array temperature, (b) measurements of incident solar irradiance and approximation of the PV array temperature, (c) estimation of incident solar irradiance and measurements of the PV array temperature, and (d) estimation of incident solar irradiance and approximation of the PV array temperature. Figure 3.17 shows scatter plots of the PV array power production model without correction (blue markers) for the considered four data sets, and numeric values of the performance indicators are given in Table 3.3a. As expected, the best performance is achieved on the data set (a), since real measurements of incident solar irradiance and the PV array temperature are used. However, performance indicators calculated on the data set (d) give more realistic information for practical applications, since incident solar irradiance must be calculated by the tilted surface model, and the PV array thermal model is approximated by the air temperature. Scatter plots also reveal that the thermal model approximation causes less dispersion



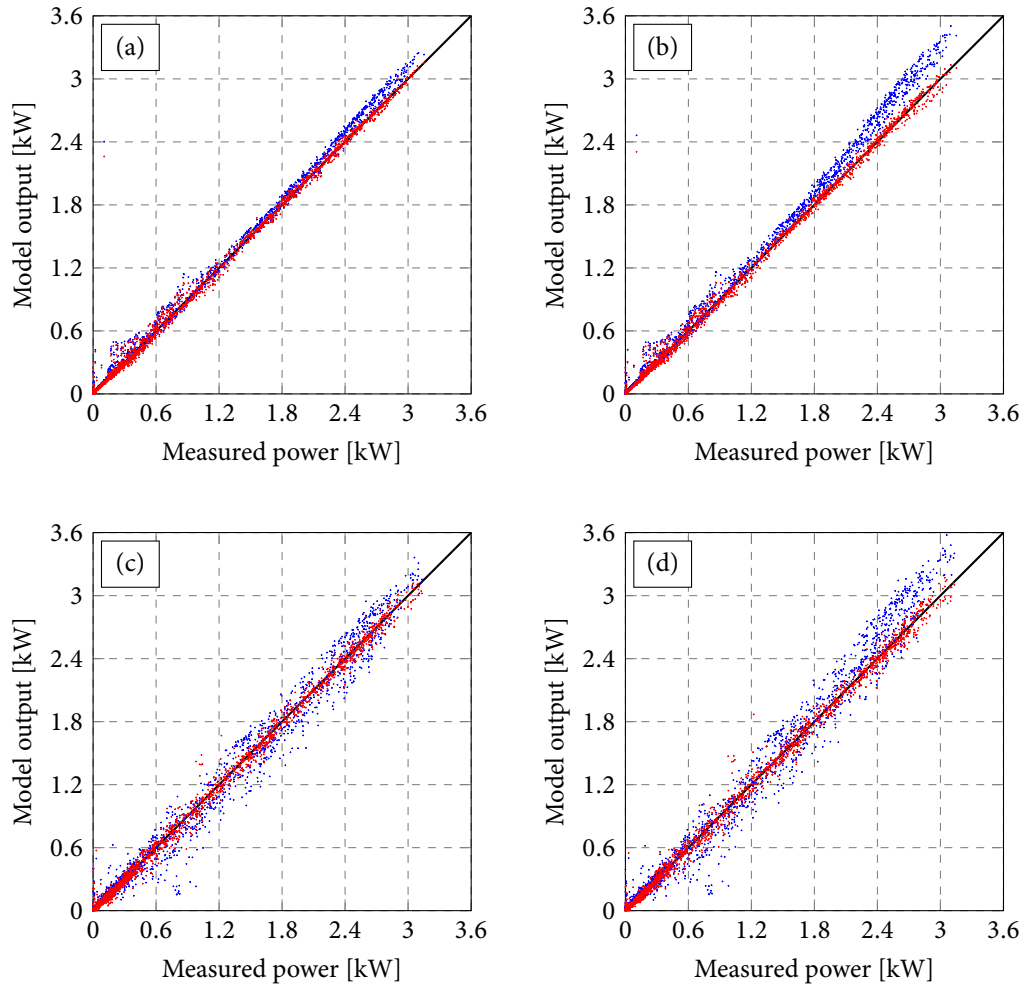


Figure 3.17: Scatter plots of the PV array power production model on the considered four data sets (a)–(d), formed from the testing data subset only, without (blue markers) and with (red markers) static correction. Incident solar irradiance measurements used in (a) and (b), and estimation in (c) and (d); PV array temperature measurements used in (a) and (c), and approximation in (b) and (d).

Table 3.3: Performance indicators of the PV array power production model on the considered four data sets (a)–(d), formed from the testing data subset only, without and with static correction

(a) Performance indicators without correction					
Data set	MBE [W]	RMSE [W]	$\sigma$ [W]	RMSE <sub>n</sub>	RMSE <sub>m</sub>
(a)	-35.08	78.56	70.31	2.23%	7.72%
(b)	-79.74	138.64	113.43	3.93%	13.63%
(c)	5.96	128.60	128.48	3.65%	12.65%
(d)	-37.39	156.85	152.35	4.45%	15.43%

(b) Performance indicators with static correction					
Data set	MBE [W]	RMSE [W]	$\sigma$ [W]	RMSE <sub>n</sub>	RMSE <sub>m</sub>
(a)	-3.17	59.47	59.39	1.69%	5.85%
(b)	-3.88	61.08	60.96	1.73%	6.00%
(c)	8.61	68.90	68.36	1.95%	6.78%
(d)	6.66	65.56	65.23	1.86%	6.45%

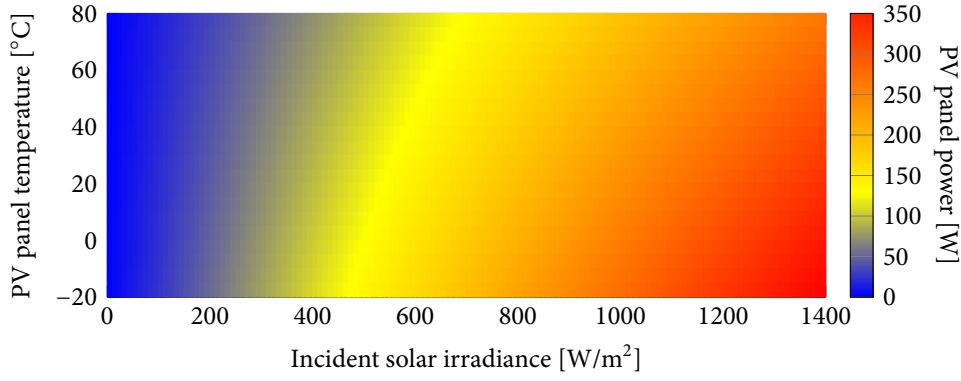


Figure 3.18: Surface plot of the PV panel power production at the MPP.

(i.e., uncertainty) than the tilted surface model. Additionally, the thermal model approximation shows more expressed dispersion for higher power productions, more specifically, the PV array power production model in general tends to overestimate the power production. This behavior is expected since higher power production is related to higher solar irradiance and also to higher PV array temperatures. Since the actual PV array temperature is usually higher than the air temperature used for its approximation, and the PV array power production drops with the temperature increase (see Fig. 3.18), the PV array power production model that uses such thermal model approximation will overestimate the power production. Note that in practical applications, instead of using actual measurements, predictions of meteorological variables will have to be used, which will introduce additional uncertainty in the power production prediction.

#### § LIMIT PERFORMANCE ASSESSMENT

Limit performance of the PV array power production model is assessed by introducing a neural-network-based static corrector [45]. Same variables are used for corrector inputs as to calculate the PV array power production, whereas the corrector is trained to learn the power production model error. The corrector output, i.e., prediction of the PV array power production model error, is added to the original power production prediction to obtain corrected prediction. A data-flow diagram of the PV array power production model with the neural-network-based corrector for the data set (d), i.e., when the tilted surface model is used together with the PV array thermal model approximation, is shown in Fig. 3.19. Each of the considered four data sets is divided into training, validation, and testing data subsets for neural network (i.e., corrector) training, as previously explained, and the performance verification is done only on the testing subset.

Figure 3.17 shows scatter plots of the PV array power production model, without correction (blue markers) and with correction (red markers), for the considered four data sets, and numeric values of the performance indicators are given in Table 3.3b. It can be seen that correctors significantly reduce the dispersion in the scatter plots, as well as the prediction bias, which is an indicator of a

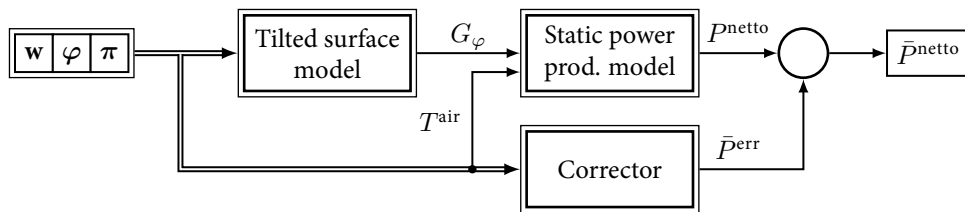


Figure 3.19: Data-flow diagram of the PV array power production model with static correction.

well trained corrector. Performance indicators on the data set (d) show that  $\text{RMSE}_m$  is around 15% without correction and 7% with static correction. In practical applications, instead of using real solar irradiance and temperature measurements, correctors will have to be trained on predictions of meteorological variables. A more detailed analysis is needed to see whether or not it is economically viable to use solar irradiance measurement equipment, especially in case of smaller PV power plants. Since in this section actual measurements were used for performance verification, given results reveal the limit performance of the PV array power production model.

### 3.5.3 Static and dynamic correction of a prediction sequence

The most critical inputs for the PV array power production prediction are predictions of meteorological variables, such as solar irradiance components and the air temperature, which are main sources of the output power prediction uncertainty. The prediction model itself is also a source of the power prediction uncertainty, as discussed in Section 3.4. In this subsection a predictor-corrector method for one-day-ahead PV array power production prediction is developed and verified.

#### § PREDICTOR-CORRECTOR METHOD

In numerical analysis, a predictor-corrector method is an algorithm that proceeds in two steps: (i) prediction step first calculates a rough approximation of the desired quantity, and then (ii) correction step refines the initial approximation by using other means, e.g., known error realizations. Since fresh predictions of meteorological variables become available every 6 h, the PV array power production prediction sequence is calculated every 6 h, i.e., the prediction step is performed every 6 h. Note that near-history realizations of the predicted power production are only relevant to correct near-future predictions, and for that reason only 24-h-ahead corrections of the original 72-h-ahead prediction sequence are considered. In this subsection a mathematical description of the corrector model is given, which corrects the PV array power production prediction sequence as soon as new averaged power measurement becomes available, i.e., every 1 h.

The true power prediction error  $P^{\text{err}}$  at the time instant  $t + k$  on the prediction horizon is

$$P_{t+k}^{\text{err}} = P_{t+k}^{\text{meas}} - P_{t+k}^{\text{netto}}, \quad 1 \leq k \leq 72, \quad (3.27)$$

where  $P_{t+k}^{\text{meas}}$  and  $P_{t+k}^{\text{netto}}$  are measurement and prediction of the PV array netto power production, for the time instant  $t + k$  that was done at the time instant  $t$ . Note that the first usable power production prediction sample is  $P_{t+5}^{\text{netto}}$  since the prediction sequence becomes available with 4-h lag.

Let us assume that the prediction sequence error can be decomposed into two components: (i) the one which can be modeled  $\bar{P}^{\text{err}}$ , and to (ii) the noise  $\tilde{P}^{\text{err}}$ , as follows:

$$P_{t+k}^{\text{err}} = \bar{P}_{t+k}^{\text{err}} + \tilde{P}_{t+k}^{\text{err}}, \quad \forall t, k. \quad (3.28)$$

In the correction step, the prediction error along the prediction horizon is calculated as soon as new local measurements become available, i.e., every 1 h, as follows:

$$\bar{P}_{t+j+i|t+j}^{\text{err}} = f_i(\mathcal{I}_{t,j,i}), \quad \begin{array}{l} 4 \leq j \leq 9, \\ 1 \leq i \leq 24, \end{array} \quad (3.29)$$

where  $\bar{P}_{t+j+i|t+j}^{\text{err}}$  is the prediction error for the time instant  $t + j + i$  calculated at the time instant  $t + j$  based on the input data set  $\mathcal{I}_{t,j,i}$ , and  $f_i$  is the neural-network-based corrector for the  $i$ th instant in the future beginning at the instant  $t + j$ . Index  $j$  denotes time instant on the prediction horizon, beginning at  $t$ , when the correction of the next 24-h prediction sequence  $\{P_{t+j+1}^{\text{netto}}, P_{t+j+2}^{\text{netto}}, \dots, P_{t+j+24}^{\text{netto}}\}$  is performed, and it goes from  $j = 4$ , i.e., when the prediction sequence becomes available, up to an hour before new prediction sequence becomes available, i.e., to  $j = 9$  (see timeline in Fig. 3.4).

The PV array power production prediction sequence can be corrected as follows:

$$\tilde{P}_{t+j+i|t+j}^{\text{netto}} = P_{t+j+i}^{\text{netto}} + \tilde{P}_{t+j+i|t+j}^{\text{err}}, \quad (3.30)$$

where  $\tilde{P}^{\text{netto}}$  is the corrected power production prediction based on the input data set  $\mathcal{I}$ , and  $P^{\text{netto}}$  is the original prediction obtained in the prediction step by employing Eq. (3.25) on weather forecast data, including (i) PV array thermal model approximation, (ii) tilted surface model, and (iii) solar position algorithm. The correction step is repeated as soon as new averaged power measurement becomes available, i.e., every 1 h. In this way it is possible to refresh the prediction sequence as soon as new local measurements become available by simply using neural networks (i.e., correctors)  $f_i$ , which are trained on historical data. It should be noted that a separate corrector  $f_i$  is trained for each  $i$ , regardless of  $t$  and  $j$ . One can additionally consider identifying a separate corrector for each combination  $\{t, j, i\}$  for even better corrector approximation ability, but in that case a significantly larger training data set is needed in order not to lose neural-network generalization ability.

As for the input data set  $\mathcal{I}$ , the following three correction scenarios are considered: (i) static correction, (ii) dynamic correction, and (iii) combined static and dynamic correction, as follows:

$$\mathcal{I}_{t,j,i}^{\text{static}} = \{ \{T, T^{\text{air}}\}_{t+j}, \{\beta, \gamma, \theta_z, \gamma_s\}_{t+j+i}, \{T^{\text{air}}, G_h, D_h, \hat{B}_n\}_{t+j+i} \}, \quad (3.31a)$$

$$\mathcal{I}_{t,j}^{\text{dynamic}} = \{ P_{t+j}^{\text{err}}, P_{t+j-1}^{\text{err}}, \dots, P_{t+j-8}^{\text{err}} \}, \quad (3.31b)$$

$$\mathcal{I}_{t,j,i}^{\text{combined}} = \{ \mathcal{I}_{t,j}^{\text{dynamic}}, \mathcal{I}_{t,j,i}^{\text{static}} \}, \quad (3.31c)$$

where  $T$  and  $T^{\text{air}}$  are the PV array and air temperatures,  $\beta$  and  $\gamma$  are the tilted surface tilt and azimuth angles,  $\theta_z$  and  $\gamma_s$  are solar zenith and azimuth angles,  $G_h$  and  $D_h$  are predicted global and diffuse horizontal solar irradiance components,  $\hat{B}_n$  is the estimated direct (normal) solar irradiance component, and  $P^{\text{err}}$  are prediction error realizations defined in Eq. (3.27), whereas

$$P_{t+j-p}^{\text{err}} = 0, \text{ for } j-p \leq 0, \text{ where } \begin{cases} 4 \leq j \leq 9, \\ 0 \leq p \leq 8. \end{cases} \quad (3.32)$$

Time instant  $t$  corresponds to the instant of weather forecast issuing, time instant  $t+j$  is related to current measurements (present), time instants  $t+j+i$  are related to predictions (future), while time instants  $t+j-p$  are related to measured realizations (past). In the static-correction input data set, future angles data are completely deterministic, i.e., solar zenith and azimuth angles are calculated for any time instant by using the solar position algorithm given in [82], while tilted surface tilt and azimuth angles are defined by the user. The dynamic-correction input data set includes only measured prediction error realizations (past), while the combined-correction input data set consists of all variables in dynamic- and static-correction input data sets.

It is expected that the static corrector will learn systematic error of the PV array power production model, as already indicated in limit performance assessment presented in Fig. 3.17. For instance, reflectivity of the PV array front surface changes with the sun position on the sky dome, which is not taken into account by the PV array power production model developed in Section 3.4. The static corrector can capture phenomena that are not initially modeled by the prediction model, as long as the corrector has relevant input variables at its disposal. For the example of the front surface reflectivity, the most relevant input variables are solar zenith and azimuth angles. The static corrector input data set consists of (i) all variables needed for the tilted surface model, (ii) air temperature used for the PV array thermal model approximation, and of (iii) PV array and air temperature measurements which can be used to capture thermal model approximation error for small values of  $i$ , i.e., for those where the current PV array temperature measurement is still relevant for the

temperature of the PV array at  $t + j + i$  time instant. Except for the systematic error of the PV array power production model, the static corrector will also learn a systematic error of meteorological variables predictions. This is especially important due to the fact that predictions are usually not done for the exact location of a PV power plant, since the spatial grid resolution of numerical weather prediction models is usually limited to  $2 \times 2$  km. Additionally, the static corrector can also capture some other unpredicted phenomena such as partial shading of the PV array at certain times of day, time-dependent degradation of the PV array etc.

Dynamic corrector takes advantage of the known power prediction error realizations. In the simplest case, if original prediction sequence obtained by the prediction step constantly underestimates or overestimates the actual PV array power production along the prediction horizon, the dynamic corrector can easily capture this phenomena and correct the original prediction sequence. In general, dynamic correction will be possible only if there is a correlation between power prediction errors within the prediction sequence and this is usually the case: near-in-time weather forecasts of a certain variable usually all underestimate or all overestimate realizations of the predicted variable. It is expected that the dynamic correction intensity will fade away as the prediction step increases relative to the time instant when dynamic correction was performed, which is the main reason why only one-day-ahead prediction corrections are considered here. The static correction will also perform somewhat better for smaller prediction steps  $i$  as it uses information on the PV array temperature realization at  $t + j$ , which can be used to correct the PV array thermal model approximation errors that are closer on the prediction horizon.

#### § PERFORMANCE VERIFICATION

Performance verification is given for the considered three correction scenarios: (i) static, (ii) dynamic, and (iii) combined corrections. Correctors are trained and validated on data obtained during the 1-year time period, and are tested on data obtained during the following 12-month time period. Since the testing data subset is not used for correctors training in any way, performance obtained on this data subset gives the most relevant information for practical applications. To achieve best results possible, it is suggested that correctors are trained and validated on a data set that spans at least throughout a one whole year, in order to account for atmospheric processes that are specific for each season of the year, whereas correctors should be trained only on daytime hours.

Standard deviation of the prediction sequence with respect to the prediction step  $i$ , for the three data subsets (training, validation, and testing) and the three correction scenarios (static, dynamic, and combined), is shown in Fig. 3.20. It can be seen that the initial hypothesis is confirmed: (i) influence of the static correction is near-constant over the prediction horizon, whereas it shows somewhat better performance for smaller  $i$  since it uses information on the PV array temperature realization at the time instant  $t + j$ ; (ii) the dynamic correction has more significant influence for time instants on the prediction horizon that are closer to the time instant when dynamic correction is performed; and (iii) the combined static and dynamic correction shows the best performance since it includes the best from both worlds, i.e., static and dynamic corrections. Performance verification on the testing data subset confirms that the proposed approach can significantly improve predictions of the PV array power production, especially for shorter prediction horizons where dynamic correction is more prominent. Standard deviation of the power production prediction error is reduced up to 50% for near future, i.e., for smaller values of  $i$  up to 6–8 h ahead, by using the combined static and dynamic correction. After that period, correctors seem to have a little or no impact at all on the original prediction sequence, which is expected since near-history realizations are only relevant for corrections of near-future predictions.

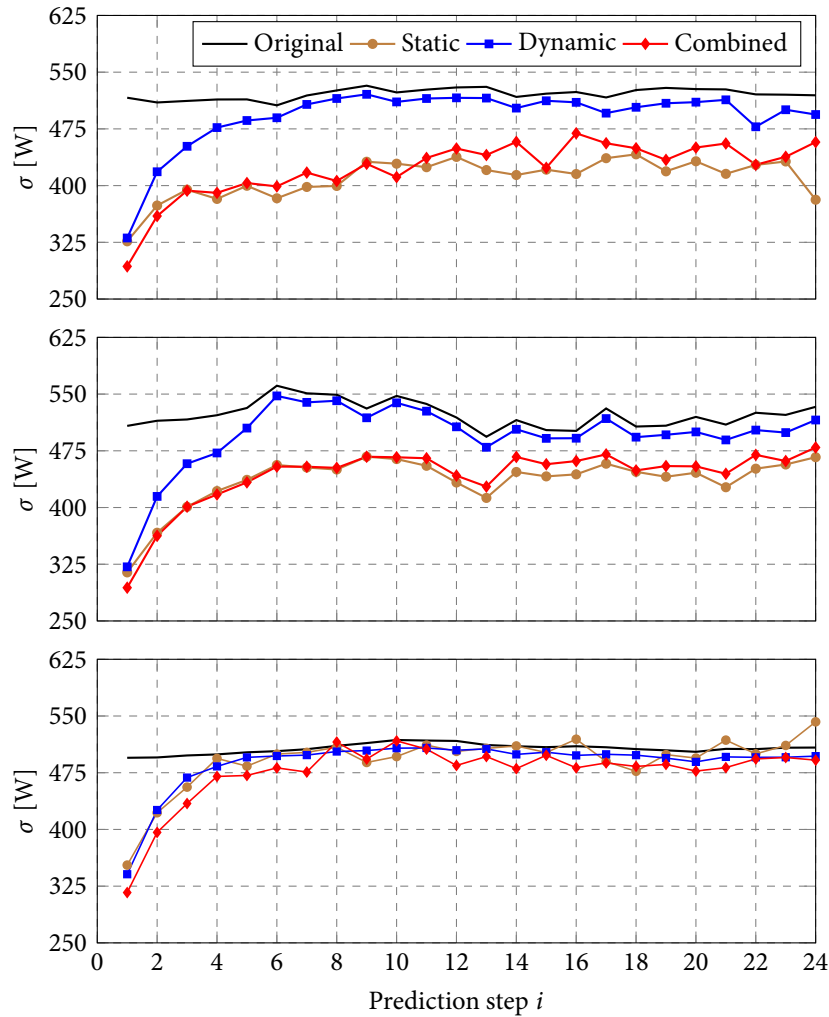


Figure 3.20: Standard deviation of the prediction sequence error with respect to the prediction step, for the three data subsets. From top to bottom: (i) training, (ii) validation, and (iii) testing data subset. The nighttime hours are excluded from the analysis not to influence the performance indicators. Standard deviation profile of the uncorrected prediction sequence error is labeled as *Original*.

The interesting thing about standard deviation profiles shown in Fig. 3.20 is that the static correction does not work that well on the testing data set as on training and validation data sets. Moreover, it seems that the static correction has the same impact on the correction quality as the dynamic correction. One of the possible reasons might be that variables used in the static correction carry the same information about prediction error as variables used in the dynamic correction. Since static corrections on training and validation data sets are much better than the static correction on the testing data set, one may conclude that static correctors captured the noise during the training procedure, which is useless for the testing data set. There may be many other reasons for this behavior, and to confirm these assumptions, a more thorough statistical analysis has to be performed.

Figure 3.21 shows measurements and predictions of (i-iii) global and diffuse horizontal and tilted solar irradiance components, (iv) the air temperature, and (v) the PV array temperature, for the considered exemplary period that begins on 28 Dec 2015 at 00:00. The shown prediction sequence of the incident solar irradiance is calculated by the tilted surface model based on predictions of global and diffuse horizontal solar irradiance components. An example of series of corrections performed over a single prediction sequence for the considered exemplary period is shown in Fig. 3.22. It can be

seen that the PV array power production prediction error follows the prediction error of the incident solar irradiance, which is mainly due to the uncertain predictions of global and diffuse horizontal solar irradiance components. This simple example confirms that predictions of meteorological variables, i.e., of solar irradiance components in particular, are the main sources of the PV array power production prediction uncertainty. Prediction sequence of the PV array power production begins on 28 Dec 2015 at 00:00 for the next 72-h time period, whereas correction steps are performed using the combined corrector on every full hour from 04:00 to 09:00. Note that *Measured* and *Predicted* profiles in Fig. 3.22 are the same for all 6 subplots, whereas the *Predicted* profile is calculated by the prediction step performed at 04:00, i.e., when meteorological predictions became available. On every full hour, the combined corrector refines the *Predicted* profile based on prediction error realizations, whereas measurements available at the time of the correction are marked with symbol  $\times$ . It can be seen that the combined corrector shows no improvement until there are some prediction error realizations available, which is evident from correction steps performed at 08:00 and 09:00.

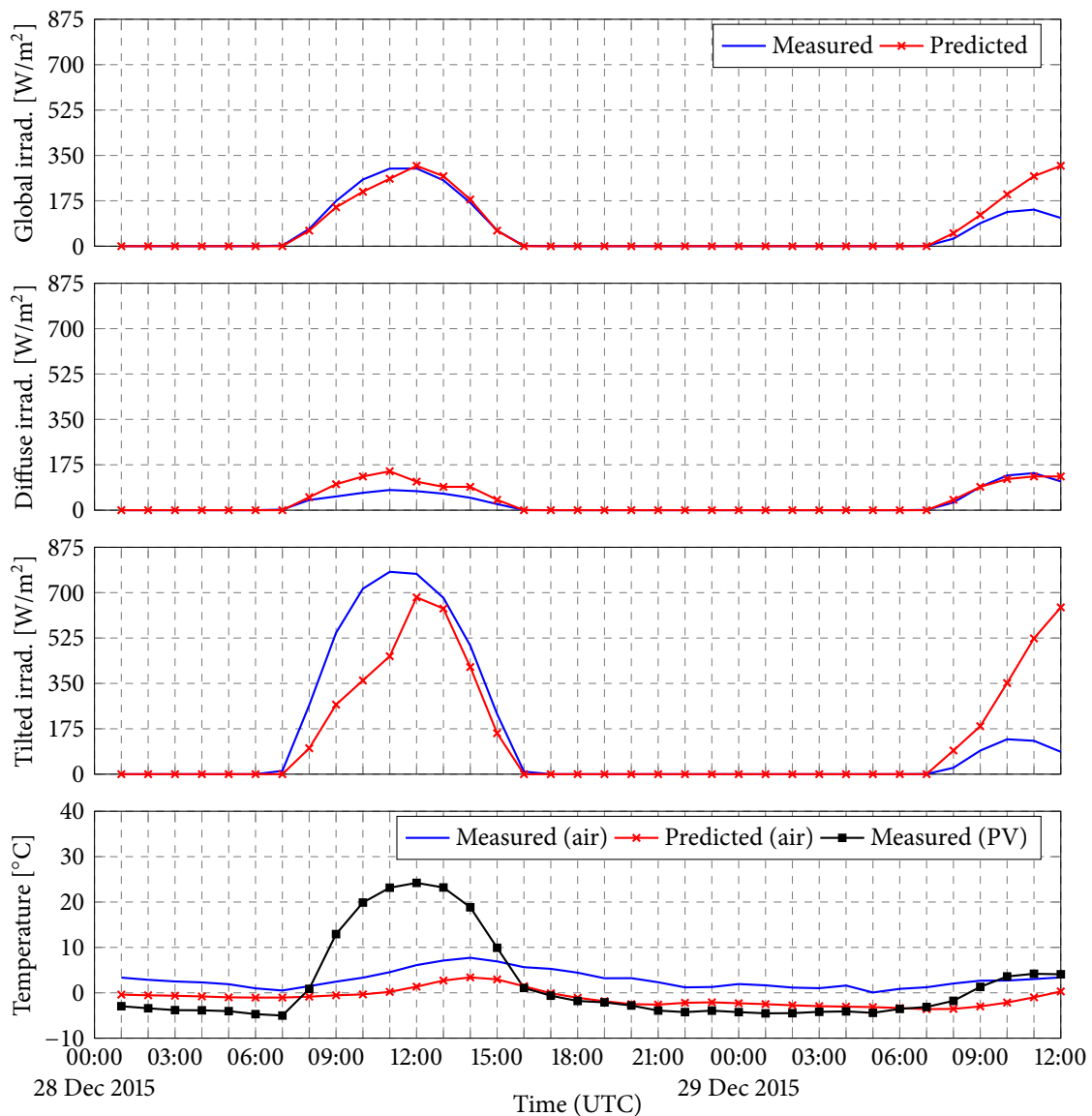


Figure 3.21: Measurements and predictions of relevant meteorological variables for the considered exemplary period. From top to bottom: (i-ii) global and diffuse horizontal solar irradiance components, respectively, (iii) solar irradiance incident on the PV array active surface, and (iv) air and PV array temperatures.

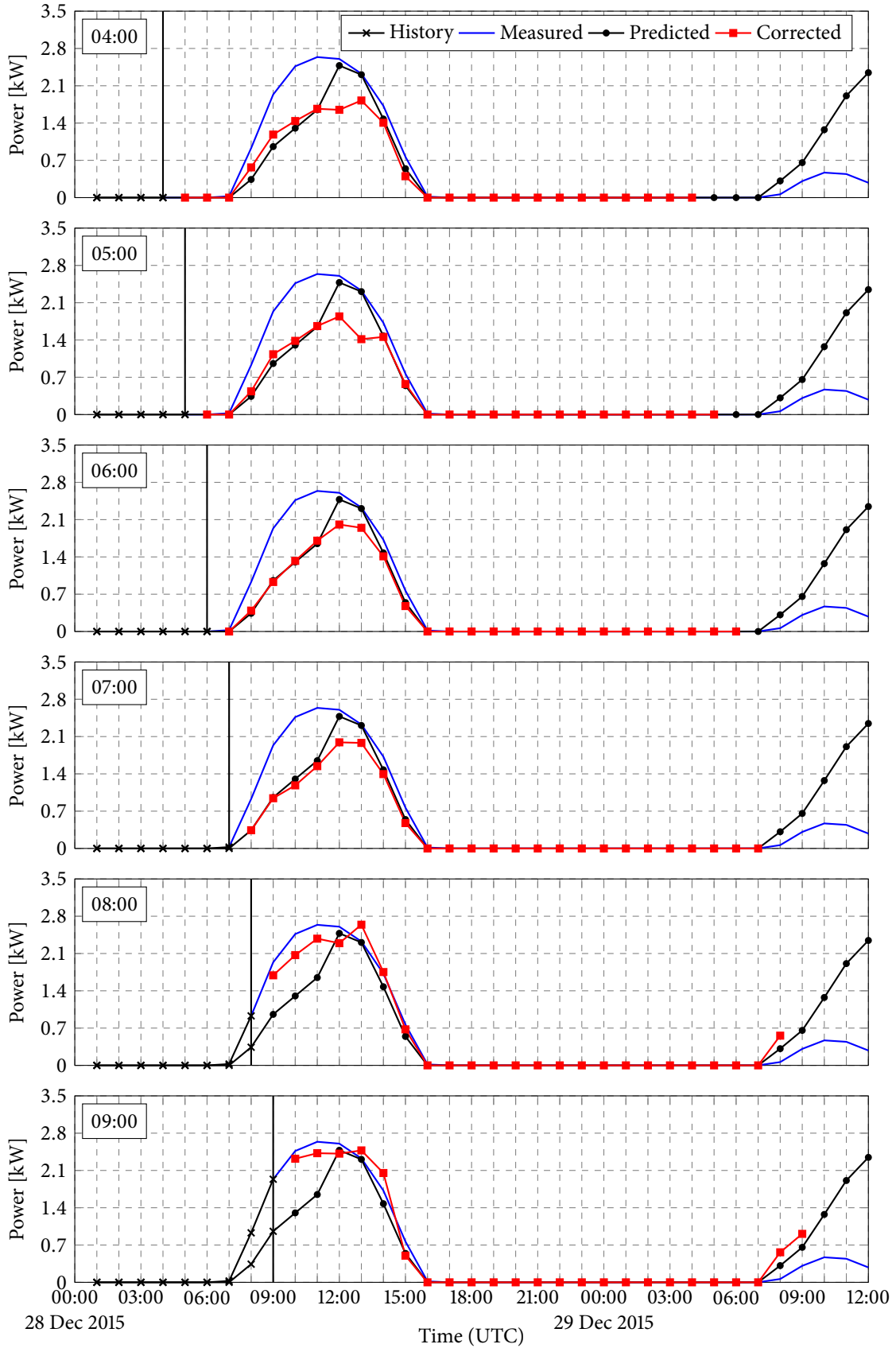


Figure 3.22: Example of series of corrections performed over a single prediction sequence for period from 28 Dec 2015 at 00:00 to 29 Dec 2015 at 12:00, whereas correction steps are performed using the combined corrector on every full hour from 04:00 to 09:00 on 28 Dec 2015.



## § FINAL REMARKS AND FUTURE WORK

In order to be able to use the proposed predictor-corrector method in practical applications, end-users must ensure that the net power production by the PV power plant is measured and recorded. This is usually not an issue, since most of the commercially available solar inverters have built-in acquisition of the PV array net power production. The PV array and air temperature measurements are optional considering investment costs, having in mind that better correction quality can be achieved if these variables are also taken into account. Other major costs include predictions of relevant meteorological variables, i.e., predictions of solar irradiance components and air temperature, which are today still too expensive for commercial applications unless the cost is shared over larger number of local users. For this purpose, one can consider using free weather forecasts which are in general much more uncertain due to a rougher spatial grid and time resolution, but also due to the fact that free forecasts are refreshed less frequently. Economic viability of using commercial weather forecasts, which are more accurate than free weather forecasts, mainly depends on the size of the PV plant and on the electricity regulation context imposed by a distribution system operator, and also on the number of meteorological variables used as inputs to a corrector.

In this section it was shown how the predictor-corrector method can significantly improve predictions of the PV array power production. It should be noted that there are scenarios for which correction does not show any improvement, and can even worsen the original prediction sequence, but in general the developed correction method significantly improves quality of prediction sequences, as it can be seen from standard deviation profiles for the three considered correction scenarios, shown in Fig. 3.20. The correction quality most probably could be additionally improved by using other neural-network structures, or other combinations of corrector inputs. One may also consider using seasonal correctors, but in that case a classification model is needed. However, the main idea here is not to give answer for which combination of neural-network structure and input variables is the best correction performance achieved, but instead to present an innovative method through simulations on real measurements and meteorological variables predictions.

There are many possible evolutions of the presented research, and here only few of them that seem to be promising are pointed out. (i) A deeper statistical analysis of the proposed method, together with a cost-benefit analysis, to check which inputs have the largest impact on a prediction of a PV array output power. Maybe it is possible to use less prediction variables for corrector inputs, or to refresh predictions of relevant meteorological variables less frequently, without losing generalization ability, which would lead to reduced prediction costs. (ii) Current prediction costs of relevant meteorological variables might still be too high for small PV power plants. The estimated cost for predictions of the three relevant meteorological variables (72 h ahead, refreshed 4 times a day) is 200 EUR per month. In that sense, it would be interesting to check the effectiveness of the presented method using free weather forecasts. The prediction error would for sure be much higher, but the question is how much higher and is it worth the savings. For large PV power plants it might not be worth the savings, which also depends on the electricity regulation context. (iii) The focus here was not on finding the best performing neural-network structure for correctors training. Significant improvements in modeling high-level abstractions in data have been achieved recently using deep-learning methods. (iv) The proposed method should be tested for different environmental conditions, i.e., for different locations, which might be possible without any additional investments. To test the presented method for another location, one would only need historical measurements of the PV power plant output power, and of PV panels' temperature if possible, while historical prediction sequences of relevant meteorological variables can be supplied by meteorological services.

## 4.1 Introduction

With the expected growth in the adoption of microgrids, advanced tools and techniques are required for their optimal operation [103, 104]. Among them, short-term load forecasting is a fundamental and essential task for optimal energy management in a microgrid [105]. Short-term load forecast is a complex procedure, mainly because of the highly nonsmooth and nonlinear relationship between the considered load-driving variables and the load itself [106]. In this chapter a neural-network-based one-day-ahead load forecast with uncertainty characterization of a typical university building is developed and verified [52]. Neural network inputs are lagged load data, as well as relevant meteorological and time data, while output is the active electricity consumption of the UNIZG-FER building. Using all possible input variables in neural network training can be very challenging for the training algorithm since the number of samples required for training and neural network complexity increase abruptly with the number of inputs. In order to keep only relevant inputs that contain no redundant information, input variables selection (IVS) algorithm based on partial mutual information (PMI) is applied [107–110], which unlike correlation-based methods does not assume linear relationship between inputs and outputs. Note that in the sequel, term *prediction* will be used with equal meaning to term *forecast*, since *prediction* is a more common term considering microgrid energy management based on model predictive control.

### § LITERATURE REVIEW

There is a number of procedures developed recently for short-term load prediction [111–120], whereas most of these procedures include neural networks without any uncertainty description of the prediction sequence. The authors in [112] introduce functional time-series methodology for short-term load prediction, a method performed by means of a weighted average of past daily load segments. The authors in [113] propose a two-level wavelet neural network based on back-propagation together with estimation of prediction intervals by using hybrid Kalman filters. The authors in [117] propose a semi-parametric additive models to estimate relationship between load and its driving variables. These models do not give load profile prediction uncertainty assessment, which is crucial when stochastic weather forecast data is used as prediction model input, and also considering that building's consumption is a stochastic variable itself largely influenced by human behavior [121]. The latter indicates that, except for input data uncertainty, the developed load prediction model itself is also a source of prediction uncertainty, which must be taken into account.

---

Research presented in this chapter is published in the following paper:

■ M. Gulin, M. Vašak, G. Banjac, and T. Tomiša, "Load Forecast of a University Building for Application in Microgrid Power Flow Optimization," in *Proceedings of the 2014 IEEE International Energy Conference, EnergyCon 2014*, pp. 1284–1288, Dubrovnik, Croatia, 2014.

## § METHODOLOGY

Not many authors use partial mutual information (PMI) for input variables selection, e.g., the authors in [115] use correlation analysis in order to derive the relative importance of each input to the output profile. Correlation analysis, unlike partial mutual information, assumes linear transformation between inputs and outputs and can provide misleading information on inputs' usefulness when considering nonlinear transformation, which is the case with most of the real physical systems [107]. After the input variables for prediction model are carefully selected, one-hour-ahead load prediction model is developed and verified [52], which is later extended with input variables and model uncertainty description for one-day-ahead load prediction in a stochastic framework by sequentially using the Unscented transformation [122, 123] along the prediction horizon. Effectiveness of the developed load prediction model in commissioning and operation of optimal energy management in a microgrid is also discussed, which is important considering that most likely there will be no available load data for the period before the microgrid is installed. Therefore, performance of the developed load prediction model is also tested for on-line tuning in order to assess its behavior when commissioned without available historical data.

## § CHAPTER STRUCTURE

This chapter is organized as follows. In Section 4.2 one-hour-ahead prediction model is developed and verified, as follows: (i) input variables selection procedure is described, (ii) neural-network-based prediction model structure is given, (iii) performance verification on a historical data set is given, and (iv) prediction model on-line tuning for real-world applications is considered. In Section 4.3 the developed one-hour-ahead prediction model for one-day-ahead load prediction is extended for operation in a stochastic framework, as follows: (i-ii) input data and model uncertainty are described, (iii) the Unscented transformation is extended to also include the model uncertainty, and (iv) performance verification on a historical data set is given.

## 4.2 One-hour-ahead prediction

In this section one-hour-ahead load prediction model is developed and verified, as follows: (i) input variables selection procedure based on partial mutual information is applied to carefully select input variables that are most relevant for load prediction, (ii) the optimal neural network structure used for one-hour-ahead load prediction is obtained by trial-error method, (iii) performance verification results on historical data set are presented, and (iv) load prediction model performance is also verified for on-line tuning and real-world applications.

### 4.2.1 Input variables selection

The input variables selection (IVS) is a procedure of appropriately selecting a subset  $S \subseteq C$ , where  $C$  is a set of all potential input variables (i.e., candidates) to a prediction model. An inaccurate prediction model is obtained when the input set is underspecified, as the selected variables do not fully describe the observed behavior within the system under consideration. On the other hand, the inclusion of input variables that are either irrelevant or redundant increases the size and complexity of the prediction model, which makes it difficult to tune. Given these considerations, the appropriate set of prediction model input variables is considered to be the smallest set of input variables required to adequately describe the observed behavior of the system.

If a linear relationship characterizes the underlying system (the dependent variable being a linear function of all model inputs), linear dependence measures such as the coefficient of correlation may suffice. However, if the underlying system is more complex, as is usually the case with most of real physical systems, linear methods are likely to result in misleading inputs and a badly formulated prediction approach. In this section the IVS procedure is presented for selecting the appropriate subset of 52 possible input variables for short-term load prediction, which include lagged load, relevant meteorological and time data. The IVS procedure used here relies on the concept of a partial mutual information (PMI) which is, unlike correlation analysis, not limited to linear transformations. This concept is first introduced in [107] for the identification of input variables for hydrological models, and is later used by many authors [108–110] as it is proved to be very efficient.

#### § HISTORICAL DATA SET

For the prediction model performance verification, energy consumption and meteorological data measurements for three consecutive years are used, in period from 2011 to 2013. Active electricity consumption of UNIZG-FER building is recorded every 15 min and represents mean active power within the 15-min interval that ends at the timestamp. Meteorological data provided by DHMZ are recorded at the meteorological station Maksimir Zagreb every 10 min and represent mean values within the 10-min interval that ends at the timestamp. Both data sets are integrated on a 60-min interval to match the sample time of a microgrid energy management system.

#### § INPUT VARIABLES FOR LOAD PREDICTION

Input variables set  $C$  consists of 52 possible candidates in total, as follows: (i) 40 candidates of lagged load data, which consists of load measurements up to 5 h before the considered hour, and of load measurements in interval between 2 h before and after the considered hour up to 7 days before the considered day, as illustrated in Fig. 4.1; (ii) 5 candidates of meteorological data for the considered hour, which consists of temperature, pressure, humidity, global and diffuse solar irradiance measurements; and (iii) 7 candidates of time data, which consists of day-in-year, hour-in-week, hour-in-day, and binary flag denoting whether the considered day is a working or non-working day (e.g., weekends, national holidays etc.).

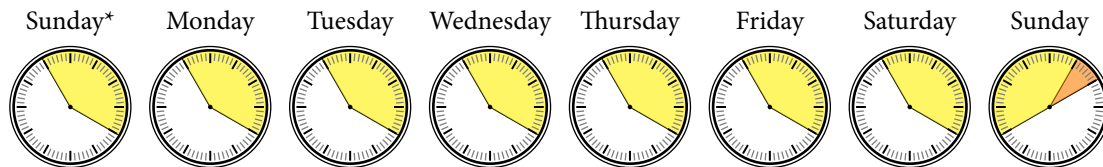


Figure 4.1: Time instances of lagged load data used as prediction model inputs (in yellow) to predict load for an hour instance at Sun 14:00 h (in orange).

Time data is represented via periodical cos and sin functions of days (for day-in-year) and hours (for hour-in-week and hour-in-day) in order to avoid discontinuities, e.g., after 23:00 h there is a step-wise jump to 00:00 h which might be problematic for neural network training. Periodical functions used are defined as  $\cos(\omega_0 t^*)$  and  $\sin(\omega_0 t^*)$ , where  $t^*$  is (i) number of days that have passed from Jan 1 00:00 h in the considered year, (ii) number of hours that have passed from Mon 00:00 h in the considered week, or (iii) number of hours that have passed from 00:00 h in the considered day, where definition for  $t^*$  depends on the time data type, and  $\omega_0$  is frequency for variable of interest ( $\frac{2\pi}{365}$  or  $\frac{2\pi}{366}$  for day-in-year,  $\frac{2\pi}{168}$  for hour-in-week, and  $\frac{2\pi}{24}$  for hour-in-day variable).

## § PMI-BASED IVS ALGORITHM

Mutual information is generally considered as a measure of dependence between two variables [108]. It can also be considered as a measure of stored information in one variable about another, or the measure of degree of predictability of the output variable knowing the input variable. Given two discrete random variables  $X$  and  $Y$ , the mutual information between the two variables is defined as:

$$\text{MI} = \frac{1}{N} \sum_{i=1}^N \ln \left[ \frac{f_{X,Y}(\mathbf{x}_i, \mathbf{y}_i)}{f_X(\mathbf{x}_i) f_Y(\mathbf{y}_i)} \right], \quad (4.1)$$

where  $(\mathbf{x}_i, \mathbf{y}_i)$  is the  $i$ -th bivariate sample data pair from a set of  $N$  samples,  $f_{X,Y}$  is the joint probability density function (pdf), while  $f_X$  and  $f_Y$  are the marginal probability density functions.

Efficient and accurate estimation of mutual information is largely dependent on a technique employed to estimate the marginal and joint pdfs. For that purpose a kernel density estimator is used, which is a non-parametric way to estimate the pdf of a random variable, that is proved to be more accurate than the histogram-based techniques. Given these considerations, pdf estimation at a certain point  $\mathbf{x}^*$  can be formulated as:

$$\hat{f}_X(\mathbf{x}^*) = \frac{1}{N} \sum_{i=1}^N K_h(\mathbf{x}^* - \mathbf{x}_i), \quad \mathbf{x}^*, \mathbf{x}_i \in \mathbb{R}^d, \quad (4.2)$$

where  $\hat{f}_X(\mathbf{x}^*)$  is the estimate of pdf  $f_X$  at  $\mathbf{x}^*$  considering  $N$  observations  $\mathbf{x}_i \in X$ , and  $K_h(\cdot)$  is some kernel function for which  $h$  denotes the kernel smoothing parameter. A common choice for  $K_h(\cdot)$  is the Gaussian kernel [108] defined as follows:

$$K_h(\mathbf{x}^* - \mathbf{x}_i) = \frac{1}{(\sqrt{2\pi}h)^d \sqrt{|\Sigma|}} \exp\left(-\frac{\|\mathbf{x}^* - \mathbf{x}_i\|_{\Sigma}}{2h^2}\right), \quad (4.3)$$

where  $d$  denotes dimension of a vector from  $X$  (i.e., number of elements in  $\mathbf{x}^*$  or  $\mathbf{x}_i$ ),  $\Sigma$  and  $|\Sigma|$  are the sample covariance matrix on the whole data set  $X$  and its determinant, while term  $\|\mathbf{x}^* - \mathbf{x}_i\|_{\Sigma}$  is the Mahalanobis distance metric given by:

$$\|\mathbf{x}^* - \mathbf{x}_i\|_{\Sigma} = (\mathbf{x}^* - \mathbf{x}_i) \Sigma^{-1} (\mathbf{x}^* - \mathbf{x}_i)^{\top}. \quad (4.4)$$

As for smoothing parameter  $h$ , the Gaussian reference bandwidth [109] is used here:

$$h = \left( \frac{1}{N} \frac{4}{d+2} \right)^{\frac{1}{d+4}}. \quad (4.5)$$

Identification of multiple system predictors (i.e., candidates) necessitates the use of a partial measure of dependence between the dependent and independent variable set. The partial dependence between an independent variable  $x \in X$  and a dependent variable  $y \in Y$  depends on the pre-existing set of inputs  $\mathbf{z} \in Z$  that are already found to be good predictors of the system. The PMI between independent and dependent variable with respect to pre-existing set of inputs is defined as:

$$\text{PMI} = \frac{1}{N} \sum_{i=1}^N \ln \left[ \frac{f_{U,V}(u_i, v_i)}{f_U(u_i) f_V(v_i)} \right], \quad (4.6)$$

where  $u_i \in U$  and  $v_i \in V$  are residuals of  $x_i$  and  $y_i$  with respect to  $\mathbf{z}$ , respectively, defined as:

$$u_i = x_i - \hat{\mathbb{E}}[x|\mathbf{z}], \quad (4.7a)$$

$$v_i = y_i - \hat{\mathbb{E}}[y|\mathbf{z}], \quad (4.7b)$$

where  $\mathbb{E}[\cdot]$  is the expectation operation.

Use of the conditional expectations in Eq. (4.7) ensures that the resulting variables  $u$  and  $v$  represent the residual information in variables  $x$  and  $y$ , once the effect of the existing predictor(s)  $\mathbf{z}$  has been taken into consideration. The conditional expectation estimate can be calculated as [109]:

$$\hat{\mathbb{E}}[x|\mathbf{z}] = \sum_{i=1}^N w_i \left( x_i + (\mathbf{z} - \mathbf{z}_i) \boldsymbol{\Sigma}_{zz}^{-1} \boldsymbol{\Sigma}_{xz} \right), \quad (4.8)$$

where  $\boldsymbol{\Sigma}_{zz}$  is the sample covariance of  $\mathbf{z}$  on the whole set  $Z$ ,  $\boldsymbol{\Sigma}_{xz}$  is the sample cross-covariance between  $x$  and  $\mathbf{z}$  on the whole set  $(X, Z)$ , and weighting factor  $w_i$  is defined as [107]:

$$w_i = \frac{K_h(\mathbf{z}^* - \mathbf{z}_i)}{\hat{f}_Z(\mathbf{z}^*)}, \quad (4.9)$$

where  $\hat{f}_Z(\mathbf{z}^*)$  is the estimate of pdf  $f_Z$  at  $\mathbf{z}^*$  considering  $N$  observations  $\mathbf{z}_i \in Z$ . Note that the same principle is used for estimation of the conditional expectation  $\hat{\mathbb{E}}[y|\mathbf{z}]$ .

#### § PMI-BASED IVS ALGORITHM IMPLEMENTATION

The basic operating principle of the PMI-based IVS algorithm is simple: for a given input variables set  $C$  and output set  $Y$ , the IVS algorithm proceeds at each iteration by finding the candidate  $c_k$  that maximizes the PMI with respect to the output variable, conditional on the inputs  $\mathbf{z}$  that have been previously selected. Once the candidate  $c_k$  is determined, it is added to the set  $Z$  and removed from the set  $C$ . Although some authors propose algorithm stopping criteria based on bootstrapping [108] or mean squared error (MSE) [109], stopping criteria are not considered here, i.e., the IVS algorithm runs until all candidates from  $C$  are exhausted. In this way, the set  $Z$  will include all candidates from the set  $C$  ordered from the most- to the least-relevant candidate for output prediction.

The major drawback of the PMI-based IVS algorithm is that it requires significant computational effort and memory, especially if not coded properly. Two major algorithm bottlenecks considering memory requirements are identified: (i) calculation of the term  $(\mathbf{z}^* - \mathbf{z}_i)$  for all combinations of  $\mathbf{z}^*, \mathbf{z}_i \in Z$ , which will yield a matrix  $\bar{\mathbf{Z}}$  of dimension  $\frac{N(N-1)}{2} \times d_Z$ , where  $d_Z$  denotes number of candidates in set  $Z$ , which is constantly increasing during the algorithm runtime; and (ii) calculation of the  $\exp(\cdot)$  term in Eq. (4.3) for each  $i$  independently, which will yield a matrix of dimension  $N \times N$ . To conclude, the PMI-based IVS algorithm memory requirements increase quadratically with the number of samples  $N$ . Considering a one-year data set with 1-h resolution (about 8750 samples) and 52 candidates, and considering calculation with a double-float precision (8 bytes), the PMI-based algorithm requires approximately 16 GB of memory at its peak.

#### § IVS RESULTS

Due to considerable memory requirements of the PMI-based IVS algorithm, the IVS procedure is performed for each year independently. The following variables annotation is introduced: (i)  $yc$  and  $ys$  for day-in-year, whereas letters "c" and "s" denote cos and sin functions, respectively,  $wc$  and  $ws$  for hour-in-week,  $dc$  and  $ds$  for hour-in-day, and  $wf$  for type-of-day flag (1 for working day, 0 otherwise); (ii)  $te$  for temperature,  $hu$  for humidity,  $pr$  for pressure,  $ig$  for global irradiance, and  $id$  for diffuse irradiance; and (iii)  $ac_d^h$ , where  $d$  denotes number of days before the considered day, and  $h$  denotes hour offset from the considered hour. For example, if Fri 14:00 h hour-instance is considered, then  $ac_3^{-1}$  would denote Tue 13:00 h, while  $ac_7^0$  would denote Fri 14:00 h for a week before the considered day. Although PMI-based algorithm should give the same results considering normalized and non-normalized input and output data sets, it is recommended to normalize data sets on a symmetrical interval for better numerical stability.

Algorithm 4.1: PMI-based IVS algorithm without stopping criteria

---

```

1: Inputs: Set of all candidates  $C$  and outputs  $Y$ 
   Output: Set of candidates  $Z$  ordered from the most- to the least-relevant candidate from the set  $C$ 
2: Initialization:  $Z \leftarrow \emptyset$ 
3: while  $C \neq \emptyset$  do
4:   Construct an estimator  $\hat{\mathbb{E}}[y|\mathbf{z}]$ 
5:   Calculate residual outputs  $v_i \leftarrow (y_i - \hat{\mathbb{E}}[y|\mathbf{z}])$ 
6:   Calculate the marginal pdf estimation  $\hat{f}_V(v)$ 
7:   for all  $c \in C$  do
8:     Construct an estimator  $\hat{\mathbb{E}}[c|\mathbf{z}]$ 
9:     Calculate residual outputs  $u_i \leftarrow (c_i - \hat{\mathbb{E}}[c|\mathbf{z}])$ 
10:    Calculate the marginal pdf estimation  $\hat{f}_U(u)$ 
11:    Calculate the joint pdf estimation  $\hat{f}_{U,V}(u, v)$ 
12:    Determine the PMI defined in Eq. (4.1)
13:   end for
14:   Find candidate  $c_k \in C$  that maximizes the PMI
15:   Add candidate  $c_k$  at the end of the set  $Z$ 
16:   Remove candidate  $c_k$  from the set  $C$ 
17: end while

```

---

Results obtained are not identical for each year considered, but are very similar. For instance, working day flag is identified as one of the most significant inputs in 2011 and 2013, and as one of the least significant inputs in 2012. This is mainly due to the unpredicted events such as UNIZG-FER building renovation during shutdown in summer 2012. The following inputs order was obtained as a combination of importance orders obtained for years 2011–2013 independently:  $ac_0^{-1}$ ,  $ac_0^{-3}$ ,  $ac_1^2$ ,  $ac_7^1$ ,  $ac_7^{-1}$ ,  $ac_7^0$ ,  $ac_0^{-2}$ ,  $ac_7^{-2}$ ,  $ys$ ,  $te$ ,  $hu$ ,  $ac_1^0$ ,  $ac_1^{-1}$ ,  $ac_1^{-2}$ ,  $ac_3^{-1}$ ,  $ac_2^{-1}$ ,  $ac_4^{-1}$ ,  $ac_5^{-1}$ ,  $ac_6^{-1}$ ,  $ac_3^0$ ,  $ac_2^0$ ,  $ac_4^0$ ,  $ac_5^0$ ,  $ac_6^0$ ,  $wf$ ,  $yc$ ,  $ws$ ,  $wc$ ,  $ds$ ,  $ac_3^{-2}$ ,  $ac_2^{-2}$ ,  $ac_4^{-2}$ ,  $ac_5^{-2}$ ,  $ac_6^{-2}$ ,  $ig$ ,  $ac_0^{-4}$ ,  $ac_0^{-5}$ ,  $dc$ ,  $ac_4^1$ ,  $ac_1^1$ ,  $ac_2^1$ ,  $ac_3^1$ ,  $ac_6^1$ ,  $ac_5^1$ ,  $pr$ ,  $id$ ,  $ac_2^2$ ,  $ac_3^2$ ,  $ac_4^2$ ,  $ac_7^2$ ,  $ac_6^2$ ,  $ac_5^2$ . These results are expected since it is reasonable that most recent load values ( $ac_0^{-1}$ ,  $ac_0^{-2}$ ,  $ac_0^{-3}$ ) have the largest impact on the current load value, as well as load values from 7 days ago ( $ac_7^1$ ,  $ac_7^{-1}$ ,  $ac_7^0$ ,  $ac_7^{-2}$ ), which is especially evident for weekend days.

#### 4.2.2 Neural network structure

There are several neural network properties that need to be defined by the user before neural network training can begin: (i) cost function and training method, (ii) training stop criteria to prevent overfitting, and (iii) neural network complexity considering number of input variables, hidden layers, and neurons in hidden layers.

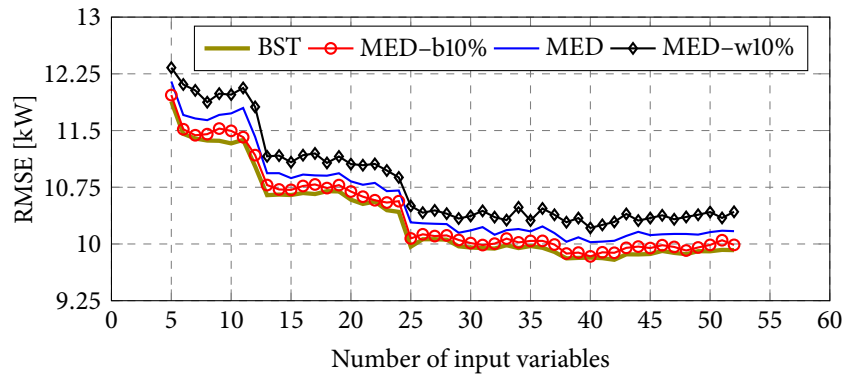
The cost function used for neural network training is based on MSE as follows:

$$J = \frac{1}{N} \sum_{s=1}^N (y_s - f_{nn}(\mathbf{x}_s, \boldsymbol{\theta}))^2, \quad (4.10)$$

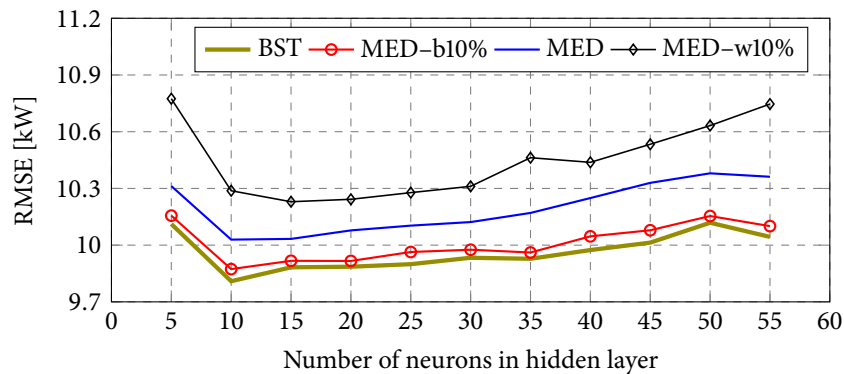
where  $N$  is the number of input-target measurement pairs,  $(\mathbf{x}_s, y_s)$  is the  $s$ -th input-target pair,  $f_{nn}(\cdot, \cdot)$  is a mathematical function that describes the neural network, and  $\boldsymbol{\theta}$  is the parameters vector that is tuned by the training procedure based on Levenberg-Marquardt algorithm. To prevent overfitting, data set is divided into training and validation data sets, whereas years 2011 and 2012 are used for training, and 2013 is used for validation. Neural network parameters are tuned only considering the training data set, and when the cost function considering only validation data set shows no improvement through some number of iterations, training procedure is stopped and the best performing parameters vector considering validation data set is used.

Due to the bias-variance trade-off, the number of input variables and neurons in hidden layer should be carefully selected. In most practical problems of fitting, one hidden layer with 10 to 30 neurons is enough for neural network to perform well. Optimal number of input variables and neurons in hidden layer is set by trial-error method so that neural network training is repeated 50 times for (i) 11 different number of neurons uniformly distributed from 5 to 55 neurons, and (ii) by adding input variables one-by-one with respect to the results obtained by the IVS procedure. This yields  $52 \times 11$  different neural network structures that are trained 50 times each.

For neural network evaluation, root mean square error (RMSE) performance indicator is used, which is defined as a square root of MSE defined in Eq. (4.10). Instead of showing RMSE for each of the  $50 \times (52 \times 11)$  trained neural networks, only the following candidates are considered: (i) best performing (BST), (ii) median performing (MED), and (iii-iv) median in 10% of the best (MED-b10%) and the worst performing (MED-w10%) neural networks among 50 trained neural networks for each of the  $52 \times 11$  different neural network structures. Figure 4.2a shows RMSE for different number of input variables with respect to the results obtained by the IVS procedure and for optimal number of neurons for each of the 52 structures. Figure 4.2b shows RMSE for different number of neurons in hidden layer and for optimal number of inputs for each of the 11 structures. It is shown that 38 is the optimal number of input variables with respect to the IVS results, and 10 is the optimal number of neurons in hidden layer for that number of inputs. This neural network configuration is used in the subsequent analysis and design of short-term load prediction.



(a) RMSE for different number of input variables



(b) RMSE for different number of neurons in hidden layer for 38 inputs

Figure 4.2: RMSE considering different number of input variables and neurons in hidden layer (BST is best performing, MED is median performing, MED-b10% is median in 10% best and MED-w10% is median in 10% worst performing neural networks among 50 trained neural networks for each of the  $52 \times 11$  different neural network structures).



### 4.2.3 Performance verification

In this subsection a performance analysis is given for the best performing neural network (BST) considering optimal neural network structure, i.e., 38 input variables with respect to the IVS procedure results, and 10 neurons in hidden layer. Error histogram, RMSE by week periods and load time-series for best and worst performing week periods considering only the validation data set are shown in Fig. 4.3. In order to obtain a more detailed information on neural network model performance, model error is calculated for each week period in the validation data set independently:

$$\mathbf{E}_{[1,51]} = [ \mathbf{e}_1, \mathbf{e}_2, \dots, \mathbf{e}_{51} ]^T, \quad (4.11)$$

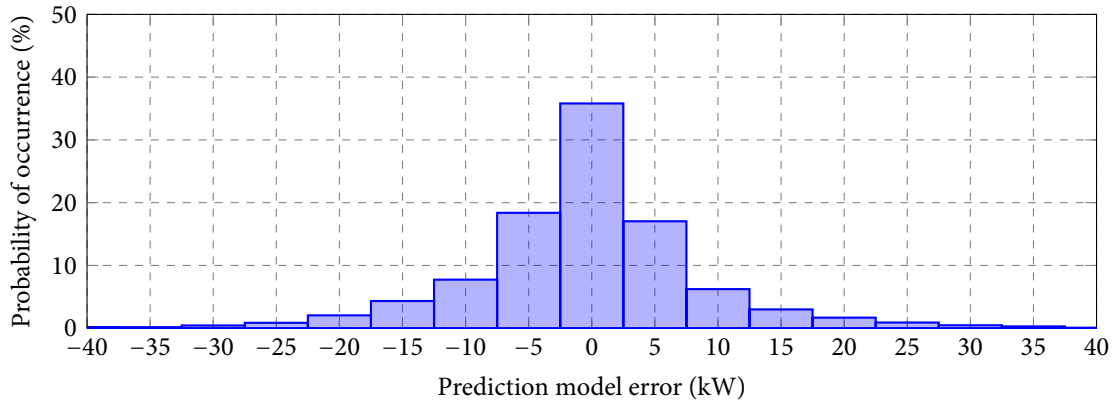
where  $\mathbf{E}_{[1,51]}$  is the matrix formed of neural network model error vectors  $\mathbf{e}_k$  for a week period in the validation data set in 1-h resolution, i.e.,  $\mathbf{e}_k \in \mathbb{R}^{168 \times 1}$ , where  $k$  is the week index. RMSE is calculated for each week-period error vector  $\mathbf{e}_k$  independently, denoted as  $\text{RMSE}_k$ , as well as on the whole set of error vectors up to week  $k$  ( $\mathbf{E}_{[1,k]}$ ), denoted as  $\text{RMSE}_{[1,k]}$ , and the results are shown in Fig. 4.3b. It can be seen that RMSE performance by week periods does not vary significantly, except for few week periods in June and August. Sudden RMSE increase in June is mainly caused by the increase in energy consumption because of the final exams that together with high ambient temperature require more cooling for auditoriums. On the other hand, sudden RMSE decrease in August is mainly caused by the decrease in energy consumption because of the summer shutdown. From the load time-series for best and worst performing week periods in the validation data set, it can be seen that low and high RMSE values are not only caused by good and poor neural network performance, but also by decrease and increase in energy consumption. Note that at this moment only a one-hour-ahead load prediction is considered, i.e., real measurements are used for load prediction at a certain time instant. For the case of a one-day-ahead load prediction, predicted load ( $ac_0^{i-1}$ ,  $ac_0^{i-2}$ ,  $ac_0^{i-3}$ ,  $ac_0^{i-4}$ ,  $ac_0^{i-5}$ ) and meteorological data (te, hu, ig), together with time and other measured load data, are used for load prediction at a certain time instant  $i$  ( $ac_0^{i-0}$ ).

### 4.2.4 On-line model tuning

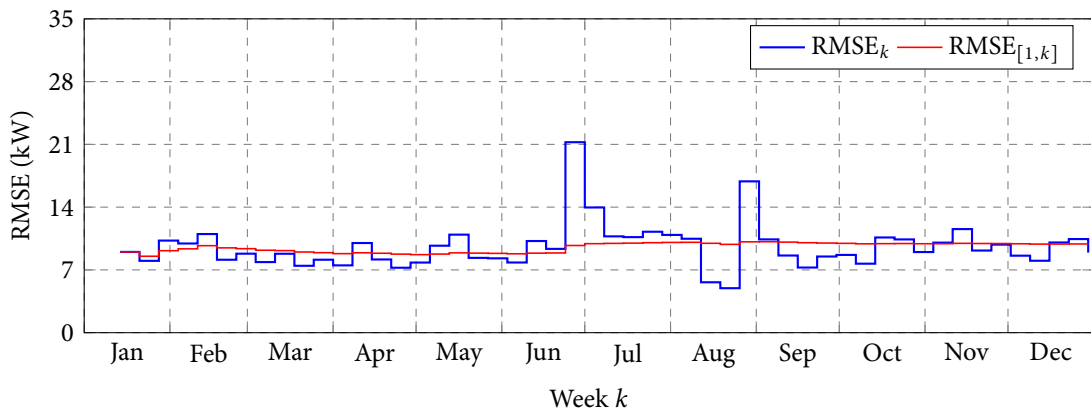
In this subsection the neural network model on-line tuning is discussed, considering optimal neural network structure, i.e., 38 input variables with respect to the IVS procedure results, and 10 neurons in hidden layer. This analysis is performed to show effectiveness of the prediction model even in the case when training data set is scarce, since in most practical applications there will be no available data for period before the microgrid is installed. At the end of each week, 50 neural network training procedures were performed using all available historical data up until that moment, whereas training and validation data set for each neural network training are generated randomly with respect to predefined ratio, i.e., 75% of data samples are used for training, and the other 25% are used for validation. Best performing neural network out of 50 trials at the end of each week is tested on data samples from the next week, denoted as the next-week data set. It should be noted that these data samples were not used for training or validation during neural network training, i.e., neural network is trained without any information on the next-week data samples since these data samples have not yet occurred in a real-world environment.

Error histogram, RMSE by week periods and load time-series for best and worst performing week periods on the next-week data set are shown in Fig. 4.4. The matrix of model error vectors on the next-week data samples is:

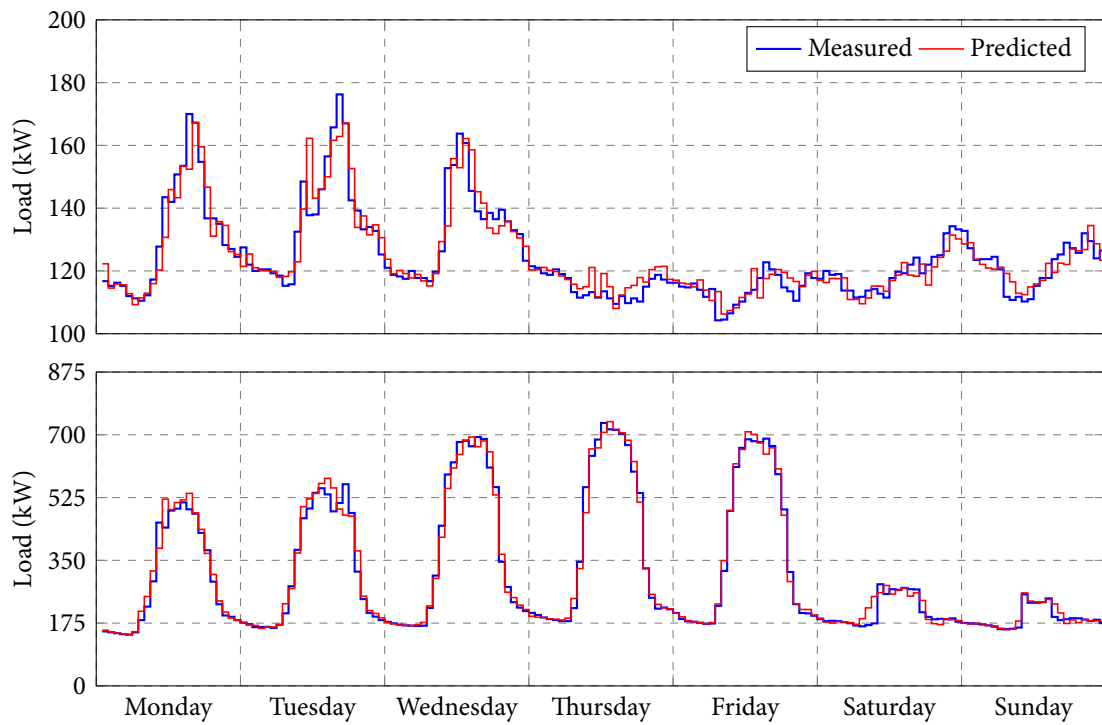
$$\mathbf{E}_{[9,156]} = [ \mathbf{e}_9, \mathbf{e}_{10}, \dots, \mathbf{e}_{156} ]^T, \quad (4.12)$$



(a) Neural network model error histogram on the validation data set.

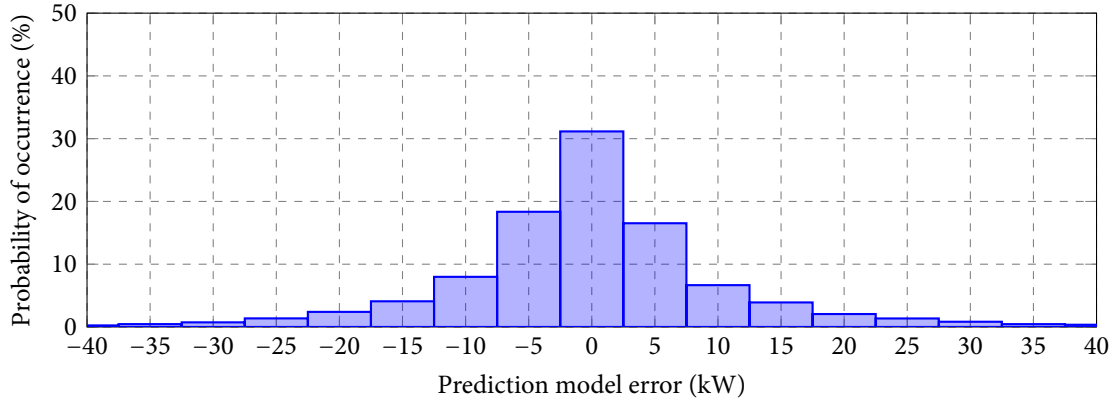


(b) RMSE by weeks on the validation data set.

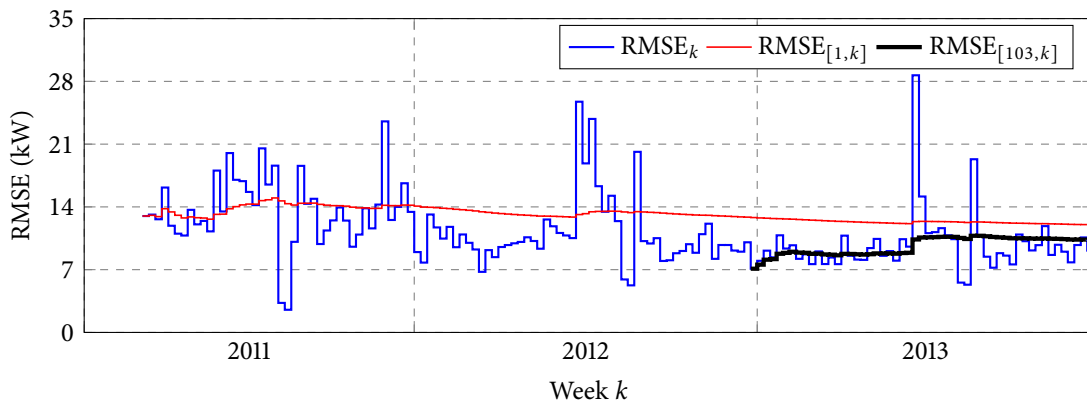


(c) Load time-series in best (upper) and worst performing (lower) week periods in the validation data set.

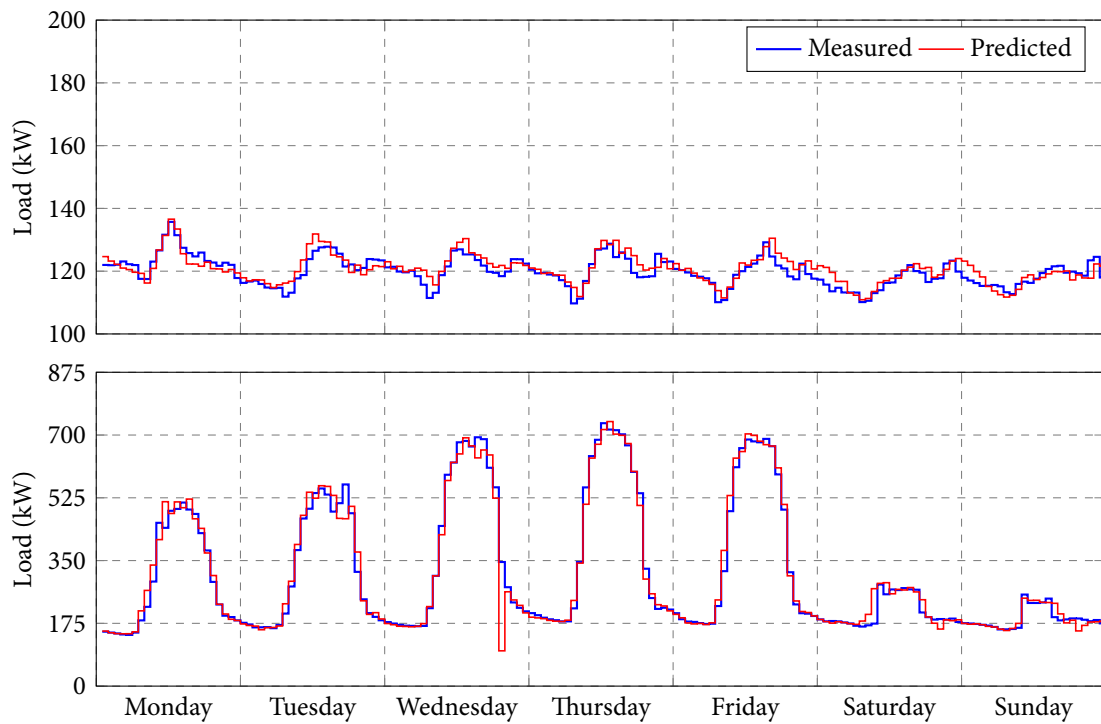
Figure 4.3: Performance of the best performing neural network with optimal structure for one-hour-ahead prediction considering only the validation data set.



(a) Neural network model error histogram on the next-week data set.



(b) RMSE by weeks on the next-week data set.



(c) Load time-series in best (upper) and worst performing (lower) week periods in the next-week data set.

Figure 4.4: Performance of the best performing neural network with optimal structure for one-hour-ahead prediction considering only the next-week data set.

where the error vector  $\mathbf{e}_{k+1} \in \mathbb{R}^{168 \times 1}$  is calculated using best performing neural network trained on data for weeks from 1 to  $k$ . Note that first 8 weeks are omitted from the procedure since there are not enough historical data for neural network to be able to perform well on next-week data samples. RMSE by weeks is calculated in the same way as described in the previous subsection, and the results are shown in Fig. 4.4b. It can be seen that RMSE performance varies significantly in 2011 since there is not enough historical data, but in general tends to decrease with increase of historical data samples number. There are also few outlier weeks that are mainly related to final exams and summer shutdown periods, as described in the previous subsection.

In order to be able to compare the results shown in Fig. 4.3b and Fig. 4.4b, RMSE performance for next-week data set is also calculated considering only  $\mathbf{E}_{[103,k]}$ , i.e., *history* in this case starts with year 2013. In this way it is shown that week-based on-line tuning can benefit neural network approximation ability. Note that data aging strategy can be applied in order to account only for most recent historical data samples, since they are expected to have greatest impact on current conditions. However, performance analysis presented here is done only on a 3-year historical data set, which is not enough for data aging strategy to show effect.

### 4.3 One-day-ahead prediction

Since developed neural-network-based load prediction model uses meteorological and lagged load data as inputs, which are in general uncertain, load prediction must be extended with the uncertainty description. This is especially important considering lagged load input data, since a single bad load prediction can corrupt all other predictions from that moment onward, i.e., load prediction error is accumulated along the prediction horizon. Except for input data uncertainty, the developed load prediction model itself is also uncertain, which is evident from model error histograms shown in Fig. 4.3a and Fig. 4.4a.

The developed neural network model uses 38 inputs in total, some of which are deterministic (e.g., all time inputs  $y_s, y_c, w_s, w_c, d_s, d_c, w_f$ ), some are deterministic if measurement uncertainty is neglected (e.g., all lagged load inputs except for  $ac_0^{-1}, ac_0^{-2}, ac_0^{-3}, ac_0^{-4}$ , and  $ac_0^{-5}$ ), and some are not deterministic, i.e., they contain uncertainty (e.g., all lagged load inputs that are not deterministic and all meteorological inputs  $t_e, h_u, i_g$ ). Except for input data, developed prediction model is also uncertain which must be taken into account.

#### 4.3.1 Input data uncertainty

Meteorological data ( $t_e, h_u, i_g$ ) uncertainty is described with a linearly increasing function, whereas deviation increases from 0% of the expected value at the beginning of the prediction horizon, to 5% of the expected value at the end of the prediction horizon, i.e., 24 h ahead. Note that in case of global solar irradiance ( $i_g$ ) there is no uncertainty for night hours. Uncertainty of lagged load data for most recent hours comes out as a model output uncertainty estimation. For example, for load prediction one hour ahead ( $ac_0^1$ ), only meteorological data and model itself contribute to the load prediction uncertainty, since lagged load data at this moment are known by measurements. For load prediction two hours ahead ( $ac_0^2$ ), except for meteorological data and prediction model, load predicted for one hour ahead also contributes to the load prediction uncertainty, since that time instance is used as model input, i.e.,  $ac_0^{-1} \leftarrow ac_0^1$ . In this way prediction error is accumulated through the prediction horizon, which is the main reason for load predicted to be characterized with the uncertainty description.

### 4.3.2 Model uncertainty

Except for input data, the developed load prediction model itself is also uncertain which is evident from error histograms shown in Fig. 4.3a and Fig. 4.4a. There are several ways to describe model uncertainty, e.g., model error mean and variance can be calculated on the whole set of historical data samples. However, much more accurate description can be achieved by observing only a limited number of data samples that are carefully chosen. For model error mean and variance calculation, historical data samples that are chosen according to 10% nearest input vectors by means of the Euclidean distance are used. It is shown that the error distribution calculated in this way can still be approximated by a normal (or Gaussian) distribution function defined as:

$$f(x, \mu, \sigma) = \frac{1}{\sqrt{2\pi\sigma^2}} \exp\left[-\frac{(x - \mu)^2}{2\sigma^2}\right], \quad (4.13)$$

where  $x$  is the observed stochastic variable, i.e., model error in this example, while  $\mu$  and  $\sigma^2$  are the expectation and variance of the normal distribution. Model error distribution for one exemplary day from the next-week data set (corresponds to Monday from the worst performing week shown in Fig. 4.4c) is shown in Fig. 4.6, with mean and standard deviation for each hour instant shown in Fig. 4.5. It can be seen that the prediction model error distribution can be approximated with a normal distribution with very good accuracy. Also, the model error expectation is always around zero value, while the variance varies significantly for night and day hours since the absolute amounts of error variance depends on the absolute load expectation. To conclude, model error is assumed to be subject to a normal (or Gaussian) distribution defined in Eq. (4.13), whereas the statistics (i.e., expectation  $\mu$  and variance  $\sigma^2$ ) of the model error is calculated by observing a limited number of (historical) data samples according to 10% nearest input vectors by means of an Euclidean distance. Model uncertainty is used together with input data uncertainty to estimate load prediction uncertainty by using the Unscented transformation.

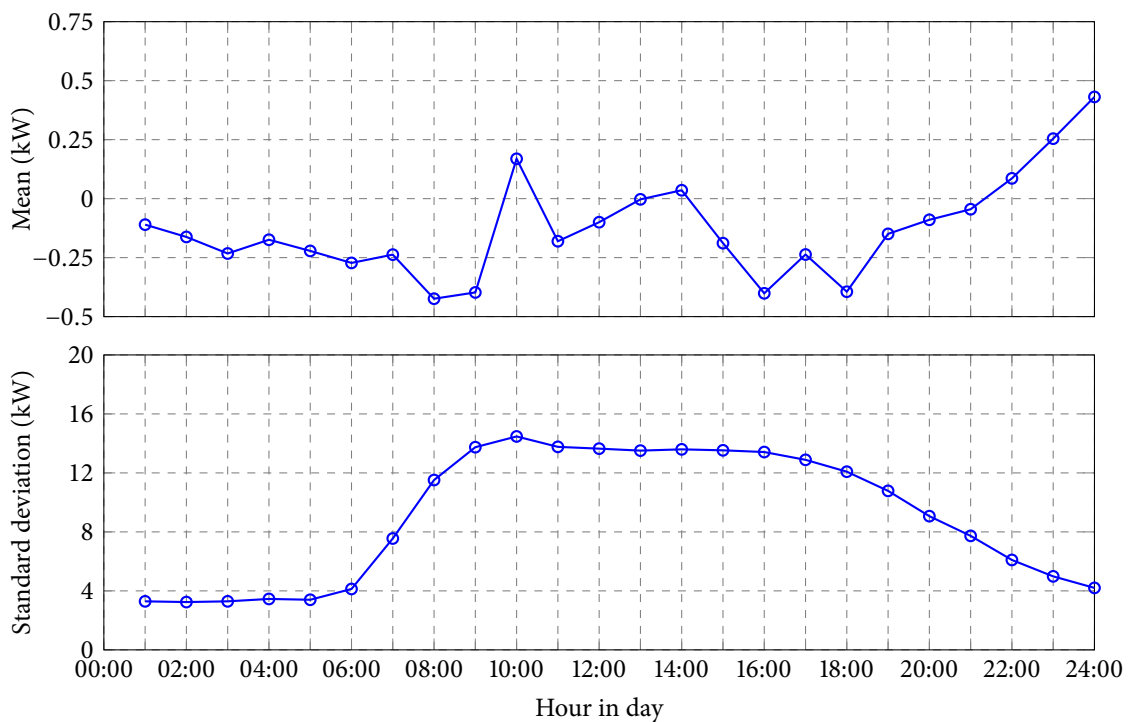


Figure 4.5: Model error mean and standard deviation for each hour instant in the exemplary day.

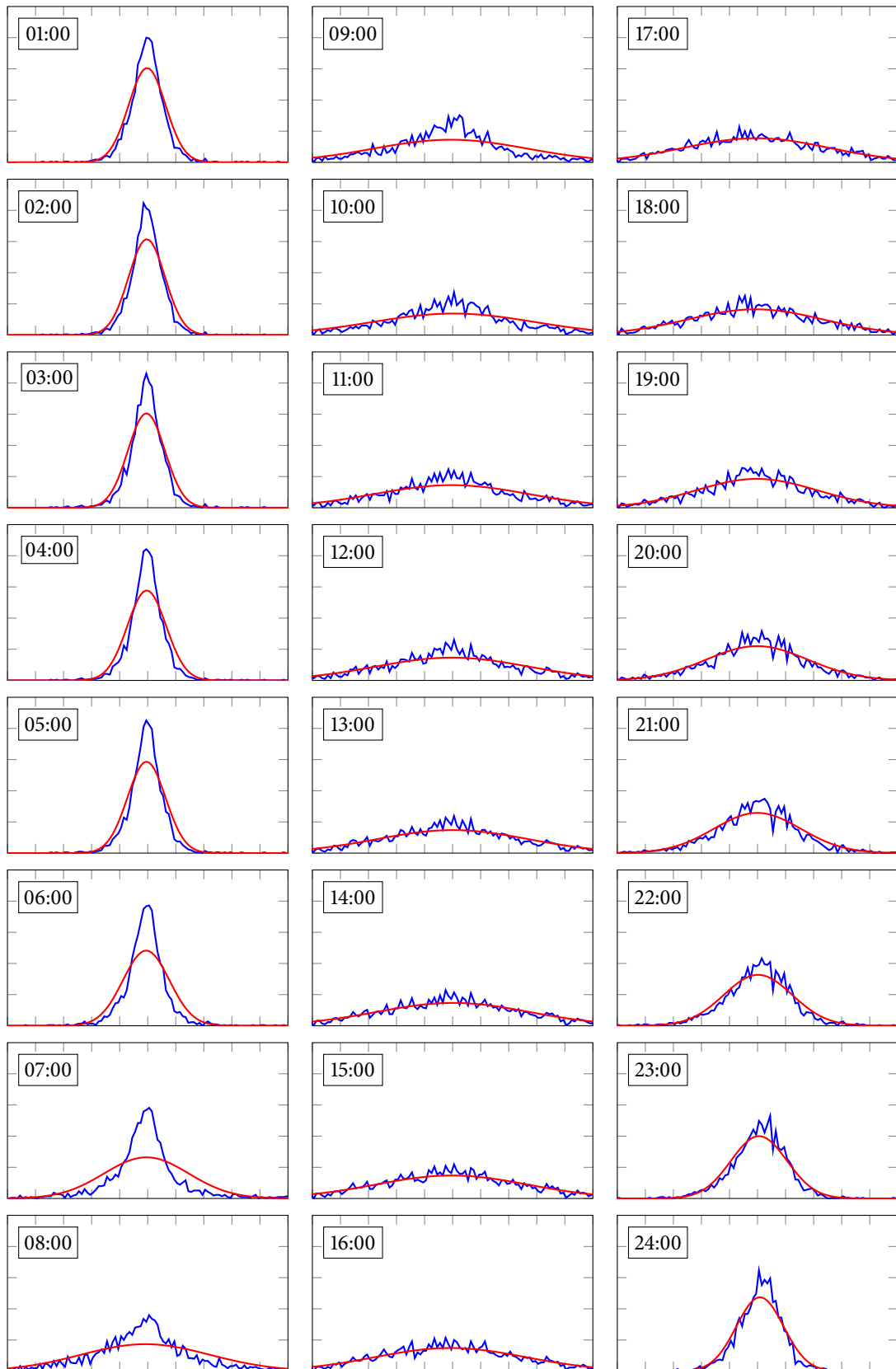


Figure 4.6: Estimated pdf of the prediction model error and its approximation by normal distribution for each hour instant in the exemplary day (on x-axis: model error from  $-50$  kW to  $50$  kW with  $10$ -kW step).

### 4.3.3 Unscented transformation extension

The well known Unscented transformation (UT) [122,123] was used for calculation of model output statistics based on a known statistics of input data and the model uncertainty. Unlike other methods, the UT does not rely on linearization of a nonlinear transformation (i.e., model), but instead it relies only on model evaluations through the use of deterministically drawn samples [123]. It is shown that the UT achieves second-order accuracy in the estimation of output mean and covariance, as opposed to the first-order accuracy for the methods that rely on model linearization [122]. The UT in its original form [122] assumes only input data uncertainty, and here an extension of the original form is proposed to also include the model uncertainty.

Consider a random variable  $\mathbf{x} \in \mathbb{R}^L$  that undergoes a nonlinear transformation  $h : \mathbb{R}^L \rightarrow \mathbb{R}$

$$y = h(\mathbf{x}) + \tilde{y}, \quad y \in \mathbb{R}, \quad (4.14)$$

where  $\tilde{y}$  is a model uncertainty assumed to follow a Gaussian distribution, i.e.,  $\tilde{y} \sim \mathcal{N}(\bar{\tilde{y}}, \sigma_y^2)$ , where  $\bar{\tilde{y}}$  is mean and  $\sigma_y^2$  is variance of model error. If input variable  $\mathbf{x}$  is perturbed about its mean  $\bar{\mathbf{x}}$  by a zero-mean disturbance  $\tilde{\mathbf{x}}$  with covariance  $\mathbf{P}_{\mathbf{x}}$ , i.e.,  $\mathbf{x} = \bar{\mathbf{x}} + \tilde{\mathbf{x}}$ , then the Taylor series expansion of the nonlinear transformation  $h(\mathbf{x})$  about  $\bar{\mathbf{x}}$  is

$$y = h(\bar{\mathbf{x}} + \tilde{\mathbf{x}}) + \tilde{y} = h(\bar{\mathbf{x}}) + \sum_{n=1}^{\infty} \frac{1}{n!} \mathbf{D}_{\bar{\mathbf{x}}}^n h + \tilde{y}, \quad (4.15)$$

where operator  $\mathbf{D}_{\bar{\mathbf{x}}}^n h$  is defined as:

$$\mathbf{D}_{\bar{\mathbf{x}}}^n h \triangleq \left[ (\tilde{\mathbf{x}} \cdot \nabla_{\mathbf{x}})^n h(\mathbf{x}) \right] \Big|_{\mathbf{x}=\bar{\mathbf{x}}}. \quad (4.16)$$

It is assumed here that the nonlinear function  $h(\cdot)$  can be expressed as a multi-dimensional Taylor series consisting of an arbitrary number of terms. As the number of terms in the sum tends to infinity, the residual of the series tends to zero. This implies that the series always converges to the true value of the function.

#### § ACCURACY OF MEAN

The true mean of  $y$  is given by expectation, i.e.,  $\bar{y} = \mathbb{E}[y]$ , as follows:

$$\bar{y} = \mathbb{E}[y] = \mathbb{E}[h(\mathbf{x}) + \tilde{y}] = \mathbb{E}\left[ h(\bar{\mathbf{x}}) + \sum_{n=1}^{\infty} \frac{1}{n!} \mathbf{D}_{\bar{\mathbf{x}}}^n h + \tilde{y} \right]. \quad (4.17)$$

If  $\tilde{\mathbf{x}}$  is a symmetrically distributed<sup>1</sup> random variable, then all odd moments will be zero, i.e.,  $\mathbb{E}[\tilde{\mathbf{x}}^n] = 0$  for odd  $n \in \mathbb{N}$ . Also note that the second moment is  $\mathbb{E}[\tilde{\mathbf{x}}\tilde{\mathbf{x}}^T] = \mathbf{P}_{\mathbf{x}}$ . Considering that the expectation is a linear operator, the true mean in Eq. (4.17) can be reduced to:

$$\bar{y} = h(\bar{\mathbf{x}}) + \frac{1}{2} \left( (\nabla_{\bar{\mathbf{x}}}^T \mathbf{P}_{\mathbf{x}} \nabla_{\bar{\mathbf{x}}}) h(\bar{\mathbf{x}}) \right) + \mathbb{E}\left[ \sum_{n=2}^{\infty} \frac{1}{(2n)!} \mathbf{D}_{\bar{\mathbf{x}}}^{2n} h \right] + \mathbb{E}[\tilde{y}]. \quad (4.18)$$

The UT calculates the posterior mean from the propagated sigma points, given by:

$$\mathcal{X}_0 = \bar{\mathbf{x}}, \quad (4.19a)$$

$$\mathcal{X}_i = \bar{\mathbf{x}} + \hat{\sigma}_{\mathbf{x},i}, \quad 1 \leq i \leq L, \quad (4.19b)$$

$$\mathcal{X}_{i+L} = \bar{\mathbf{x}} - \hat{\sigma}_{\mathbf{x},i}, \quad 1 \leq i \leq L, \quad (4.19c)$$

<sup>1</sup> This includes distributions like Uniform, Normal etc.

where  $\hat{\sigma}_{\mathbf{x},i} = \sqrt{L + \lambda} \cdot \sigma_{\mathbf{x},i}$ ,  $\lambda$  is user-defined scaling parameter, and  $\sigma_{\mathbf{x},i}$  denotes the  $i$ -th column of the matrix square root of  $\mathbf{P}_{\mathbf{x}}$ . This implies that  $\sum_{i=1}^L \sigma_{\mathbf{x},i} \sigma_{\mathbf{x},i}^{\top} = \mathbf{P}_{\mathbf{x}}$ . Given this formulation of sigma points, the propagation of each point through the nonlinear function is written in the form of the Taylor series expansion about  $\bar{\mathbf{x}}$ :

$$\mathcal{Y}_i = h(\mathcal{X}_i) + \tilde{y}_i = h(\bar{\mathbf{x}}) + \sum_{n=1}^{\infty} \frac{1}{n!} \mathbf{D}_{\hat{\sigma}_{\mathbf{x},i}}^n h + \tilde{y}_i, \quad (4.20)$$

where operator  $\mathbf{D}_{\hat{\sigma}_{\mathbf{x},i}}^n h$  is defined as:

$$\mathbf{D}_{\hat{\sigma}_{\mathbf{x},i}}^n h \triangleq \left[ (\hat{\sigma}_{\mathbf{x},i} \cdot \nabla_{\mathcal{X}_i})^n h(\mathcal{X}_i) \right] \Big|_{\mathcal{X}_i = \bar{\mathbf{x}}}. \quad (4.21)$$

Predicted mean by UT is defined as weighted sum of the transformed sigma points:

$$\bar{y}_{\text{UT}} = \frac{\lambda}{L + \lambda} \left( h(\bar{\mathbf{x}}) + \tilde{y}_0 \right) + \frac{1}{2} \frac{1}{L + \lambda} \sum_{i=1}^{2L} \mathcal{Y}_i, \quad (4.22)$$

where  $\mathcal{Y}_i$  can be replaced by Eq. (4.20):

$$\bar{y}_{\text{UT}} = h(\bar{\mathbf{x}}) + \frac{1}{2} \frac{1}{L + \lambda} \sum_{i=1}^{2L} \sum_{n=1}^{\infty} \frac{1}{n!} \mathbf{D}_{\hat{\sigma}_{\mathbf{x},i}}^n h + \left( \frac{\lambda}{L + \lambda} \tilde{y}_0 + \frac{1}{2} \frac{1}{L + \lambda} \sum_{i=1}^{2L} \tilde{y}_i \right), \quad (4.23)$$

Since sigma points are symmetrically distributed about  $\bar{\mathbf{x}}$ , all terms with odd  $n$  are zero. Let us now expand the sum for  $n = 2$  with respect to Eq. (4.21):

$$\frac{1}{2} \frac{1}{L + \lambda} \sum_{i=1}^{2L} \frac{1}{2!} \mathbf{D}_{\hat{\sigma}_{\mathbf{x},i}}^2 h = \frac{1}{2} \sum_{i=1}^L \left[ (\nabla_{\mathcal{X}_i}^{\top} \sigma_{\mathbf{x},i}^{\top} \sigma_{\mathbf{x},i} \nabla_{\mathcal{X}_i}) h(\mathcal{X}_i) \right] \Big|_{\mathcal{X}_i = \bar{\mathbf{x}}} = \frac{1}{2} \left( (\nabla_{\mathbf{x}}^{\top} \mathbf{P}_{\mathbf{x}} \nabla_{\mathbf{x}}) h(\mathbf{x}) \right) \Big|_{\mathbf{x} = \bar{\mathbf{x}}}. \quad (4.24)$$

The mean in Eq. (4.23) is now defined as:

$$\bar{y}_{\text{UT}} = h(\bar{\mathbf{x}}) + \frac{1}{2} \left( (\nabla_{\mathbf{x}}^{\top} \mathbf{P}_{\mathbf{x}} \nabla_{\mathbf{x}}) h(\mathbf{x}) \right) \Big|_{\mathbf{x} = \bar{\mathbf{x}}} + \left( \frac{\lambda}{L + \lambda} \tilde{y}_0 + \frac{1}{2} \frac{1}{L + \lambda} \sum_{i=1}^{2L} \tilde{y}_i \right) + \mathcal{R}, \quad (4.25)$$

where  $\mathcal{R}$  is the higher-order residual of the Taylor series expansion.

By comparing Eq. (4.18) and Eq. (4.25) it is clear that the true posterior mean and the mean calculated by the UT agree exactly to the third order and that errors are only introduced in the third and higher-order terms. The magnitudes of these errors depend on the choice of the composite scaling parameter  $\lambda$ , as well as on the higher-order derivatives of nonlinear function  $h$ .

#### § ACCURACY OF COVARIANCE

The true posterior covariance is given by:

$$\mathbf{P}_y = \mathbb{E}[(y - \bar{y})(y - \bar{y})^{\top}] = \mathbb{E}[yy^{\top}] - \bar{y}\bar{y}^{\top}. \quad (4.26)$$

By following the same procedure as for calculating the mean, the following equation for calculating the covariance is obtained:

$$\mathbf{P}_{y,\text{UT}} = \frac{1}{2L} \sum_{i=0}^{2L} W_i \left( (\mathcal{Y}_i - \bar{y}_{\text{UT}})(\mathcal{Y}_i - \bar{y}_{\text{UT}})^{\top} + \tilde{y}_i \tilde{y}_i^{\top} \right), \quad (4.27)$$

where  $W_i$  is a weighting factor defined in the same way as for calculating the mean in Eq. (4.22):

$$W_i = \begin{cases} \frac{\lambda}{L + \lambda}, & i = 0, \\ \frac{1}{2} \frac{1}{L + \lambda}, & i > 0. \end{cases} \quad (4.28)$$



#### 4.3.4 Performance verification

In this subsection a performance analysis of one-day-ahead load prediction considering prediction uncertainty is given. The best- and worst-performing weeks from the next-week data set are considered. Load time series for the considered week periods are shown in Fig. 4.4c. Load prediction is performed every hour for the next 24-hour period, i.e., as soon as new information becomes available. However, to simplify the results presentation, only prediction sequences done at midnight of each day for the next 24-hour period are presented here.

Load predictions for one-day-ahead with uncertainty area for the best- and worst-performing week periods in the next-week data set are shown in Fig. 4.7. Shaded area corresponds to the load expectation plus/minus the deviation  $\sigma$  estimated by UT. Note that the main difference between the load prediction presented in Fig. 4.4c and Fig. 4.7 is that the latter is updated once a day for the next 24-hour period (one-day-ahead prediction), and the former is updated every hour for the next 1-hour period (one-hour-ahead prediction). It is shown that load prediction contains significant amount of uncertainty considering its deviation, especially towards the end of the prediction horizon. This is the result of prediction error accumulation along the prediction horizon, since prediction model uses lagged load data as inputs. It must be noted that uncertainty characterization obtained by using UT does not give any information on probability density function (pdf) of the load predicted, but only its statistics, i.e., expectation and deviation.

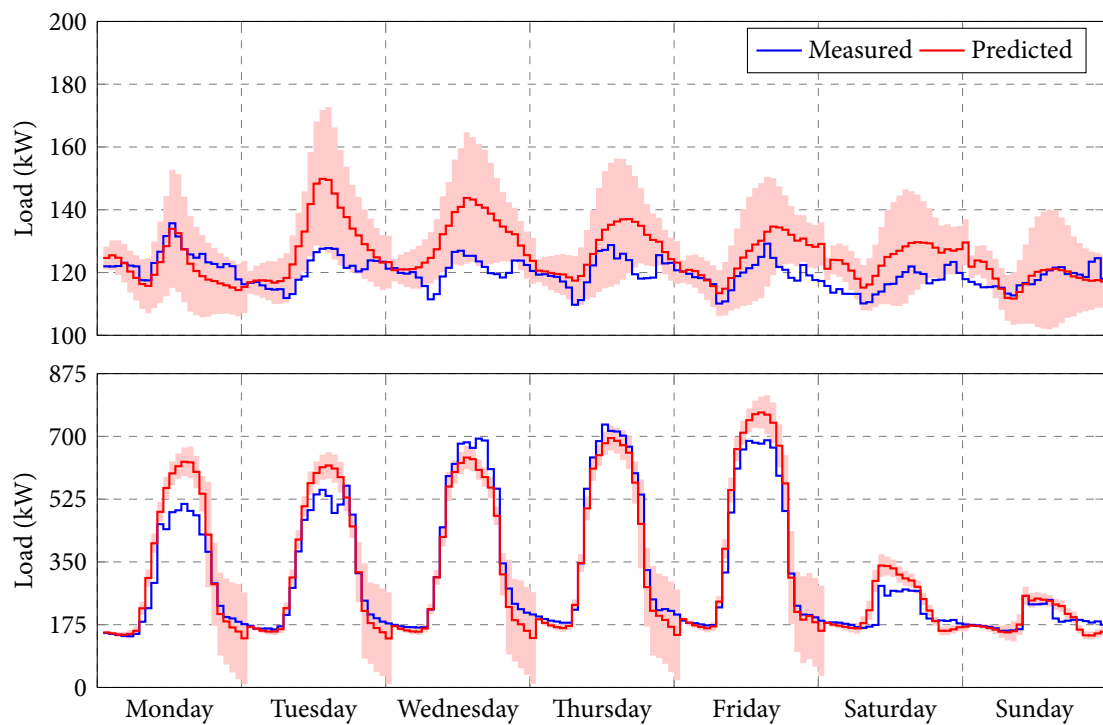


Figure 4.7: One-day-ahead load prediction assessment for best- and worst-performing week periods in the next-week data set (shaded area corresponds to  $\pm\sigma$  around load expectation, where  $\sigma$  is the prediction uncertainty obtained by UT).

## **Part III**

# **Optimal control**

## 5.1 Introduction

Microgrid concept is expected to enhance utilization of renewable energy sources [30] through distributed storage (e.g., batteries in plug-in electric and hybrid vehicles) by enabling time-shift between power production and consumption. More importantly, these distributed storage systems can also be used for electricity peak (price) shaving by buying and selling energy to the utility grid when it is most convenient for the end-user [124]. In this way, microgrid becomes an active part of the power system and enables decentralization of today's still centralized power system, thus increasing its reliability and stability [125]. In this chapter a power flow optimization [41–43] in a residential DC microgrid [47] is presented, whereas the DC microgrid consists of a photovoltaic (PV) array, valve-regulated lead-acid (VRLA) batteries stack, fuel-cell (FC) stack with electrolyzer, and is connected to the grid via bidirectional power converter. The optimization problem aims to minimize microgrid operating costs and is formulated using a linear program that takes into account the energy storage system charge and discharge efficiency. The model predictive control (MPC) scheme is used for closed-loop power management in the considered microgrid. Considering hierarchical design of microgrid controllers, the focus is here put on high-level optimization of power flows, whereas voltage stability and power quality are supposed to be controlled at lower microgrid control levels which are not discussed in this chapter.

A decision of when to buy and sell energy to the utility grid and in which amount, i.e., when to charge and discharge storage systems, is a complex function of the predicted microgrid load, power production (mainly by renewables), current storage systems state of charge, and predicted electricity price profile. This function is also subject to various constraints like capacity of energy storage system, power rating of power converters, and even to possible reduced availability of the utility grid. As it will be shown in this chapter, instead of using a mixed integer linear program (MILP) formulation, which is often used [126–129] due to taking into account different charge and discharge efficiency coefficients of energy storage systems, the described decision-making process can be formulated as a linear program (LP) under mild conditions, which significantly simplifies optimization and control, as well as microgrid interaction with utility grid and building energy management.

---

Research presented in this chapter is published in the following papers:

- M. Gulin, M. Vašak, and M. Baotić, "Analysis of Microgrid Power Flow Optimization with Consideration of Residual Storages State," in *Proceedings of the 2015 European Control Conference, ECC 2015*, pp. 3131–3136, Linz, Austria, 2015.
- M. Gulin, J. Matuško, and M. Vašak, "Stochastic Model Predictive Control for Optimal Economic Operation of a Residential DC Microgrid," in *Proceedings of the 2015 IEEE International Conference on Industrial Technology, ICIT 2015*, pp. 505–510, Sevilla, Spain, 2015.
- M. Gulin, A. Martinčević, V. Lešić, and M. Vašak, "Multi-level Optimal Control of a Microgrid-supplied Cooling System in a Building," in *Proceedings of the IEEE PES Innovative Smart Grid Technologies Conference Europe, ISGT Europe 2016*, pp. 1–6, Ljubljana, Slovenia, 2016.

Because of the economic and environmental benefits that stem from the optimal microgrid power flow, considerable attention is directed to development of better optimization algorithms and suitable modeling frameworks [62]. Authors in [130–133] use metaheuristic and heuristic algorithms to solve the power dispatch problem for microgrids, such as evolutionary and genetic algorithms. The advantage of these methods is in possibility to implement more complex models compared to those modeled by LP or MILP formulations, but at a cost of not being able to guarantee optimality of the found solution. Authors in [126–129] use MILP formulation [134] for the microgrid power management optimization problem to take into account predicted future electricity price, power production by renewable energy systems and microgrid load. Justification of using MILP instead of LP formulation is in different charge and discharge efficiency coefficients of energy storage systems, and in different price when selling and buying electrical energy. Despite the piece-wise affine nature of the storage systems model, the optimization problem can still be formulated as an LP under mild conditions. A special attention is paid to penalization of residual storage systems state in objective function, since stored energy at the end of the prediction horizon can also be transformed into economic gain [49]. This is particularly interesting for shorter prediction horizons when disturbance effects, such as power production, consumption and price profiles, are more prominent. The length of the prediction horizon is also very important when power flow is optimized, since optimization is based on future predictions of electricity price, power production and consumption profiles. An academic-free professional solver IBM ILOG CPLEX 12.6 was used to solve optimization problems, and YALMIP [135] was used for easier and faster control algorithm implementation.

When using predictions as optimization inputs, quality of the found solution to the optimization problem strongly depends on the accuracy of the used predictions. Since power predictions largely depend on weather forecast, in particular solar irradiance and temperature forecast, as well as on prediction model accuracy, predictions have to be described with uncertainty. If uncertainty is neglected, optimal solution found is only optimal for the considered scenario, whereas realizations can significantly deviate from predictions. This is why optimization should be done in a stochastic framework, taking into account predictions uncertainty [63, 121, 136–138]. Methods for power flow optimization that account for predictions uncertainty mainly include two-stage stochastic programming and scenario-based stochastic modeling. In two-stage stochastic programming [121], decision variables are partitioned into two sets: (i) the first stage variables are those that have to be decided before the actual realization of the uncertainty becomes available, and (ii) once the random events occur, the values of the second stage variables can be decided. Scenario-based stochastic modeling [137] is based on generating a number of scenarios with corresponding probability of occurrence, after which optimization problem is solved for each scenario as if there is no uncertainty. The solutions obtained from solving an optimization problem using generated scenarios are then aggregated according to the probability of occurrence of the corresponding scenario. However, if these solutions are aggregated linearly, the obtained solution might be far from optimal if the considered optimization problem is nonlinear, which is usually the case. Power flow management in stochastic framework can be implemented in many different ways, each having its pros and cons. Stochastic framework based on chance constraints is used here, that are defined as a probability that the system constraints will be violated at certain time instant. It is shown that the optimization problem remains in LP form, which is important from the optimization-complexity point of view.

This chapter is organized as follows. In Section 5.2 a dynamic model of the considered residential DC microgrid formed in LARES is given. A closed-loop power management in a deterministic framework based on model predictive control scheme is developed and verified in Section 5.3, and is extended for a stochastic framework in Section 5.4. In Section 5.5 a case-study on multi-level optimal control of a microgrid-supplied cooling system in a building is presented.

## 5.2 DC microgrid model

In this section a mathematical model of the considered residential DC microgrid formed in LARES is developed, which is used in all subsequent sections. It includes a discrete-time dynamic model of energy storage systems and power balance equation in the microgrid. The microgrid model is written in (augmented) matrix form to make it suitable for available optimization solvers.

### 5.2.1 Power balance

The residential DC microgrid formed in LARES consists of a wind turbine emulator and PV array, ultracapacitor, VRLA batteries stack, fuel-cell stack with electrolyzer, and is connected to the utility grid via bidirectional power converter. Note that fuel-cell stack with electrolyzer can also be considered as an energy storage system, since electrolyzer produces hydrogen when there is excess power, while fuel-cell stack uses the stored hydrogen when there is power shortage. Figure 5.1 shows a power balance diagram for the considered DC microgrid.

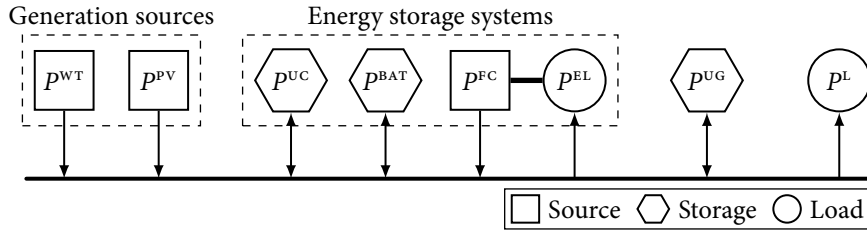


Figure 5.1: Power balance diagram of the DC microgrid formed in LARES.

The following power balance equation in the microgrid is always satisfied:

$$P^{WT} + P^{PV} + P^{UC} + P^{BAT} + (P^{FC} - P^{EL}) + P^{UG} = P^L, \quad (5.1)$$

where  $P^{WT}$  and  $P^{PV}$  are power production by wind turbine emulator and PV array,  $P^{UC}$  and  $P^{BAT}$  are net power exchange with the ultracapacitor and the battery,  $P^{FC}$  and  $P^{EL}$  are power production by the fuel-cell stack and consumption by the electrolyzer, respectively,  $P^{UG}$  is net power exchange with the utility grid, and  $P^L$  is power consumption by microgrid loads. Any deviation in the microgrid power balance equation will result in voltage oscillations on the DC link. For the sake of simplicity, wind turbine emulator is not considered here and the system of fuel-cell stack with electrolyzer is considered as a single controllable energy storage unit denoted as  $P^{FCE}$ . Since ultracapacitor has much lower energy storage capacity compared to bulk storage systems such as batteries and fuel-cell system, this component is also neglected in the subsequent power flow management. The power balance equation is now redefined as follows:

$$P^{PV} + P^{BAT} + P^{FCE} + P^{UG} = P^L. \quad (5.2)$$

By convention used here, power components are positive when supplying power to the microgrid DC link, e.g., power components  $P^{BAT}$  and  $P^{FCE}$  will be negative for charging and positive for discharging from the energy-storage-system point of view, power component  $P^{UG}$  will be negative for exporting (selling) and positive for importing (buying) power from the utility grid, and power component  $P^{PV}$  is always positive. Load is assumed always to be uncontrollable and unidirectional, and due to the convention the power component  $P^L$  is always positive which is why it enters the power balance equation from the other side of the equality sign.

### 5.2.2 Dynamic system model

Microgrid energy storage systems are modeled by discrete-time first-order difference equations with 1-h sample time, as follows:

$$\begin{cases} x_{k+1}^{\text{BAT}} = x_k^{\text{BAT}} - P_k^{\text{BAT}} \eta_k^{\text{BAT}} (P_k^{\text{BAT}}) \Delta T, \\ x_{k+1}^{\text{FCE}} = x_k^{\text{FCE}} - P_k^{\text{FCE}} \eta_k^{\text{FCE}} (P_k^{\text{FCE}}) \Delta T, \end{cases} \quad (5.3)$$

where  $k$  is the discrete time instant,  $\Delta T = 1$  h is the sample time,  $x_k$  is the state of charge at  $k\Delta T$ ,  $P_k$  is the mean power within one time step starting at  $k\Delta T$ , and  $\eta_k(\cdot)$  is charge or discharge efficiency that depends on the sign of the corresponding power component  $P_k$ . Authors in [62] use binary variables to decide which value of  $\eta$  to use at  $k$ -th time instant. However, instead of introducing binary variables, power components of energy storage systems can be split into charge and discharge components,  $P_{\text{ch},k}$  and  $P_{\text{dch},k}$ , as follows:

$$\begin{cases} x_{k+1}^{\text{BAT}} = x_k^{\text{BAT}} - \left( \frac{1}{\eta_{\text{dch}}^{\text{BAT}}} P_{\text{dch},k}^{\text{BAT}} + \eta_{\text{ch}}^{\text{BAT}} P_{\text{ch},k}^{\text{BAT}} \right) \Delta T, \\ x_{k+1}^{\text{FCE}} = x_k^{\text{FCE}} - \left( \frac{1}{\eta_{\text{dch}}^{\text{FCE}}} P_{\text{dch},k}^{\text{FCE}} + \eta_{\text{ch}}^{\text{FCE}} P_{\text{ch},k}^{\text{FCE}} \right) \Delta T, \end{cases} \quad (5.4)$$

where  $P_{\text{ch}} \leq 0$  and  $P_{\text{dch}} \geq 0$  represent charge and discharge components, respectively. Note that situation where both  $P_{\text{ch},k}$  and  $P_{\text{dch},k}$  components of a single storage system are different than zero at the same time instant  $k$  would correspond to a (practically) unacceptable scenario, since it would imply that it "pays off" to charge and discharge the storage system at the same time. In all realistic optimization problems (i.e., objective functions) this will never be true since it implies more power dissipation at the DC link, and thus higher microgrid operating costs. This hypothetical situation would only make sense when there is excess power that cannot be exported to the grid, e.g., PV array produces more power than the current load demand, energy storage systems are full, and the power surplus cannot be exported to the grid due to the grid-tied bidirectional power converter power rating limits. In such hypothetical situation, PV array should leave the maximum power point tracking (MPPT) mode and deliver only the necessary amount of power and not misuse storage systems to dissipate power. An expensive MILP formulation of the optimization problem is avoided by using much simpler and more effective LP formulation, while also gaining an insight into any possible misuse of the resources or storage systems in the microgrid.

Given the previously introduced decomposition to charge and discharge components for energy storage systems, from power balance defined in Eq. (5.2) it follows that the utility grid power component  $P_k^{\text{UG}}$  at each time instant  $k$  must satisfy:

$$P_k^{\text{UG}} = -(P_{\text{dch},k}^{\text{BAT}} + P_{\text{dch},k}^{\text{FCE}} + P_{\text{ch},k}^{\text{BAT}} + P_{\text{ch},k}^{\text{FCE}}) - (P_k^{\text{PV}} - P_k^{\text{L}}). \quad (5.5)$$

It should be noted that  $P^{\text{PV}}$  and  $P^{\text{L}}$  are prediction variables subject to uncertainty:

$$P_k^{\text{PV}} = \bar{P}_k^{\text{PV}} + \tilde{P}_k^{\text{PV}}, \quad P_k^{\text{L}} = \bar{P}_k^{\text{L}} + \tilde{P}_k^{\text{L}}, \quad (5.6)$$

where  $\bar{P}_k^{\text{PV}} = \mathbb{E}[P_k^{\text{PV}}]$  and  $\bar{P}_k^{\text{L}} = \mathbb{E}[P_k^{\text{L}}]$  are prediction expectation, while  $\tilde{P}_k^{\text{PV}}$  and  $\tilde{P}_k^{\text{L}}$  are prediction uncertainty. Note that the two prediction variables are assumed to be independent.

The microgrid equations (5.4) and (5.5) can be written in a matrix form as follows:

$$x_{k+1} = Ax_k + Bu_k, \quad (5.7a)$$

$$P_k^{\text{UG}} = Du_k + Vv_k, \quad (5.7b)$$

where  $x = [x^{\text{BAT}}, x^{\text{FCE}}]^{\text{T}}$  is the system state vector,  $u = [P_{\text{dch}}^{\text{BAT}}, P_{\text{dch}}^{\text{FCE}}, P_{\text{ch}}^{\text{BAT}}, P_{\text{ch}}^{\text{FCE}}]^{\text{T}}$  is the input variables vector,  $v = [P^{\text{PV}}, P^{\text{L}}]^{\text{T}}$  is the disturbance vector, and system matrices  $A$ ,  $B$ ,  $D$ , and  $V$  are calculated with respect to Eqs. (5.4)–(5.6).

### 5.2.3 Augmented dynamic system model

The system model in Eq. (5.7) fully describes the power flow in the considered microgrid. The model is written in augmented form for the whole prediction horizon, as the augmented form is more suitable for available optimization solvers:

$$\mathbf{x} = \mathbf{A}x_0 + \mathbf{B}\mathbf{u}, \quad (5.8a)$$

$$\mathbf{P}^{\text{UG}} = \mathbf{D}\mathbf{u} + \mathbf{V}\mathbf{v}, \quad (5.8b)$$

where  $x_0$  is the initial state of energy storage systems, system matrices  $\mathbf{A}$ ,  $\mathbf{B}$ ,  $\mathbf{D}$ , and  $\mathbf{V}$  are calculated with respect to Eq. (5.7), and augmented vectors are defined as:

$$\mathbf{x} = \begin{bmatrix} x_1 \\ x_2 \\ \vdots \\ x_N \end{bmatrix}, \quad \mathbf{u} = \begin{bmatrix} u_0 \\ u_1 \\ \vdots \\ u_{N-1} \end{bmatrix}, \quad \mathbf{v} = \begin{bmatrix} v_0 \\ v_1 \\ \vdots \\ v_{N-1} \end{bmatrix}, \quad \tilde{\mathbf{v}} = \begin{bmatrix} \tilde{v}_0 \\ \tilde{v}_1 \\ \vdots \\ \tilde{v}_{N-1} \end{bmatrix}, \quad \mathbf{P}^{\text{UG}} = \begin{bmatrix} P_0^{\text{UG}} \\ P_1^{\text{UG}} \\ \vdots \\ P_{N-1}^{\text{UG}} \end{bmatrix}, \quad \mathbf{c} = \begin{bmatrix} c_0 \\ c_1 \\ \vdots \\ c_{N-1} \end{bmatrix}, \quad (5.9)$$

where  $N$  is length of the prediction horizon, and  $c$  is electricity price used in the objective function.

### 5.2.4 Electricity price

When operating in grid-connected mode, the microgrid can import or export power to the utility grid through the grid-tied bidirectional power converter. Although electricity price can vary when buying or selling, for simplicity the same price is assumed in both cases. Electricity price  $c_k$  is obtained from the electricity market data on EPEX SPOT<sup>1</sup>. It should be noted that there are situations when electricity price is negative on the market, which mainly occurs during holidays due to decreased industrial production. The main reason for this phenomena is that it pays off to keep a power plant running and have someone to take the produced power, rather than having to shut down and restart the power plant few days later. All negative prices are saturated to 0 EUR/MWh, otherwise, the simplified storage system dynamic model introduced in Eq. (5.4) could not be applied.

## 5.3 Power flow management in deterministic framework

The power flow optimization is formulated based on (i) the initial state of the microgrid energy storage systems  $x_0$ , (ii) the predicted local power production and consumption profiles in the microgrid  $\tilde{\mathbf{v}}$ , and (iii) the information obtained from the utility grid, i.e., predicted electricity price profile  $c_k$ , where  $k$  is the discrete time instant in range from 0 to  $N-1$ , where  $N$  is the prediction horizon length. Results of the power flow optimization are charge and discharge profiles for the microgrid energy storage systems throughout the prediction horizon, which achieve the best possible economic gain for the microgrid operation under presence of specified technical and other constraints. It should be noted that the prediction uncertainty is neglected in deterministic framework, i.e., only prediction mean  $\tilde{\mathbf{v}}$  is considered in the optimization.

### 5.3.1 Objective function

The following economic criterion  $J$  of the microgrid operation is considered, where negative values represent revenue for the microgrid:

$$J(\mathbf{u}, x_0, \mathbf{c}, \tilde{\mathbf{v}}) = -\hat{c}_N \hat{x}_N + \sum_{k=0}^{N-1} c_k P_k^{\text{UG}} \Delta T, \quad (5.10)$$

<sup>1</sup> European Power EXchange (EPEX), url: [www.epexspot.com/en/market-data/elix](http://www.epexspot.com/en/market-data/elix)

where  $N$  is the prediction horizon length,  $c_k$  is the electricity price,  $\hat{c}_N$  is the estimated final electricity price under which the equivalent electricity contained in energy storage systems  $\hat{x}_N$  could be sold to the utility grid or could replace the utility grid after the  $N$ -th hour in the future, hence the negative sign in the objective function, and vectors  $\mathbf{u}$ ,  $\mathbf{c}$ , and  $\bar{\mathbf{v}}$  are augmented control, electricity price, and mean (expected) disturbance sequences defined in Eq. (5.9).

The equivalent electricity contained in energy storage systems at the end of the prediction horizon  $\hat{x}_N$  is a function of control sequence  $\mathbf{u}$  and initial energy storage systems state  $x_0$ :

$$\hat{x}_N = \begin{bmatrix} \eta_{\text{dch}}^{\text{BAT}} & \eta_{\text{dch}}^{\text{FCE}} \end{bmatrix} x_N, \quad (5.11a)$$

$$x_N = A^N x_0 + \sum_{i=0}^{N-1} A^i B u_{N-1-i}, \quad (5.11b)$$

where the latter equation is an explicit form of the microgrid dynamic model in Eq. (5.7a). Selection of the final electricity price  $\hat{c}_N$  determines to which extent will the power flow optimization algorithm force energy storage systems to be full at the end of the prediction horizon. One possible strategy is to have the final price set to a maximum value achieved on a prediction horizon. This implies that the energy contained in energy storage systems will be sold (i.e., used) only when maximum prices, at some instant in the future, take place, and will implicitly force the power flow optimization algorithm to keep the energy storage systems nearly full and ready for peak (prices) shaving in the future. As it will be shown by simulations, influence of the residual energy storage system state penalization on the optimization results vanishes out as the prediction horizon gets longer.

### 5.3.2 System constraints

Minimization of the objective function defined in Eq. (5.10) is subject to various constraints on microgrid variables over the future horizon. These constraints can be either physical or designer-introduced in order to protect the system and prolong its life.

Storage system state  $x_k$  must always be inside capacity limits:

$$x_{\min} \leq x_k \leq x_{\max}, \quad 1 \leq k \leq N, \quad (5.12)$$

where  $x_{\min}, x_{\max} \in \mathbb{R}^2$ .

Limits on power components are defined by the corresponding power converter power rating, i.e., how much energy can they exchange within one time step, and also by their physical constraints, e.g.,  $P_{\text{ch}} \leq 0$  and  $P_{\text{dch}} \geq 0$ :

$$u_{\min} \leq u_k \leq u_{\max}, \quad 0 \leq k \leq N-1, \quad (5.13a)$$

$$P_{\min}^{\text{UG}} \leq P_k^{\text{UG}} \leq P_{\max}^{\text{UG}}, \quad 0 \leq k \leq N-1, \quad (5.13b)$$

where  $u_{\min}, u_{\max} \in \mathbb{R}^4$  and  $P_{\min}^{\text{UG}}, P_{\max}^{\text{UG}} \in \mathbb{R}$ . If information about the predicted utility grid availability is at disposal, one can also include this information by modifying the constraint (5.13b) as:

$$P_{\min,k}^{\text{UG}} \leq P_k^{\text{UG}} \leq P_{\max,k}^{\text{UG}}, \quad 0 \leq k \leq N-1, \quad (5.14)$$

where  $P_{\min,k}^{\text{UG}}, P_{\max,k}^{\text{UG}} \in \mathbb{R}$  is the information about predicted utility grid availability at the time instant  $k$  on the prediction horizon. However, no additional limitations on utility grid availability are considered in this chapter, except for grid-tied bidirectional power converter power rating which is already captured by constraint in Eq. (5.13b).



### 5.3.3 LP formulation

Once objective function and constraints have been defined, the power flow optimization problem can be written in LP form as follows:

$$\begin{aligned} \min_{\mathbf{u}} \quad & \mathbf{f}^\top \mathbf{u} + \text{const.}, \\ \text{s.t.} \quad & \mathbf{I}_x x_0 + \mathbf{I}_u \mathbf{u} + \mathbf{I}_v \bar{\mathbf{v}} \leq \mathbf{g}, \end{aligned} \quad (5.15)$$

where constant, vectors  $\mathbf{f}$  and  $\mathbf{g}$ , and matrices  $\mathbf{I}_x$ ,  $\mathbf{I}_u$  and  $\mathbf{I}_v$  are calculated from Eqs. (5.10)–(5.13), while  $\mathbf{u}$  and  $\bar{\mathbf{v}}$  are augmented vectors defined in Eq. (5.9).

### 5.3.4 Closed-loop control

The model predictive control (MPC) scheme [139] with receding horizon principle is used for closed-loop power flow management in the considered microgrid. Solution to the MPC problem yields a trajectory of states and inputs (i.e., control signals) that satisfy the dynamics and constraints of microgrid operation while optimizing some given criteria [62].

Let the real system dynamics be

$$x(t+1) = Ax(t) + Bu(t), \quad (5.16)$$

with electricity prices  $c(t)$  and disturbances  $\bar{v}(t)$ . At each discrete time instant  $t$  the MPC scheme computes the optimal control sequence  $\mathbf{u}^*$  given initial energy storage systems state  $x_0 = x(t)$ , electricity price  $\mathbf{c} = [c(t), c(t+1), \dots, c(t+N-1)]^\top$  and disturbance  $\bar{\mathbf{v}} = [\bar{v}(t), \bar{v}(t+1), \dots, \bar{v}(t+N-1)]^\top$  sequences:

$$\begin{aligned} \mathbf{u}^* = \arg \min_{\mathbf{u}} \quad & J(\mathbf{u}, x_0, \mathbf{c}, \bar{\mathbf{v}}), \\ \text{s.t.} \quad & (5.12), (5.13), \end{aligned} \quad (5.17)$$

where  $J$  is the objective function defined in Eq. (5.10), which is a linear function in  $\mathbf{u}$ . According to the receding horizon principle, only the first control vector  $u_0^*$  from the optimal augmented control sequence  $\mathbf{u}^*$  is applied, i.e.,  $u(t) = u_0^*$ . The optimization problem in Eq. (5.17) is repeated again at the next time instant, with new initial energy storage systems state, electricity price and disturbance sequences. By this approach, new optimal control plan can potentially compensate any disturbance that has meanwhile acted on the system.

### 5.3.5 Simulation results

Performance of the proposed approach is verified on year-scale simulations based on (i) meteorological data provided by DHMZ from which PV array power production is calculated, (ii) electricity price data obtained from EPEX SPOT, and (iii) consumption data for FER building scaled to match power levels in the microgrid, all for year 2013. Numeric values for all microgrid parameters defined in this section are given in Table 5.1. The MPC-based closed-loop control scheme with receding horizon principle is employed, for different prediction horizon lengths  $N$  and final price values  $\hat{c}_N$ , where the final price value is calculated as a share of maximum price over the prediction horizon:

$$\hat{c}_N(t) = \frac{p_{\text{pct}}}{100} \max_k c_k, \quad t \leq k \leq t + N - 1, \quad (5.18)$$

where  $t$  is the discrete time instant as discussed in the previous subsection, and  $p_{\text{pct}}$  is a parameter that goes from 0% to 120%: (i) for  $p_{\text{pct}} = 0\%$  there is no penalization of the residual energy storage systems state, and (ii) for  $p_{\text{pct}} = 120\%$  the power flow optimization algorithm will try to keep the energy storage systems nearly full and ready for peak (prices) shaving in the future.

Table 5.1: Microgrid parameters used in simulation

$\eta_{\text{ch}}^{\text{BAT}}$	0.9	$\eta_{\text{dch}}^{\text{BAT}}$	0.9	Battery charge and discharge efficiency
$\eta_{\text{ch}}^{\text{FCE}}$	0.7	$\eta_{\text{dch}}^{\text{FCE}}$	0.4	Fuel-cell charge and discharge efficiency
$x_{\text{min}}^{\text{BAT}}$	1.0	$x_{\text{max}}^{\text{BAT}}$	10.0	Battery state of charge limits (kWh)
$x_{\text{min}}^{\text{FCE}}$	0.0	$x_{\text{max}}^{\text{FCE}}$	2.5	Fuel-cell state of charge limits (kWh)
$P_{\text{ch,min}}^{\text{BAT}}$	-3.0	$P_{\text{ch,max}}^{\text{BAT}}$	0.0	Battery power converter power limits (kW)
$P_{\text{dch,min}}^{\text{BAT}}$	0.0	$P_{\text{dch,max}}^{\text{BAT}}$	3.0	Battery power converter power limits (kW)
$P_{\text{ch,min}}^{\text{FCE}}$	-1.2	$P_{\text{ch,max}}^{\text{FCE}}$	0.0	Fuel-cell power converter power limits (kW)
$P_{\text{dch,min}}^{\text{FCE}}$	0.0	$P_{\text{dch,max}}^{\text{FCE}}$	0.5	Fuel-cell power converter power limits (kW)
$P_{\text{min}}^{\text{UG}}$	-3.0	$P_{\text{max}}^{\text{UG}}$	3.0	Utility grid power converter power limits (kW)

Revenue (i.e., economic gain) at the end of the considered one-year period can be calculated as:

$$c_{\text{rev}} = \sum_{t=0}^{8759} c(t) \left( \bar{P}^{\text{PV}}(t) - \bar{P}^{\text{L}}(t) - P^{\text{UG}}(t) \right) \Delta T, \quad (5.19)$$

where  $c(t)$  is the electricity price,  $\bar{P}^{\text{PV}}(t) - \bar{P}^{\text{L}}(t)$  is the net power shortage or surplus in the microgrid, and  $P^{\text{UG}}(t)$  is the power exchange with the utility grid at the time instant  $t$ . In other words, revenue at the time instant  $t$  is defined as a difference between power exchange with the utility grid and power demand, multiplied by the electricity price at that time instant.

Figure 5.2 shows revenue at the end of the considered one-year period for different prediction horizon lengths  $N$ , and for different final price values  $\hat{c}_N$  which are calculated as a share of the maximum price value over the prediction horizon defined by  $p_{\text{pct}}$  in Eq. (5.18). Figure 5.3 shows revenue when the final price value is determined as a mean electricity price over the prediction horizon. Longer prediction horizons lead to higher revenue, while shorter prediction horizons are more sensitive to penalization of the residual energy storage system state.

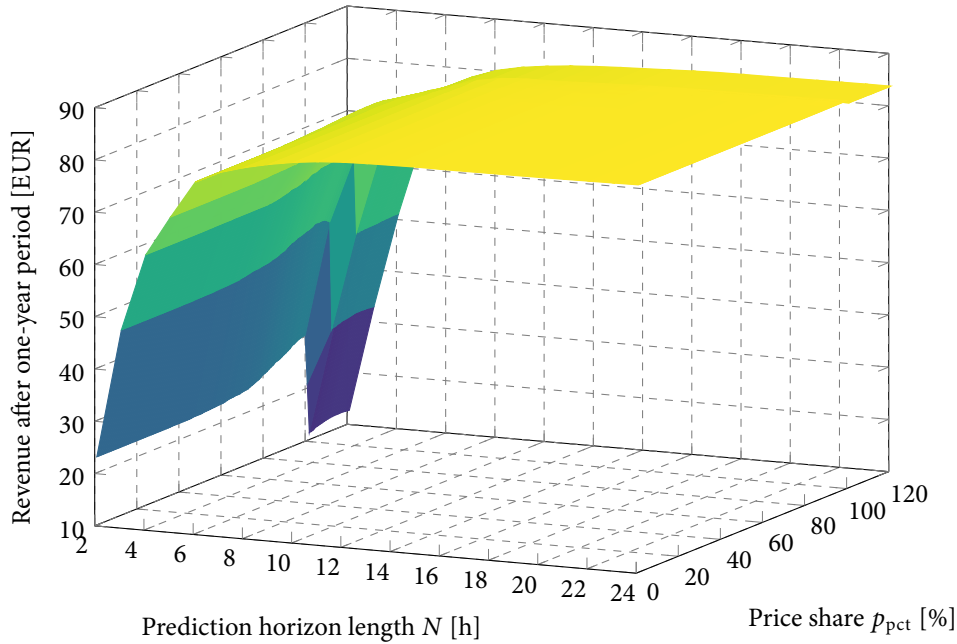


Figure 5.2: Revenue at the end of the one-year period for different prediction horizon lengths  $N$  and final price values  $\hat{c}_N$ , which are given as a share  $p_{\text{pct}}$  of the maximum price value over the prediction horizon.

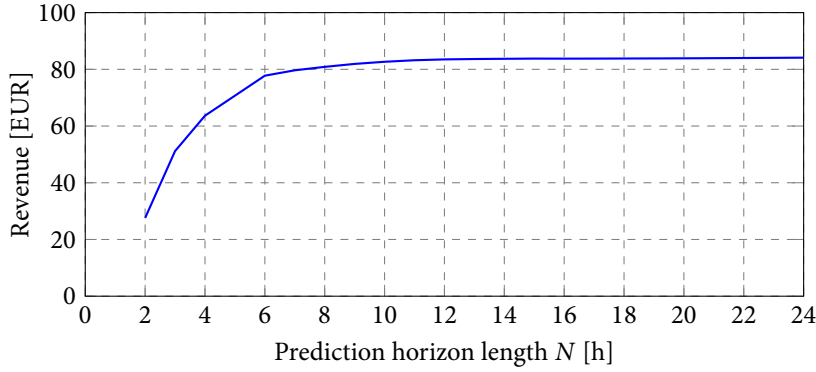


Figure 5.3: Revenue at the end of the one-year period when the final price value  $\hat{c}_N$  is determined as the mean electricity price over the prediction horizon.

Numeric values of revenues for different prediction horizon lengths and final price values are shown in Table 5.2. Three different scenarios for the final price value selection are considered: (i) no penalization of the residual energy storage systems state, i.e.,  $p_{\text{pct}} = 0\%$ , (ii) the final price is selected as the mean electricity price over the prediction horizon, and (iii) the final price is selected as the best-performing electricity price over the prediction horizon considering the revenue. For the prediction horizon length  $N = 2$  there is a significant improvement in the revenue when using residual energy storage systems state penalization, i.e., revenue improvement is 7.2 EUR (31.3%) in comparison between the best case and the case where no penalization is used. However, the improvement vanishes out as the prediction horizon length gets longer, e.g., for the prediction horizon length  $N = 24$  the improvement is only 0.1 EUR (0.09%).

Figure 5.4 shows profiles for closed-loop control simulation with 1-h sample time over 48-h exemplary period beginning on 1 Jul 2013 at 00:00, using MPC scheme with  $N = 24$  and  $p_{\text{pct}} = 90\%$ : (i) electricity price, (ii) power production by the PV system and consumption by microgrid loads, (iii) power exchange with the utility grid, (iv) optimal control sequence, i.e., net power exchange with battery and fuel-cell, and (v) normalized state of charge of battery and fuel-cell. It should be noted that the power exchange with the utility grid is not a decision (control) variable, but is determined by the power balance in the microgrid defined in Eq. (5.5), i.e., it enters the optimization algorithm as an equality constraint. The control algorithm uses fuel-cell system as little as possible compared to batteries stack, since overall efficiency of the fuel-cell system is below 30%, and the overall efficiency of the batteries stack is over 80%. As for buying and selling electricity from the utility grid, microgrid is importing power from the utility grid mainly during lower electricity prices, while exporting power to the utility grid during higher electricity prices. In the whole considered one-year period there were no optimization problem solutions for which both energy storage system power components, charge and discharge, were different than zero at the same time instant, which confirms validity of the used LP formulation of the optimization problem.

Table 5.2: Revenue in EUR at the end of the one-year period

Scenario	Prediction horizon length (h)											
	2	4	6	8	10	12	14	16	18	20	22	24
No penalization	23.0	62.6	77.2	80.8	82.6	83.5	83.7	83.8	83.8	83.9	84.0	84.1
Mean price	27.6	63.7	77.8	80.9	82.7	83.5	83.7	83.8	83.8	83.9	84.0	84.1
Best case	30.2	66.4	78.4	80.8	82.8	83.5	83.7	83.8	83.9	83.9	84.0	84.2

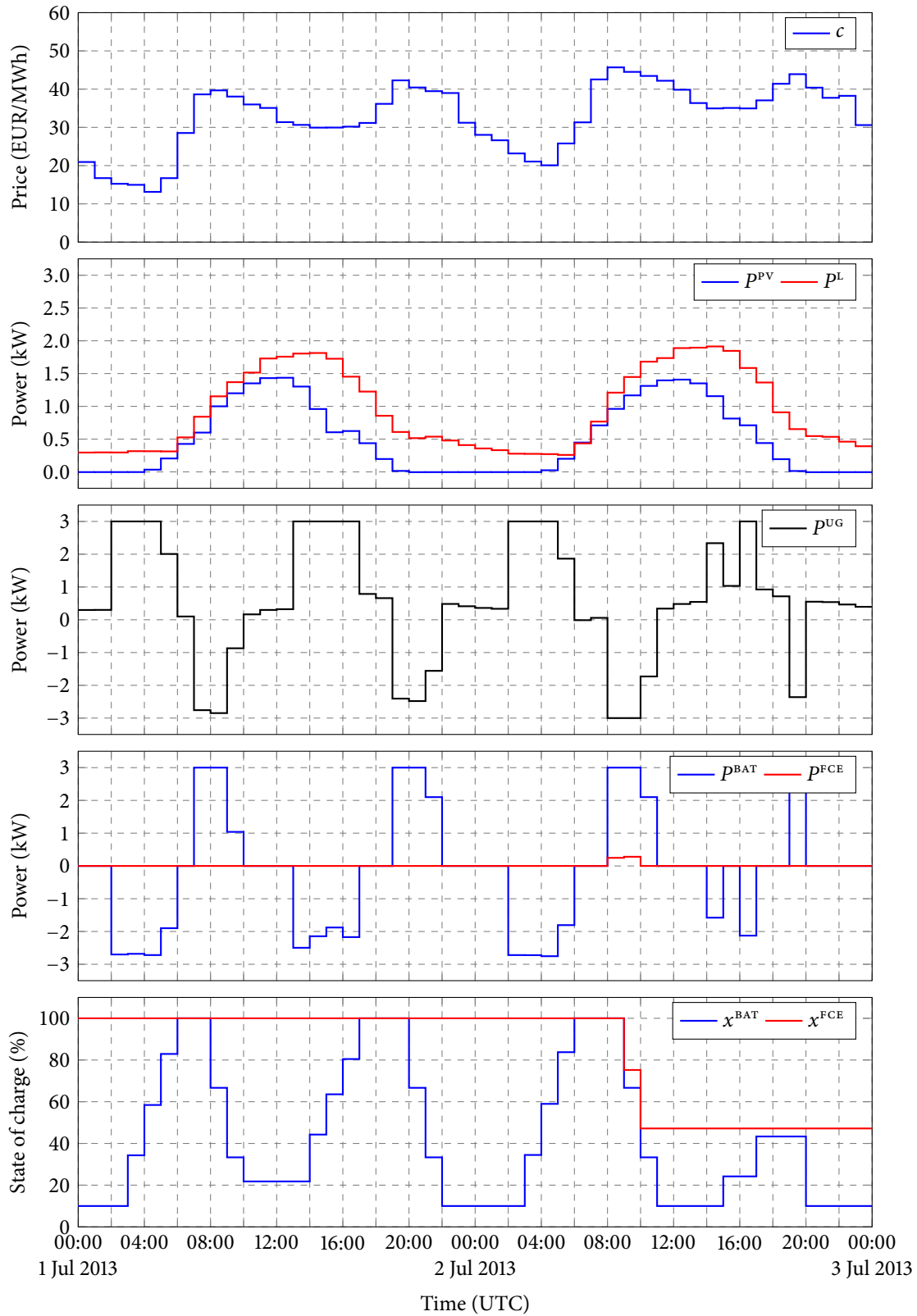


Figure 5.4: Profiles for closed-loop control simulation over 48-h exemplary period beginning on 1 Jul 2013 at 00:00, using MPC scheme with  $N = 24$  and  $p_{\text{pct}} = 90\%$ , ordered from top to bottom as follows: (i) electricity price  $c$ , (ii) power production by the PV system  $P^{PV}$  and consumption by microgrid loads  $P^L$ , (iii) power exchange with the utility grid  $P^{UG}$ , (iv) optimal control sequence, i.e., net power exchange with battery  $P^{BAT}$  and fuel-cell  $P^{FCE}$ , and (v) normalized state of charge of battery  $x^{BAT}$  and fuel-cell  $x^{FCE}$ .

## 5.4 Power flow management in stochastic framework

Power flow management in a stochastic framework can be implemented in many different ways, each having its pros and cons. In this section power flow management in deterministic framework developed in previous section is extended to include prediction uncertainty by means of chance constraints applied to the utility grid constraints.

### 5.4.1 Objective function

To account for power prediction uncertainty, the economic criterion in Eq. (5.10) is redefined via expectation operator  $\mathbb{E}[\cdot]$  as follows:

$$J(\mathbf{u}, x_0, \mathbf{c}, \mathbf{v}) = \mathbb{E} \left[ \sum_{k=0}^{N-1} c_k P_k^{\text{UG}} \Delta T \right]. \quad (5.20)$$

It should be noted that the penalization of residual energy storage systems state  $\hat{c}_N \hat{x}_N$  is not considered here since it was shown by simulations that it does not have any effect on the revenue for longer prediction horizons. The disturbance is defined as:

$$\mathbf{v} = \bar{\mathbf{v}} + \tilde{\mathbf{v}}, \quad (5.21)$$

where  $\bar{\mathbf{v}}$  is the disturbance mean (expectation), and  $\tilde{\mathbf{v}}$  is the disturbance uncertainty which is assumed to follow the Gaussian distribution, i.e.,  $\tilde{\mathbf{v}} \sim \mathcal{N}(0, \sigma^2)$ . Since uncertainty  $\tilde{\mathbf{v}}$  is assumed to be white noise, i.e.,  $\mathbb{E}[\tilde{\mathbf{v}}] = 0$ , the prediction uncertainty does not affect the objective function in Eq. (5.20).

### 5.4.2 System constraints

All system constraints are the same as in the previous section, except for the utility grid constraints defined in Eq. (5.13b) with respect to power balance in Eq. (5.5), since that is the only place where stochastic disturbances enter the microgrid equations. The utility grid constraints are redefined via chance constraints, i.e., as a probability that the constraints on  $P_k^{\text{UG}}$  will not be violated at a certain time instant  $k$ , as follows:

$$\mathbf{prob}(S_i P_k^{\text{UG}} \leq s_i) \geq 1 - \alpha_i, \quad 0 < \alpha_i < 1, \quad \forall i, \quad (5.22)$$

where  $\mathbf{prob}(\cdot)$  is probability function,  $S_i$  and  $s_i$  are parameters that are defined with respect to Eqs. (5.2), (5.7b) and (5.13b), and  $\alpha_i$  is the user-defined probability level that the  $i$ -th constraint will be violated. In this way, the utility grid will compensate any error in realization of power production and consumption predictions. Note that the hard constraints can be approximated with chance constraints by setting the  $\alpha_i$  to a very small positive value.

In two-stage stochastic programming [121], the number of constraint violations is minimized in the objective function, without any real measure when will these violations occur. Also, there is no real measure in which amount the utility grid constraints will be violated, since stochastic variable  $\tilde{\mathbf{v}}$  is unbounded due to the definition of Gaussian distribution. This feature can be easily implemented in the objective function defined in Eq. (5.20) by redefining the electricity price not to be constant outside defined range, but to penalize any constraint violation with higher or lower electricity price for power exchange outside of the defined limits, imposed to the microgrid by the utility grid. However, this feature would not completely prevent the constraints violation, but it would rather keep the violation occurrence as rare as possible.

To solve the probability inequality (i.e., chance constraints) defined in Eq. (5.22), two mathematical rules were used: (i) rule for addition of independent variables that follow Gaussian distribution, and (ii) probability calculation via cumulative distribution function (cdf). If  $X$  and  $Y$  are two independent random processes with  $X \sim \mathcal{N}(\mu_X, \sigma_X^2)$  and  $Y \sim \mathcal{N}(\mu_Y, \sigma_Y^2)$ , then:

$$a_X X + a_Y Y \sim \mathcal{N}(a_X \mu_X + a_Y \mu_Y, a_X^2 \sigma_X^2 + a_Y^2 \sigma_Y^2), \quad (5.23a)$$

$$\mathbf{prob}(X \leq \lambda) \geq \xi \rightarrow \sigma_X \Phi^{-1}(\xi) \leq \lambda - \mu_X, \quad (5.23b)$$

where  $a_X, a_Y \in \mathbb{R}$  are real coefficients,  $\lambda \in \mathbb{R}$  is a scalar variable,  $\xi$  is a probability level, and  $\Phi(\cdot)$  is the standard Gaussian cumulative probability function. With respect to these rules, the chance constraints in Eq. (5.22) become:

$$\left\| S_i V \odot \sigma_k \right\|_2 \Phi^{-1}(1 - \alpha_i) \leq s_i - S_i (D u_k + V \tilde{v}_k), \quad (5.24)$$

where  $\sigma = [\sigma^{pv}, \sigma^l]^\top$  is the vector with deviations of random variables in  $\tilde{v}_k$ , and  $\odot$  is the operator for element-wise multiplication.

#### 5.4.3 LP formulation

Once objective function and constraints have been defined, the power flow optimization problem in LP form can be written as follows:

$$\begin{aligned} \min_{\mathbf{u}} \quad & \mathbf{f}^\top \mathbf{u} + \text{const.}, \\ \text{s.t.} \quad & \mathbf{I}_x x_0 + \mathbf{I}_u \mathbf{u} + \mathbf{I}_v \tilde{\mathbf{v}} \leq \mathbf{g}, \end{aligned} \quad (5.25)$$

where constant, vectors  $\mathbf{f}$  and  $\mathbf{g}$ , and matrices  $\mathbf{I}_x$ ,  $\mathbf{I}_u$ , and  $\mathbf{I}_v$  are calculated from Eqs. (5.7), (5.12), (5.13a), and (5.24), while  $\mathbf{u}$  and  $\tilde{\mathbf{v}}$  are augmented vectors defined in Eq. (5.9).

#### 5.4.4 Closed-loop control

To assess the performance of the proposed approach for microgrid control in the stochastic framework, the following two closed-loop control schemes are considered: (i) deterministic MPC using only prediction mean and by neglecting uncertainty, as defined in Eq. (5.17), denoted as *certainty equivalence*, and (ii) stochastic MPC that includes prediction uncertainty, denoted as *SMPC*. Uncertainty description in the latter control scheme is utilized via chance constraints that are defined only for the utility grid in Eq. (5.24).

The stochastic MPC scheme, with respect to the real system dynamics defined in Eq. (5.16), is defined as follows:

$$\begin{aligned} \mathbf{u}^* = \arg \min_{\mathbf{u}} \quad & J(\mathbf{u}, x_0, \mathbf{c}, \mathbf{v}), \\ \text{s.t.} \quad & (5.12), (5.13a), (5.24), \end{aligned} \quad (5.26)$$

where  $J$  is the objective function defined in Eq. (5.20), which is a linear function in  $\mathbf{u}$ . According to the receding horizon principle, only the first control vector  $u_0^*$  from the optimal augmented control sequence  $\mathbf{u}^*$  is applied, i.e.,  $u(t) = u_0^*$ . The optimization problem, deterministic in Eq. (5.17) or stochastic in Eq. (5.26), is repeated again at the next time instant, with new initial energy storage systems state, electricity price and stochastic disturbance sequences. By this approach, new optimal control plan can potentially compensate any disturbance that has meanwhile acted on the system, which is especially important when using uncertain predictions as inputs to control algorithm.

### 5.4.5 Simulation results

Performance of the proposed approach is verified on two-month simulations based on actual meteorological, electricity price and consumption data for period from 1 Aug 2014 to 30 Sep 2014. Numerical values for all microgrid parameters is given in Table 5.1. The stochastic MPC-based closed-loop control scheme with receding horizon principle is employed with  $N = 24$  and different probability level  $\alpha$  which is taken to be constant over the prediction horizon.

Optimal control sequences obtained by certainty equivalence and SMPC are calculated on production and consumption predictions without or with taking into account prediction uncertainty, respectively, whereas evaluation is done on actual measurements. Performance indicators for the considered two-month period are shown in Table 5.3. It can be seen that by using SMPC, constraints violations can be managed by setting the probability level  $\alpha$ , i.e., for  $\alpha = 0$  SMPC operates in a robust control fashion (no constraints violations), while for  $\alpha = 0.5$  it behaves as certainty equivalence since disturbance is assumed to have symmetrical (Gaussian) distribution.

The utility grid constraints are mainly imposed to the microgrid due to (i) the contracted power rating between distribution system operator and the microgrid owner, and (ii) power rating limitations on the grid-tied bidirectional power converter. The former constraint is considered to be *soft* since it can be violated, but most probably with some penalization involved, and the latter constraint is *hard* due to the technical limitation of the power converter. Therefore, a more realistic scenario would be to include penalization of constraints violations in the objective function, which is a standard practice in power systems with big producers and consumers. In this scenario, SMPC allows more flexibility than certainty equivalence, since it enables a trade-off between constraints violations and total revenue achieved.

Figures 5.5 and 5.6 show profiles for closed-loop control simulation by using stochastic MPC scheme with receding horizon principle with 1-h sample time over 48-h exemplary period beginning on 6 Aug 2014 at 00:00, with prediction horizon length  $N = 24$  and with constraints violation probability level set to  $\alpha = 0.50$  and  $\alpha = 0.05$ : (i) electricity price profile, (ii) power production by the PV system and consumption by microgrid loads, (iii) power exchange with the utility grid, (iv) optimal control sequence, i.e., microgrid energy storage systems charge and discharge profiles, and (v) system state responses, i.e., microgrid energy storage systems state of charge. It should be noted that the power exchange with the utility grid is not a decision (control) variable, but is determined by the power balance in the microgrid defined in Eq. (5.2). Optimal control sequence and system states do not violate any constraints. As for the utility grid, constraints are violated at some time instants indicated by red arrows, which is more frequent as  $\alpha$  approaches  $\alpha = 0.50$ . The control algorithm uses fuel-cell system as little as possible compared to batteries stack, due to the much lower overall efficiency of the fuel-cell system. As for buying and selling electricity from the utility grid, microgrid is importing power from the utility grid mainly during lower electricity prices, while exporting power to the utility grid during higher electricity prices.

Table 5.3: Performance indicators for different closed-loop control schemes

Closed-loop control scheme	Violations (kWh)	Violations (number of)	Revenue (€)
Certainty equivalence	7.03	102	-0.05
SMPC with $\alpha = 0.05$	1.11	12	0.15
SMPC with $\alpha = 0.25$	3.42	24	0.03
SMPC with $\alpha = 0.50$	7.03	102	-0.05

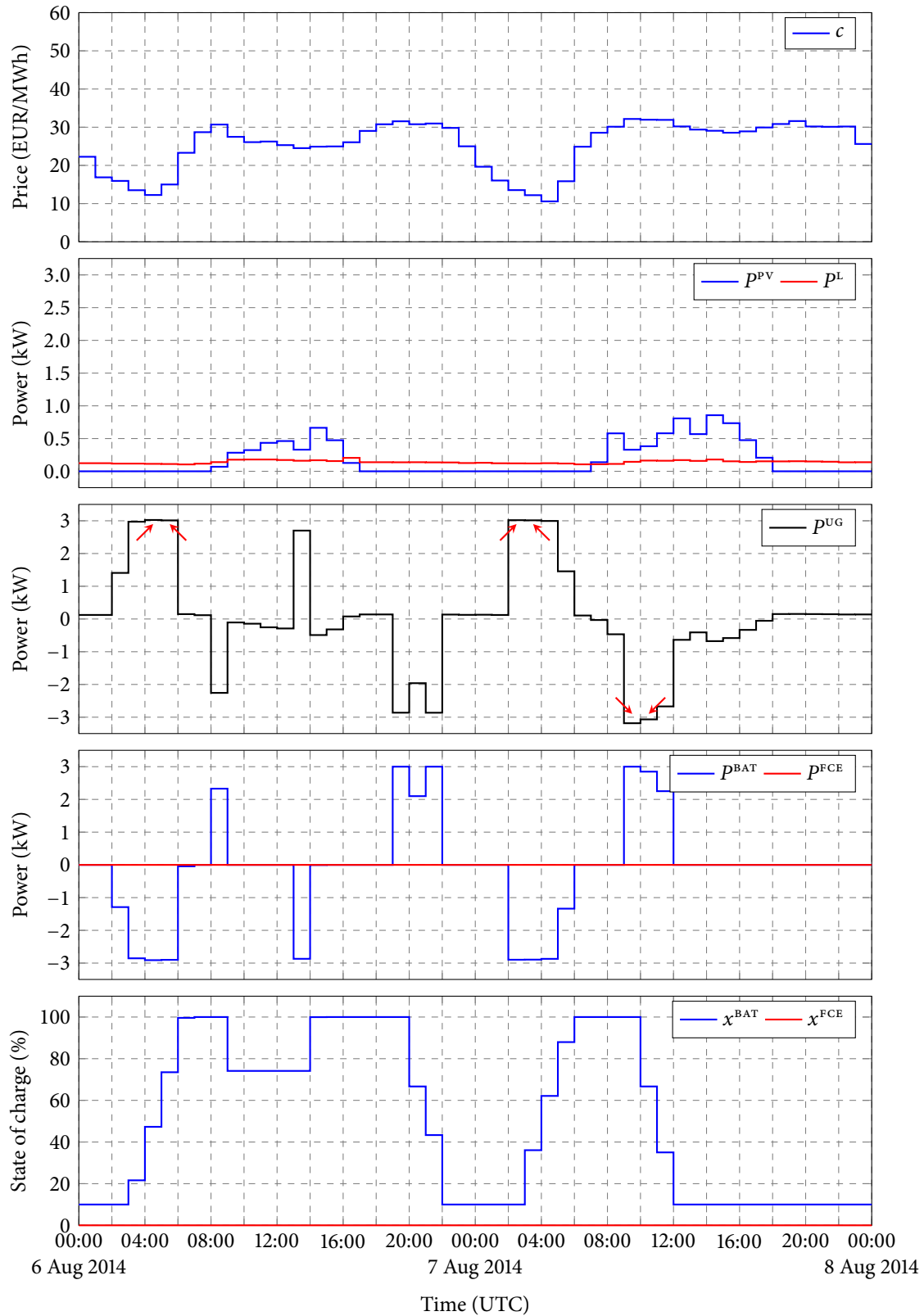


Figure 5.5: Profiles for closed-loop control simulation over 48-h exemplary period beginning on 6 Aug 2014 at 00:00, using SMPC scheme with  $N = 24$  and  $\alpha = 0.50$ , ordered from top to bottom as follows: (i) electricity price  $c$ , (ii) power production by the PV system  $P^{PV}$  and consumption by microgrid loads  $P^L$ , (iii) power exchange with the utility grid  $P^{UG}$ , (iv) optimal control sequence, i.e., net power exchange with battery  $P^{BAT}$  and fuel-cell  $P^{FCE}$ , and (v) normalized state of charge of battery  $x^{BAT}$  and fuel-cell  $x^{FCE}$ .



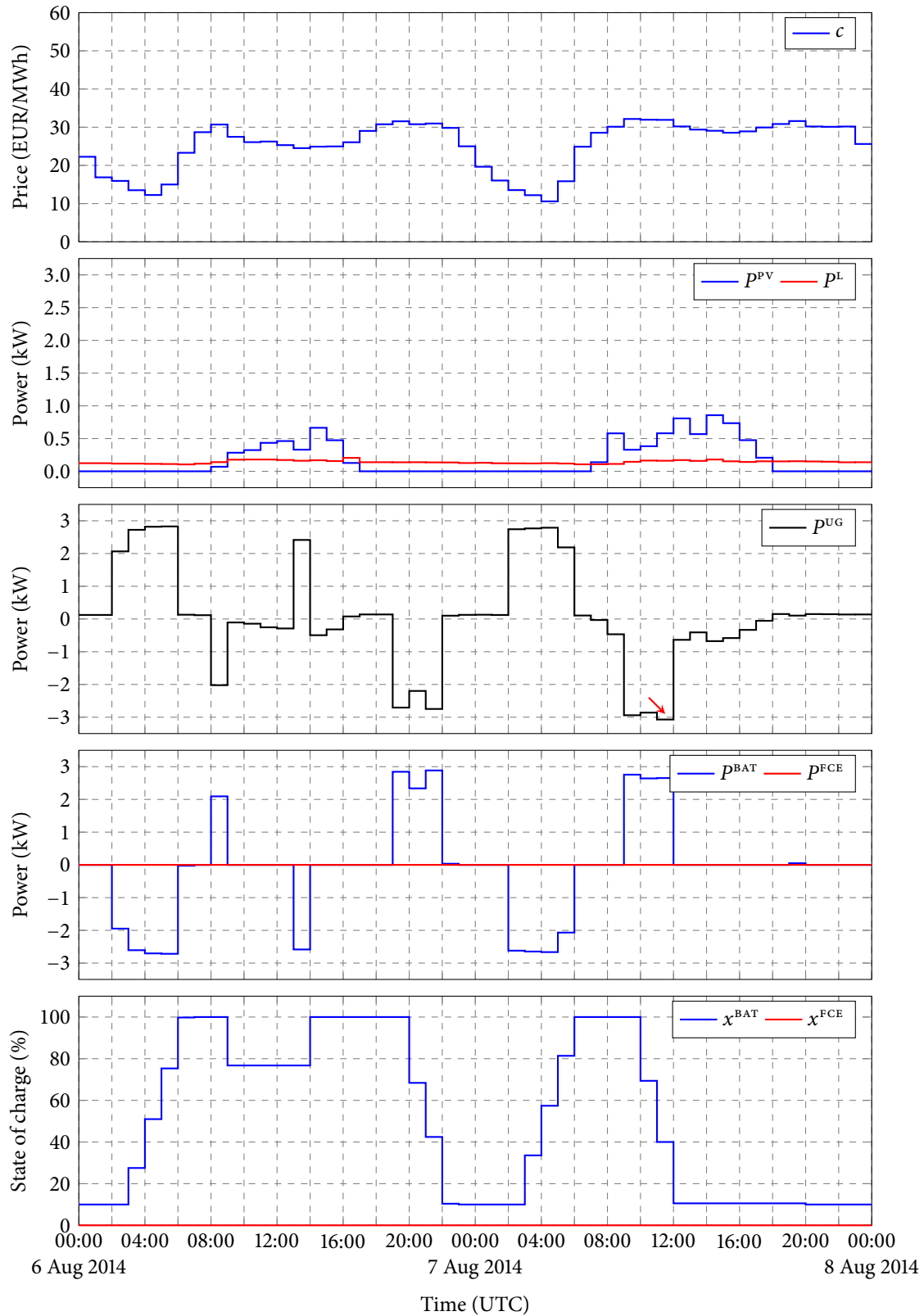


Figure 5.6: Profiles for closed-loop control simulation over 48-h exemplary period beginning on 6 Aug 2014 at 00:00, using SMPC scheme with  $N = 24$  and  $\alpha = 0.05$ , ordered from top to bottom as follows: (i) electricity price  $c$ , (ii) power production by the PV system  $P^{PV}$  and consumption by microgrid loads  $P^L$ , (iii) power exchange with the utility grid  $P^{UG}$ , (iv) optimal control sequence, i.e., net power exchange with battery  $P^{BAT}$  and fuel-cell  $P^{FCE}$ , and (v) normalized state of charge of battery  $x^{BAT}$  and fuel-cell  $x^{FCE}$ .

## 5.5 Multilevel optimal control in a building

In this section, a case-study on multilevel optimal control of a microgrid-supplied cooling system in a building is presented. Besides the DC microgrid formed in LARES, a cooling system based on a central chiller unit which operates over 23 controllable zones equipped with fan coil units is also considered. Performance of the proposed approach is verified through four-month simulations of the microgrid integrated with the building cooling system, in actual meteorological and electricity price data scenario for period from 1 Jun 2014 to 30 Sep 2014.

A decision of when to buy and sell power to the utility grid and in which amount, i.e., when to charge and discharge energy storage systems, is a complex function of the predicted microgrid load, power production (mainly by renewable energy sources), current energy storage systems state of charge, and of the predicted electricity price profile [41, 42, 121]. This function is also subject to various constraints like capacity of energy storage systems, possible reduced availability of the utility grid etc. Building's cooling system control problem is defined as a tracking problem with properly designed weighting matrices to ensure high level of comfort and minimal energy consumption at the same time. This approach is proved to outperform conventional zone controllers in terms of energy efficiency even in very strict comfort bounds of  $\pm 0.2$  °C around temperature set point [140]. The two described optimization problems can be formulated as a linear program.

These two separate control problems are integrated together by using the MPC scheme with receding horizon principle, such that the energy consumption plan obtained by solving the temperature tracking problem is passed to the microgrid power flow management problem. In this way, energy storage systems within the microgrid, together with the proposed multilevel optimal control method, fully exploit possibilities of dynamic pricing and greatly reduce cooling system operation costs while ensuring high level of user comfort. For simplicity, only microgrid control algorithm in deterministic framework is presented. For more details on the cooling system control see [43, 140].

### 5.5.1 Microgrid optimization problem

The power flow optimization problem introduced in Section 5.3 is modified as follows: (i) penalization of residual energy storage systems state  $\hat{c}_N \hat{x}_N$  is not considered, (ii) different electricity price is assumed when buying and selling electricity, (iii) utility grid power component is treated as a decision (control) variable with its buy and sell components, and (iv) only net disturbance, i.e., difference between production and consumption in the microgrid, is considered. With respect to this, the economic criterion in Eq. (5.10) is redefined as follows:

$$J(\mathbf{u}, x_0, \mathbf{c}, \bar{\mathbf{v}}) = \sum_{k=0}^{N-1} c_k P_{\text{buy},k}^{\text{UG}} \Delta T + (0.9c_k) P_{\text{sell},k}^{\text{UG}} \Delta T, \quad (5.27)$$

where the electricity price when selling is equal to 90% of the price when buying. The power balance in the microgrid defined in Eq. (5.2) is implemented in a form of an equality constraint, as follows:

$$\mathbf{1}^T u_k = \bar{v}_k, \quad \bar{v}_k = \bar{P}_k^L - \bar{P}_k^{\text{PV}}, \quad 0 \leq k \leq N-1, \quad (5.28)$$

where  $\mathbf{1} \in \mathbb{N}^6$  is the column-vector with all elements equal to 1,  $\bar{v}$  is the net disturbance mean in the microgrid, and  $u = [P_{\text{dch}}^{\text{BAT}}, P_{\text{dch}}^{\text{FCE}}, P_{\text{buy}}^{\text{UG}}, P_{\text{ch}}^{\text{BAT}}, P_{\text{ch}}^{\text{FCE}}, P_{\text{sell}}^{\text{UG}}]^T$  is the input variables vector, where  $P_{\text{sell}}^{\text{UG}} \leq 0$  and  $P_{\text{buy}}^{\text{UG}} \geq 0$ . The same reasoning applies to utility grid's buy and sell components as to storage systems' charge and discharge components, i.e., only buy or sell component is allowed to be different than zero at the same time, but not both of them, as that would imply economic losses due to different electricity prices when buying and selling.

Minimization of the criterion (5.27) is subject to various constraints on microgrid variables over the future horizon. Energy storage systems state  $x_k$  must always be inside the capacity limits:

$$x_{\min} \leq x_k \leq x_{\max}, \quad 1 \leq k \leq N, \quad (5.29)$$

where  $x_{\min}, x_{\max} \in \mathbb{R}^2$ . Limits on power components are defined by the corresponding power converter power rating, i.e., how much energy can they exchange within one time step, and also by their physical constraints, e.g.,  $P_{\text{ch}}^{\text{BAT}} \leq 0$  and  $P_{\text{dch}}^{\text{BAT}} \geq 0$ :

$$u_{\min} \leq u_k \leq u_{\max}, \quad 0 \leq k \leq N-1, \quad (5.30)$$

where  $u_{\min}, u_{\max} \in \mathbb{R}^6$ .

Once objective function and constraints have been defined, the power flow optimization problem in LP form can be written as follows:

$$\begin{aligned} \min_{\mathbf{u}} \quad & \mathbf{f}^T \mathbf{u}, \\ \text{s.t.} \quad & \mathbf{I}_x \mathbf{x}_0 + \mathbf{I}_u \mathbf{u} \leq \mathbf{g}, \\ & \mathbf{E}_u \mathbf{u} = \mathbf{E}_v \bar{\mathbf{v}}, \end{aligned} \quad (5.31)$$

where vectors  $\mathbf{f}$  and  $\mathbf{g}$ , and matrices  $\mathbf{I}_x$ ,  $\mathbf{I}_u$ ,  $\mathbf{E}_u$ , and  $\mathbf{E}_v$ , are calculated from Eqs. (5.27)–(5.30), while  $\mathbf{u}$  and  $\bar{\mathbf{v}}$  are augmented vectors defined in Eq. (5.9).

### 5.5.2 Closed-loop control

The deterministic MPC scheme with receding horizon principle, with respect to the real system dynamics defined in Eq. (5.16), is defined as follows:

$$\begin{aligned} \mathbf{u}^* = \arg \min_{\mathbf{u}} \quad & J(\mathbf{u}, \mathbf{x}_0, \mathbf{c}, \bar{\mathbf{v}}), \\ \text{s.t.} \quad & (5.28), (5.29), (5.30), \end{aligned} \quad (5.32)$$

where  $J$  is the objective function defined in Eq. (5.27), which is a linear function in  $\mathbf{u}$ .

### 5.5.3 Simulation results

Performance of the proposed optimal control algorithm is verified on four-month simulations based on actual meteorological and electricity price data, for period from 1 Jun 2014 to 30 Sep 2014. Historical meteorological data are provided by Meteorological and Hydrological Service (DHMZ), Croatia, from which power production by PV array is calculated. The deterministic MPC-based closed-loop control scheme with receding horizon principle is employed with  $N = 24$ , where microgrid consumption data is obtained by solving the temperature tracking problem [43]. Building operates in two working modes: (i) the daily mode (from 06:00 to 18:00) during which temperature requirements of end-users are set to 24 °C, and (ii) the night mode (from 18:00 to 06:00) during which cooling is unavailable. Allowed temperature deviations from the set-point  $\Delta$  are chosen to be  $\pm 0.2$  °C,  $\pm 0.5$  °C, and  $\pm 0.7$  °C, which corresponds to limits of cyclic temperature variations of A, B and C classes of the thermal environment defined by the ISO 7730 standard [141].

Revenue, i.e., economic gain, at the end of the four-month period can be calculated as:

$$c_{\text{rev}} = \sum_{t=0}^{2927} c(t) P_{\text{buy}}^{\text{UG}}(t) \Delta T + (0.9c(t)) P_{\text{sell}}^{\text{UG}}(t) \Delta T, \quad (5.33)$$

where  $c(t)$  is the electricity price, and 2928 is the total number of hours in the considered time period. In other words, revenue at the time instant  $t$  is defined as a difference between electricity demand and imported electricity from the utility grid, multiplied by the respective electricity price. In order to be able to evaluate impact of energy storage systems on the revenue, revenue for the case when there are no energy storage systems involved is also calculated as:

$$\hat{c}_{\text{rev}} = \sum_{t=0}^{2927} c(t) \max\{0, \bar{v}(t)\} + (0.9c(t)) \min\{0, \bar{v}(t)\}, \quad (5.34)$$

where  $\bar{v}$  is the difference between production and consumption in the microgrid, defined in Eq. (5.28).

Figure 5.7 shows operating costs of the microgrid and the electricity exchanged between the microgrid and the utility grid at the end of the considered four-month period, for the three considered values of  $\Delta$ . It is shown that microgrid operating costs are significantly lower when using energy storage systems with the proposed multilevel control. However, total exchanged electricity is higher when energy storage systems are involved, since storage systems are used for electricity trading (buy when price is low, sell when price is high), and although economic gain is higher due to the optimal microgrid control, some electricity is lost on charging and discharging due to storage efficiency.

Figure 5.8 shows profiles for closed-loop control simulation by using deterministic MPC scheme with receding horizon principle with 1-h sample time over 48-h exemplary period beginning on 6 Jul 2014 at 00:00, with prediction horizon length  $N = 24$  and with microgrid consumption data obtained by solving the temperature tracking problem [140]. Meteorological profiles over the considered 48-h exemplary period are shown in Fig. 5.9. It is shown that the microgrid control algorithm uses fuel-cell system as little as possible compared to batteries stack, due to much lower overall efficiency, i.e., fuel-cell system is used only when the difference between the maximum and minimum electricity prices along the prediction horizon is large enough, so that electricity loss is justified by economic gain. Similar logic is applied to batteries, i.e., they are charged during night-hours when electricity price is low, and are discharged during the daylight when electricity price is high. In this way, energy storage systems in the microgrid make it act as energy buffer and energy cost reducer between dynamic profiles of the cooling system electricity consumption and variable electricity prices. This is especially important considering integration of renewable energy systems, since their electricity production is highly variable (intermittent) due to the strong dependence on atmospheric conditions.

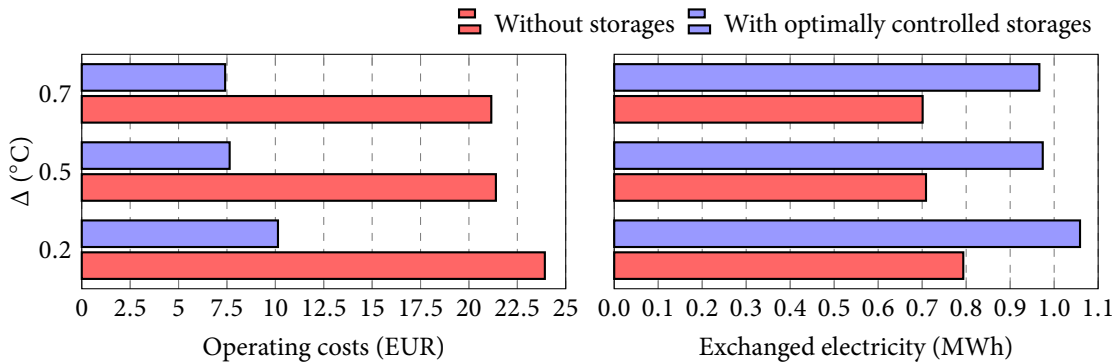


Figure 5.7: Microgrid operating costs and total electricity exchanged with the utility grid at the end of the four-month period, for the three considered values of  $\Delta$  ( $\pm 0.2$  °C,  $\pm 0.5$  °C, and  $\pm 0.7$  °C), and two microgrid scenarios (without and with energy storage systems). Positive cost denotes charge imposed to the microgrid, while positive energy denotes imported electricity from the utility grid.

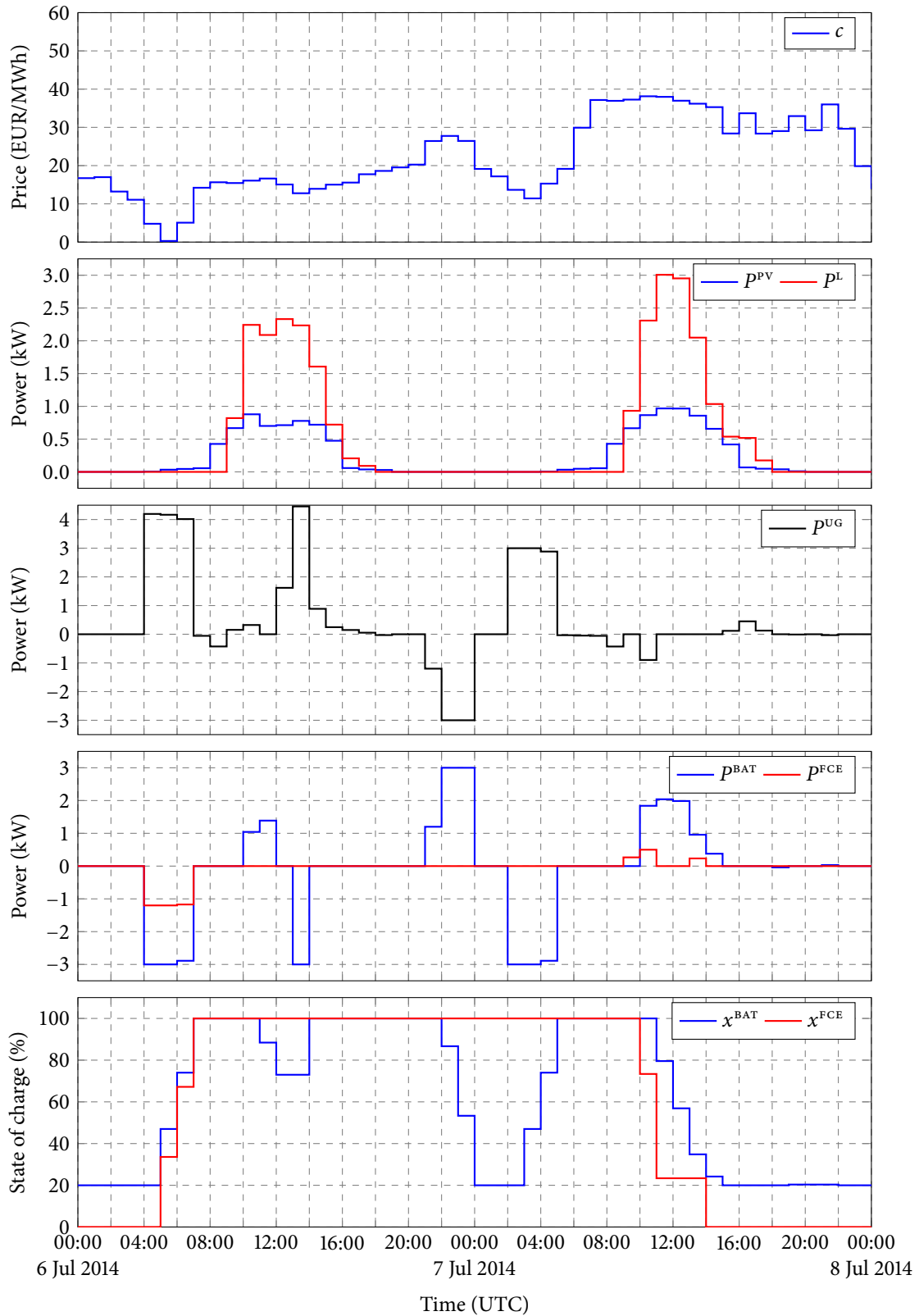


Figure 5.8: Profiles for closed-loop control simulation over 48-h exemplary period beginning on 6 Jul 2014 at 00:00, using MPC scheme with  $N = 24$ , ordered from top to bottom as follows: (i) electricity price  $c$ , (ii) power production by the PV system  $P^{PV}$  and consumption by the cooling system  $P^L$  for  $\Delta = 0.2$  °C and  $\eta = 1$ , (iii) power exchange with the utility grid  $P^{UG}$ , (iv) optimal control sequence, i.e., net power exchange with battery  $P^{BAT}$  and fuel-cell  $P^{FCE}$ , and (v) normalized state of charge of battery  $x^{BAT}$  and fuel-cell  $x^{FCE}$ .

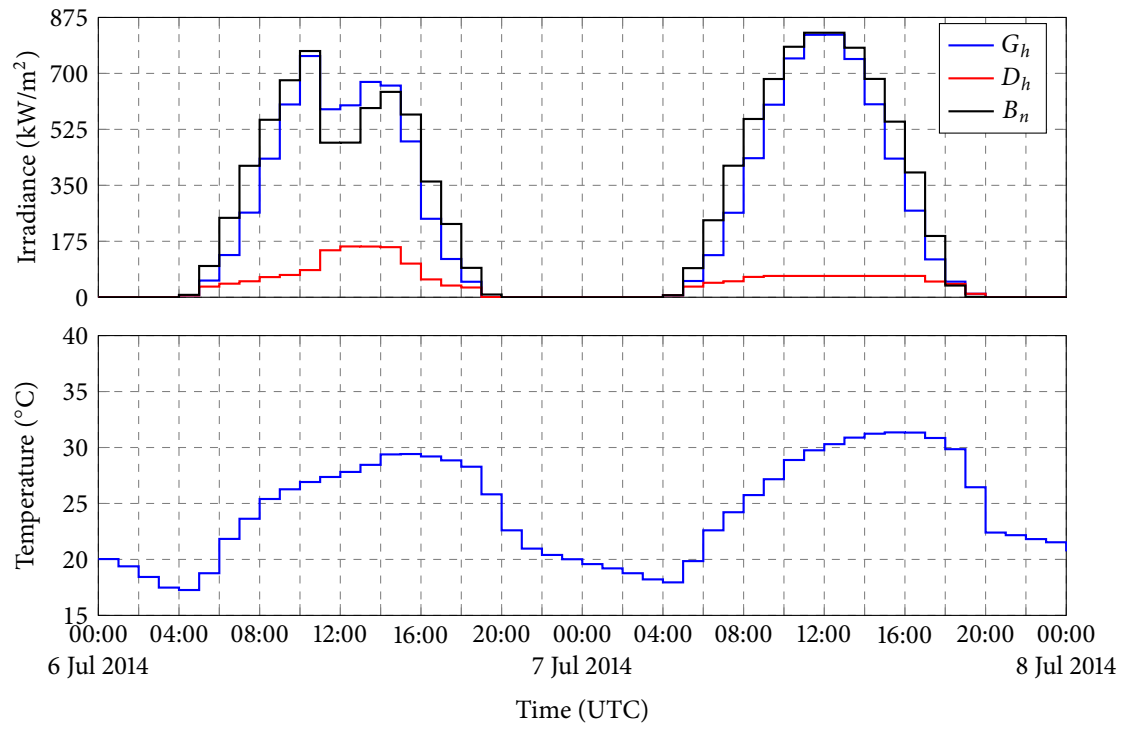


Figure 5.9: Meteorological profiles over 48-h exemplary period beginning on 6 Aug 2014 at 00:00, ordered from top to bottom as follows: (i) global horizontal  $G_h$ , diffuse horizontal  $D_h$ , and direct normal  $B_n$  solar irradiance components, and (ii) outside air temperature.

## 6.1 Introduction

Voltage stability in a microgrid is of great importance considering strict requirements imposed by modern-world electronic devices. There are two main philosophies for microgrid's power link voltage control, namely distributed and centralized [44]. In distributed voltage control configuration, all sources and storage systems in the microgrid contribute to the voltage control by means of a virtual impedance introduced in their control loop feedback, more commonly known as a droop control method [142–144]. However, in this scenario it is difficult to implement power profiles obtained by the power flow management algorithm on the level of a single microgrid energy storage unit, as all sources and storage systems participate in voltage control with respect to droop coefficients. This is especially important considering that key components in residential microgrids are renewable energy systems, e.g., photovoltaic (PV) arrays, which in distributed control configuration have to cut-down their power output just to be able to participate in voltage control. In centralized voltage control configuration, one of the microgrid components (a master) controls the voltage level, while other components (slaves) can inject any current within technical limits of the microgrid. It should be noted that the master has to be able to both sink and source current in order to compensate for sudden voltage swell and sag, respectively, which is why the master is usually an energy storage system or the utility grid. In this chapter the centralized voltage control configuration is considered in which (i) an ultracapacitor controls the DC link voltage, (ii) power exchange with battery and utility grid is controlled with respect to optimal power flows obtained by the power flow management algorithm, (iii) PV array operates in the maximum power point tracking (MPPT) mode to deliver the maximum available power, and (iv) microgrid load is assumed to be unidirectional and uncontrollable.

The power flow references for battery and utility grid obtained by the power flow management algorithm with 1-h sample time, discussed in Chapter 5, achieve optimal microgrid techno-economic operation with respect to defined objective and system constraints, and to system current state and future stochastic disturbances such as power production by PV array and consumption by microgrid loads. Disturbances used by the power flow management algorithm are predicted with 1-h time resolution for one-day ahead, i.e., as averages within the hour period. However, disturbances realization can significantly deviate from their hour averages on a faster time scale which could lead to microgrid constraints violation if power flow references in 1-h domain are directly applied. For example, if ultracapacitor is set to control the DC link voltage and optimal 1-h-average power flow references are directly applied to battery and utility grid, due to relatively low ultracapacitor

---

Part of the research presented in this chapter is published in the following paper:

■ M. Gulin, M. Vašak, and T. Pavlović, "Dynamical Behaviour Analysis of a DC Microgrid in Distributed and Centralized Voltage Control Configurations," in *Proceedings of the 2014 IEEE 23rd International Symposium on Industrial Electronics, ISIE 2014*, pp. 2361–2366, Istanbul, Turkey, 2014.

capacity it could easily happen that the ultracapacitor gets fully charged or discharged depending on disturbances realization, in which case some other microgrid component has to take control of the DC link voltage. This leads to a complex microgrid control structure based on state machines and does not guarantee that microgrid will always operate in optimal way and within its technical constraints. In this chapter a power flow reference tracking control algorithm is developed which adjusts optimal 1-h-average power flow references for battery and utility grid on a much faster time scale, i.e., every 10 s, and makes sure that the microgrid operates within its constraints. The tracking algorithm is based on convex optimization and is formulated as a linear program (LP), and the model predictive control (MPC) scheme with receding horizon principle is employed for closed-loop control. An academic-free professional solver IBM ILOG CPLEX 12.6 was used to solve optimization problems, and YALMIP [135] was used for easier and faster control algorithm implementation.

This chapter is organized as follows. In Section 6.2 a dynamic model of the considered DC microgrid is given. In Section 6.3 a closed-loop power flow reference tracking control algorithm based on the model predictive control scheme is developed. Simulation results of the DC link voltage control based on real data are given in Section 6.4.

## 6.2 DC microgrid model

### 6.2.1 Power balance

The DC microgrid considered here consists of (i) PV array, (ii) battery, (iii) ultracapacitor, (iv) uncontrollable load, and (v) is connected to the utility grid via bidirectional power converter. Optimal power flows for battery and utility grid with 1-h sample time is obtained by the power flow management algorithm, while the PV array operates in MPPT mode to deliver the maximum available power. It should be noted that the ultracapacitor is not considered in the power flow management algorithm as its capacity is much lower compared to the battery capacity. Figure 6.1 shows a power balance diagram for the considered DC microgrid.

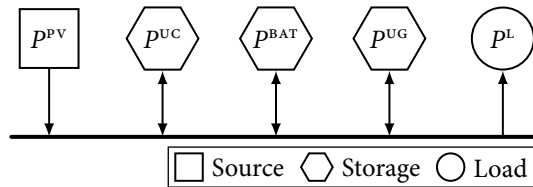


Figure 6.1: Power balance diagram in the considered DC microgrid.

The following power balance equation in the microgrid is always satisfied:

$$P^{PV} + P^{UC} + P^{BAT} + P^{UG} = P^L, \quad (6.1)$$

where  $P^{PV}$  is power production by the PV array,  $P^L$  is power consumption by microgrid loads, while  $P^{UC}$ ,  $P^{BAT}$ , and  $P^{UG}$  are net power exchange with ultracapacitor, battery, and utility grid. By convention used here, power components are positive when supplying power to the microgrid's DC link, e.g., power components  $P^{BAT}$  and  $P^{UC}$  will be negative for charging and positive for discharging from the energy-storage-system point of view, and power component  $P^{UG}$  will be negative for exporting (selling) and positive for importing (buying) power from the utility grid. Load is assumed always to be unidirectional, and due to the convention the power component  $P^L$  is always positive which is why it enters the power balance equation from the other side of the equality sign.



### 6.2.2 Dynamic system model

Energy storage systems are modeled by discrete-time first-order difference equations with 10-s sample time. The utility grid is treated here also as an energy storage system, for reasons that will be obvious once the objective function is defined. The dynamic system model is:

$$\begin{cases} x_{k+1}^{\text{BAT}} = x_k^{\text{BAT}} - P_k^{\text{BAT}} \Delta T, \\ x_{k+1}^{\text{UC}} = x_k^{\text{UC}} - P_k^{\text{UC}} \Delta T, \\ x_{k+1}^{\text{UG}} = x_k^{\text{UG}} - P_k^{\text{UG}} \Delta T, \end{cases} \quad (6.2)$$

where  $k$  is the discrete time instant,  $\Delta T = 10$  s is the sample time,  $P_k$  is the mean power within one time step starting at  $k\Delta T$ , and  $x_k$  is state of charge of a particular energy storage system at  $k\Delta T$ . Unlike the approach introduced in Section 5.2 based on power components decomposition to charge and discharge components, efficiency of energy storage systems is neglected here, i.e., it is assumed that storage systems are 100% efficient which will be discussed in more detail later.

The equality constraint in the microgrid follows from the power balance defined in Eq. (6.1):

$$P_k^{\text{UC}} = -(P_k^{\text{BAT}} + P_k^{\text{UG}}) - (P_k^{\text{PV}} - P_k^{\text{L}}), \quad (6.3)$$

where  $P^{\text{PV}}$  and  $P^{\text{L}}$  are prediction variables subject to unpredictable noise:

$$P_k^{\text{PV}} = \bar{P}_k^{\text{PV}} + \tilde{P}_k^{\text{PV}}, \quad P_k^{\text{L}} = \bar{P}_k^{\text{L}} + \tilde{P}_k^{\text{L}}, \quad (6.4)$$

where  $\bar{P}_k^{\text{PV}} = \mathbb{E}[P_k^{\text{PV}}]$  and  $\bar{P}_k^{\text{L}} = \mathbb{E}[P_k^{\text{L}}]$  are prediction expectation, while  $\tilde{P}_k^{\text{PV}}$  and  $\tilde{P}_k^{\text{L}}$  are prediction uncertainty, i.e., unpredictable noise. Considering that the DC link has a finite capacity, any deviation in the power balance due to unpredictable noise that acts on disturbances leads to voltage fluctuations. In centralized voltage control configuration it is expected that the ultracapacitor will compensate unpredictable power deviations, but without the power flow tracking algorithm it could happen that the ultracapacitor gets fully charged or discharged depending on disturbances realization, in which case it cannot control the DC link voltage anymore.

The microgrid equations (6.2) and (6.3) can be written in a matrix form as follows:

$$x_{k+1} = Ax_k + Bu_k + Vv_k, \quad (6.5)$$

where  $x = [x^{\text{BAT}}, x^{\text{UC}}, x^{\text{UG}}]^{\text{T}}$  is the system state vector,  $u = [P^{\text{BAT}}, P^{\text{UG}}]^{\text{T}}$  is the input variables vector,  $v = [P^{\text{PV}}, P^{\text{L}}]^{\text{T}}$  is the disturbance vector, and system matrices  $A$ ,  $B$ , and  $V$  are calculated with respect to Eqs. (6.2)–(6.4).

## 6.3 Tracking problem formulation

The power flow tracking optimization is formulated based on (i) current battery and ultracapacitor state of charge, (ii) current measurements of disturbances that act on the microgrid, i.e., power production by PV array and consumption by microgrid loads, (iii) optimal power flows for battery and utility grid with 1-h sample time obtained by the power flow management algorithm, and (iv) user-defined weighting coefficients that define the tracking algorithm strategy. Results of the power flow tracking optimization are modified power flows for battery and utility grid with 10-s sample time that ensure microgrid stability with respect to disturbances realization by keeping the ultracapacitor state of charge always at half of its usable capacity. The model predictive control scheme with receding horizon principle is used for closed-loop power flow reference tracking control.

### 6.3.1 Objective function

The power flow management algorithm that operates with 1-h sample time outputs optimal power flow references for battery and utility grid, on every full hour for the next 24 hours. The microgrid is simulated with 10-s sample time by using optimal power flows to generate state of charge trajectories of energy storage systems, as follows:

$$\begin{cases} \mathcal{X}_{j+1}^{\text{BAT}} = \mathcal{X}_j^{\text{BAT}} - \mathcal{P}_h^{\text{BAT}} \eta^{\text{BAT}} (\mathcal{P}_h^{\text{BAT}}) \Delta T, \\ \mathcal{X}_{j+1}^{\text{UG}} = \mathcal{X}_j^{\text{UG}} - \mathcal{P}_h^{\text{UG}} \eta^{\text{UG}} (\mathcal{P}_h^{\text{UG}}) \Delta T, \end{cases} \quad 0 \leq j \leq 8639, \quad (6.6)$$

where  $j$  is the discrete time instant,  $\Delta T = 10$  s is the sample time, 8640 is the total number of 10-s intervals within a day,  $h = \lfloor \frac{j}{360} \rfloor$  is the discrete time instant with 1-h sample time,  $\mathcal{X}$  is simulated state of charge of the energy storage system,  $\mathcal{P}$  are optimal power flows with 1-h sample time, and  $\eta(\cdot)$  is the efficiency function of the corresponding energy storage system. It should be noted that  $\mathcal{X}_0^{\text{UG}} = 0$  Wh and  $\eta^{\text{UG}} = 1$ , battery efficiency is  $\eta^{\text{BAT}} = 0.9$  for charging and  $\eta^{\text{BAT}} = \frac{1}{0.9}$  for discharging, while  $\mathcal{X}_0^{\text{BAT}}$  is equal to the current (estimated) battery state of charge, i.e.,  $\mathcal{X}_0^{\text{BAT}} = x_0^{\text{BAT}}$ .

The following power flow reference tracking criterion  $J$  of the microgrid operation is considered:

$$J(\mathbf{u}, x_0, \mathcal{X}, \nu_{-1}) = \sum_{k=0}^{N-1} \left( W^{\text{BAT}} |\delta_k^{\text{BAT}}| + W^{\text{UC}} |\delta_k^{\text{UC}}| + W^{\text{UG}} |\delta_k^{\text{UG}}| \right), \quad (6.7)$$

where  $N$  is the prediction horizon length,  $W$  are weighting coefficients whose ratio will determine which deviation will be penalized more,  $\nu_{-1}$  is the disturbance measurement,  $\mathbf{u}$  and  $\mathcal{X}$  are augmented input and state of charge trajectory vectors for the whole prediction horizon, and  $\delta_k$  is deviation from the optimal state of charge trajectory at the discrete time instant  $k$ , as follows:

$$\delta_k = \mathcal{X}_k - x_k, \quad (6.8)$$

where  $\mathcal{X}$  is the optimal state of charge trajectory, and  $x$  is state of charge of the energy storage system, evolution of which is defined in Eq. (6.5). Unlike in the power flow management algorithm, power production by PV array and consumption by microgrid loads are not predicted here, as it is difficult to predict such disturbances on a 10-s time scale. Disturbances are kept constant throughout the prediction horizon, i.e., they are set to measured values at the beginning of the prediction horizon  $\nu_{-1}$ . Target for the ultracapacitor state of charge  $\mathcal{X}^{\text{UC}}$  is set to half of its usable capacity, in which case the ultracapacitor is always ready to compensate power surplus and shortage in the microgrid. The only reason to treat the utility grid as an energy storage system is to be able to generate a trajectory for optimal power exchange between the microgrid and the utility grid with 10-s sample time.

In Section 5.2 it is proposed to decompose power components to charge and discharge components due to different efficiency when charging and discharging an energy storage system, in order to avoid binary variables in the microgrid model which would lead to a computationally expensive mixed integer linear program (MILP) formulation of the optimization problem. However, this works only in case when the objective function is defined to penalize charge and discharge power components of a single energy storage system being different than zero at the same time, which is true in case of economic-based criterion since charging and discharging at the same time implies power losses on storage efficiency. Considering the tracking criterion defined in Eq. (6.7), depending on the weighting coefficients and operating conditions, it could happen that optimization results in profiles that would tend to dissipate power by trying to charge and discharge the storage system at the same time, which is physically not possible. For that reason, storage system efficiency is not considered in the dynamic model defined in Eq. (6.2), whereas the alternative would be to introduce binary variables to the dynamic model. It is expected that the introduced microgrid model error does not affect optimization results at faster time scales, and is compensated in the closed-loop control.

### 6.3.2 System constraints

Minimization of the objective function defined in Eq. (6.7) is subject to various constraints on microgrid variables over the future horizon. These constraints can be either physical or designer-introduced in order to protect the system and prolong its life. Storage systems state  $x_k$  must always be inside capacity limits, while limits on power components  $u_k$  are defined by the corresponding power converter power rating, i.e., how much energy can they exchange within one time step:

$$x_{\min} \leq x_k \leq x_{\max}, \quad 1 \leq k \leq N, \quad (6.9a)$$

$$u_{\min} \leq u_k \leq u_{\max}, \quad 0 \leq k \leq N-1, \quad (6.9b)$$

where  $x_{\min}, x_{\max} \in \mathbb{R}^3$  and  $u_{\min}, u_{\max} \in \mathbb{R}^2$ .

### 6.3.3 LP formulation

Once objective function and constraints have been defined, the power flow reference tracking problem in LP form can be written as follows:

$$\begin{aligned} \min_{\mathbf{u}} \quad & \mathbf{f}^T \mathbf{u} + \text{const.}, \\ \text{s.t.} \quad & \mathbf{I}_x x_0 + \mathbf{I}_u \mathbf{u} + \mathbf{I}_v v_{-1} \leq \mathbf{g}, \end{aligned} \quad (6.10)$$

where constant, vectors  $\mathbf{f}$  and  $\mathbf{g}$ , and matrices  $\mathbf{I}_x$ ,  $\mathbf{I}_u$ , and  $\mathbf{I}_v$  are calculated from Eqs. (6.5)–(6.9).

### 6.3.4 Closed-loop control

The model predictive control (MPC) scheme [139] is used for closed-loop power flow reference tracking in the considered microgrid. Solution to the MPC problem yields a trajectory of states and inputs (i.e., control signals) that satisfy the dynamics and constraints of microgrid operation while optimizing some given criteria [62].

Let the real system dynamics be

$$x(t+1) = Ax(t) + Bu(t) + Vv(t). \quad (6.11)$$

At each discrete time instant  $t$ , i.e., every 10 s, the MPC scheme computes the optimal control sequence  $\mathbf{u}^*$  given initial energy storage systems state  $x_0 = x(t)$ , the disturbance measurements  $v_{-1} = v(t-1)$ , and state of charge trajectory  $\mathcal{X}$  calculated from optimal power flows  $\mathcal{P}$  obtained by the power flow management algorithm with respect to  $t$ , as defined in Eq. (6.6):

$$\begin{aligned} \mathbf{u}^* = \arg \min_{\mathbf{u}} \quad & J(\mathbf{u}, x_0, \mathcal{X}, v_{-1}), \\ \text{s.t.} \quad & (6.9), \end{aligned} \quad (6.12)$$

where  $J$  is the objective function defined in Eq. (6.7), which is a linear function in  $\mathbf{u}$ . According to the receding horizon principle, only the first control vector  $u_0^*$  from the optimal augmented control sequence  $\mathbf{u}^*$  is applied, i.e.,  $u(t) = u_0^*$ . Note that  $u_0^*$  contains control inputs only for the battery and utility grid, while the ultracapacitor controls the DC link voltage by compensating any deviation in the power balance due to unpredictable disturbances. The optimization problem in Eq. (6.12) is repeated again at the next time instant with new initial storage systems state, optimal state of charge trajectory, and disturbance measurements. By this approach, new optimal control plan can potentially compensate any disturbance that has meanwhile acted on the system.

## 6.4 Simulation results

In this section performance verification of the proposed power flow reference tracking control algorithm is presented. For the sake of simplicity the microgrid load is assumed to be constant throughout an hour period, whereas true (measured) PV array power production data from LARES for 9 Aug 2016 in 1-s time base shown in Fig. 6.2 is used for verification. The initial state of charge and optimal hour-based power flow profiles for battery and utility grid are carefully designed to generate a scenario that best shows effectiveness of the proposed approach. Numeric values of all microgrid parameters defined in this chapter are given in Table 6.1.

The weighting coefficients  $w$  in objective function defined in Eq. (6.7) are designed to penalize the ultracapacitor state of charge deviation the most. In this way, the power flow reference tracking control algorithm will prevent the ultracapacitor from participating in power flow management, and use it only to compensate fast stochastic changes in disturbances. Target for the ultracapacitor state of charge is constant throughout the prediction horizon, and is set to half of its usable capacity in order to keep the ultracapacitor always ready to compensate both power shortage and surplus, which addresses the stochastic nature of disturbances. Two different scenarios are considered for the battery and utility grid weighting coefficients: (i) battery state of charge deviation is penalized more than the utility grid deviation, and (ii) the utility grid deviation is penalized more than the battery deviation. The optimization algorithm will adapt the power flow reference with respect to disturbances realization for the system with smaller weighting coefficient. The prediction horizon length is designed with respect to ultracapacitor's capacity and power rating and is set to  $N = 6$  which corresponds to 60 s. During this time, starting at half of its usable capacity at the beginning of the prediction horizon, in worst case scenario the ultracapacitor reaches its capacity limits.

In the centralized voltage control configuration, the ultracapacitor controls the DC link voltage by compensating unpredictable power shortage or surplus due to disturbances realization, as follows:

$$P^{UC}(t) = -P^{BAT}(t) - P^{UG}(t) - P^{PV}(t) + P^L(t), \quad (6.13)$$

where  $P^{BAT}$  and  $P^{UG}$  are modified power flow references applied to battery and utility grid, obtained by solving the optimization problem in Eq. (6.12), while  $P^{PV}$  and  $P^L$  are PV array power production and microgrid consumption realization. It should be noted that if hour-average power flow references are directly applied to battery and utility grid, the ultracapacitor would soon be unable to control the DC link voltage as its capacity is not large enough to be able to compensate deviations in power production and consumption disturbances for too long. The ultracapacitor should only compensate fast stochastic changes and should not participate in the power flow management.

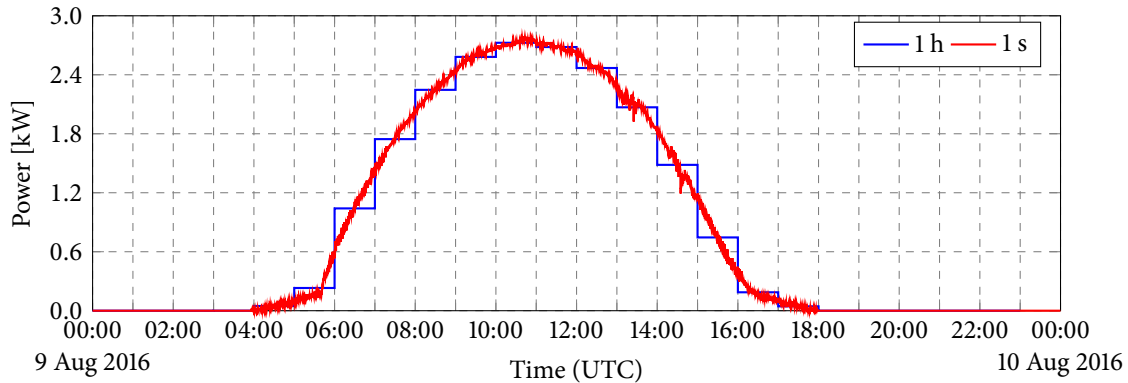


Figure 6.2: Power output of the PV array in LARES on 9 Aug 2016 in 1-h and 1-s time bases.

Table 6.1: Microgrid parameters used in simulation

$\eta_{\text{ch}}^{\text{BAT}}$	0.9	$\eta_{\text{dch}}^{\text{BAT}}$	0.9	Battery charge and discharge efficiency
$\eta_{\text{ch}}^{\text{UC}}$	1.0	$\eta_{\text{dch}}^{\text{UC}}$	1.0	Ultracapacitor charge and discharge efficiency
$\eta_{\text{ch}}^{\text{UG}}$	1.0	$\eta_{\text{dch}}^{\text{UG}}$	1.0	Utility grid charge and discharge efficiency
$x_{\text{min}}^{\text{BAT}}$	2000	$x_{\text{max}}^{\text{BAT}}$	10000	Battery state of charge limits (Wh)
$x_{\text{min}}^{\text{UC}}$	10	$x_{\text{max}}^{\text{UC}}$	100	Ultracapacitor state of charge limits (Wh)
$x_{\text{min}}^{\text{UG}}$	$-\infty$	$x_{\text{max}}^{\text{UG}}$	$\infty$	Utility grid state of charge limits (Wh)
$P_{\text{min}}^{\text{BAT}}$	-3.5	$P_{\text{max}}^{\text{BAT}}$	3.5	Battery power converter power limits (kW)
$P_{\text{min}}^{\text{UC}}$	-3.5	$P_{\text{max}}^{\text{UC}}$	3.5	Ultracapacitor power converter power limits (kW)
$P_{\text{min}}^{\text{UG}}$	-3.5	$P_{\text{max}}^{\text{UG}}$	3.5	Utility grid power converter power limits (kW)

Two characteristic hour periods are identified from the considered exemplary day shown in Fig. 6.2: (i) from 07:00 to 08:00, i.e., when true power production is lower than the hour-average at the beginning and higher at the end of the hour period, and (ii) from 14:00 to 15:00, i.e., when true power production is higher than the hour-average at the beginning and lower at the end of the hour period. The two characteristic hour periods combined with considered two different strategies to penalize state of charge deviations for battery and utility grid yield 4 simulation scenarios in total. Additional two simulation scenarios are built from the two considered hour periods for case when battery state of charge deviation is penalized the least and it operates near its physical limits. Profiles for closed-loop control simulation in 1-s time base for the considered 6 simulation scenarios are shown in Figs. 6.3–6.8, while numeric values of all control-related parameters are given in Table 6.2. Simulation results confirm the initial hypothesis, i.e., the power flow reference tracking control algorithm (i) adapts power flow reference for the system with lowest weighting coefficient value, (ii) ensures that the microgrid will always operate within its limits (see Figs. 6.5 and 6.8), and (iii) uses only the ultracapacitor to compensate fast stochastic disturbances, thus keeping the DC link voltage stable. It should be noted that in practical microgrid applications it might be beneficial to prefer that the utility grid helps with the power flow management (see Figs. 6.3 and 6.6), in order to avoid fast transitions between battery charge and discharge cycles, especially considering that deviations from the optimal state of charge trajectory for the utility grid within an hour do not impose any additional costs, as long as power exchange with the utility grid at the end of the hour period corresponds to the original plan agreed with the distribution system operator.

Table 6.2: Numeric values of control-related parameters for the considered simulation scenarios

Scenario	${}^1N$	${}^1W^{\text{UC}}$	${}^1W^{\text{BAT}}$	${}^1W^{\text{UG}}$	${}^2x^{\text{BAT}}$	${}^2x^{\text{UC}}$	${}^2x^{\text{UG}}$	${}^3P^{\text{PV}}$	${}^4P^{\text{L}}$	${}^5\mathcal{P}^{\text{BAT}}$	${}^5\mathcal{P}^{\text{UG}}$
Figure 6.3	6	20	15	10	8000	55	0	1745	1945	100	100
Figure 6.4	6	20	10	15	8000	55	0	1745	1945	100	100
Figure 6.5	6	20	10	15	2140	55	0	1745	1945	100	100
Figure 6.6	6	20	15	10	4000	55	0	1484	1284	-100	-100
Figure 6.7	6	20	10	15	4000	55	0	1484	1284	-100	-100
Figure 6.8	6	20	10	15	9880	55	0	1484	1284	-100	-100

<sup>1</sup> User-defined optimization parameters that define power flow reference tracking strategy<sup>2</sup> State of charge at the beginning of the hour period in Wh<sup>3</sup> Measured (true) PV array power production hour-average in W<sup>4</sup> Microgrid load in W, assumed to be constant throughout the hour period<sup>5</sup> Optimal battery and utility grid power flow references for the considered hour period in W

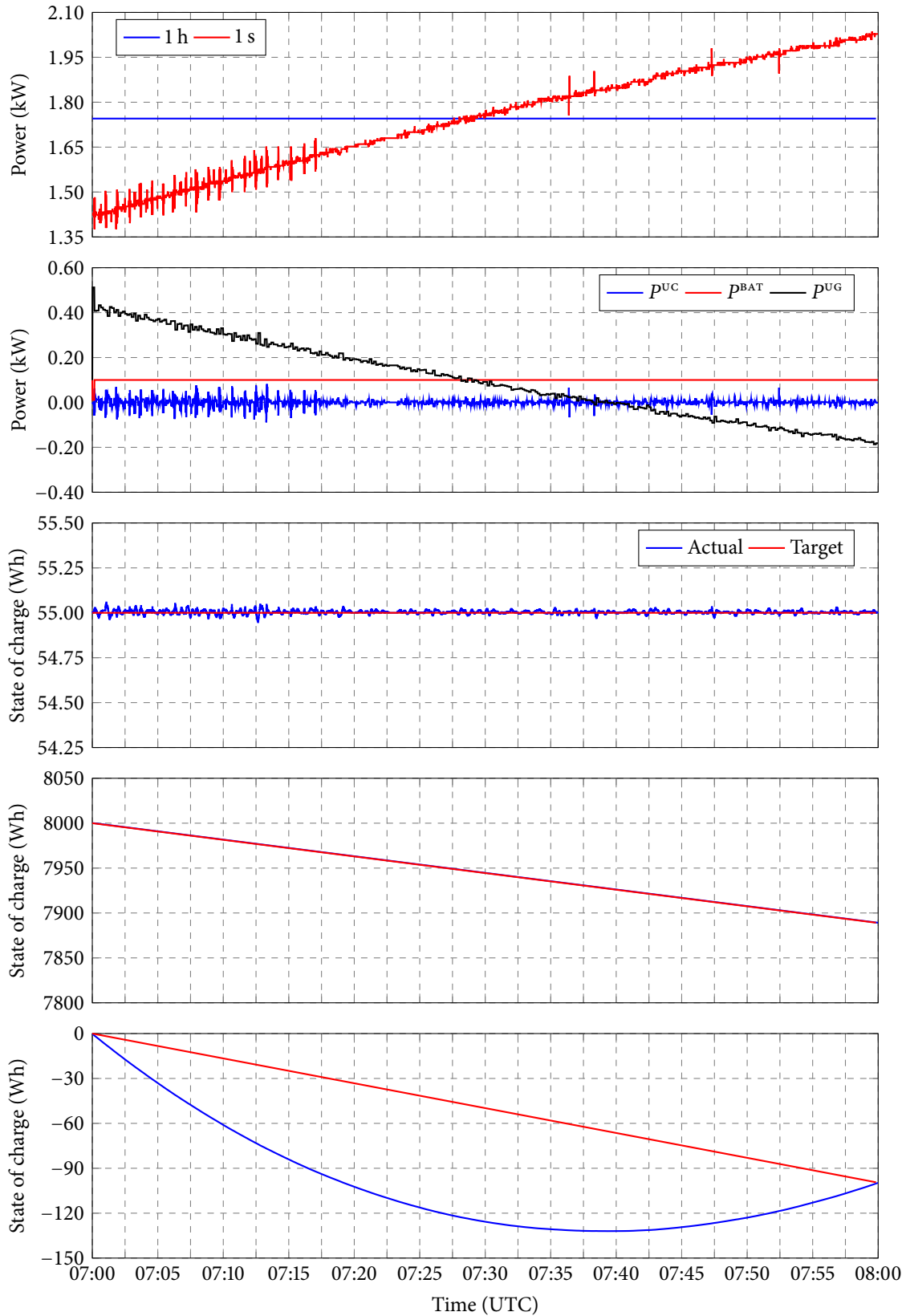


Figure 6.3: Profiles for closed-loop control simulation in 1-s time base over 1-h exemplary period beginning on 9 Aug 2016 at 07:00 for case when utility grid state of charge deviation is penalized the least. From top to bottom: (i) power output from the PV array in LARES, (ii) ultracapacitor, battery, and utility grid power components, (iii-v) ultracapacitor, battery, and utility grid state of charge.

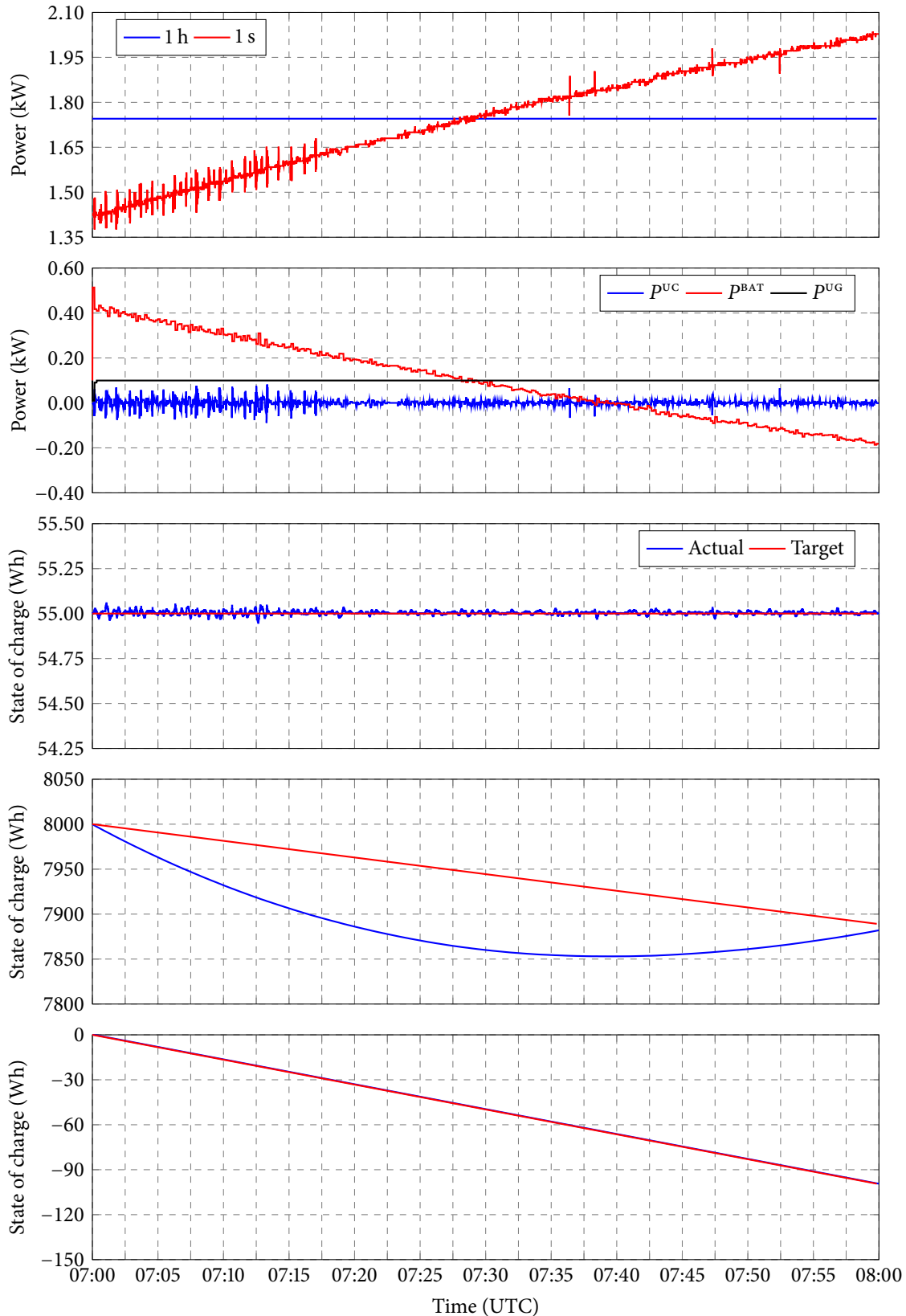


Figure 6.4: Profiles for closed-loop control simulation in 1-s time base over 1-h exemplary period beginning on 9 Aug 2016 at 07:00 for case when battery state of charge deviation is penalized the least. From top to bottom: (i) power output from the PV array in LARES, (ii) ultracapacitor, battery, and utility grid power components, (iii-v) ultracapacitor, battery, and utility grid state of charge.

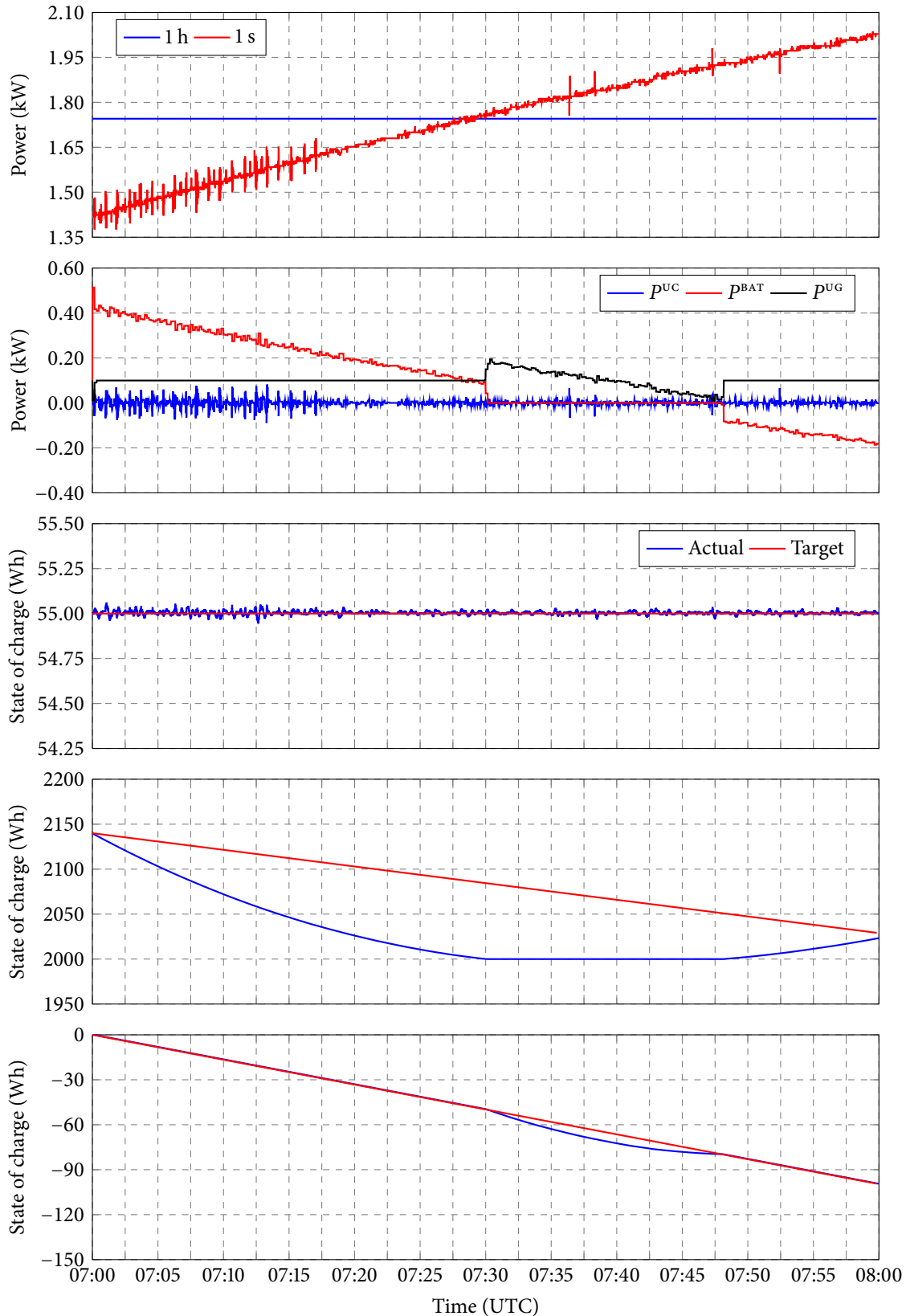


Figure 6.5: Profiles for closed-loop control simulation in 1-s time base over 1-h exemplary period beginning on 9 Aug 2016 at 07:00 for case when battery state of charge deviation is penalized the least and it operates near its physical limits. From top to bottom: (i) power output from the PV array in LARES, (ii) ultracapacitor, battery, and utility grid power components, (iii-v) ultracapacitor, battery, and utility grid state of charge.



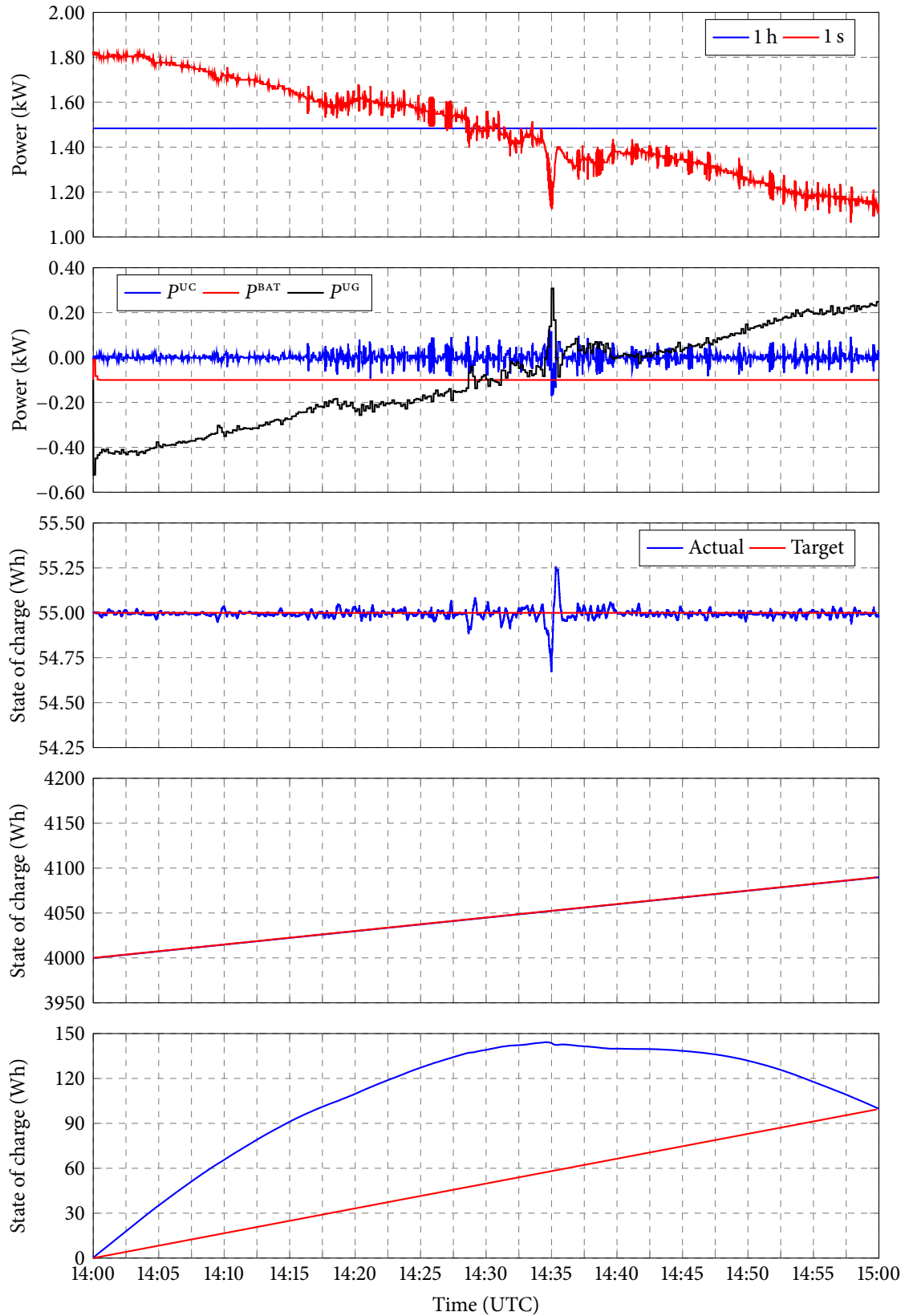


Figure 6.6: Profiles for closed-loop control simulation in 1-s time base over 1-h exemplary period beginning on 9 Aug 2016 at 14:00 for case when utility grid state of charge deviation is penalized the least. From top to bottom: (i) power output from the PV array in LARES, (ii) ultracapacitor, battery, and utility grid power components, (iii-v) ultracapacitor, battery, and utility grid state of charge.

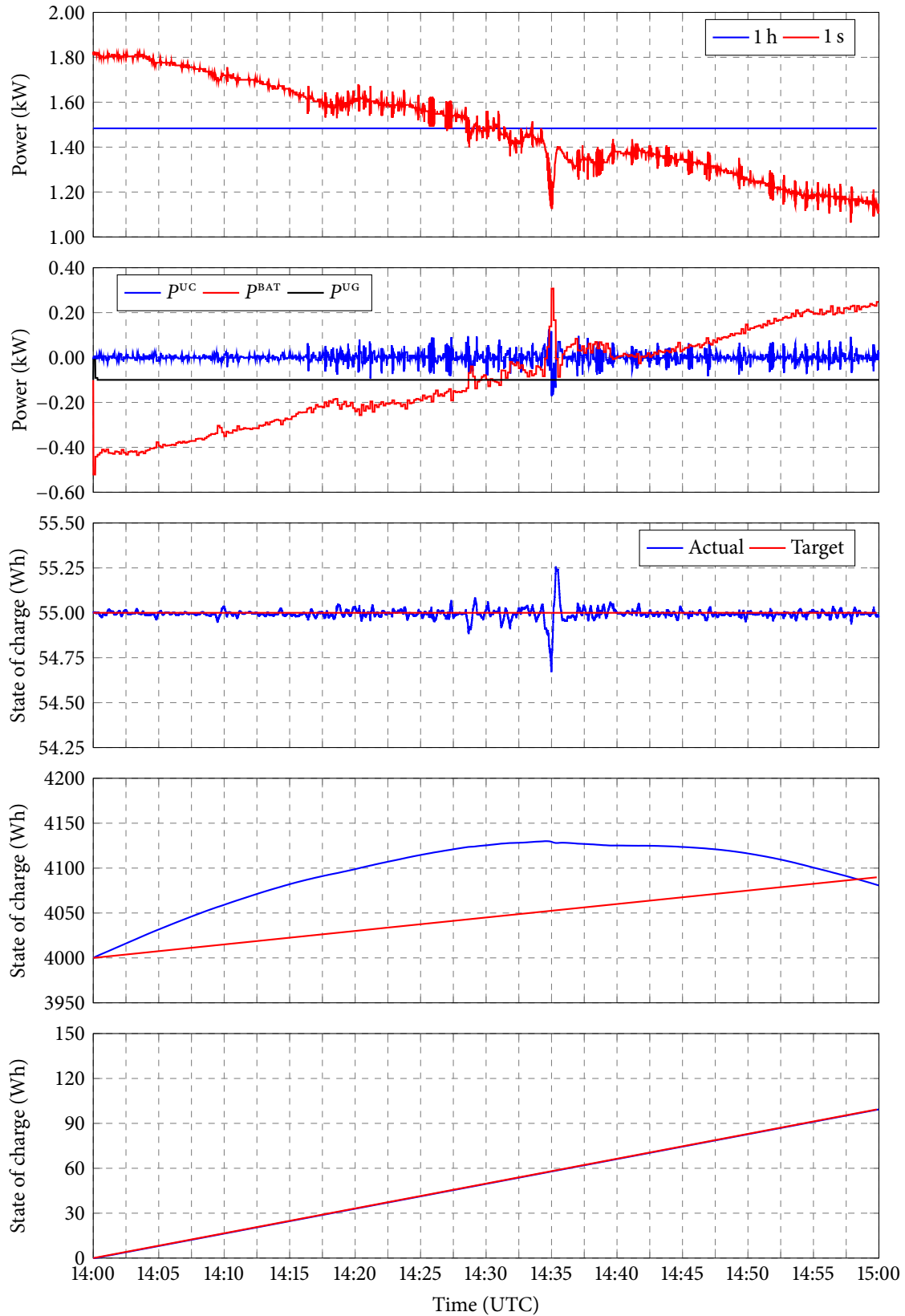


Figure 6.7: Profiles for closed-loop control simulation in 1-s time base over 1-h exemplary period beginning on 9 Aug 2016 at 14:00 for case when battery state of charge deviation is penalized the least. From top to bottom: (i) power output from the PV array in LARES, (ii) ultracapacitor, battery, and utility grid power components, (iii-v) ultracapacitor, battery, and utility grid state of charge.

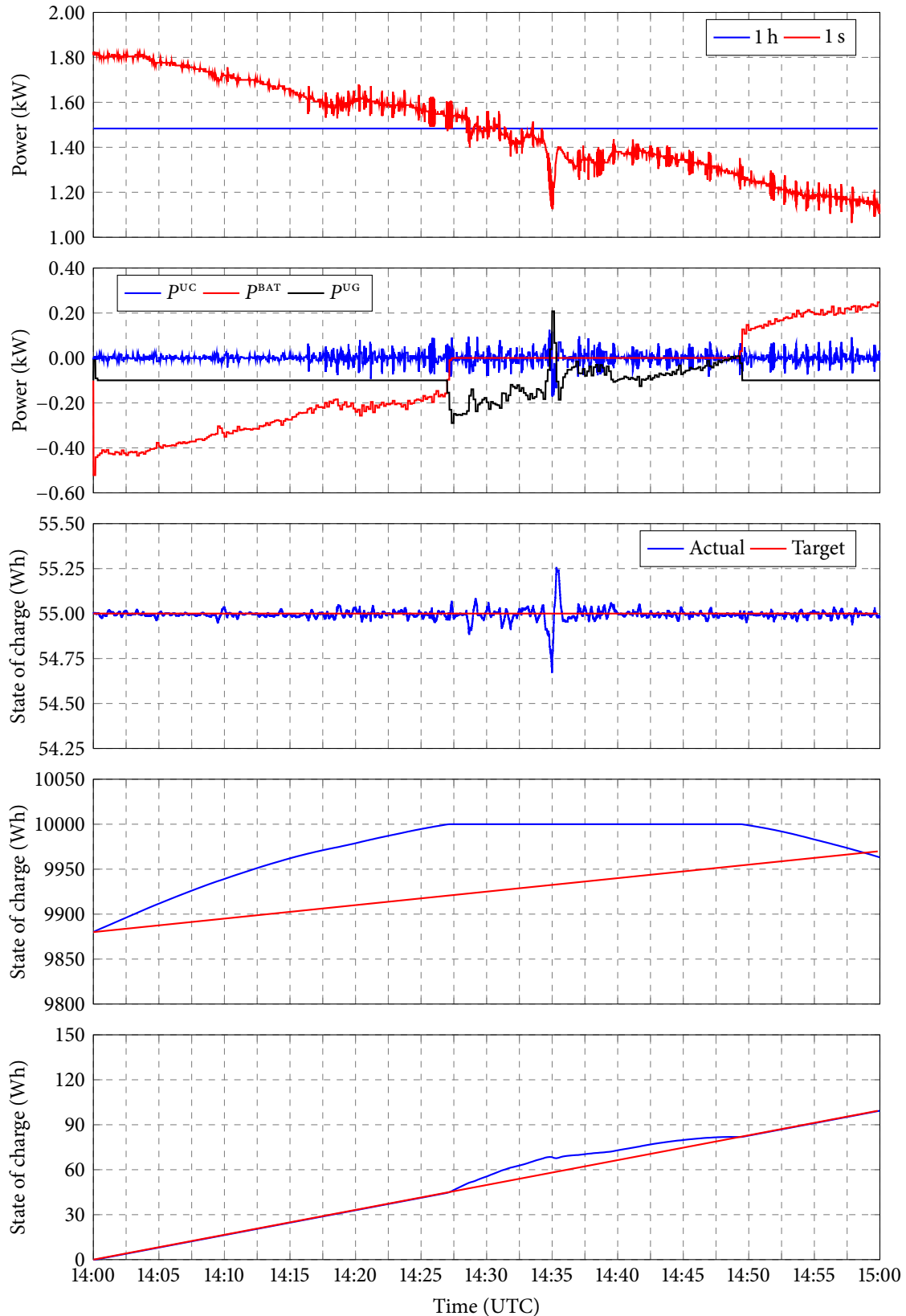


Figure 6.8: Profiles for closed-loop control simulation in 1-s time base over 1-h exemplary period beginning on 9 Aug 2016 at 14:00 for case when battery state of charge deviation is penalized the least and it operates near its physical limits. From top to bottom: (i) power output from the PV array in LARES, (ii) ultracapacitor, battery, and utility grid power components, (iii-v) ultracapacitor, battery, and utility grid state of charge.

---

## BIBLIOGRAPHY

- [1] M. Brower, *Cool Energy: Renewable Solutions to Environmental Problems*. The MIT Press, 1 ed., 1992.
- [2] J. M. Guerrero, F. Blaabjerg, T. Zhelev, K. Hemmes, E. Monmasson, S. Jemei, M. Comech, R. Granadino, and J. I. Frau, "Distributed Generation: Toward a New Energy Paradigm," *IEEE Industrial Electronics Magazine*, vol. 4, no. 1, pp. 52–64, 2010.
- [3] I. J. Perez-Arriaga, "The Transmission of the Future: The Impact of Distributed Energy Resources on the Network," *IEEE Power and Energy Magazine*, vol. 14, no. 4, pp. 41–53, 2016.
- [4] D. Bartz, ed., *Energy Atlas 2018: Facts and Figures about Renewables in Europe*. Heinrich Böll Foundation, 1 ed., 2018.
- [5] D. Manz, R. Walling, N. Miller, B. LaRose, R. D'Aquila, and B. Daryanian, "The Grid of the Future: Ten Trends That Will Shape the Grid Over the Next Decade," *IEEE Power & Energy Magazine*, vol. 12, no. 3, pp. 26–36, 2014.
- [6] P. Kundur, *Power System Stability and Control*. McGraw-Hill Education, 1 ed., 1994.
- [7] A. Ipakchi and F. Albuyeh, "Grid of the Future: We Are Ready to Transition to a Smart Grid?," *IEEE Power and Energy Magazine*, vol. 7, no. 2, pp. 52–62, 2009.
- [8] X. Yu, C. Cecati, T. Dillon, and M. G. Simoes, "The New Frontier of Smart Grids: An Industrial Electronics Perspective," *IEEE Industrial Electronics Magazine*, vol. 5, no. 3, pp. 49–63, 2011.
- [9] D. Stenclik, P. Denholm, and B. Chalamala, "Maintaining Balance: The Increasing Role of Energy Storage for Renewable Integration," *IEEE Power and Energy Magazine*, vol. 15, no. 6, pp. 31–39, 2017.
- [10] Z. Ma, A. Pesaran, V. Gevorgian, D. Gwinner, and W. Kramer, "Energy Storage, Renewable Power Generation, and the Grid," *IEEE Electrification Magazine*, vol. 3, no. 3, pp. 30–40, 2015.
- [11] A. Izadian, N. Girrens, and P. Khayyer, "Renewable Energy Policies: A Brief Review of the Latest U.S. and E.U. Policies," *IEEE Industrial Electronics Magazine*, vol. 7, no. 3, pp. 21–34, 2013.
- [12] G. Fulli, M. Masera, A. Spisto, and S. Vitiello, "A Change is Coming: How Regulation and Innovation Are Reshaping the European Union's Electricity Markets," *IEEE Power and Energy Magazine*, vol. 17, no. 1, pp. 53–66, 2019.
- [13] M. Ahlstrom, E. Ela, J. Riesz, J. O'Sullivan, B. F. Hobbs, M. O'Malley, M. Milligan, P. Sotkiewicz, and J. Caldwell, "The Evolution of the Market: Designing a Market for High Levels of Variable Generation," *IEEE Power and Energy Magazine*, vol. 13, no. 6, pp. 60–66, 2015.
- [14] "Energy Independence and Security Act of 2007." <https://www.govinfo.gov/content/pkg/PLAW-110publ140/html/PLAW-110publ140.htm>. Accessed: 2019-06-05.
- [15] H. Novak, *Coordinated multi-level model predictive control of energy in electric railway traction systems*. Phd thesis, University of Zagreb Faculty of Electrical Engineering and Computing, 2019.
- [16] B. Novoselnik, *Optimal coordinated and robust control of electrical power distribution system*. Phd thesis, University of Zagreb Faculty of Electrical Engineering and Computing, 2018.
- [17] N. Hure, *Set-theoretic control of a wind turbine*. Phd thesis, University of Zagreb Faculty of Electrical Engineering and Computing, 2017.

- [18] G. Kujundžić, *Estimation and predictive control of a battery in a microgrid*. Phd thesis, University of Zagreb Faculty of Electrical Engineering and Computing, 2017. In Croatian.
- [19] T. Hadjina, *Wind turbine grid side converter control under grid disturbances*. Phd thesis, University of Zagreb Faculty of Electrical Engineering and Computing, 2015. In Croatian.
- [20] V. Bobanac, *Linear Parameter Varying Control of Large Wind Turbines*. Phd thesis, University of Zagreb Faculty of Electrical Engineering and Computing, 2015. In Croatian.
- [21] V. Lešić, *Fault-tolerant control of a wind turbine subject to generator electromechanical faults*. Phd thesis, University of Zagreb Faculty of Electrical Engineering and Computing, 2014.
- [22] T. Pavlović, *Control of a DC-DC boost converter supplied by photovoltaic module for maximum power production*. Phd thesis, University of Zagreb Faculty of Electrical Engineering and Computing, 2014. In Croatian.
- [23] T. Dragičević, *Hierarchical control of a direct current microgrid with energy storage systems in a distributed topology*. Phd thesis, University of Zagreb Faculty of Electrical Engineering and Computing, 2013.
- [24] V. Petrović, *Wind turbine optimal control for reduction of structural loads in strong winds*. Phd thesis, University of Zagreb Faculty of Electrical Engineering and Computing, 2013.
- [25] V. Spudić, *Coordinated optimal control of wind farm active power*. Phd thesis, University of Zagreb Faculty of Electrical Engineering and Computing, 2012.
- [26] T. Bjažić, *Adaptive control of the DC/DC boost converter supplied by the fuel cell*. Phd thesis, University of Zagreb Faculty of Electrical Engineering and Computing, 2010. In Croatian.
- [27] M. Jelavić, *Wind turbine control for structural dynamic loads reduction*. Phd thesis, University of Zagreb Faculty of Electrical Engineering and Computing, 2009. In Croatian.
- [28] N. Hatziargyriou, H. Asano, R. Iravani, and C. Marnay, "Microgrids: An Overview of Ongoing Research, Development, and Demonstration Projects," *IEEE Power and Energy Magazine*, vol. 5, no. 4, pp. 78–94, 2007.
- [29] B. Kroposki, R. Lasseter, T. Ise, S. Morozumi, S. Papathanassiou, and N. Hatziargyriou, "Making Microgrids Work: A Look at Microgrid Technologies and Testing Projects from Around the World," *IEEE Power & Energy Magazine*, vol. 6, no. 3, pp. 40–53, 2008.
- [30] F. Farzan, S. Lahiri, M. Kleinberg, K. Gharieh, F. Farzan, and M. Jafari, "Microgrids for Fun and Profit: The Economics of Installation Investments and Operations," *IEEE Power & Energy Magazine*, vol. 11, no. 4, pp. 52–58, 2013.
- [31] C. Abbey, D. Cornforth, N. Hatziargyriou, A. Kwasinski, E. Kyriakides, G. Platt, L. Reyes, and S. Suryanarayanan, "Powering Through the Storm: Microgrids Operation for More Efficient Disaster Recovery," *IEEE Power & Energy Magazine*, vol. 12, no. 3, pp. 67–76, 2014.
- [32] G. Strbac, N. Hatziargyriou, J. P. Lopes, C. Moreira, A. Dimeas, and D. Papadaskalopoulos, "Microgrids: Enhancing the Resilience of the European Megagrid," *IEEE Power & Energy Magazine*, vol. 13, no. 3, pp. 35–43, 2015.
- [33] B. T. Patterson, "DC, Come Home: DC Microgrids and the Birth of the "Enernet"," *IEEE Power & Energy Magazine*, vol. 10, no. 6, pp. 60–69, 2012.
- [34] G. AlLee and W. Tschudi, "Edison Redux: 380 Vdc Brings Reliability and Efficiency to Sustainable Data Centers," *IEEE Power & Energy Magazine*, vol. 10, no. 6, pp. 50–59, 2012.
- [35] R. Majumder, C. Bartzsch, P. Kohnstam, E. Fullerton, A. Finn, and W. Galli, "Magic Bus: High-Voltage DC on the New Power Transmission Highway," *IEEE Power & Energy Magazine*, vol. 10, no. 6, pp. 39–49, 2012.
- [36] P. Lundberg, M. Callavik, M. Bahrman, and P. Sandeberg, "Platforms for Change: High-Voltage DC Converters and Cable Technologies for Offshore Renewable Integration and DC Grid Expansions," *IEEE Power & Energy Magazine*, vol. 10, no. 6, pp. 30–38, 2012.

- [37] “Micro-Grid infographic.” <https://www.mckibillo.com/fast-company-micro-grids>. Accessed: 2019-06-05.
- [38] F. Katiraei, R. Iravani, N. Hatziargyriou, and A. Dimeas, “Microgrids Management: Controls and Operation Aspects of Microgrids,” *IEEE Power & Energy Magazine*, vol. 6, no. 3, pp. 54–65, 2008.
- [39] J. C. Vasquez, J. M. Guerrero, J. Miret, M. Castilla, and L. G. De Vicuña, “Hierarchical Control of Intelligent Microgrids: Integration of Distributed Energy Resources into the Smart Grid,” *IEEE Industrial Electronics Magazine*, vol. 4, no. 4, pp. 23–29, 2010.
- [40] T. L. Vandoorn, J. D. M. De Kooning, B. Meersman, J. M. Guerrero, and L. Vandeveldel, “Voltage-Based Control of a Smart Transformer in a Microgrid,” *IEEE Transactions on Industrial Electronics*, vol. 60, no. 4, pp. 1291–1305, 2013.
- [41] M. Gulin, M. Vašak, and M. Baotić, “Analysis of Microgrid Power Flow Optimization with Consideration of Residual Storages State,” in *Proceedings of the 2015 European Control Conference, ECC 2015*, (Linz, Austria), pp. 3126–3131, 2015.
- [42] M. Gulin, J. Matuško, and M. Vašak, “Stochastic Model Predictive Control for Optimal Economic Operation of a Residential DC Microgrid,” in *Proceedings of the 2015 IEEE International Conference on Industrial Technology, ICIT 2015*, (Seville, Spain), pp. 505–510, 2015.
- [43] M. Gulin, A. Martinčević, V. Lešić, and M. Vašak, “Multi-level Optimal Control of a Microgrid-supplied Cooling System in a Building,” in *Proceedings of the IEEE PES Innovative Smart Grid Technologies, Europe, ISGT Europe 2016*, (Ljubljana, Slovenia), 2016.
- [44] M. Gulin, M. Vašak, and T. Pavlović, “Dynamical Behaviour Analysis of a DC Microgrid in Distributed and Centralized Voltage Control Configurations,” in *Proceedings of the IEEE 23rd International Symposium on Industrial Electronics, ISIE 2014*, (Istanbul, Turkey), pp. 2365–2370, 2014.
- [45] M. Gulin, T. Pavlović, and M. Vašak, “Photovoltaic panel and array static models for power production prediction: Integration of manufacturers’ and on-line data,” *Renewable Energy*, vol. 97, pp. 399–413, 2016.
- [46] M. Gulin, M. Vašak, and N. Perić, “Dynamical optimal positioning of a photovoltaic panel in all weather conditions,” *Applied Energy*, vol. 108, pp. 429–438, 2013.
- [47] M. Gulin, M. Vašak, and T. Pavlović, “Model Identification of a Photovoltaic System for a DC Microgrid Simulation,” in *Proceedings of the 16th International Power Electronics and Motion Control Conference and Exposition, PEMC 2014*, (Antalya, Turkey), pp. 413–418, 2014.
- [48] M. Gulin, M. Vašak, and M. Baotić, “Estimation of the global solar irradiance on tilted surfaces,” in *Proceedings of the 17th International Conference on Electrical Drives and Power Electronics, EDPE 2013*, (Dubrovnik, Croatia), pp. 334–339, 2013.
- [49] M. Vašak, M. Gulin, J. Čeović, D. Nikolić, T. Pavlović, and N. Perić, “Meteorological and weather forecast data-based prediction of electrical power delivery of a photovoltaic panel in a stochastic framework,” in *2011 Proceedings of the 34th International Convention on Information and Communication Technology, Electronics and Microelectronics, MIPRO 2011*, (Opatija, Croatia), pp. 733–738, 2011.
- [50] M. Gulin, T. Pavlović, and M. Vašak, “A one-day-ahead photovoltaic array power production prediction with combined static and dynamic on-line correction,” *Solar Energy*, vol. 142, pp. 49–60, 2017.
- [51] M. Gulin, M. Vašak, and J. Matuško, “Predictor-Corrector Method for Weather Forecast Improvement using Local Measurements,” in *Proceedings of the 2015 International Conference on Electrical Drives and Power Electronics, EDPE 2015*, (Tatranska Lomnica, The High Tatras, Slovakia), pp. 167–172, 2015.
- [52] M. Gulin, M. Vašak, G. Banjac, and T. Tomiša, “Load Forecast of a University Building for Application in Microgrid Power Flow Optimization,” in *Proceedings of the 2014 IEEE International Energy Conference, EnergyCon 2014*, (Dubrovnik, Croatia), pp. 1223–1227, 2014.

- [53] M. Gulin, M. Vašak, and M. Baotić, “Joint Estimation of Equivalent Electrical Model Parameters and State-of-Charge for VRLA Batteries,” in *Proceedings of the 17th International Conference on Electrical Drives and Power Electronics, EDPE 2013*, (Dubrovnik, Croatia), pp. 10–15, 2013.
- [54] J. Machowski, J. W. Bialek, and J. R. Bumby, *Power System Dynamics: Stability and Control*. John Wiley & Sons, 2 ed., 2008.
- [55] D. Eltigani and S. Masri, “Challenges of integrating renewable energy sources to smart grids: A review,” *Renewable and Sustainable Energy Reviews*, vol. 52, pp. 770–780, 2015.
- [56] F. Steinke, P. Wolfrum, and C. Hoffmann, “Grid vs. storage in a 100% renewable Europe,” *Renewable Energy*, vol. 50, pp. 826–832, 2013.
- [57] J. S. González and R. Lacal-Arántegui, “A review of regulatory framework for wind energy in European Union countries: Current state and expected developments,” *Renewable and Sustainable Energy Reviews*, vol. 56, pp. 588–602, 2016.
- [58] S. Pineda, J. M. Morales, and T. K. Boomsma, “Impact of Forecast Errors on Expansion Planning of Power Systems with a Renewables Target,” *European Journal of Operational Research*, no. 12, pp. 1–8, 2014.
- [59] I. Milstein and A. Tishler, “Can price volatility enhance market power? The case of renewable technologies in competitive electricity markets,” *Resource and Energy Economics*, vol. 41, pp. 70–90, 2015.
- [60] J. J. Justo, F. Mwasilu, J. Lee, and J.-W. Jung, “AC-microgrids versus DC-microgrids with distributed energy resources: A review,” *Renewable and Sustainable Energy Reviews*, vol. 24, pp. 387–405, 2013.
- [61] D. Pavković, M. Lobrović, M. Hrgetić, and A. Komljenović, “A design of cascade control system and adaptive load compensator for battery/ultracapacitor hybrid energy storage-based direct current microgrid,” *Energy Conversion and Management*, vol. 114, pp. 154–167, 2016.
- [62] A. Parisio, E. Rikos, and L. Glielmo, “A Model Predictive Control Approach to Microgrid Operation Optimization,” *IEEE Transactions on Control Systems Technology*, vol. 22, no. 5, pp. 1813–1827, 2014.
- [63] W. Su, J. Wang, and J. Roh, “Stochastic Energy Scheduling in Microgrids With Intermittent Renewable Energy Resources,” *IEEE Transactions on Smart Grid*, vol. 5, no. 4, pp. 1876–1883, 2014.
- [64] F. Bizzarri, A. Brambilla, L. Caretta, and C. Guardiani, “Monitoring performance and efficiency of photovoltaic parks,” *Renewable Energy*, vol. 78, pp. 314–321, 2015.
- [65] A. Firman, V. Toranzos, L. Vera, A. Busso, and J. De La Casa, “Passive monitoring of the power generated in grid connected PV systems,” *Energy Procedia*, vol. 57, no. 129, pp. 235–244, 2014.
- [66] S. Spataru, D. Sera, T. Kerekes, and R. Teodorescu, “Diagnostic method for photovoltaic systems based on light I-V measurements,” *Solar Energy*, vol. 119, pp. 29–44, 2015.
- [67] M. De Felice, M. Petitta, and P. M. Ruti, “Short-term predictability of photovoltaic production over Italy,” *Renewable Energy*, vol. 80, pp. 197–204, 2015.
- [68] T. Soubdhan, J. Ndong, H. Ould-Baba, and M.-T. Do, “A robust forecasting framework based on the Kalman filtering approach with a twofold parameter tuning procedure: Application to solar and photovoltaic prediction,” *Solar Energy*, vol. 131, pp. 246–259, 2016.
- [69] H.-T. Yang, C.-M. Huang, Y.-C. Huang, and Y.-S. Pai, “A Weather-Based Hybrid Method for 1-Day Ahead Hourly Forecasting of PV Power Output,” *IEEE Transactions on Sustainable Energy*, vol. 5, no. 3, pp. 917–926, 2014.
- [70] M. G. De Giorgi, P. M. Congedo, M. Malvoni, and D. Laforgia, “Error analysis of hybrid photovoltaic power forecasting models: A case study of mediterranean climate,” *Energy Conversion and Management*, vol. 100, pp. 117–130, 2015.
- [71] A. Mellit, A. Massi Pavan, and V. Lughi, “Short-term forecasting of power production in a large-scale photovoltaic plant,” *Solar Energy*, vol. 105, pp. 401–413, 2014.

- [72] M. P. Almeida, O. Perpiñán, and L. Narvarte, "PV power forecast using a nonparametric PV model," *Solar Energy*, vol. 115, pp. 354–368, 2015.
- [73] M. Zamo, O. Mestre, P. Arbogast, and O. Pannekoucke, "A benchmark of statistical regression methods for short-term forecasting of photovoltaic electricity production, part I: Deterministic forecast of hourly production," *Solar Energy*, vol. 105, pp. 792–803, 2014.
- [74] M. Zamo, O. Mestre, P. Arbogast, and O. Pannekoucke, "A benchmark of statistical regression methods for short-term forecasting of photovoltaic electricity production. Part II: Probabilistic forecast of daily production," *Solar Energy*, vol. 105, pp. 804–816, 2014.
- [75] B. Wolff, J. Kühnert, E. Lorenz, O. Kramer, and D. Heinemann, "Comparing support vector regression for PV power forecasting to a physical modeling approach using measurement, numerical weather prediction, and cloud motion data," *Solar Energy*, vol. 135, pp. 197–208, 2016.
- [76] A. D. Jones and C. P. Underwood, "A thermal model for photovoltaic systems," *Solar Energy*, vol. 70, no. 4, pp. 349–359, 2001.
- [77] Y. Wu and J. Wang, "A novel hybrid model based on artificial neural networks for solar radiation prediction," *Renewable Energy*, vol. 89, pp. 268–284, 2016.
- [78] C. Demain, M. Journée, and C. Bertrand, "Evaluation of different models to estimate the global solar radiation on inclined surfaces," *Renewable Energy*, vol. 50, pp. 710–721, 2013.
- [79] M. David, P. Lauret, and J. Boland, "Evaluating tilted plane models for solar radiation using comprehensive testing procedures, at a southern hemisphere location," *Renewable Energy*, vol. 51, pp. 124–131, 2013.
- [80] J. Twidell and T. Weir, *Renewable Energy Resources*. Taylor & Francis, 2 ed., 2006.
- [81] J. E. Hay, "Calculation of monthly mean solar radiation for horizontal and inclined surfaces," *Solar Energy*, vol. 23, no. 4, pp. 301–307, 1979.
- [82] I. Reda and A. Andreas, "Solar position algorithm for solar radiation applications," *Solar Energy*, vol. 76, no. 5, pp. 577–589, 2003.
- [83] C. Brancucci Martinez-Anido, B. Botor, A. R. Florita, C. Draxl, S. Lu, H. F. Hamann, and B.-M. Hodge, "The value of day-ahead solar power forecasting improvement," *Solar Energy*, vol. 129, pp. 192–203, 2016.
- [84] A. Sedić, D. Pavković, and M. Firak, "A methodology for normal distribution-based statistical characterization of long-term insolation by means of historical data," *Solar Energy*, vol. 122, pp. 440–454, 2015.
- [85] A. M. Humada, M. Hojabri, S. Mekhilef, and H. M. Hamada, "Solar cell parameters extraction based on single and double-diode models: A review," *Renewable and Sustainable Energy Reviews*, vol. 56, pp. 494–509, 2016.
- [86] S. Lineykin, M. Averbukh, and A. Kuperman, "An improved approach to extract the single-diode equivalent circuit parameters of a photovoltaic cell/panel," *Renewable and Sustainable Energy Reviews*, vol. 30, pp. 282–289, 2014.
- [87] M. G. Villalva, J. R. Gazoli, and E. R. Filho, "Comprehensive Approach to Modeling and Simulation of Photovoltaic Arrays," *IEEE Transactions on Power Electronics*, vol. 24, no. 5, pp. 1198–1208, 2009.
- [88] J. Y. Park and S. J. Choi, "A novel datasheet-based parameter extraction method for a single-diode photovoltaic array model," *Solar Energy*, vol. 122, pp. 1235–1244, 2015.
- [89] Y. Xu, X. Kong, Y. Zeng, S. Tao, and X. Xiao, "A modeling method for photovoltaic cells using explicit equations and optimization algorithm," *International Journal of Electrical Power and Energy Systems*, vol. 59, pp. 23–28, 2014.
- [90] K. Ishaque and Z. Salam, "An improved modeling method to determine the model parameters of photovoltaic (PV) modules using differential evolution (DE)," *Solar Energy*, vol. 85, no. 9, pp. 2349–2359, 2011.



- [91] M. H. Deihimi, R. A. Naghizadeh, and A. F. Meyabadi, "Systematic derivation of parameters of one exponential model for photovoltaic modules using numerical information of data sheet," *Renewable Energy*, vol. 87, pp. 676–685, 2016.
- [92] N. Yildiran and E. Tacer, "Identification of photovoltaic cell single diode discrete model parameters based on datasheet values," *Solar Energy*, vol. 127, pp. 175–183, 2016.
- [93] E. Kaplani and S. Kaplanis, "Thermal modelling and experimental assessment of the dependence of PV module temperature on wind velocity and direction, module orientation and inclination," *Solar Energy*, vol. 107, pp. 443–460, 2014.
- [94] D. Torres-Lobera and S. Valkealahti, "Inclusive dynamic thermal and electric simulation model of solar PV systems under varying atmospheric conditions," *Solar Energy*, vol. 105, pp. 632–647, 2014.
- [95] M. Tudor, S. Ivatek-Šahdan, A. Stanešić, K. Horvath, and A. Bajić, "Forecasting Weather in Croatia Using ALADIN Numerical Weather Prediction Model," in *Climate Change and Regional/Local Responses* (Y. Zhang and P. Ray, eds.), ch. 2, InTech, 2013.
- [96] T. Kovačić, I. Horvat, M. Hrastinski, K. Horvath, S. Ivatek Šahdan, and A. Stanešić, "Solar radiation forecast verification and post processing," in *Proceedings of the 14th EMS Annual Meeting & 10th European Conference on Applied Climatology, ECAC*, (Prague, Czech Republic), 2014.
- [97] J. A. Duffie and W. A. Beckman, *Solar Engineering of Thermal Processes*. John Wiley & Sons, 4 ed., 2013.
- [98] N. A. Kamarzaman and C. W. Tan, "A comprehensive review of maximum power point tracking algorithms for photovoltaic systems," *Renewable and Sustainable Energy Reviews*, vol. 37, pp. 585–598, 2014.
- [99] A. Z. Ramírez and C. B. Muñoz, "Albedo Effect and Energy Efficiency of Cities," in *Sustainable Development: Energy, Engineering and Technologies - Manufacturing and Environment* (C. Ghenai, ed.), ch. 2, InTech, 1 ed., 2012.
- [100] "Product manual: PVS300 string inverters," 2013.
- [101] "Neural Network Toolbox."
- [102] B. G. Kermani, S. S. Schiffman, and H. T. Nagle, "Performance of the Levenberg-Marquardt neural network training method in electronic nose applications," *Sensors and Actuators B: Chemical*, vol. 110, no. 1, pp. 13–22, 2005.
- [103] N. Amjady, F. Keynia, and H. Zareipour, "Short-Term Load Forecast of Microgrids by a New Bilevel Prediction Strategy," *IEEE Transactions on Smart Grid*, vol. 1, no. 3, pp. 286–294, 2010.
- [104] A. Chaouachi, R. M. Kamel, R. Andoulsi, and K. Nagasaka, "Multiobjective Intelligent Energy Management for a Microgrid," *IEEE Transactions on Industrial Electronics*, vol. 60, no. 4, pp. 1688–1699, 2013.
- [105] Q. Jiang, M. Xue, and G. Geng, "Energy Management of Microgrid in Grid-Connected and Stand-Alone Modes," *IEEE Transactions on Power Systems*, vol. 28, no. 3, pp. 3380–3389, 2013.
- [106] N. Amjady, "Short-Term Bus Load Forecasting of Power Systems by a New Hybrid Method," *IEEE Transaction on Power Systems*, vol. 22, no. 1, pp. 333–341, 2007.
- [107] A. Sharma, "Seasonal to interannual rainfall probabilistic forecasts for improved water supply management: Part 1 - A strategy for system predictor identification," *Journal of Hydrology*, vol. 239, no. 1-4, pp. 232–239, 2000.
- [108] R. J. May, H. R. Maier, G. C. Dandy, and T. M. K. G. Fernando, "Non-linear variable selection for artificial neural networks using partial mutual information," *Environmental Modelling & Software*, vol. 23, no. 10-11, pp. 1312–1326, 2008.
- [109] I. Marković, S. Jurić-Kavelj, and I. Petrović, "Partial mutual information based input variable selection for supervised learning approaches to voice activity detection," *Applied Soft Computing*, vol. 13, no. 11, pp. 4383–4391, 2013.

- [110] T. M. K. G. Fernando, H. R. Maier, and G. C. Dandy, "Selection of input variables for data driven models: An average shifted histogram partial mutual information estimator approach," *Journal of Hydrology*, vol. 367, no. 3-4, pp. 165–176, 2009.
- [111] S. Li, "A MPPT control strategy with variable weather parameter and no DC/DC converter for photovoltaic systems," *Solar Energy*, vol. 108, pp. 117–125, 2014.
- [112] E. Paparoditis and T. Sapatinas, "Short-Term Load Forecasting: The Similar Shape Functional Time-Series Predictor," *IEEE Transactions on Power Systems*, vol. 28, no. 4, pp. 3818–3825, 2013.
- [113] C. Guan, P. B. Luh, L. D. Michel, and Z. Chi, "Hybrid Kalman Filters for Very Short-Term Load Forecasting and Prediction Interval Estimation," *IEEE Transactions on Power Systems*, vol. 28, no. 4, pp. 3806–3817, 2013.
- [114] S. Kouhi and F. Keynia, "A new cascade NN based method to short-term load forecast in deregulated electricity market," *Energy Conversion and Management*, vol. 71, pp. 76–83, 2013.
- [115] J. C. Sousa, L. P. Neves, and H. M. Jorge, "Assessing the relevance of load profiling information in electrical load forecasting based on neural network models," *International Journal of Electrical Power and Energy Systems*, vol. 40, no. 1, pp. 85–93, 2012.
- [116] M. Alamaniotis, A. Ikononopoulos, and L. H. Tsoukalas, "Evolutionary Multiobjective Optimization of Kernel-Based Very-Short-Term Load Forecasting," *IEEE Transactions on Power Systems*, vol. 27, no. 3, pp. 1477–1484, 2012.
- [117] S. Fan and R. J. Hyndman, "Short-Term Load Forecasting Based on a Semi-Parametric Additive Model," *IEEE Transactions on Power Systems*, vol. 27, no. 1, pp. 134–141, 2012.
- [118] J. W. Taylor, "Short-Term Load Forecasting With Exponentially Weighted Methods," *IEEE Transactions on Power Systems*, vol. 27, no. 1, pp. 458–464, 2012.
- [119] N. Amjady and A. Daraeepour, "Midterm Demand Prediction of Electrical Power Systems Using a New Hybrid Forecast Technique," *IEEE Transactions on Power Systems*, vol. 26, no. 2, pp. 755–765, 2011.
- [120] Y. Chakhchoukh, P. Panciatici, and L. Mili, "Electric Load Forecasting Based on Statistical Robust Methods," *IEEE Transactions on Power Systems*, vol. 26, no. 3, pp. 982–991, 2011.
- [121] A. Parisio and L. Glielmo, "Stochastic Model Predictive Control for Economic/Environmental Operation Management of Microgrids," in *Proceedings of the 2013 European Control Conference, ECC*, (Zürich, Switzerland), pp. 2014–2019, 2013.
- [122] S. Julier, J. Uhlmann, and H. F. Durrant-Whyte, "A New Method for the Nonlinear Transformation of Means and Covariances in Filters and Estimators," *IEEE Transactions on Automatic Control*, vol. 45, no. 3, pp. 477–482, 2000.
- [123] K. Ito and K. Xiong, "Gaussian Filters for Nonlinear Filtering Problems," *IEEE Transactions on Automatic Control*, vol. 45, no. 5, pp. 910–927, 2000.
- [124] G. Byeon, T. Yoon, S. Oh, and G. Jang, "Energy Management Strategy of the DC Distribution System in Buildings Using the EV Service Model," *IEEE Transactions on Power Electronics*, vol. 28, no. 4, pp. 1544–1554, 2013.
- [125] R. H. Lasseter, "Smart Distribution: Coupled Microgrids," *Proceedings of the IEEE*, vol. 99, no. 6, pp. 1074–1082, 2011.
- [126] A. Parisio and L. Glielmo, "Energy Efficient Microgrid Management using Model Predictive Control," in *Proceedings of the 2011 50th IEEE Conference on Decision and Control and European Control Conference, CDC-ECC*, (Orlando, Florida, USA), pp. 5449–5454, 2011.
- [127] Y. Riffonneau, S. Bacha, F. Barruel, and S. Ploix, "Optimal Power Flow Management for Grid Connected PV Systems With Batteries," *IEEE Transactions on Sustainable Energy*, vol. 2, no. 3, pp. 309–320, 2011.
- [128] P. O. Kriett and M. Salani, "Optimal control of a residential microgrid," *Energy*, vol. 42, no. 1, pp. 321–330, 2012.

- [129] P. Malysz, S. Sirouspour, and A. Emadi, "An Optimal Energy Storage Control Strategy for Grid-Connected Microgrids," *IEEE Transactions on Smart Grid*, vol. 5, no. 4, pp. 1785–1796, 2014.
- [130] W. Al-Saedi, S. W. Lachowicz, D. Habibi, and O. Bass, "Power flow control in grid-connected microgrid operation using Particle Swarm Optimization under variable load conditions," *Electrical Power and Energy Systems*, vol. 49, no. 1, pp. 76–85, 2013.
- [131] A. Takeuchi, T. Hayashi, Y. Nozaki, and T. Shimakage, "Optimal Scheduling Using Metaheuristics for Energy Networks," *IEEE Transactions on Smart Grid*, vol. 3, no. 2, pp. 968–974, 2012.
- [132] G.-C. Liao, "Solve environmental economic dispatch of Smart MicroGrid containing distributed generation system – Using chaotic quantum genetic algorithm," *Electrical Power and Energy Systems*, vol. 43, no. 1, pp. 779–787, 2012.
- [133] M. Y. El-Sharkh, A. Rahman, and M. S. Alam, "Evolutionary programming-based methodology for economical output power from PEM fuel cell for micro-grid application," *Journal of Power Sources*, vol. 139, no. 1-2, pp. 165–169, 2005.
- [134] A. Bemporad and M. Morari, "Control of systems integrating logic, dynamics, and constraints," *Automatica*, vol. 35, no. 3, pp. 407–427, 1999.
- [135] J. Löfberg, "YALMIP : A toolbox for modeling and optimization in MATLAB," in *Proceedings of the 2004 IEEE International Symposium on Computer Aided Control Systems Design, CACSD 2004*, (Taipei, Taiwan), pp. 284–289, 2004.
- [136] J. Matusko and F. Borrelli, "Scenario-Based Approach to Stochastic Linear Predictive Control," in *Proceedings of the 51st IEEE Conference on Decision and Control, CDC 2012*, (Maui, Hawaii, USA), pp. 5194–5199, 2012.
- [137] S. Mohammadi, S. Soleymani, and B. Mozafari, "Scenario-based stochastic operation management of MicroGrid including Wind, Photovoltaic, Micro-Turbine, Fuel Cell and Energy Storage Devices," *Electrical Power and Energy Systems*, vol. 54, pp. 525–535, 2014.
- [138] T. Ma, H. Yang, and L. Lu, "Solar photovoltaic system modeling and performance prediction," *Renewable and Sustainable Energy Reviews*, vol. 36, pp. 304–315, 2014.
- [139] C. E. García, D. M. Prett, and M. Morari, "Model Predictive Control: Theory and Practice—a Survey," *Automatica*, vol. 25, no. 3, pp. 335–348, 1989.
- [140] A. Martinčević, M. Vašak, and V. Lešić, "Model Predictive Control for Energy-saving and Comfortable Temperature Control in Buildings," in *Proceedings of the 24th Mediterranean Conference on Control and Automation, MED 2016*, (Athens, Greece), pp. 298–303, 2016.
- [141] "[ISO 7730:2005] Ergonomics of the thermal environment - Analytical determination and interpretation of thermal comfort using calculation of the PMV and PPD indices and local thermal comfort criteria," 2005.
- [142] T. Dragičević, J. M. Guerrero, J. C. Vasquez, and D. Škrlec, "Supervisory Control of an Adaptive-Droop Regulated DC Microgrid With Battery Management Capability," *IEEE Transactions on Power Electronics*, vol. 29, no. 2, pp. 695–706, 2014.
- [143] J. M. Guerrero, J. C. Vasquez, J. Matas, L. G. De Vicuña, and M. Castilla, "Hierarchical Control of Droop-Controlled AC and DC Microgrids - A General Approach Toward Standardization," *IEEE Transactions on Industrial Electronics*, vol. 58, no. 1, pp. 158–172, 2011.
- [144] J. M. Guerrero, L. Hang, and J. Uceda, "Control of Distributed Uninterruptible Power Supply Systems," *IEEE Transactions on Industrial Electronics*, vol. 55, no. 8, pp. 2845–2859, 2008.

---

## CURRICULUM VITAE

Marko Gulin was born in Šibenik, Croatia, in 1988. He graduated from math-oriented high school in Šibenik in 2006 and earned his bachelor's and master's degrees in electrical engineering and information technology from the University of Zagreb Faculty of Electrical Engineering and Computing (UNIZG-FER), Croatia, in 2009 and 2011, respectively. His research interests are in the domain of optimal control, machine learning, estimation theory, and model identification with application in power electronics, microgrids, and smart grids.

After earning his master's degree, he was employed at the Department of Control and Computer Engineering (ZARI) within UNIZG-FER as research assistant on projects funded by the Croatian Science Foundation (HRZZ) and the European Union. Besides scientific work, he also worked as teaching assistant in several courses. From 2012 to 2014 he was a two-term president of the Student Council at FER. In 2014 he was a visiting researcher at the Eidgenössische Technische Hochschule Zürich (ETHZ), Switzerland. From 2014 to 2015 he was a member of a working group to establish the Study for energy efficiency and renewable sources of University of Zagreb in Šibenik, where he also worked as teaching assistant. In 2016 he founded a company GULIN Automation and Control d.o.o. for research and development in the field of electrical engineering, power electronics, and industrial automation and control. From 2016 to 2017 he worked at the Rochester Institute of Technology (RIT), Croatia, as lecturer in the field of information technology and computing. From 2017 to 2019 he worked at Rimac Automobili d.o.o. as control engineer in the field of power electronics and electric drives for the hypercar Rimac C\_Two. Since 2020 he has been employed at Advantics Sarl, France, as control and software engineer in the field of power electronics for electric vehicle charging stations.

From 2007 to 2011 he received a scholarship for exceptional students from the City of Šibenik. In 2011 he was awarded with the "Rector Award" for the student scientific paper "Model predictive control for raising efficiency of renewable electrical energy sources." He graduated *magna cum laude* in 2011. From 2011 to 2017 he was a student member of IEEE. Papers published at the time of his doctoral dissertation are listed in the sequel.

---

## MY PUBLICATIONS

### JOURNAL PUBLICATIONS:

- [1] M. Gulin, T. Pavlović, and M. Vašak, "A one-day-ahead photovoltaic array power production prediction with combined static and dynamic on-line correction," *Solar Energy*, vol. 142, pp. 49–60, 2017.
- [2] M. Gulin, T. Pavlović, and M. Vašak, "Photovoltaic panel and array static models for power production prediction: Integration of manufacturers' and on-line data," *Renewable Energy*, vol. 97, pp. 399–413, 2016.
- [3] M. Gulin, M. Vašak, and N. Perić, "Dynamical optimal positioning of a photovoltaic panel in all weather conditions," *Applied Energy*, vol. 108, pp. 429–438, 2013.

### CONFERENCE PUBLICATIONS:

- [1] M. Gulin, A. Martinčević, V. Lešić, and M. Vašak, "Multi-level Optimal Control of a Microgrid-supplied Cooling System in a Building," in *Proceedings of the IEEE PES Innovative Smart Grid Technologies Conference Europe, ISGT Europe 2016*, pp. 1–6, Ljubljana, Slovenia, 2016.
- [2] M. Gulin, M. Vašak, and M. Baotić, "Analysis of Microgrid Power Flow Optimization with Consideration of Residual Storages State," in *Proceedings of the 2015 European Control Conference, ECC 2015*, pp. 3131–3136, Linz, Austria, 2015.
- [3] M. Gulin, J. Matuško, and M. Vašak, "Stochastic Model Predictive Control for Optimal Economic Operation of a Residential DC Microgrid," in *Proceedings of the 2015 IEEE International Conference on Industrial Technology, ICIT 2015*, pp. 505–510, Sevilla, Spain, 2015.
- [4] M. Gulin, M. Vašak, and J. Matuško, "Predictor-Corrector Method for Weather Forecast Improvement using Local Measurements," in *Proceedings of the 18th International Conference on Electrical Drives and Power Electronics, EDPE 2015*, pp. 167–172, Tatranská Lomnica, The High Tatras, Slovakia, 2015.
- [5] V. Lešić, M. Vašak, A. Martinčević, M. Gulin, A. Starčić, and H. Novak, "Computer-assisted Management of Building Climate and Microgrid with Model Predictive Control," in *Proceedings of the 17th International Conference on Civil and Building Engineering, ICCBE 2015*, pp. 1009–1020, Dubai, UAE, 2015.
- [6] H. Novak, M. Vašak, M. Gulin, and V. Lešić, "Railway Transport System Energy Flow Optimization with Integrated Microgrid," in *Proceedings of the 12th International Conference on Modern Electrified Transport, MET 2015*, pp. 88–94, Trogir, Croatia, 2015.
- [7] M. Gulin, M. Vašak, and T. Pavlović, "Model Identification of a Photovoltaic System for a DC Microgrid Simulation," in *Proceedings of the 16th International Power Electronics and Motion Control Conference and Exposition, PEMC 2014*, pp. 501–506, Antalya, Turkey, 2014.
- [8] M. Gulin, M. Vašak, and T. Pavlović, "Dynamical Behaviour Analysis of a DC Microgrid in Distributed and Centralized Voltage Control Configurations," in *Proceedings of the 2014 IEEE 23rd International Symposium on Industrial Electronics, ISIE 2014*, pp. 2361–2366, Istanbul, Turkey, 2014.
- [9] M. Gulin, M. Vašak, G. Banjac, and T. Tomiša, "Load Forecast of a University Building for Application in Microgrid Power Flow Optimization," in *Proceedings of the 2014 IEEE International Energy Conference, EnergyCon 2014*, pp. 1284–1288, Dubrovnik, Croatia, 2014.
- [10] M. Gulin, M. Vašak, and M. Baotić, "Estimation of the global solar irradiance on tilted surfaces," in *Proceedings of the 17th International Conference on Electrical Drives and Power Electronics, EDPE 2013*, pp. 334–339, Dubrovnik, Croatia, 2013.

- [11] M. Gulin, M. Vašak, and M. Baotić, "Joint Estimation of Equivalent Electrical Model Parameters and State-of-Charge for VRLA Batteries," in *Proceedings of the 17th International Conference on Electrical Drives and Power Electronics, EDPE 2013*, pp. 10–15, Dubrovnik, Croatia, 2013.
- [12] M. Vašak, M. Gulin, J. Čeović, D. Nikolić, T. Pavlović, and N. Perić, "Meteorological and weather forecast data-based prediction of electrical power delivery of a photovoltaic panel in a stochastic framework," in *2011 Proceedings of the 34th International Convention on Information and Communication Technology, Electronics and Microelectronics, MIPRO 2011*, pp. 93–98, Opatija, Croatia, 2011.
- [13] M. Gulin, J. Matuško, and F. Kolonić, "Control of a single pendulum gantry with friction compensation," in *2011 Proceedings of the 34th International Convention on Information and Communication Technology, Electronics and Microelectronics, MIPRO 2011*, pp. 206–211, Opatija, Croatia, (in Croatian), 2011.

**RESEARCH STUDIES:**

- [1] I. Petrović, M. Baotić, J. Matuško, M. Vašak, I. Marković, M. Gulin, and M. Đalto, "Aplikacija za predviđanje satne potrošnje električne energije i izračun gubitaka," *HEP - Operator distribucijskog sustava d.o.o.*, (in Croatian), 2015.

---

## ŽIVOTOPIS

Marko Gulin rođen je 1988. godine u Šibeniku, Hrvatska. Prirodoslovno-matematičku gimnaziju u Šibeniku završio je 2006. godine, te je stekao titulu sveučilišnog prvostupnika i magistra inženjera u polju elektrotehnike i informacijske tehnologije na Sveučilištu u Zagrebu Fakultetu elektrotehnike i računarstva (FER), Hrvatska, 2009. i 2011. godine, tim redom. Njegovi istraživački interesi su u području optimalnog upravljanja, strojnog učenja, teorije estimacije i metoda identifikacije sustava s primjenom u energetskej elektronici, mikromrežama i naprednim energetskej mrežama.

Po završetku studija zapošljava se u Zavodu za automatiku i računalno inženjerstvo (ZARI) na FER-u, gdje je do 2016. godine radio kao znanstveni novak na istraživačkim projektima financiranima od strane Hrvatske zaklade za znanost (HRZZ) i Europske unije. Uz znanstveni rad bio je i asistent na nekoliko kolegija. Od 2012. do 2014. godine bio je predsjednik Studentskog zbora FER-a u dva mandata. U 2014. godini bio je gostujući istraživač na Eidgenössische Technische Hochschule Zürich (ETHZ), Švicarska. Od 2014. do 2015. godine bio je član radne skupine za uspostavljanje dislociranog Studija energetske učinkovitosti i obnovljivih izvora pri Sveučilištu u Zagrebu u Šibeniku, gdje je također radio kao asistent. U 2016. godini osnovao je tvrtku GULIN Automation and Control d.o.o. za istraživanje i razvoj u području elektrotehnike, energetske elektronike, upravljanja i industrijske automatizacije. Od 2016. do 2017. godine radio je na Rochester Institute of Technology (RIT), Hrvatska, kao predavač u području informacijske tehnologije i računarstva. Od 2017. do 2019. godine radio je u tvrtki Rimac Automobili d.o.o. kao inženjer u području energetske elektronike i upravljanja električnim pogonima za superbrzi automobil Rimac C\_Two. Od 2020. godine radi u tvrtki Advantics Sarl, Francuska, kao inženjer u području razvoja uređaja energetske elektronike i upravljanja s primjenom na punionice za električna vozila.

Od 2007. do 2011. godine primao je stipendiju za nadarene studente Grada Šibenika. U 2011. godini nagrađen je "Rektorovom nagradom" za studentski rad znanstvenog sadržaja pod nazivom "Modelsko prediktivno upravljanje za povećanje efikasnosti agregata obnovljivih izvora električne energije". Diplomski studij završio je 2011. godine s velikom pohvalom (*magna cum laude*). Od 2011. do 2017. godine bio je studentski član udruge IEEE.

#### COLOPHON

This document was typeset in  $\text{\LaTeX}$  by using `ferphd` style developed by Marko Gulin, which is inspired by the typographical look-and-feel `ferbook` developed by Jadranko Matuško and Ivan Marković.